



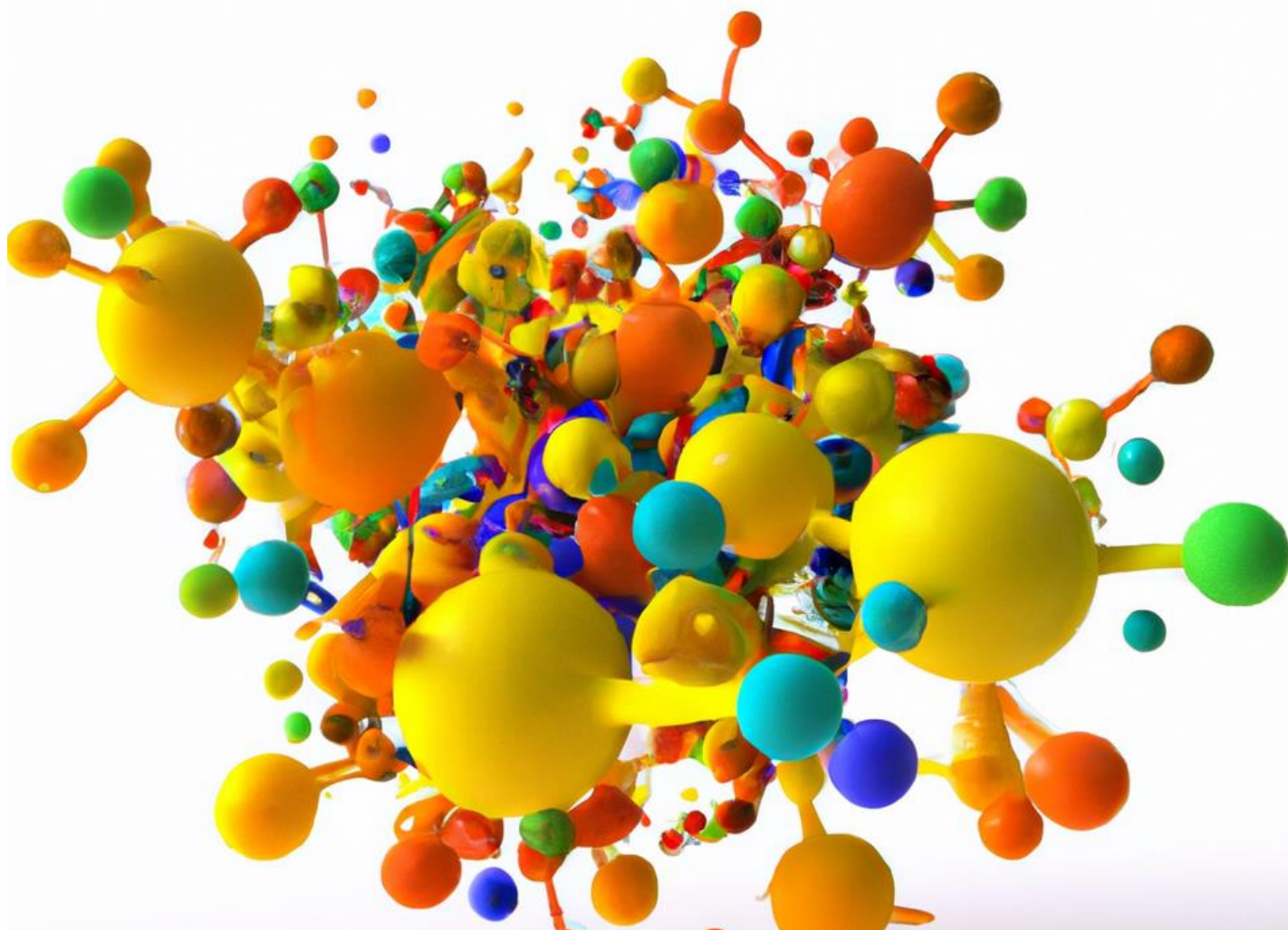
PhD Thesis

**Novel promising antibacterial agents and carbon dioxide capture and valorization materials based on pyrazolate Coordination Polymers and Metal-Organic Frameworks**

Cycle XXXV, 2019/20-2022/23

Scientific Sector CHIM/03

PhD Candidate: Patrizio Campitelli







# UNIVERSITY OF CAMERINO

School of Advanced Studies  
*Doctorate Course in Chemical and Pharmaceutical  
Sciences and Biotechnology – Chemical Sciences*

---

## **Novel promising antibacterial agents and carbon dioxide capture and valorization materials based on pyrazolate Coordination Polymers and Metal-Organic Frameworks**

PhD Thesis

Cycle XXXV

Scientific Sector CHIM/03

*PhD Candidate*

Patrizio Campitelli

*Supervisor*

Prof. Corrado Di Nicola

---

2019/20-2022/23



# Summary

Abstract.....	V
List of abbreviations .....	VII
List of Figures .....	X
<b>CHAPTER 1: Introduction.....</b>	<b>2</b>
1.1 Nomenclature notions: Coordination Polymers, Coordination Networks and Metal-Organic Frameworks ... Let's make it clear! .....	2
1.2 The birth of Reticular Chemistry.....	7
1.3 CPs and MOFs structural motifs .....	13
1.4 Synthetic routes for CPs and MOFs production.....	22
1.5 Activation of MOFs .....	30
1.6 Determination of MOFs porosity.....	34
1.7 Pyrazolate-based linker for the synthesis of CPs and MOFs.....	42
1.8 Applications of MOFs: antibacterial activity and carbon dioxide capture and reutilization .....	48
<b>CHAPTER 2: Antibacterial Activity of Cu(II) Pyrazolate-based Coordination Polymers .....</b>	<b>55</b>
2.1 Aim of the research work.....	56
2.2 Experimental section .....	57
2.2.1 Material and methods.....	57
2.2.2 Synthesis of CP 2, $[\text{Cu}(\mu\text{-NO}_2\text{-pz})_2]_n$ .....	58
2.2.3 Synthesis of CP 5, $[\text{Cu}(\mu\text{-NO}_2\text{-pz})_2\cdot\text{DMF}]_n$ .....	58
2.2.4 Crystal structure of CP 2, $[\text{Cu}(\mu\text{-NO}_2\text{-pz})_2]_n$ and CP 5, $[\text{Cu}(\mu\text{-NO}_2\text{-pz})_2\cdot\text{DMF}]_n$ .....	59
2.2.5 Bacterial culture .....	60
2.2.6 Antibacterial Rate (%) and Viable Cells (%).....	60
2.2.7 Bacterial Growth curve.....	61

2.2.8	Detection Reactive Oxygen Species (ROS)	61
2.2.9	Propidium Iodide (PI) uptake	62
2.2.10	Metal ions release test	62
2.3	Results and discussions	63
2.3.1	Synthetic procedures	63
2.3.2	Infrared characterization	63
2.3.3	Thermogravimetric analyses	65
2.3.4	Crystal structure of 2 [Cu( $\mu$ -NO <sub>2</sub> -pz) <sub>2</sub> ] <sub>n</sub>	67
2.3.5	Antibacterial activity: bacterial growth curve and antibacterial rate	69
2.3.6	Antibacterial mechanism: ROS production test, PI uptake and metal ions release test	73
2.4	Conclusions	77
<b>CHAPTER 3: Antibacterial Activity of zinc and copper bis(pyrazolate)-based MOFs</b>		<b>79</b>
3.1	Aim of the research work	80
3.2	Experimental section	81
3.2.1	Materials and methods	81
3.2.2	Bacterial culture	81
3.2.3	Antibacterial rate (%)	81
3.2.4	Detection Reactive Oxygen Species (ROS)	82
3.2.5	Propidium Iodide (PI) uptake	82
3.3	Results and discussions	83
3.3.1	Preparation of Zinc and Copper bis(pyrazolate)-based MOFs	83
3.3.2	Zinc and Copper bis(pyrazolate)-based MOFs structures and BET Surface Area	83
3.3.3	Antibacterial activity: antibacterial rate	85
3.3.4	Antibacterial mechanism: ROS production test and PI uptake	86
3.4	Conclusions	88

<b>CHAPTER 4: Carbon dioxide capture and conversion through fixation with epoxides in diamino-decorated Zn(II)-bipyrazolate MOFs.....</b>	<b>89</b>
4.1 Aim of the research work.....	90
4.2 Experimental section.....	91
4.2.1 Material and methods.....	91
4.2.2 Synthesis of 3,3'-H <sub>2</sub> L.....	92
4.2.3 Synthesis of Zn(3,3'-L).....	92
4.2.4 Synthesis of Zn(3,5-L).....	93
4.2.5 Preparation of [epibromohydrin@Zn(3,3'-L)].....	93
4.2.6 Powder X-ray diffraction (PXRD) structure determination.....	93
4.2.7 Variable-temperature powder X-ray diffraction.....	95
4.2.8 Water vapor stability test.....	95
4.2.9 N <sub>2</sub> and CO <sub>2</sub> adsorption and BET Surface Area determination.....	95
4.2.10 Catalytic CO <sub>2</sub> epoxidation with Zn(3,3'-L) and Zn(3,5-L).....	96
4.3 Results and discussions.....	97
4.3.1 Synthetic procedures.....	97
4.3.2 Infrared characterization.....	98
4.3.3 Thermal behavior.....	98
4.3.4 Crystal structure of 3,3'- H <sub>2</sub> L and Zn(3,3'-L).....	99
4.3.5 N <sub>2</sub> adsorption and BET Surface Area determination.....	101
4.3.6 CO <sub>2</sub> adsorption at 273 and 298 K.....	102
4.3.7 Zn(3,3'-L) and Zn(3,5-L) catalytic activity in CO <sub>2</sub> cycloaddition to halogenated epoxides.....	104
4.4 Conclusions.....	107
<b>CHAPTER 5: Carbon dioxide capture and electroreduction with mixed Cu(II)/Ni(II) bipyrazolate MOFs.....</b>	<b>109</b>
5.1 Aim of the research.....	110

5.2 Experimental section .....	111
5.2.1 Materials and methods .....	111
5.2.2 Synthesis of [Cu <sub>0.05</sub> Ni <sub>0.95</sub> (3,5-L)] (Cu <sub>0.05</sub> Ni <sub>0.95</sub> ).....	111
5.2.3 Synthesis of [Cu <sub>0.1</sub> Ni <sub>0.9</sub> (3,5-L)] (Cu <sub>0.1</sub> Ni <sub>0.9</sub> ).....	112
5.2.4 Synthesis of [Cu <sub>0.2</sub> Ni <sub>0.8</sub> (3,5-L)] (Cu <sub>0.2</sub> Ni <sub>0.8</sub> ).....	112
5.2.5 Synthesis of [Cu <sub>0.5</sub> Ni <sub>0.5</sub> (3,5-L)] (Cu <sub>0.5</sub> Ni <sub>0.5</sub> ).....	112
5.2.6 Crystal structure of Cu <sub>0.5</sub> Ni <sub>0.5</sub> .....	113
5.2.7 N <sub>2</sub> and CO <sub>2</sub> adsorption and BET Surface Area determination .....	114
5.2.8 CO <sub>2</sub> electroreduction tests with Cu/Ni mixed MOFs.....	114
5.3 Results and discussions .....	115
5.3.1 Synthesis of the mixed Cu/Ni MOFs .....	115
5.3.2 Preliminary characterization of the mixed Cu/Ni MOFs .....	116
5.3.3 Thermal behavior .....	118
5.3.4 Crystal structure of Cu <sub>0.5</sub> Ni <sub>0.5</sub> .....	119
5.3.5 N <sub>2</sub> and CO <sub>2</sub> adsorption and BET Surface Area determination.....	120
5.3.6 Electrocatalytic performances of Cu/Ni mixed MOFs .....	124
5.4 Conclusions.....	127
<b>Bibliography.....</b>	<b>128</b>
<b>List of publications .....</b>	<b>140</b>
<b>Contributions to conferences.....</b>	<b>141</b>



## Abstract

Coordination Polymers (CPs) and Metal-Organic Frameworks (MOFs) have emerged in the last thirty years, due to their hybrid organic/inorganic nature and incredible versatility, which has allowed their wide use in various fields: catalysis, sensing, luminescence, magnetism, conductivity, antimicrobial activity etc. Crystallinity and porosity of MOFs, in addition, open to other interesting applications such as gas storage and conversion, separation and drug delivery.

The thesis work has focused on two main aspects: the antibacterial activity of CPs and MOFs exploring the simultaneous activity of the metal center and the organic molecules, and the capture and conversion of carbon dioxide in useful chemicals within MOFs pores.

In detail, eight Cu(II) CPs based on 4-X-pyrazolate linkers (X= H, Cl, Br, I and NO<sub>2</sub>) have been investigated as antibacterial agents against *S. aureus*, *E. coli* and *P. aeruginosa*, whereas six MOFs consisting of zinc or copper metal centers and three different bipyrazolate linkers (4,4'-bipyrazole, 1,4-bis(1H-pyrazol-4-yl-3,5-dimethyl)benzene and 3-amino-4,4'-bipyrazole) have been tested against *S. aureus* and *E. coli*. Bacterial growth inhibition, antibacterial rate (%), ROS and PI assays and metal ions release tests revealed the action mechanism which is expressed in the interaction between the CP/MOF surface with the bacterial cell in combination with metal ions release, and in the production of ROS damaging the bacterial cell content.

The second issue deals with CO<sub>2</sub> trapping and its conversion by two distinct techniques: i) fixation by reaction with activated epoxides and ii) electroreduction.

In the first case, two Zn(II) MOFs based on isomeric forms of diamino-4,4'-bipyrazole linkers have been synthesized, solid-state characterized (PXRD, TGA, IR, porosimetry) and tested as heterogeneous catalysts in the conversion of carbon dioxide and epibromohydrin or epichlorohydrin into the corresponding cyclic carbonates in solvent-free conditions, at 393K and 5 bar of CO<sub>2</sub> pressure. Lastly, four mixed-metal MOFs with formula unit [Cu<sub>x</sub>Ni<sub>1-x</sub>(3,5-diamino-4,4'-bipyrazolate)] (Cu<sub>x</sub>Ni<sub>1-x</sub>, x = 0.05, 0.1, 0.2, 0.5) were synthesized, characterized (PXRD, TGA, IR, porosimetry, SEM, EDX, ICP, XPS) and employed for carbon dioxide electroreduction to produce methane and carbon monoxide.



## List of abbreviations

1,3-BDP:	1,3-benzenedipyrazolate
2mIM:	2-methylimidazolate
3,5-PDC:	3,5-pyridinedicarboxylic acid
4,4'-Bpe:	<i>trans</i> -bis(4-pyridyl)ethylene)
BASF:	Badische Anilin und Soda Fabrik
BDC:	1,4-benzenedicarboxylate
BDP:	1,4-benzenedipyrazolate
BET:	Brunauer, Emmett and Teller
BIPY:	4,4'-bipyridine
BJH:	Barrett, Joyner and Halenda
BPDC:	biphenyl-4,4'-dicarboxylate
bpe:	1,2-bis(4'-pyridyl)ethylene
BPZ:	bipyrazolate
BTC:	benzene-1,3,5-tricarboxylate
CA:	chronoamperometry
CB:	4-cyanobenzoate
CDC:	<i>trans</i> -1,4-cyclohexanedicarboxylate
cdipz:	4-chloride-3,5-diisopropyl-1-pyrazolate anion
CLSM:	Confocal Laser Scanning Microscopy
CN:	Coordination Network
COF:	Covalent-Organic Framework
CP:	Coordination Polymer
CV:	Cyclic Voltammetry
DCFH-DA:	dichlorofluorescein diacetate
dcppy:	2-phenylpyridine-5,4'-dicarboxylic acid
DEE:	N,N-diethylethanamide
DEF:	N,N-diethylformamide
DEP:	N,N-diethylpropanamide
DFT:	Density Functional Theory
dhtp:	2,5-dihydroxyterephthalate
dhtp:	2,5-dihydroxyterephthalate
DMA:	N,N-dimethylacetamide
DMF:	N,N-dimethylformamide
DMSO:	dimethylsulfoxide
DPE:	N,N-dipropylethanamide
DPP:	N,N-dipropylpropanamide
<i>E. coli</i> :	<i>Escherichia coli</i>
F <sub>4</sub> TCNQ:	2,3,5,6-tetrafluoro-7,7,8,8-tetracyanoquinodimethane
H <sub>2</sub> BDMPX:	1,4-bis((3,5-dimethyl-1H-pyrazol-4-yl)methyl)benzene

H<sub>2</sub>BDPNH<sub>2</sub>: 2-amino-1,4-bis(1H-pyrazol-4-yl)benzene  
 H<sub>2</sub>BPE: 4,4'-buta-1,3-diyne-1,4-diylbis(3,5-dimethyl-1H-pyrazole)  
 H<sub>2</sub>BPEB: 4,4'-(benzene-1,4-diyl)diethyne-2,1-diylbis(1H-pyrazole)  
 H<sub>2</sub>BPZNO<sub>2</sub>: 3-nitro-4,4'-bipyrazole  
 H<sub>2</sub>DMPMB: 4,4'-bis((3,5-dimethyl-1H-pyrazol-4-yl)methyl)biphenyl  
 H<sub>2</sub>NDI-H: bis(N-(3,5-dimethyl-1H-pyrazol-4-yl))naphthalenetetracarboxylicdianhydrid  
 H<sub>2</sub>PBP: 4,4'-bis(1H-pyrazol-4-yl)biphenyl  
 H<sub>3</sub>BTPP: 1,3,5-tris((1H-pyrazol-4-yl)phenyl)benzene  
 Hf-NU-1000: Zr<sub>6</sub>(μ<sub>3</sub>-OH/O)<sub>8</sub>(H<sub>2</sub>O,OH)<sub>8</sub>(TBAPy)<sub>2</sub>  
 HKUST: Hong Kong University of Science and Technology  
 HKUST-1: MOF-199, Cu-BTC, Cu<sub>2</sub>(BTC)<sub>3</sub>, Cu<sub>3</sub>(BTC)<sub>2</sub>  
 HNDX: nalidixic acid  
 IL: Ionic Liquid  
 IN: pyridylcarboxylate or isonicotinate  
 IRMOFs: IsoReticular MOFs  
 IUPAC: International Union of Pure and Applied Chemistry  
 LAG: Liquid-Assisted Grinding  
 LB: Lewis Base  
 L-Tyr: L-Tyrosinate  
 mbih: 1,6-bis(2-methylbenzimidazolyl)hexane  
 Me4BPZ: 3,3',5,5'-tetramethyl-4,4'-bipyrazolate  
 MOF: Metal-Organic Framework  
 MOF-199: HKUST-1, Cu-BTC, Cu<sub>2</sub>(BTC)<sub>3</sub>, Cu<sub>3</sub>(BTC)<sub>2</sub>  
 MOF-2: Zn(BDC)(H<sub>2</sub>O)  
 MOF-5: Zn<sub>4</sub>O(BDC)<sub>3</sub>  
 MOF-74 (Ni): Ni<sub>2</sub>(dhtp)  
 NLDFE: Non-Local Density Functional Theory  
 NU: Northwestern University  
 NU109E: Cu(tcepbb)  
 NU110E: Cu(tcepepb)  
 NU-1501 Al: Al<sub>3</sub>(μ<sub>3</sub>-O)(H<sub>2</sub>O)<sub>2</sub>(OH)(PET)<sub>2</sub>  
*P. aeruginosa*: *Pseudomonas aeruginosa*  
 PCN: Porous Coordination Network  
 PCN-222 (Fe):Zr<sub>6</sub>(μ<sub>3</sub>-OH)<sub>8</sub>(OH)<sub>8</sub>(TCPP)<sub>2</sub>  
 PEBA 4-[2-(4-pyridyl)ethenyl]benzoate  
 PET: Peripherally Extended Triptycene  
 phen: 1,10-phenanthroline  
 PI: Propidium Iodide  
 PSM: Post-Synthetic Modification  
 Py: Pyridine  
 pydc: pyridine-2,3-dicarboxylate  
 pyr2c: pyrimidine-2-carboxylate

pz:	pyrazolate
RTIL:	Room Temperature Ionic Liquid
<i>S. aureus</i> :	<i>Staphylococcus aureus</i>
SBU:	Secondary Building Unit
SDBA:	4,4'-sulfonyldibenzoate
SNU-70:	Zn <sub>4</sub> O(4-carboxylate-cinnamate) <sub>3</sub>
SPC:	Soft Porous Crystal
TBAB:	tetrabutylammonium bromide
TBAPy:	4,4',4'',4'''-(1,8-dihydropyrene-1,3,6,8-tetrayl)tetrabenzoate
tcepbb:	1,3,5-tris[(1,3-carboxylate-5-(4-(ethynyl)phenyl))butadiynyl]-benzene
tcepepb:	1,3,5-tris[((1,3-carboxylate-5-(4-(ethynyl)phenyl))ethynyl)phenyl]-benzene
TCPP:	4,4',4'',4'''-(porphyrin-5,10,15,20-tetrayl)tetrabenzoate
TMA:	3-thiophenemalonate
UiO:	University of Oslo
UiO-67:	Zr <sub>6</sub> O <sub>4</sub> (OH) <sub>4</sub> (BPDC) <sub>12</sub>
ULMOF:	Ultra-Light MOF
ULMOF-4:	Li <sub>2</sub> (3,5-PDC)
UMCM-9:	Zn <sub>4</sub> O(naphthalene-2,6-dicarboxylate) <sub>1.5</sub> (biphenyl-4,4'-dicarboxylate) <sub>1.5</sub>
ZIF:	Zeolite Imidazolate Framework
ZIF-8:	Zn(2mIM) <sub>2</sub>

# List of Figures

Figure 1 Structure of 1D-CP $[Ag(Me_4BPZ)NO_3 \cdot CH_3OH]_n$ . Carbon (grey), nitrogen (violet), oxygen (red) and silver (white) atoms are shown. Hydrogen atoms and methanol coordinating molecules are omitted for clarity. CCDC Database Identifier: QOTHIO; CCDC Deposition Number: 148207. <sup>5</sup>	3
Figure 2 $Ag(1,4\text{-pyrazine})_{1.5}CF_3SO_3$ coordination network structure. Carbon (grey), nitrogen (violet), and silver (white) atoms are indicated. Hydrogen atoms and trifluoromethane-sulfonate coordinating molecules aren't shown. CCDC Database Identifier: TOZGOE; CCDC Deposition Number: 1274955. <sup>6</sup>	3
Figure 3 Hoffmann Clathrate original structure: $[Ni(CN)_2(NH_3)]C_6H_6$ . Carbon (grey), nitrogen (green), and nickel (light blue) atoms are indicated. <sup>10</sup>	4
Figure 4 ZIF-8: $Zn(2mIM)_2$ crystal structure showing free cavities. Carbon (grey), nitrogen (violet), and zinc (orange) atoms are indicated. Hydrogen atoms are omitted for clarity. CCDC Database Identifier: FAWCEN03; CCDC Deposition Number: 864312. <sup>11</sup>	5
Figure 5 Scheme of the various types of coordination compounds, adapted from Batten et al. <sup>4</sup>	6
Figure 6 $Cu(BIPY)_{1.5}(NO_3)$ crystal structure. Carbon (grey), nitrogen (green), and copper (light blue) atoms are indicated. Hydrogen atoms are omitted for clarity. <sup>15</sup>	7
Figure 7 $Co(BTC)(Py)_2$ crystal structure. Carbon (grey), nitrogen (blue), oxygen (red) and cobalt (green) atoms are indicated. Hydrogen atoms are omitted for clarity. <sup>17</sup>	8
Figure 8 MOF-2: $Zn(BDC)(H_2O)$ crystal structure. $Zn_2(\text{carboxylate})_4$ paddle wheel SBUs are highlighted. Carbon (grey), oxygen (red) and zinc (green octahedra) atoms are indicated. Hydrogen atoms are omitted for clarity. <sup>15</sup>	9
Figure 9 Representation of $Cu[C(C_6H_4CN_4)]$ crystal structure. Carbon (black), nitrogen (blue), and copper (green) atoms are indicated. Hydrogen atoms are omitted for clarity. <sup>20</sup>	10
Figure 10 MOF-5: $Zn_4O(BDC)_3$ crystal structure. $Zn_4O(CH_3COO)_6$ cluster is evidenced. Carbon (black), oxygen (red), and zinc (green tetrahedra) atoms are indicated. Hydrogen atoms are omitted for clarity. <sup>22</sup>	10
Figure 11 Schematic representation of the four MOFs generations: 1) collapsing MOFs, 2) robust MOFs with permanent porosity, 3) flexible MOFs, and 4) Post-Synthetic Modification on MOFs.	11
Figure 12 1D CPs possible structural motifs: linear, zigzag, ribbon, ladder and helical.	13
Figure 13 a) $Cd(\text{pydc})(\text{phen})$ crystal structure showing a ribbon motif. Carbon (black), nitrogen (blue), and copper (green) atoms are indicated. Hydrogen atoms are omitted for clarity; b) Cd(II) different coordination fashions. <sup>36</sup>	14
Figure 14 Representation of ladder motif due to cyclobutane moiety in $[Pb_2(\mu\text{-bpe})_2(\mu\text{-O}_2\text{CC}_6\text{H}_5)_2(\text{O}_2\text{CC}_6\text{H}_5)_2]$ . <sup>37</sup>	15
Figure 15 Outline of 2D motifs: square, rhombic, rectangular and honeycomb grid, brick wall, herringbone, and bilayer. <sup>31</sup>	16
Figure 16 Representation of some 3D structural motifs.	18
Figure 17 a) Crystal structure of $Cu_4(CDC)_4(4,4'\text{-Bpe})$ . Carbon (grey), nitrogen (blue), oxygen (red) and copper (green) atoms are indicated. Hydrogen atoms are omitted for clarity; b) Scheme of paddle-wheel dimer motif determining the $\alpha$ -Po net topology. <sup>42</sup>	19

Figure 18 A table illustrating the most common net topologies as a result of building units geometry (up to six points of extension). <sup>45</sup>	20
Figure 19 Representation of some of the sixteen IRMOFs showing the same pcu topology of MOF-5 and based on different carboxylate linkers. <sup>15</sup>	21
Figure 20 A scheme of all the techniques adopted for the synthesis of CPs and MOFs.	23
Figure 21 Schematic illustration of in situ DMF decarbonylation occurring during the synthesis of a MOF. HNMe <sub>2</sub> then deprotonate the organic linker (BDC in the example) which will coordinate the metal center to yield the MOF.	24
Figure 22 Scheme of solvothermal synthesis of CPs/MOFs.	25
Figure 23 Scheme of microwave-assisted reaction of CPs/MOFs inspired by Lee et al. <sup>59</sup>	26
Figure 24 Scheme of mechanochemical synthesis of CPs/MOFs.	27
Figure 25 Scheme of diffusion in liquid phase method. The reaction occurs in the interphase between the two immiscible liquids.	28
Figure 26 A summary of all activation methods of MOFs.	31
Figure 27 Representation of the six different isotherms individuated by IUPAC. <sup>15</sup>	36
Figure 28 Representation of different hysteresis types. <sup>77</sup>	37
Figure 29 Outline of probe gas adsorption corresponding to a) surface area, b) micropores filling, c) mesopores filling and d) macropores filling. <sup>15</sup>	38
Figure 30 Scheme of the gases employed for the measure of the surface area with their main features.	41
Figure 31 Different ways in which the pyrazolate ion can coordinate a metal center (M). <sup>3</sup>	43
Figure 32 Zn(pz) <sub>2</sub> crystal structure. Zinc (filled circle) and carbon (empty circle) atoms are indicated. Hydrogen atoms are omitted for clarity. Cd(pz) <sub>2</sub> crystal structure is analogous. <sup>93</sup>	43
Figure 33 Representation of [Ag(μ-cdipz)] <sub>n</sub> structure showing zigzag 1D chains.	44
Figure 34 List of some bipyrazolate linkers employed for the synthesis of MOFs. <sup>102</sup>	45
Figure 35 Different topologies displayed by Zn(BPZ)/Co(BPZ) and Ni(BPZ)/Cu(BPZ). The first pair exhibits square channels, while the second pair shows rhombic channels.	46
Figure 36 Collapsed and expanded structures of Co(BDP) at different methane pressures. <sup>115</sup>	47
Figure 37 Scheme of how MOFs antimicrobial activity can be exerted. <sup>121</sup>	49
Figure 38 Representation of Lewis Base-Acid Interaction and Hydrogen Bond in the adsorption of CO <sub>2</sub> via amino group. <sup>124</sup>	51
Figure 39 Representation of carbamic acid or ammonium carbonate formation in the presence of an amino group and carbon dioxide. <sup>124</sup>	52
Figure 40 Scheme of cyclic carbonate formation in the presence of a Lewis Base (LB) such as an amino group. <sup>123</sup>	53
Figure 41 Scheme of 1-8 CPs tested as antibacterial materials in this work.	57
Figure 42 2 (blue) and 5 (black) IR spectra (4000-400 cm <sup>-1</sup> ).	65
Figure 43 2 (blue) and 5 after heating at 433 K for 1h (orange) IR spectra. The two spectra are superimposable, confirming the transformation of 5 in 2 after the thermal treatment.	65

Figure 44 TGA curves of 2 (blue), 5 (black) and 5 after thermal treatment at 433 K for 1 h (red).	67
Figure 45 Representation of the crystal structure of CP 2: (a) the coordination geometry and the stereochemistry of Cu(II) metal center; (b) the 1D chain of metal ions running along the b-axis; (c) packing of the 2D slabs viewed along the [010] direction. Carbon (grey), hydrogen (white), nitrogen (blue), oxygen (red) and copper (yellow) atoms are indicated.	68
Figure 46 PXRD pattern of 2. The structure refinement carried out with the Rietveld method is shown through experimental, calculated and difference traces (in blue, red and grey, respectively). The green markers at the bottom indicate the positions of the Bragg reflections.	68
Figure 47 Antibacterial activity of the free linkers, reported in % of viable bacterial cells as a function of time, against <i>S. aureus</i> and <i>E. coli</i> .	69
Figure 48 Bacterial growth curve of 1-8 CPs against <i>E. coli</i> (a and b), <i>S. aureus</i> (c and d), and <i>P. aeruginosa</i> (e and f) as a function of treatment time.	70
Figure 49 Antibacterial rate (%) of <i>E. coli</i> (a and b), <i>S. aureus</i> (c and d), and <i>P. aeruginosa</i> (e and f) treated with CPs 1-8.	71
Figure 50 Representation of Gram-positive (left) and Gram-negative (right) bacteria cell walls. <sup>178</sup>	73
Figure 51 Formation of ROS in <i>E. coli</i> , <i>S. aureus</i> , and <i>P. aeruginosa</i> bacteria cells exposed to 1-8 for 4 hours. The data are represented as the mean $\pm$ SD of at least three separate experiments; statistical significance* $p < 0.05$ .	75
Figure 52 PI fluorescent emission for <i>E. coli</i> , <i>S. aureus</i> , and <i>P. aeruginosa</i> cells exposed to CPs 1-8 The data are represented as the mean $\pm$ SD of at least three separate experiments; statistical significance* $p < 0.05$ .	76
Figure 53 Live <i>E. coli</i> and <i>S. aureus</i> in green color and dead <i>E. coli</i> and <i>S. aureus</i> in red color due to the SYTO9 dye of LIVE/DEAD <sup>®</sup> BacLight Kit, before a), b) and after CP 2 treatment c), d).	77
Figure 54 Representation of the three linkers employed in this work and the corresponding MOFs unit formula.	80
Figure 55 Crystal structure of Zn1 (left) and Zn3 (right). Carbon (black), Nitrogen (blue) and Zinc (pink or yellow) atoms are highlighted. The tetrahedral coordination geometry of the metal node is emphasized in the green box.	84
Figure 56 Crystal structure of Cu1 (left) and Cu3 (right). Carbon (black), Nitrogen (blue) and Copper (pink or yellow) atoms are highlighted, and the square planar coordination geometry is appreciable. Weak coordinating MeCN molecules are shown in cyan at left.	84
Figure 57 Evaluation of antibacterial rate (%) for each MOF against <i>E. coli</i> (left) and <i>S. aureus</i> (right).	86
Figure 58 ROS production test of the samples treated with the six MOFs against <i>E. coli</i> and <i>S. aureus</i> after 2h and 4h of treatment.	87
Figure 59 PI uptake of all treated samples with the six MOFs after 2h and 4 h of test.	87
Figure 60 Molecular structures of the two isomeric forms 3,3'-diamino-4,4'-bipyrazole (3,3'-H <sub>2</sub> L) and 3,5-diamino-4,4'-bipyrazole (3,5-H <sub>2</sub> L) employed as linkers for the synthesis of the corresponding MOFs.	91
Figure 61 Selective dinitration pathways of 4,4'-bipyrazole to yield either 3,5-dinitro-4,4'-bipyrazole or 3,3'-dinitro-4,4'-bipyrazole, with subsequent reduction to 3,3'-H <sub>2</sub> L and 3,5-H <sub>2</sub> L.	98



Figure 62 IR spectra of Zn(3,3'-L) and Zn(3,5-L).	99
Figure 63 a) TGA (light blue), DTG (dotted, light blue) and DTA (orange) profile of Zn(3,3'-L); b) Variable-temperature PXRD analysis on Zn(3,3'-L) in the temperature range 303-763 K.	99
Figure 64 Crystal structure of the linker 3,3'-H <sub>2</sub> L. Hydrogen bonds are highlighted with blue dashes.	100
Figure 65 Representation of the crystal structure of Zn(3,3'-L) and [epibromohydrin@Zn(3,3'-L)]: (a) the tetrahedral coordination geometry of the ZnN <sub>4</sub> node; (b) the 1D chain running along the crystallographic c-axis; (c) the packing, viewed in perspective along the crystallographic c-axis. The epibromohydrin molecules have been omitted for sake of clarity. (d) A guest epoxide molecule in the 1D channel. Carbon (gray), hydrogen (light grey), bromine (brown), nitrogen (blue), oxygen (red) and zinc (yellow) atoms are indicated. The N-H...Br and N-H...O interactions are illustrated with cyan dashed lines.	101
Figure 66 (a) N <sub>2</sub> (77 K) adsorption isotherms of Zn(3,3'-L) (red diamonds) and Zn(3,5-L) (blue diamonds) and BET Surface Area values for both. Empty symbols represent the desorption branches. (b) BJH mesopore size distribution curves for Zn(3,3'-L) (red circles) and Zn(3,5-L) (blue circles). Inset: NLDFT micropore size distribution curves.	102
Figure 67 CO <sub>2</sub> adsorption isotherms of Zn(3,3'-L) (red) and Zn(3,5-L) (blue) at 273 K (circles) and 298 K (squares).	104
Figure 68 Water stability tests performed on Zn(3,3'-L) and Zn(3,5-L) for 120 days.	104
Figure 69 Scheme of carbon dioxide cycloaddition with epichlorohydrin or epibromohydrin to yield the corresponding cyclic carbonate.	105
Figure 70 Proposed reaction mechanism of CO <sub>2</sub> conversion in cyclic carbonates in the presence of halogenated epoxides, catalyzed by Zn(BPZNH <sub>2</sub> ).	106
Figure 71 PXRD profile of Zn(3,3'-L) before (black) and after (orange) a catalytic run.	107
Figure 72 IR spectra of the four Cu/Ni mixed MOFs recorded at 4000-400 cm <sup>-1</sup> .	116
Figure 73 SEM images acquired with a 50000-fold magnification of a) Cu <sub>0.05</sub> Ni <sub>0.95</sub> , b) Cu <sub>0.1</sub> Ni <sub>0.9</sub> , c) Cu <sub>0.2</sub> Ni <sub>0.8</sub> and d) Cu <sub>0.5</sub> Ni <sub>0.5</sub> .	118
Figure 74 Copper(II) (yellow) and nickel (II) (pink) ions distribution revealed by EDX for Cu <sub>0.2</sub> Ni <sub>0.8</sub> .	118
Figure 75 TGA curves of the four Cu/Ni mixed MOFs performed in the range 303-1073 K.	119
Figure 76 Representation of a portion of Cu <sub>0.5</sub> Ni <sub>0.5</sub> crystal structure, on the left. Carbon (grey), nitrogen (blue) and copper/nickel (green) atoms are indicated. Hydrogen atoms are omitted for clarity. The square planar coordination geometry of the metal centers is highlighted. On the right, a single pore display is reported.	119
Figure 77 a) N <sub>2</sub> adsorption isotherms at 77 K and b) CO <sub>2</sub> adsorption isotherms at 298 K of the four Cu/Ni mixed MOFs. Empty symbols indicate the desorption branch.	120
Figure 78 a) CO <sub>2</sub> adsorption isotherms at 273 K and b) 195 K of the four Cu/Ni mixed MOFs.	121
Figure 79 Linear fitting of the differential form of the Clausius-Clapeyron equation for (a) Cu <sub>0.05</sub> Ni <sub>0.95</sub> , b) Cu <sub>0.1</sub> Ni <sub>0.9</sub> , c) Cu <sub>0.2</sub> Ni <sub>0.8</sub> and d) Cu <sub>0.5</sub> Ni <sub>0.5</sub> at T = 195, 273 and 298 K.	123
Figure 80 Representation of heat of adsorption of all the four Cu/Ni mixed MOFs as a function of the quantity of CO <sub>2</sub> adsorbed.	123

<i>Figure 81 Products concentration in ppm after electroreduction of CO<sub>2</sub> at different voltages (1.3, 1.5 and 1.7 V vs. Ag/AgCl) with the four Cu/Ni mixed MOFs.</i>	124
<i>Figure 82 Faradaic efficiency calculated for electroreduction tests for (in order from right): 5) Cu<sub>0.05</sub>Ni<sub>0.95</sub>, 10) Cu<sub>0.1</sub>Ni<sub>0.9</sub>, 20) Cu<sub>0.2</sub>Ni<sub>0.8</sub> and 50) Cu<sub>0.5</sub>Ni<sub>0.5</sub>.</i>	125
<i>Figure 83 PXRD profiles of the four Cu/Ni mixed MOFs before and after electrocatalytic tests.</i>	125
<i>Figure 84 TEM images of (a) Cu<sub>0.05</sub>Ni<sub>0.95</sub>, b) Cu<sub>0.1</sub>Ni<sub>0.9</sub>, c) Cu<sub>0.2</sub>Ni<sub>0.8</sub> and d) Cu<sub>0.5</sub>Ni<sub>0.5</sub>. Bars length correspond to 20 nm.</i>	126
<i>Figure 85 XPS spectra of Cu<sub>0.5</sub>Ni<sub>0.5</sub>: Ni 2p (a-b), Cu 2p (c-d) and C 1s (d-e).</i>	126

# **CHAPTER 1: Introduction**

## **1.1 Nomenclature notions: Coordination Polymers, Coordination Networks and Metal-Organic Frameworks ... Let's make it clear!**

This first subchapter aims to introduce the extended structures based on coordination units and focuses the attention on knowing the different classes of coordination compounds in order to clarify the correct terminology to use to name them.

Since the dawn of Coordination Chemistry introduced in the early 1900s by Alfred Werner, the extraordinary variety of inorganic and hybrid inorganic/organic structures obtained has aroused a great deal of interest in researchers but unfortunately it has also generated confusion in the terms used to classify these compounds, especially with regard to extended networks.

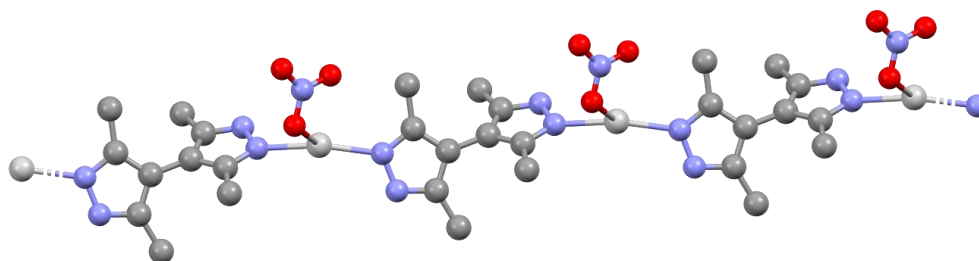
It is common, for instance, to find in the scientific literature the term Metal-Organic Framework as a synonym for Coordination Polymer and vice versa, even if the two terms have actually different meanings.

In 2013, the International Union of Pure and Applied Chemistry (IUPAC) published some helpful guidelines<sup>1</sup> with the purpose of classifying the different compounds proposing a hierarchical system in which the most general class is Coordination Polymers and Metal-Organic Frameworks are a subset of Coordination Networks which in turn are a subset of Coordination Polymers.

A Coordination Polymer (CP) is defined as a coordination compound made of discrete entities repeating endlessly in one, two or three dimensions. The coordinating units are a neutral or usually positively charged metal node (a metal ion or cluster), and a neutral or negatively charged linker (or spacer) connecting the metal nodes. Linkers can be inorganic (e.g., phosphate, cyanide, ammonia groups) or organic (e. g. carboxylate- or azolate-based) and for this reason sometimes it's possible to find the terms "inorganic coordination polymers" and "organic coordination polymers" in scientific literature to distinguish them. The prefixes 1D-, 2D- and 3D- are frequently used to indicate the number of dimensions in which the polymer extends. The expression "coordination polymer" was initially employed in 1916 by Shibata<sup>2</sup> referring to some cobalt ammine nitrates dimers and trimers without the real possibility of demonstrating that they were extended structures in the absence of a single-crystal X-Ray analysis.<sup>3</sup> However, it should be highlighted that CPs do not necessarily have to be crystalline to be classified as such. Some also believe the term "polymer" itself in "Coordination Polymers" is inaccurate referring to extended structures rather than to discrete

entities made by multiple (“*poly-*” translation from Greek) subunits, as in the case of organic polymers for which there is a degree of polymerization.<sup>4</sup> In any case, such expression has already entered the scientific language since Shibata’s paper and it would be difficult to change it now.

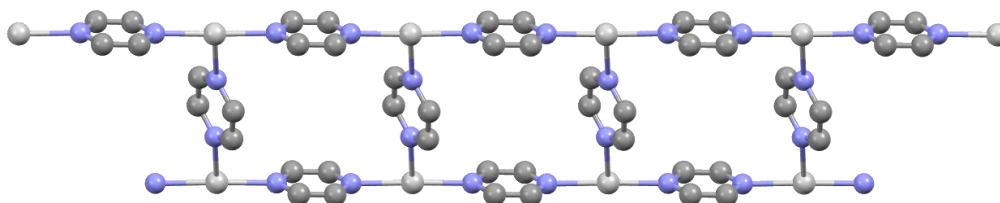
An example of a 1D CP is  $[Ag(Me_4BPZ)NO_3 \cdot CH_3OH]_n$  obtained by *Domasevitch et al.* in 2001,<sup>5</sup> in which silver ions are coordinated by bridging exobidentate 3,3',5,5'-tetramethyl-4,4'-bipyrazolate linkers and a nitrate ion to give linear one-dimensional chains, as reported in **Figure 1**.



**FIGURE 1** Structure of 1D-CP  $[Ag(Me_4BPZ)NO_3 \cdot CH_3OH]_n$ . Carbon (grey), nitrogen (violet), oxygen (red) and silver (white) atoms are shown. Hydrogen atoms and methanol coordinating molecules are omitted for clarity. CCDC Database Identifier: QOTHIO; CCDC Deposition Number: 148207.<sup>5</sup>

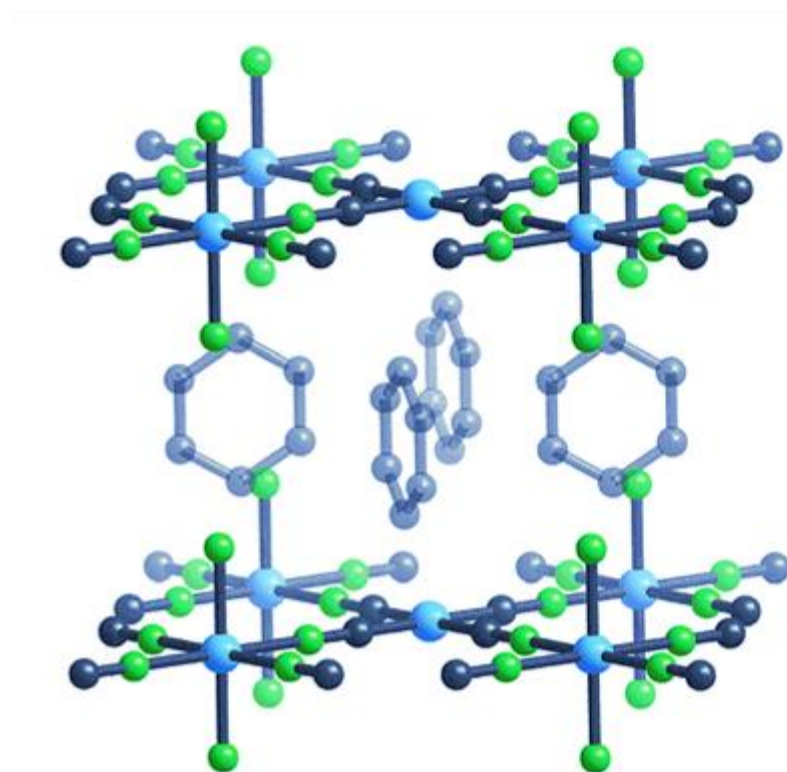
A Coordination Network (CN) can be instead defined as a 1D coordination polymer with cross-links between two or more distinct chains, loops, or spiro-links, or as a coordination polymer consisted of repeating coordination units in 2 or 3 dimensions.

$[Ag(1,4\text{-pyrazine})_{1.5}CF_3SO_3]_n$  by *Venkataraman et al.*<sup>6</sup> is a coordination network (**Figure 2**). In this case, the coordinating pyrazine molecules link  $Ag^+$  ions to form linear chains which at the same time are connected to each other through cross-linking pyrazines.



**FIGURE 2**  $Ag(1,4\text{-pyrazine})_{1.5}CF_3SO_3$  coordination network structure. Carbon (grey), nitrogen (violet), and silver (white) atoms are indicated. Hydrogen atoms and trifluoromethane-sulfonate coordinating molecules aren't shown. CCDC Database Identifier: TOZGOE; CCDC Deposition Number: 1274955.<sup>6</sup>

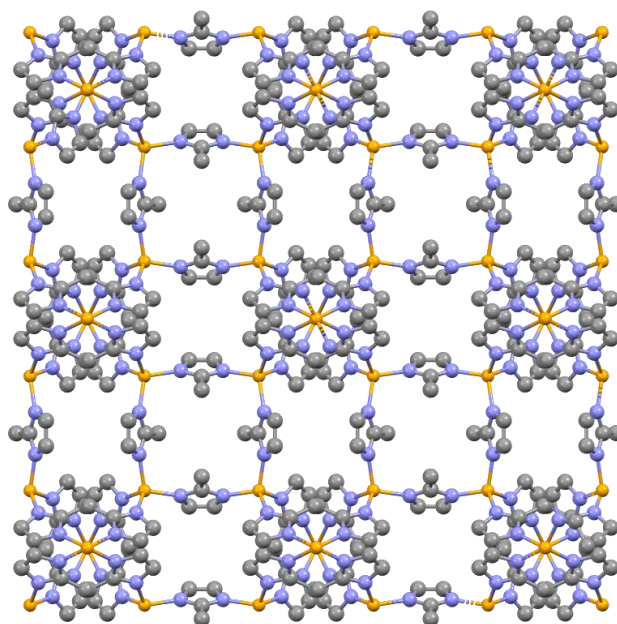
Prussian blue, considered the first documented coordination compound, and Hofmann Clathrates are inorganic CPs which extends in 3 and 2 dimensions respectively and for this reason they can be counted among the Coordination Networks. The first one shows a face-centered cubic unit cell made of  $\text{Fe}^{3+}$  ions linked by cyanides nitrogen atoms and  $\text{Fe}^{2+}$  ions connected to the carbons of  $\text{CN}^-$  ions, yielding a three-dimensional structure whose formula is  $[\text{Fe}^{\text{III}}_4[\text{Fe}^{\text{II}}(\text{CN})_6]_3 \cdot n\text{H}_2\text{O}]_n$ .<sup>7</sup> Hofmann-like clathrates, instead, are CNs in which layers of alternate metal centers and cyanide moieties are connected through N-donor linkers,<sup>8</sup> with the general formula  $[\text{M}(\text{CN})_2(\text{L})]\text{C}_6\text{H}_6$ , where M is a metal(II) and L is the N-donor linker (M = Ni(II) and L =  $\text{NH}_3$  in the original Hofmann network, obtained in 1897<sup>9</sup> and illustrated in **Figure 3**).



**FIGURE 3** Hofmann Clathrate original structure:  $[\text{Ni}(\text{CN})_2(\text{NH}_3)]\text{C}_6\text{H}_6$ . Carbon (grey), nitrogen (green), and nickel (light blue) atoms are indicated.<sup>10</sup>

Metal-Organic Frameworks (MOFs), lastly, are described as coordination networks with organic linkers and potential porosity. This means that the definition of MOF is independent of the effective porosity, even if it varies as a consequence of a structural changes due to external stimuli such as variation of pH, temperature, pressure, or removal/introduction of

guest molecules inside MOF pores. MOFs are typically crystalline materials. ZIF-8, whose structure is reported in **Figure 4**, is introduced here as an example of MOF. The  $\text{Zn}^{2+}$  ion is coordinated by 2-methylimidazolate (2mIM) linkers with a tetrahedral geometry to give an extended and porous structure analogue to zeolites.<sup>11</sup>



**FIGURE 4** ZIF-8:  $\text{Zn}(2\text{mIM})_2$  crystal structure showing free cavities. Carbon (grey), nitrogen (violet), and zinc (orange) atoms are indicated. Hydrogen atoms are omitted for clarity. CCDC Database Identifier: FAWCEN03; CCDC Deposition Number: 864312.<sup>11</sup>

Two aspects should also be underlined: the term “MOF” indicates not only porous but also robust structures, with coordination bonds of an entity comparable to that of the C-C bond (about 350 KJ/mol)<sup>12</sup>; secondly, in the approximately 30 years since the synthesis of the first MOF, various research groups around the world have adopted a specific nomenclature for MOFs,<sup>13</sup> based on numeration and on the name of the University the MOF has been primarily synthesized. Moreover, several MOFs are reported in various papers with different names. For instance, the MOF Cu-BTC where BTC = benzene-1,3,5-tricarboxylate can be found in literature as  $\text{Cu}_2(\text{BTC})_3$  or  $\text{Cu}_3(\text{BTC})_2$  and as MOF-199, but also as HKUST-1 (HKUST is the abbreviation of Hong Kong University of Science and Technology). No wonder this creates a lot of confusion in readers and researchers to the point that even different structures may have the same name. In this regard, *Bucior et al.* has begun to implement in 2019<sup>14</sup> algorithms capable of identifying a certain MOF found in the scientific literature, decomposing it into its components and assigning it specific codes corresponding to the information about the metal node, the linker and the network type, identifying the

MOF uniquely. In this way, the availability and the searchability of MOFs are improved and that could lead to greater clarity in MOFs data management if it was adopted by the whole scientific community.

Before concluding the subchapter, a resuming scheme showing all types of coordination compounds and the classification criteria is reported in **Figure 5**.

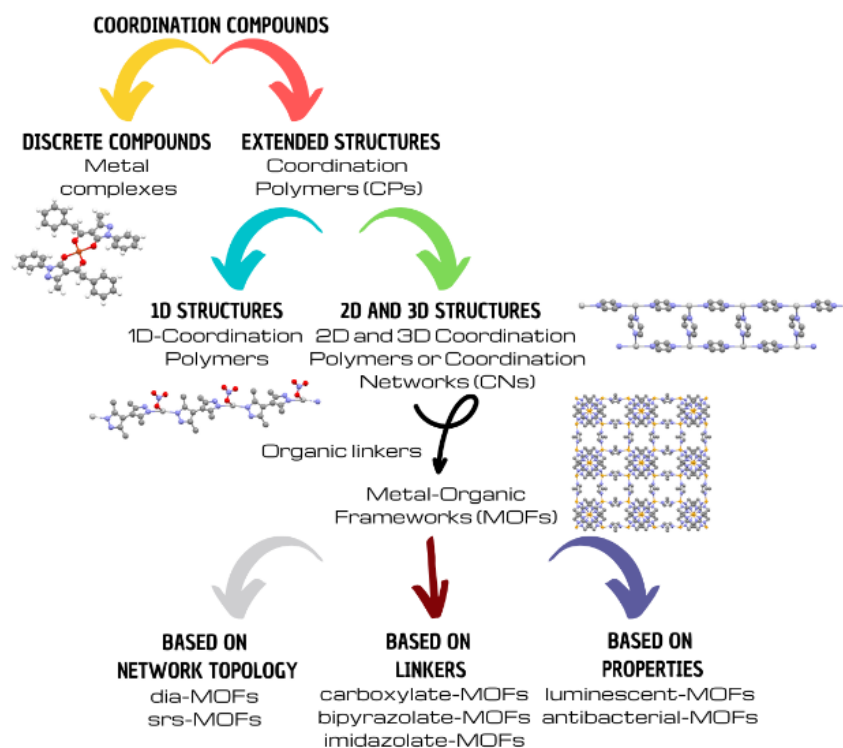


FIGURE 5 Scheme of the various types of coordination compounds, adapted from Batten et al.<sup>4</sup>



## 1.2 The birth of Reticular Chemistry

In the first chapter of “Introduction to Reticular Chemistry”<sup>15</sup> Prof. Omar Yaghi *et al.* reports the various stages that led from the synthesis of the first MOF to the birth of *Reticular Chemistry* by adopting a historical/epistemological approach.

The first described turning point towards the birth and development of MOFs was marked in 1995 when Yaghi's group first used the term *metal-organic framework* to describe the three-dimensional structure of  $\text{Cu}(\text{BIPY})_{1.5}[\text{NO}_3]$ , where BIPY = 4,4'-bipyridine.

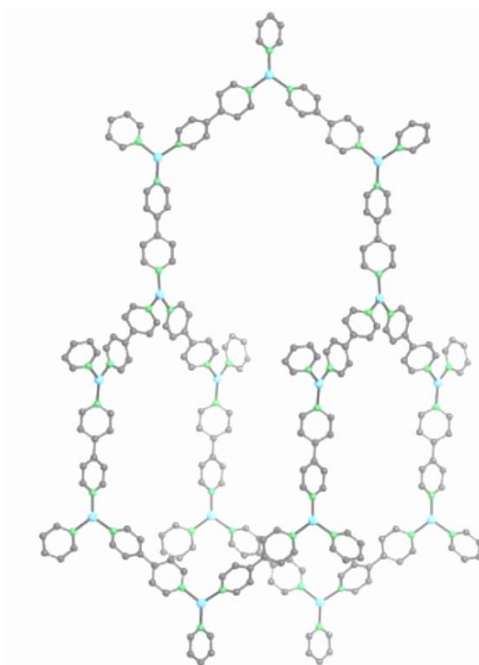


FIGURE 6  $\text{Cu}(\text{BIPY})_{1.5}[\text{NO}_3]$  crystal structure. Carbon (grey), nitrogen (green), and copper (light blue) atoms are indicated. Hydrogen atoms are omitted for clarity.<sup>15</sup>

Such new infinite network was made of trigonal planar copper(I) metal centers linked to each other through rod-like BIPY linkers yielding 3D interpenetrating frameworks, having three different pore sizes, as reported in **Figure 6**.<sup>16</sup> Since BIPY is a neutral linker, a nitrate ion is present in the structure to balance the positive charge of the  $\text{Cu}^+$  metal ion.  $\text{NO}_3^-$  ions can be also exchanged in water solution with  $\text{BF}_4^-$  and  $\text{SO}_4^{2-}$  with retaining of the network. *Metal-organic framework* initially meant an extended structure that presented a metal node and an organic linker at the same time; only later the term took on the current connotation accepted by the IUPAC regarding potential porosity. However, the introduction of an organic coordinating system in the building of infinite coordination polymers opened the doors to an

infinite of new possible structures compared to simple inorganic CPs. However, the hybrid organic/inorganic structures thus obtained showed generally poor chemical stability.

The next step was the use of negatively charged chelating linkers, usually based on carboxylate groups.

In the same year of the first MOF synthesis,  $\text{Co}(\text{BTC})(\text{Py})_2$  (Py = pyridine) was obtained, (Figure 7) starting from a mixture of Co(II) nitrate and benzene-1,3,5-tricarboxylic acid in alcohol solution and diffusing pyridine into the mixture for three days.<sup>17</sup>

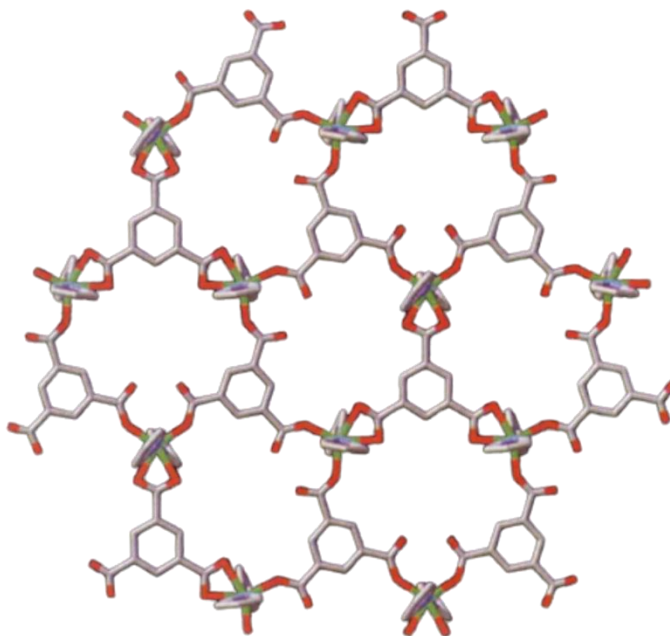


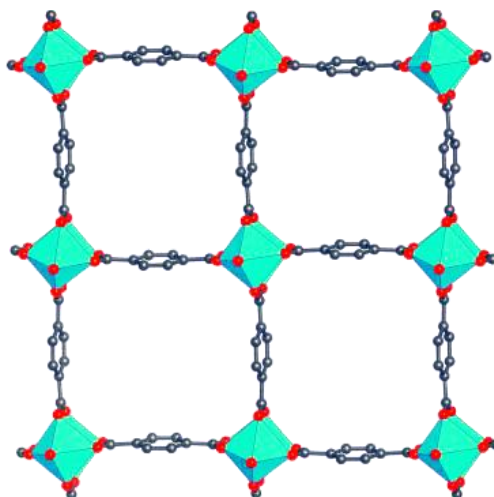
FIGURE 7  $\text{Co}(\text{BTC})(\text{Py})_2$  crystal structure . Carbon (grey), nitrogen (blue), oxygen (red) and cobalt (green) atoms are indicated. Hydrogen atoms are omitted for clarity.<sup>17</sup>

Negatively charged linkers let higher binding energy with metal centers granting higher thermal and chemical stability. Furthermore, the charge of the linkers neutralizes the positive charge of the metal centers, making sure that no counterions remain in the structure to occupy space. What has just been mentioned is confirmed by the fact that  $\text{Co}(\text{BTC})(\text{Py})_2$  is thermally stable up to 623 K and has no counterions in its network, but only pyridine guest molecules, which in any case can be removed via thermal without causing the collapse of MOF and reintroduced yielding the former structure.

One step further towards more robust networks occurred in 1998, when MOF-2 was obtained. This new metal-organic framework was based on polynuclear metal clusters (that later will be defined as *secondary building units*, SBUs), rather than single metal ions in the MOF architecture.

The presence of polymetallic clusters determines greater stability but also directionality of the bonds forming the lattice, while the negative charge on carboxylate linkers assures higher binding energies.

MOF-2 is represented by the formula  $Zn(BDC)(H_2O)$ , where BDC = 1,4-benzenedicarboxylate and is obtained by dissolving zinc(II) nitrate and BDC in a DMF/toluene mixture and diffusing a trimethylamine/toluene mixture into it.<sup>18</sup> The structure of MOF-2 is reported in **Figure 8**.



**FIGURE 8** MOF-2:  $Zn(BDC)(H_2O)$  crystal structure.  $Zn_2(\text{carboxylate})_4$  paddle wheel SBUs are highlighted. Carbon (grey), oxygen (red) and zinc (green octahedra) atoms are indicated. Hydrogen atoms are omitted for clarity.<sup>15</sup>

Dimeric  $Zn_2(\text{carboxylate})_4$  paddle wheel SBUs make the removal of solvent molecules occupying MOF pores possible, preventing MOF-2 structural collapse. The action of eliminating guest molecules inside MOF cavities is called *activation*; it is an essential step in order to correctly measure the porosity.

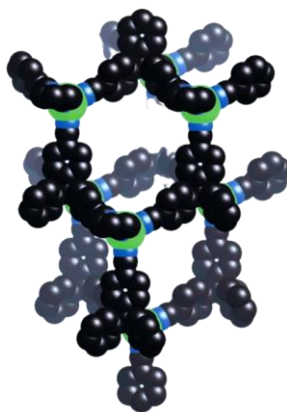
$N_2$  and  $CO_2$  Langmuir adsorption isotherms, measured at 78K and 195K respectively, confirm the permanent porosity of MOF-2.

From this point on, porosity becomes an important parameter for classifying an organic CP as a MOF.

It then became clear that the use of different metal ions or SBUs combined with various organic linkers would have led to the production of an enormous quantity of new MOFs and that the synthesis of extended and porous structures was not accidental but could boast of a specific molecular design. The pioneers in the synthetic design of infinite structures are Bernard F. Hoskins and Richard Robson who in 1989 published the synthesis and the

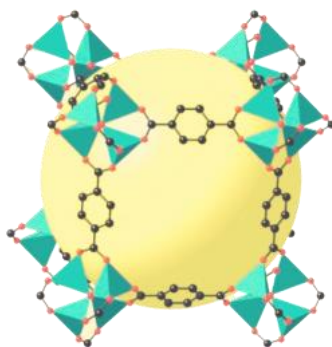
structural study of the extended network  $\text{Cu}[\text{C}(\text{C}_6\text{H}_4\text{CN}_4)]$ .<sup>19</sup> whose crystal structure is illustrated in **Figure 9**. The two authors, commenting on the compound obtained, report the following words in the publication:

*“We describe here the synthesis and X-ray crystal structure of the first example of a deliberately designed and constructed infinite framework consisting of tetrahedral centers linked together by rod-like units. An enormous range of different approaches to such frameworks can be conceived; the particular approach described here involves substitution of the acetonitrile ligands in  $\text{Cu}(\text{CH}_3\text{CN})_4^+$  by 4,4',4'',4'''-tetracyanotetraphenylmethane.”*



**FIGURE 9** Representation of  $\text{Cu}[\text{C}(\text{C}_6\text{H}_4\text{CN}_4)]$  crystal structure. Carbon (black), nitrogen (blue), and copper (green) atoms are indicated. Hydrogen atoms are omitted for clarity.<sup>20</sup>

In this respect, the synthesis of MOF-5 was planned, keeping the same organic linker BDC used for MOF-2 but adding hydrogen peroxide in an acetic acid solution of a zinc salt to form  $\text{Zn}_4\text{O}(\text{CH}_3\text{COO})_6$  cluster. It must be said that the first results were not those expected, and the synthesis procedure was subsequently changed in order to obtain MOF-5 in 1999 (**Figure 10**).<sup>21</sup>



**FIGURE 10** MOF-5:  $\text{Zn}_4\text{O}(\text{BDC})_3$  crystal structure.  $\text{Zn}_4\text{O}(\text{CH}_3\text{COO})_6$  cluster is evidenced. Carbon (black), oxygen (red), and zinc (green tetrahedra) atoms are indicated. Hydrogen atoms are omitted for clarity.<sup>22</sup>

What matters, in any case, is that it was now possible to imagine a certain structure knowing the coordination geometries of the SBUs and organic linkers and succeeded in obtaining it. Therefore, a novel chemistry was born. The Reticular Chemistry, defined by Yaghi as “*the chemistry of linking molecular building blocks by strong bonds to make extended crystalline structures as exemplified by MOFs and COFs*”<sup>1, 23</sup>

The founding father of this new chemistry underlines that three relevant concepts which have been already discussed are implied in such definition: i) the synthetic design, ii) the structural, architectural, and chemical stability and, finally, iii) their crystallinity.

But the story of MOFs hasn't finished yet.

In a review about MOFs for heterogeneous catalysis in 2014<sup>24</sup>, Liu *et al.* classify MOFs into four different generations. An illustrative scheme of MOFs classification in generations is reported in **Figure 11**.

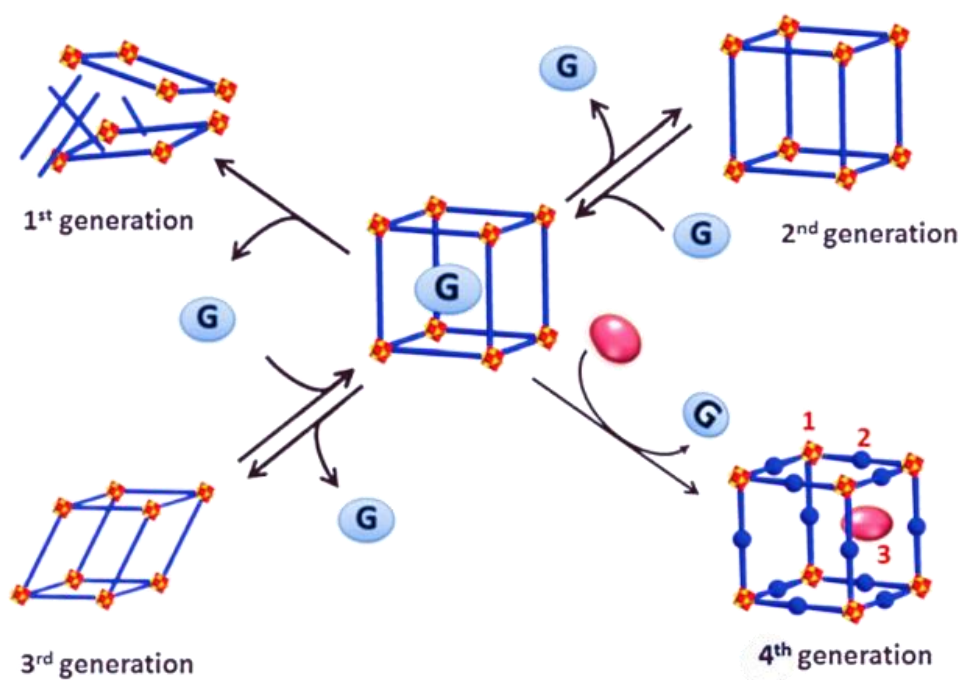


FIGURE 11 Schematic representation of the four MOFs generations: 1) collapsing MOFs, 2) robust MOFs with permanent porosity, 3) flexible MOFs, and 4) Post-Synthetic Modification on MOFs.

---

<sup>1</sup> **Note of the author:** COFs stands for *Covalent Organic Frameworks*, crystalline and porous extended structures analogues to MOFs made only by organic building blocks and are not dealt with in this chapter as they are not the object of study of this PhD thesis.

We have already encountered the first two generations in this historical journey. The former one concerns with MOFs that collapse when the guest molecules are removed from their pores, while the second generation is referred to robust MOFs with permanent porosity, such as MOF-2 and MOF-5.

Flexible MOFs with dynamic properties belong to the third generation of MOFs. Such MOFs, often named “Soft Porous Crystals” (SPCs), show the possibility of varying their structure in response to an external stimulus of a chemical-physical nature: guest molecules adsorption, photochemical stimulation, variation of temperature or pressure.<sup>25</sup> For instance, MIL-53 and MIL-88 MOFs families are well known in literature for their breathing properties, that means the possibility to reversibly change the unit cell volume as a result of an external stimulus such as the adsorption or removal of guest molecules inside the cavities.<sup>26,27</sup>

The fourth and last generation concerns instead the MOFs able to retain their network even after synthetic transformations occurring once the MOF has been already formed, defined as post-synthetic modifications (PSMs).

### 1.3 CPs and MOFs structural motifs

In the previous subchapters it has already been said that the coordinating units that make up the CPs are given by the metal center (ion or cluster) and by the linker having a certain donor atom, usually N, O or S. The way in which the units can interact involves the formation of networks very different from each other and with different dimensionality.

Therefore, it may be useful to know and analyze through some examples the most common types of motifs for one-, two- and three-dimensional CPs.

One dimensional CPs may show five different motifs illustrated in **Figure 12**: linear chain, zigzag chain, ribbon, ladder, and helical.<sup>28,29</sup>

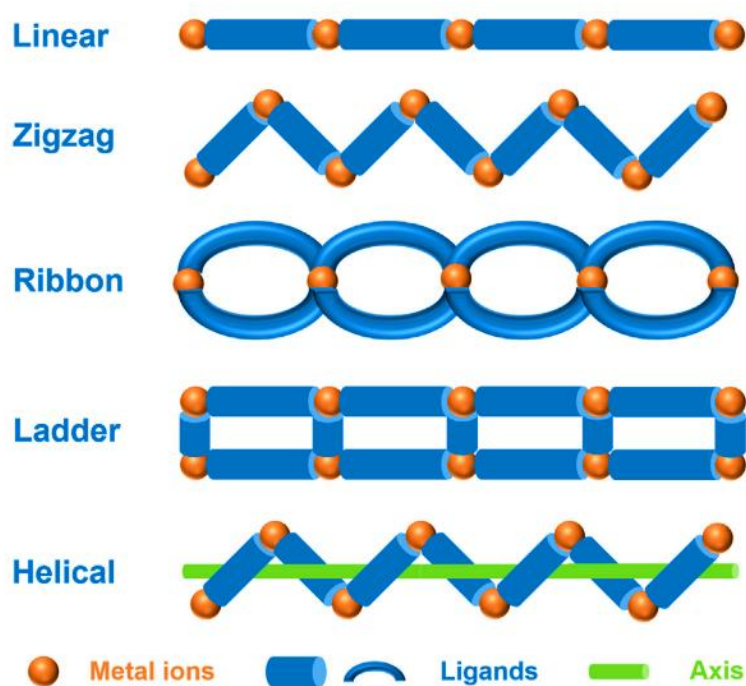


FIGURE 12 1D CPs possible structural motifs: linear, zigzag, ribbon, ladder and helical.

Linear chain CPs are widespread in scientific literature and represent the simplest structure to yield and the most intuitive. Generally, linear linkers help the formation of linear CPs, but also the use of metal centers with linear coordination geometry such as Ag(I) ion.

A lot of reported linear CPs show BIPY and analogue N-donor systems as linkers.

For example,  $\{[\text{Ni}(\text{L-Tyr})_2(\mu\text{-BIPY})]\cdot 4\text{H}_2\text{O}\}_n$ , obtained by mixing L-Tyrosine disodium salt dihydrate with an aqueous/EtOH solution of  $\text{NiCl}_2$  and BIPY, shows an octahedral geometry, where the two bidentate L-Tyrosinate (L-Tyr) anions chelate the equatorial positions, while the BIPY connects the axial positions each other giving rise to a linear CP.<sup>30</sup>

The second recurring motif for one-dimensional polymers is zigzag chain. The zigzag shape can derive from the position of the donor atom on the spacer and in this regard exoditopic ligands are to be preferred. Bent or flexible linkers can also favor zigzag conformation as well as metal ions showing a linear or tetrahedral or cis-octahedral coordination geometry.<sup>31</sup> The zigzag polymer  $\text{Cu}(\text{glycine})(\text{adenine})(\text{NO}_3)(\text{H}_2\text{O})$  is, for instance, yielded mixing  $\text{Cu}(\text{NO}_3)_2 \cdot 3\text{H}_2\text{O}$ , glycine and adenine in hot water.<sup>32</sup> In this case, each  $\text{Cu}^{2+}$  ion is coordinated to a glycine and two adenine molecules in the equatorial plane, while a  $\text{NO}_3^-$  anion and a water molecule occupy the apical positions. The structure of such CP, active as DNA scission agent, is furthermore stabilized by an array of  $\text{O}-\text{H}\cdots\text{O}$  and  $\text{N}-\text{H}\cdots\text{O}$  hydrogen bonds and also  $\text{C}-\text{H}\cdots\text{O}$  weaker interactions, occurring among adjacent chains, leading to a supramolecular ordered plane. The stabilization of zigzag chains to give 2D or 3D supramolecular networks is however recurrent in the literature and is aided by the formation of intermolecular interactions such as the already mentioned hydrogen bonds<sup>33</sup> but also through  $\pi\cdots\pi$  stacking interactions<sup>34</sup> and electrostatic interaction with ions.<sup>35</sup>

The third possible structural motif for 1D CPs is the ribbon. This type of structure involves the formation of macrocycles due to the coordination of bent and intertwist linkers to the metal nodes.  $[\text{Cd}(\text{pydc})(\text{phen})]_n$ , where  $\text{H}_2\text{pydc}$  = pyridine-2,3-dicarboxylic acid and phen = 1,10-phenanthroline, belong to the class of ribbon CPs.<sup>36</sup>  $\text{Cd}(\text{II})$  ions show an octahedral coordination environment and every  $\text{Cd}(\text{II})$  node is coordinated to three nitrogen atoms and three oxygen atoms deriving from a phen ligand and two different pydc spacers, as reported in Figure 13a.

Pydc exploits two different coordination modes (**Figure 13b**): i) chelating a  $\text{Cd}(\text{II})$  center through a carboxylic oxygen and the pyridine nitrogen, and ii) with a bridging oxygen coordinating two  $\text{Cd}(\text{II})$  ions.

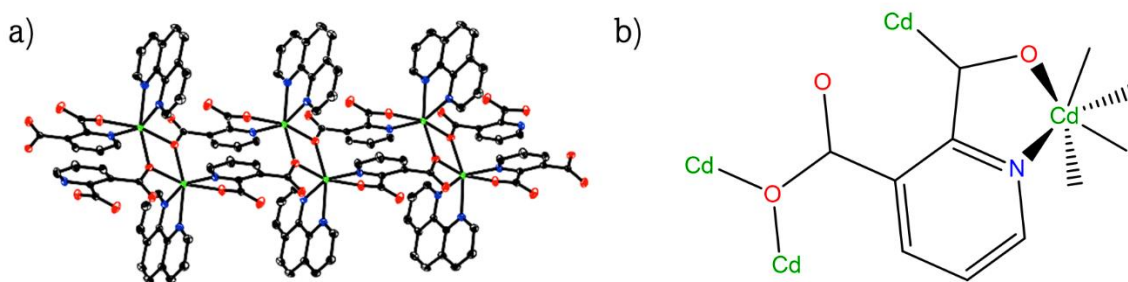


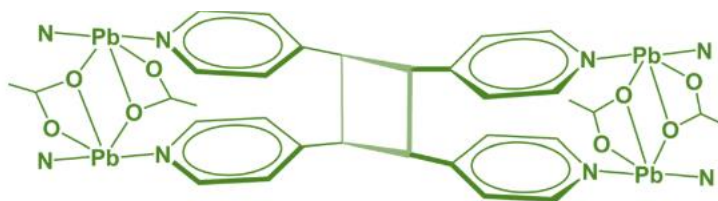
FIGURE 13 a)  $\text{Cd}(\text{pydc})(\text{phen})$  crystal structure showing a ribbon motif. Carbon (black), nitrogen (blue), and copper (green) atoms are indicated. Hydrogen atoms are omitted for clarity; b)  $\text{Cd}(\text{II})$  different coordination fashions.<sup>36</sup>



Furthermore, the possibility to form hydrogen bonds and stacking interactions among the aromatic rings result in a fascinating 3D zipper-like supramolecular network.

Ladder motif, instead, is characterised by “T-shaped” repeating units constituted by the organic linkers representing the uprights and the pegs of the ladder and by the metal nodes corresponding to the anchoring point of the steps on the uprights. A structure of this type defines the formation of cavities whose dimensions are affected by linkers lengths, their arrangement in the network and by the coordination mode.

$[Pb_2(\mu\text{-bpe})_2(\mu\text{-O}_2\text{CC}_6\text{H}_5)_2(\text{O}_2\text{CC}_6\text{H}_5)_2]$ , where  $\text{-O}_2\text{CC}_6\text{H}_5$  is the benzoate group and bpe= 1,2-bis(4'-pyridyl)ethylene, is a photoreactive ladder CP showing a four-membered  $Pb_2O_2$  cycle, as reported in **Figure 14**. The double bonds C=C deriving from bpe linkers are aligned in parallel and can easily be turned into cyclobutane moiety because of UV irradiation.<sup>37</sup>



**FIGURE 14** Representation of ladder motif due to cyclobutane moiety in  $[Pb_2(\mu\text{-bpe})_2(\mu\text{-O}_2\text{CC}_6\text{H}_5)_2(\text{O}_2\text{CC}_6\text{H}_5)_2]$ .<sup>37</sup>

The last structural motif regarding the 1D CPs to describe is the helical one. In order to obtain a helical CP, it is necessary to adopt flexible and bent spacers that twist along the extension axis of the polymer chain.  $[Mn_4Cl_3(\text{pyr}2\text{c})_4(\text{HCO}_2)]_n$  where pyr2c = pyrimidine-2-carboxylate and  $\text{HCO}_2$  = formate represents an example of such 1D CP motif.<sup>38</sup> The one-dimensional helical chains are furthermore stabilized by electrostatic interactions with chloride anions to yield a two-fold interpenetrated net.

Structural patterns for 2D structures can be instead classified into square, rhombic, rectangular or honeycomb grids, brick walls, herringbones, and bilayers, as reported in **Figure 15**.

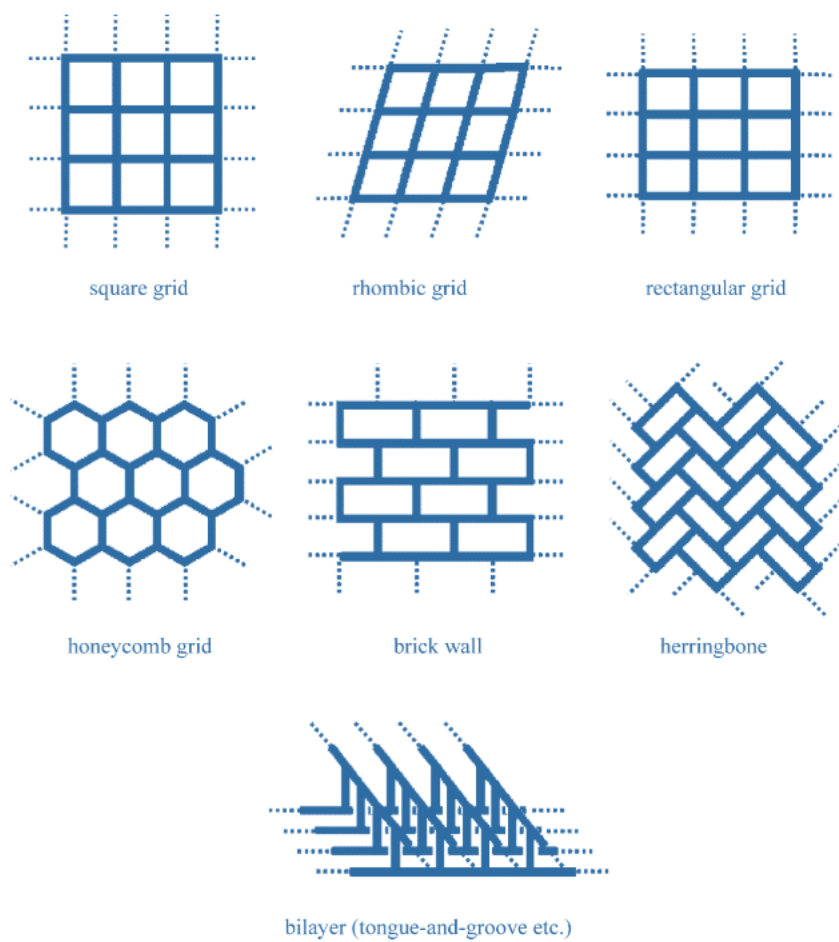


FIGURE 15 Outline of 2D motifs: square, rhombic, rectangular and honeycomb grid, brick wall, herringbone, and bilayer.<sup>31</sup>

Square grid CPs are the most common two-dimensional motifs with a recurring metal/linker ratio of 1:2. The coordination units, in this case, consist of the metal nodes and four linkers for each of them, allowing for infinite polymer extension in two dimensions.

An interesting case of flexible square grid structure can be found in  $\text{Cu}(\text{BIPY})_2(\text{BF}_4)_2$ <sup>39</sup> in which four BIPY linkers coordinate the equatorial plane of each octahedral  $\text{Cu}^{2+}$  ion. Even if it is easy to guess that the square cavities can accommodate guest molecules, for this CP no porosity would be observed due to the staggered architecture which blocks the entry of adsorbed molecules. In this specific CP, however, a gate phenomenon occurs: when  $\text{CO}_2$  is absorbed, the pyridine rings rotate and the distance between the layers increases generating usable space for guest molecules storage.

Other two-dimensional grids can be obtained with rectangular or rhombic shape and the same metal/linker ratio.

In contrast, when the metal center is coordinated by three spacer molecules with an overall metal/ligand ratio in the structure that is generally but not always equal to 2:3, “T-shape” building blocks are formed and the obtained layers result in honeycomb grid, brick wall, or herringbone designs. In order to produce “T-shaped” connectors, coordinating anions such as halides and nitrates or supplementary terminal ligand molecules are employed to occupy vacant coordination sites. However, the metal/linker ratio is not a fixed rule and can vary, also depending on the denticity of the linker and the metal coordination geometry. For instance, the 2D CP Cd(TMA) (TMA = 3-thiophenemalonate) show a undulate honeycomb motif alternating inorganic CdO<sub>6</sub> octahedra layers and organic thiophene layers with a metal/linker ratio 1:1.<sup>40</sup>

The study of the structural motifs of three-dimensional networks is usually conducted with a net-based approach, as reported by Robson in his review in 2000.<sup>20</sup>

A net is a discrete or infinite set of nodes connected to each other with a specific topology.

Net topologies often originate from minerals name and are usually indicated with a three-letter abbreviation in bold. For example, diamond-like structure is indicated as **dia**, while quartz net is **qtz**.

Some nets are very common and known, such as that of NaCl and diamond; others are rare and unique such as the chicken-wire-like architecture.

Robson assumes that *“if we can generate molecular building blocks with a functionality and stereochemistry appropriate to a particular one of the above target nets, then merely allowing these pre-organised components to react together under the correct conditions may lead to the spontaneous assembly of the intended network.”*

In the sub-chapter dedicated to coordination polymers and MOFs synthesis methods, it will be further specified how in reality it is not enough just to think of the appropriate building blocks and mix them together to create a certain structure. Each network is the result of an optimization of thermodynamic and kinetic reaction parameters. This discourse is particularly valid for the obtaining of crystalline structures.

**Figure 16** shows some common three-dimensional motifs for extended structures.

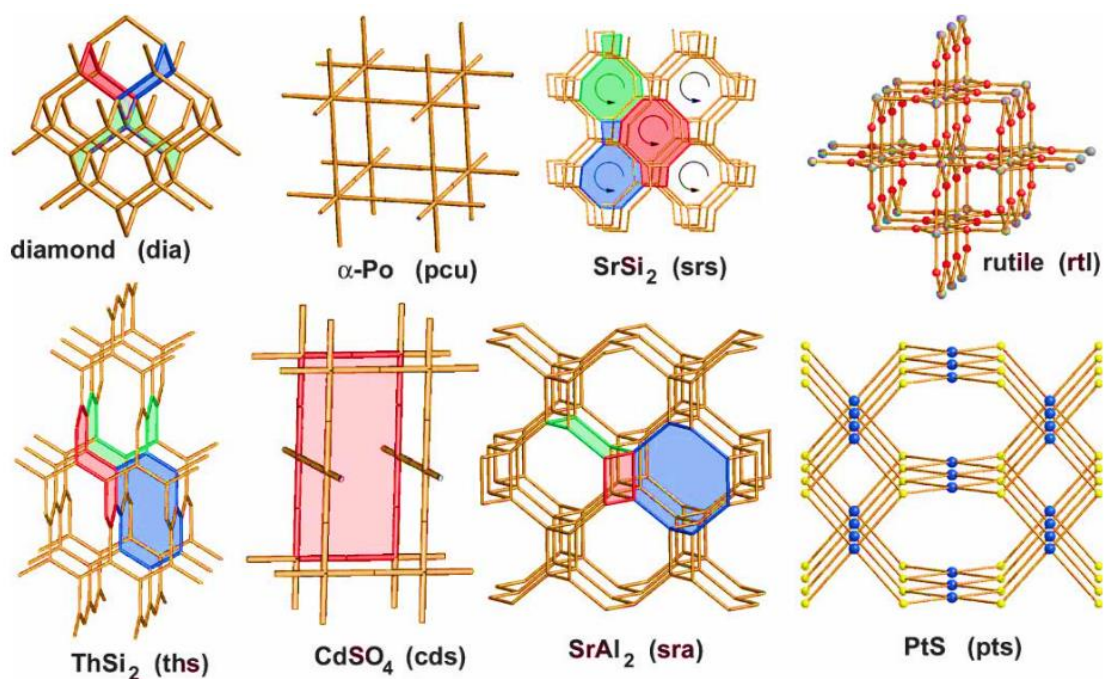


FIGURE 16 Representation of some 3D structural motifs.

The diamond net was the first net studied and is that of Robson's CP  $\text{Cu}[\text{C}(\text{C}_6\text{H}_4\text{CN}_4)]$  previously mentioned (Figure 9). The coordination geometry of  $\text{Cu}^+$  is clearly tetrahedral, simulating  $\text{sp}^3$  hybridized carbon in the diamond structure, with each metal center coordinated by four 4',4'',4'''-tetracyanotetraphenylmethane linkers.  $\text{Zn}(\text{PEBA})_2$  where PEBA is 4-[2-(4-pyridyl)ethenyl]benzoate can be cited as a diamondoid structure.<sup>41</sup> The **dia** network, in this case, is originated from the alternation of two different  $\text{Zn}^{2+}$  centers: the first one has an octahedral coordination environment because it's linked to four oxygens deriving from two chelating PEBA groups and to pyridine nitrogen atoms of other two linkers; the second one, instead, is coordinated by two pyridine nitrogen atoms and two monodentate carboxylate which derive from four different organic linkers, resulting in a tetrahedral environment.

$\alpha$ -Po or **pcu** is another very common net topology to which Prussian blue and its derivatives belong. This net can be obtained by combining an octahedral metal center with a linear or with a hexatopic linker having six donor atoms in the opportune orientation.  $\text{Cu}_4(\text{CDC})_4(4,4'\text{-Bpe})$  with  $\text{CDC} = \textit{trans}$ -1,4-cyclohexanedicarboxylate and  $4,4'\text{-Bpe} = \textit{trans}$ -bis(4-pyridyl)ethylene), shows an intriguing paddle-wheel dimer motif causing the formation of  $\alpha$ -Po net, as reported in Figure 17.<sup>42</sup>

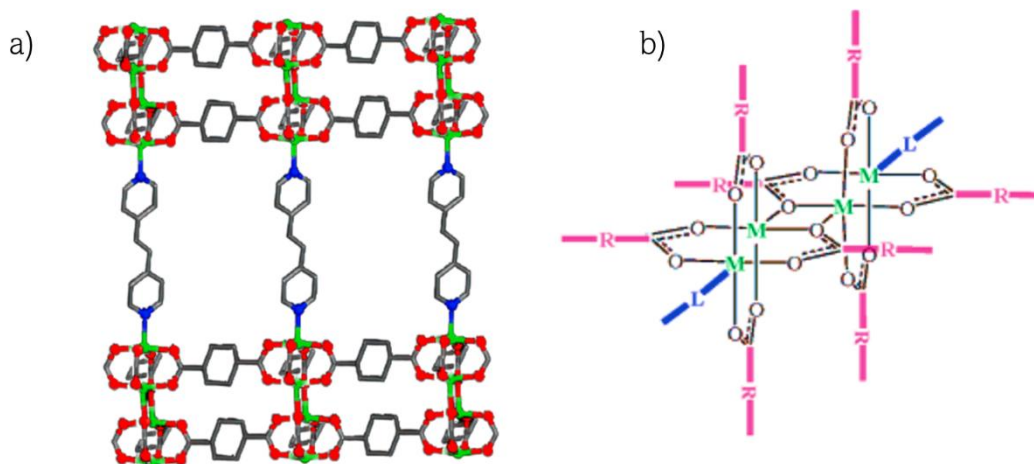


FIGURE 17 a) Crystal structure of  $\text{Cu}_4(\text{CDC})_4(4,4'\text{-Bpe})$ . Carbon (grey), nitrogen (blue), oxygen (red) and copper (green) atoms are indicated. Hydrogen atoms are omitted for clarity; b) Scheme of paddle-wheel dimer motif determining the  $\alpha$ -Po net topology.<sup>42</sup>

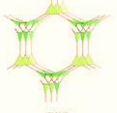
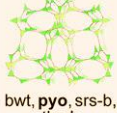


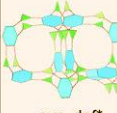


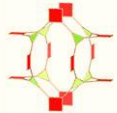

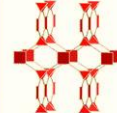
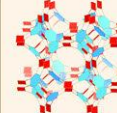
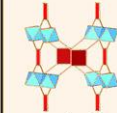
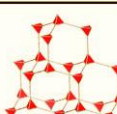
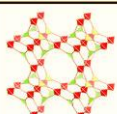

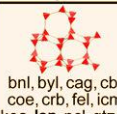
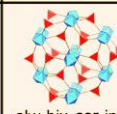
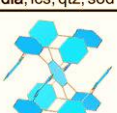
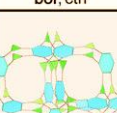
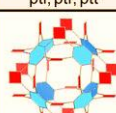
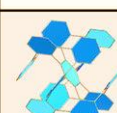
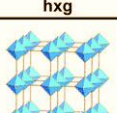
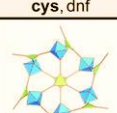
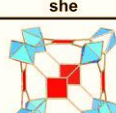
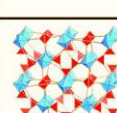
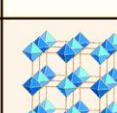
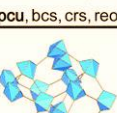
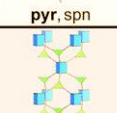
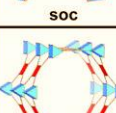
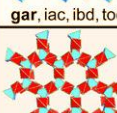

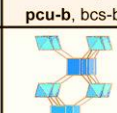
Rutile net (**rtl**) takes its name from  $\text{TiO}_2$  mineral and is a 6,3 connected net consisting of octahedral and trigonal coordination environments in a 1:2 ratio.  $\text{Cd}(\text{SDBA})(\text{H}_2\text{O})$  where SDBA = 4,4'-sulfonyldibenzoate is a rare twofold interpenetrating rutile network.<sup>43</sup> Each  $\text{Cd}^{2+}$  ion assumes a distorted pentagonal-bipyramidal configuration because it's coordinated to five oxygens: three of them derive from three carboxylate groups of three different SDBA linkers, one oxygen atom comes from the sulfonyl group from another SDBA while the last oxygen atom is from a water molecule. Hence, going into more detail, one of the two carboxylate groups coordinates with a tridentate chelating/bridging fashion linking two metal ions while the other carboxylate moiety displays a bidentate chelating fashion. Sulfonyl group, on the other hand, exhibits a monodentate coordination style.

PtS or **pts** net is made of tetrahedral and square planar 4-connecting building blocks linked to each other.  $\text{Cu}(\text{F}_4\text{TCNQ})$  is a 3D network with **pts** topology in which  $\text{F}_4\text{TCNQ}^{2-}$  = 2,3,5,6-tetrafluoro-7,7,8,8-tetracyanoquinodimethane dianion.<sup>44</sup>  $\text{Cu}^+$  ion represents the tetrahedral node while the linker shows square planar configuration. Square channels are generated from the assembling of such coordination units.

Other remarkable net topologies are  $\text{ThSi}_2$  (**ths**),  $\text{SrSi}_2$  (**srs**),  $\text{SrAl}_2$  (**sra**),  $\text{CdSO}_4$  (**cds**).

In this subchapter the most common one-, two- and three-dimensional structural morphologies have been illustrated with the aim of establishing how the nature and coordination geometry of the building blocks affect the dimensionality and the structural motif of CPs.

Based on that, **Figure 18** reports a practical table where from the encounter between the geometry of building unit 1 with the geometry of building unit 2, it is possible to verify the corresponding topology or topologies of the resultant net.<sup>45</sup> Sometimes, more nets are possible for the same combination of building block geometries; in addition, empty boxes are present meaning that some combinations are not compatible or no structures with such net topology have been synthesized up to now.

Building unit 1 \ Building unit 2	2-c Linear	3-c Triangle	4-c Square	4-c tet	6-c Hexagon	6-c oct
3-c Triangle	 srs	 bwt, pyo, srs-b, ths-b	 fjh, fmj, gee, iab, yac, yao	 asn, ept, ofp	 cys, dnf*	 anh, ant, apo, brk, cep*, cml, czz, eea, qom, rti, tsx, zzz
4-c Square	 nbo, lvt, rhr	 pto, tbo	 cev, cdl, cdm, cdm, cds, cdz, mot, muo, qdl, qzd, ssd, sse, ssf, sst	 pts	 nts	 myd, ybh
4-c tet	 dia, lcs, qtz, sod	 bor, ctn	 fgl, mog, pds, pth, pti, ptr, ptt	 bni, byl, cag, cbt, coe, crb, fel, icm, kea, lon, pcl, qtz-b, sca, tpd, ucn	-	 alw, bix, cor, ing, spl, toc
6-c Hexagon	 hxg	 cys, dnf	 she	-	 hxg-b	-
6-c oct	 pcu, bcs, crs, reo	 pyr, spn	 soc	 gar, iac, ibd, toc	-	 pcu-b, bcs-b
6-c trp	 lcy, acs	 ceq, dag, fmz, hwx, moo, sab, sit, ydq	 stp	 fsi, hea, tpt	 htp	 nia

**FIGURE 18** A table illustrating the most common net topologies as a result of building units geometry (up to six points of extension).<sup>45</sup>

Before concluding the subchapter, it is interesting to talk about isoreticularity and its relationship to the synthetic design of MOFs.

MOFs that have the same topology are called isoreticular MOFs. The concept of isoreticularity is of particular interest in the design of MOFs, because knowing the desired network topology and the constituent elements required to achieve it, one can decide to design a network with the same topology, but with larger or smaller pores or different

functional groups decorating the channel walls, in order to change the pores' features according to the different applications. This can be done simply by varying the length of the linkers used, which will have the same coordinating functional groups and the same spatial arrangement, but will vary, for example, in the number of aromatic rings in the carbon chain or will have other functional groups.

A clarifying example is shown in the paper by *Eddaoudi et al* in which sixteen MOFs with the same cubic **pcu** topology as MOF-5 were synthesized and named IRMOFs (IsoReticular MOFs),<sup>46</sup> using carboxylate linkers of various lengths and with different functional groups, as reported in **Figure 19**.

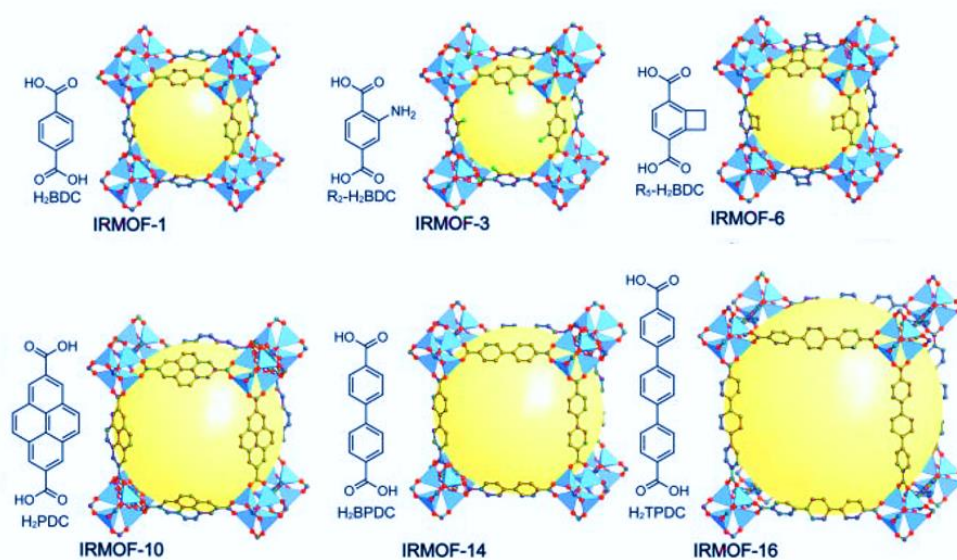


FIGURE 19 Representation of some of the sixteen IRMOFs showing the same **pcu** topology of MOF-5 and based on different carboxylate linkers.<sup>15</sup>

## 1.4 Synthetic routes for CPs and MOFs production

The most common synthetic methods mentioned in this subchapter are used for the synthesis of MOFs and CPs; therefore, no distinctions between the two classes of compounds are specified in the following discussion.

Some methods turn out to be greener than others; some approaches are in any case more employed than the others. What needs to be taken into account is that often the synthetic procedures and methods of MOFs and CPs are the culmination of careful optimization, and even small variations in the procedure could result in the failure of the synthesis, in the formation of other extended structures, in the generation of more networks simultaneously, or in the loss of crystallinity of the expected structure.

In the previous subsections, we have established what building blocks are necessary for the formation of an extended coordination structure, and we have seen in detail how the arrangement in space of coordinating units with the right coordination geometry and orientation leads to the formation of infinite chains and networks.

But how do the coordinating units all arrange themselves correctly in the right way? This is possible because of self-assembly, that is the process by which pre-existing disordered discrete entities combine to give an organized structure through the formation of specific local interactions among themselves (electrostatic interactions, hydrogen bonding, Wan der Waals forces, London dispersion forces, etc.).

Often, however, intermolecular interactions occur not only between coordinating units, but are established with solvent molecules or with modulators, precise molecules appropriately added at the synthesis stage to direct the secondary interactions and to exert control over physical parameters such as crystallinity, porosity, particle dimensions, morphology, and crystalline defects.<sup>47</sup>

In addition, we have already seen that if we want to achieve stable architectures, the use of negatively charged rather than neutral organic linkers and the use of metal clusters instead of single metal ions turn out to be winning choices. What has just been said implies that for MOF or, more generally, CP formation, deprotonation of the organic ligand must occur, which will allow more efficient and energetically stable coordination on the metal node.

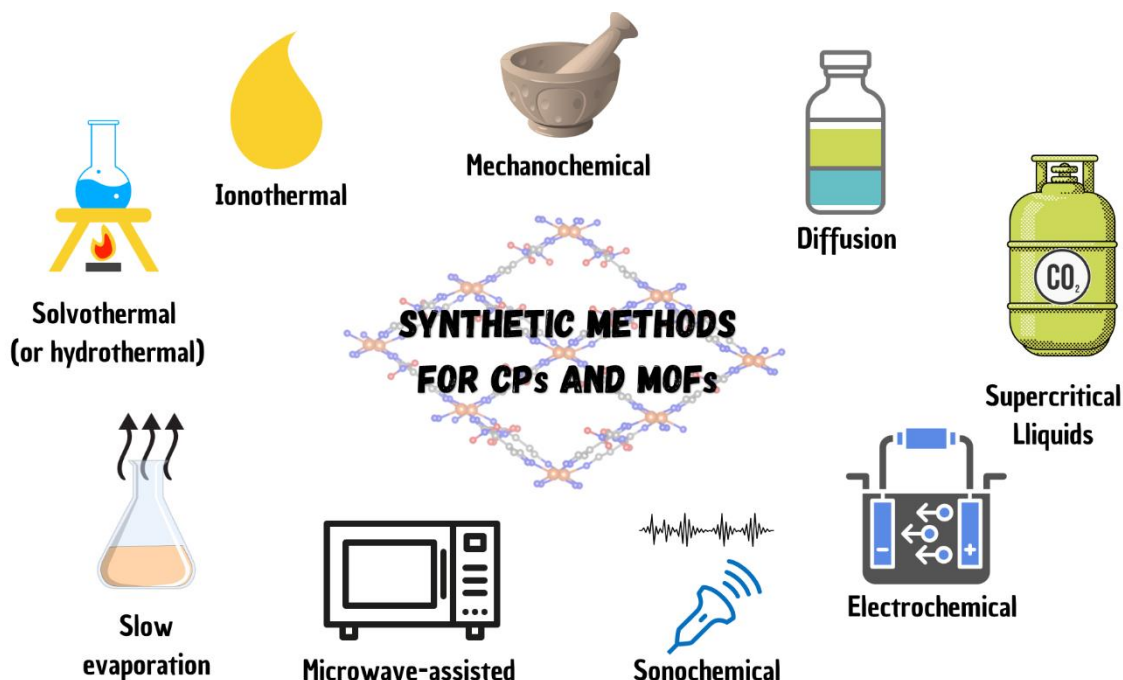
Given these premises, it is now clear that the parameters to be kept under control in the synthesis of MOFs are numerous: mode of synthesis, solvents used, reagents used and their



molar ratio, use of modulators, reaction temperature, autogenous pressure, pH, reaction time just to mention the most important ones.

Having reached this point, it is now possible to analyse in depth the best-known MOFs and CPs synthetic methods: solvothermal (or hydrothermal), microwave-assisted, electrochemical, sonochemical, ionothermal, in supercritical liquids, mechanochemical, by diffusion and by slow evaporation.<sup>48–53</sup>

A scheme of all synthetic routes is illustrated in **Figure 20**.



**FIGURE 20** A scheme of all the techniques adopted for the synthesis of CPs and MOFs.

Solvothermal synthesis is the most used method often reported in the literature for zeolites<sup>54,55</sup> and later widely applied for CPs as well.

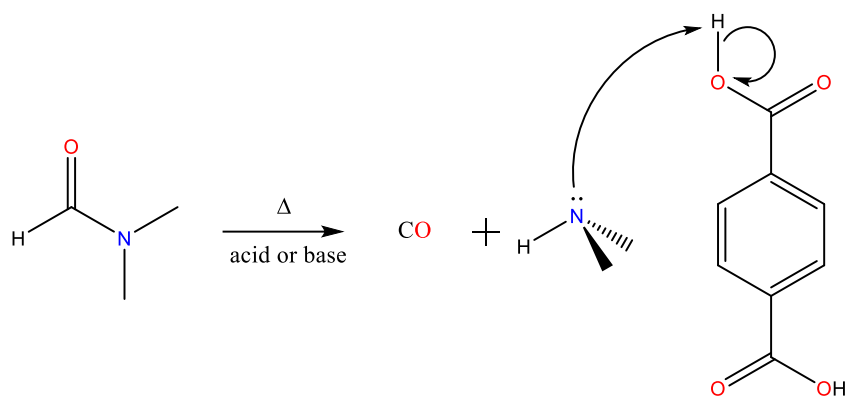
The solvothermal reaction is carried out by dissolving the metal precursor and the organic linkers in a solvent and then moving them into an autoclave. The system is heated by electrical heating and an autogenous pressure is developed inside because the temperature is set higher than the boiling point of the chosen solvent, thus allowing the assembly of the building blocks. As a result, the temperature range is usually 353–533 K depending on the nature of the solvent. When the solvent is water, the technique is named hydrothermal.

Besides water, other solvents such as methanol, ethanol, acetonitrile and dimethylsulfoxide (DMSO) are employed but the prince of solvents for MOF synthesis is definitely *N,N*-dimethylformamide (DMF) along with some of its analogues: *N,N*-diethylformamide (DEF),

*N,N*-dimethylacetamide (DMA), *N,N*-diethylethanamide (DEE), *N,N*-dipropylethanamide (DPE), *N,N*-diethylpropanamide (DEP) and *N,N*-dipropylpropanamide (DPP).

Amide solvents, despite their toxicity, are preferred in the synthesis of MOFs for two reasons: i) their high boiling temperatures allow really high synthesis temperatures, providing the necessary energy for network formation; ii) at these high temperatures, amides decompose releasing small amounts of the corresponding amines that as basic compounds deprotonate the organic linker rendering it ready for metal node coordination; in addition, the amines, being gases, generate an internal pressure that directs the assembly of building blocks.

DMF, for instance, decomposes at temperatures near the boiling point (425 K) releasing CO and NMe<sub>2</sub>. The decarbonylation can occur even at room temperature, especially if catalyzed by acids or bases,<sup>56</sup> as represented in **Figure 21**.



**FIGURE 21** Schematic illustration of *in situ* DMF decarbonylation occurring during the synthesis of a MOF. HNMe<sub>2</sub> then deprotonate the organic linker (BDC in the example) which will coordinate the metal center to yield the MOF.

Sometimes, syntheses also take place at room temperature or at temperatures below the boiling temperature of the solvent. In this case they are referred as non-solvothermal conditions.

Normally, long times are required for this type of synthesis, which can range from several hours to several days. When the reaction is concluded, the mixture is slowly cooled until the achievement of room temperature. Slow cooling, sometimes, can promote the product formation as microcrystalline powder suitable for X-rays powders diffraction.

Some issues concerning with the solvothermal synthesis method are prolonged reaction times, the occasional lack of product quality, the use of toxic solvents and the elevated energy expenditure. For this reason, greener synthetic methods have been proposed and tested for MOFs and CPs in recent years.

An example of solvothermal synthesis is that of ULMOF-4<sup>57</sup> (ULMOF stands for ultra-light MOF, due to the presence of the light metal ion Li<sup>+</sup>). The 3D network has been obtained mixing 3,5-pyridinedicarboxylic acid (3,5-PDC), LiNO<sub>3</sub> and LiOH in DMF. Once a homogeneous solution is attained, the mixture was heated at 453 K for five days. The use of DMF as solvent, the reaction temperature higher than the boiling temperature of DMF solvent (which is 425 K), and the long reaction times, are all typical features of the solvothermal method.

It should be further specified that obtaining a homogeneous reaction mixture before transferring it to the autoclave positively affects the product formation and crystallinity.

Solvothermal main features are resumed in **Figure 22**.

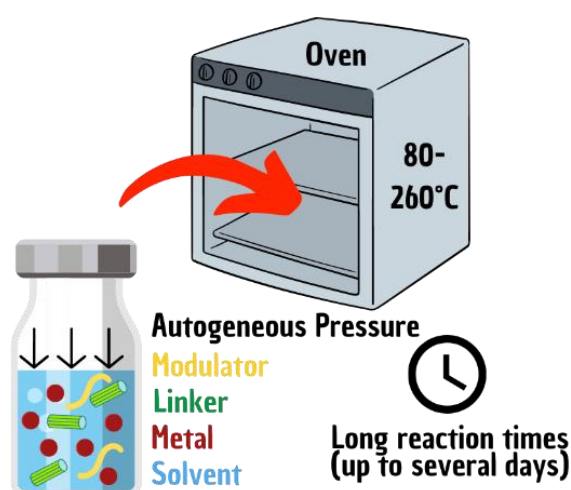


FIGURE 22 *Scheme of solvothermal synthesis of CPs/MOFs.*

The second synthetic route we are going to examine is the microwave-assisted synthesis, schematized in **Figure 23**.

Dipoles generated by molecules in solution (reactants and solvents) interact with electromagnetic waves and rotate in an attempt to align with the microwave-induced electric field. The rapid rotation produces molecular friction, generating thermal energy inside the reaction mixture. This allows reaction times to be greatly reduced from days as in the solvothermal method to minutes. Obviously, polar solvents are indispensable for this type of synthesis.

Furthermore, a great control over particle size and crystallinity can be exercised by this technique.

MOF-74 (Ni), a MOF based on 2,5-dihydroxyterephthalate (dhtp) linkers and showing hexagonal channels, was synthesized in via hydrothermal route, condensation reflux and by microwave-assisted method.<sup>58</sup> Microwaves approach has turned out to be the most efficient one, reducing reaction time from 32 hours or 24 hours to 1 hour and leading to more uniform particle dimensions and better thermal stability with respect to the other methods.

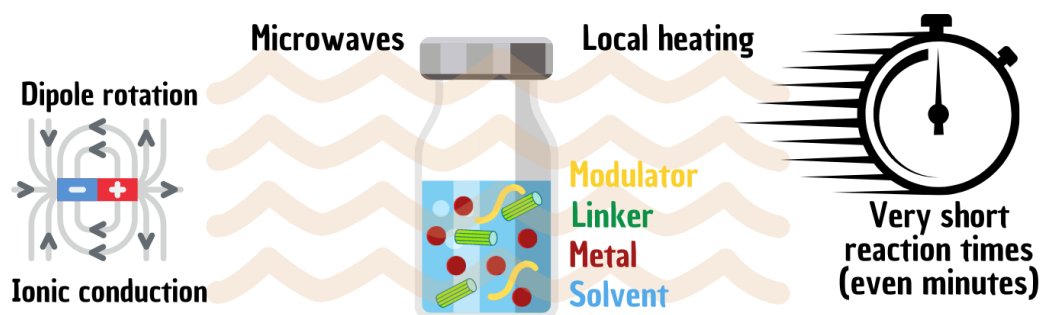


FIGURE 23 Scheme of microwave-assisted reaction of CPs/MOFs inspired by Lee et al.<sup>59</sup>

Another synthetic method is the electrochemical mode.

The first electrochemical synthesis was reported by BASF researchers in 2005 dealing with the industrial production of HKUST-1.<sup>60</sup> This MOF shows a cubic **tbo** (twisted boracite-type)<sup>61</sup> net topology. The choice to use this alternative method of synthesis lies in the possibility of not introducing anions that are difficult to process on industrial manufacture such as  $\text{Cl}^-$ ,  $\text{ClO}_4^-$  and  $\text{NO}_3^-$ , since only the metal ion is introduced into the reaction system in continuous by anodic dissolution. The use of protic solvents prevents metal deposition on the cathode but results in the formation of hydrogen gas.

This technique, hence, is advantageous for the industrial production of high quantities of MOFs as it works continuously and is particularly effective for the construction of MOFs films.<sup>62</sup> In addition, electrochemical synthesis methods introduce new parameters for optimizing syntheses such as voltage regulation or pulses imposition.

Mechanochemical synthesis, instead, involves the use of mechanical energy through mortar grinding or ball milling. Solid-state reactants interact with each other through flattening, welding, and continuous cracking of solids, which provide the energy to make the reaction take place. A representation of this method is highlighted in **Figure 24**.

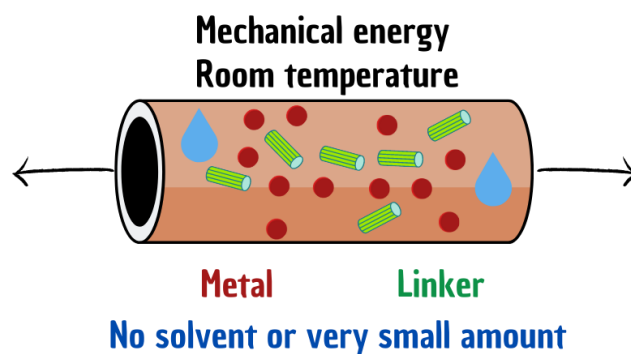


FIGURE 24 Scheme of mechanochemical synthesis of CPs/MOFs.

The mechanochemical method has many advantages, reducing the environmental impact of MOFs syntheses<sup>63</sup>: i) it is possible to work at room temperature, avoiding the heating of the reaction batch; ii) reaction times are much reduced compared to conventional solvothermal methods; iii) one can work in the total absence or with very small amounts of organic solvent, decreasing all the negative effects due to exposure to these carcinogenic and harmful substances, and iv) it is also feasible to replace metal salts with oxides, so that the reaction byproduct is exclusively water.

Some suggestions for successful mechanochemical synthesis are to use of hydrated metal salts as metal precursors and to choose metal salts in which the anion is a base that can promote deprotonation of the organic linker.

Acetic acid is a well-known modulator in MOF synthesis,<sup>64</sup> along with formic acid, propionic acid and trifluoroacetic acid. Acetic acid can be produced *in situ* when acetates are used as metal precursors, as they remove the proton from the organic linker. This fact generally results in more crystalline structures.

Finally, it has been observed that adding very small amounts of solvent in what is defined liquid assisted grinding (LAG) accelerates the reaction favoring the encounter of reactants.

However, an issue occurring with mechanochemical synthesis is the generation of structural defects by grinding process.<sup>65</sup>

Another way of synthesizing CPs is through the use of ultrasound, i.e., by sonochemical route. Ultrasounds are cyclic mechanical vibrations and their frequency ranges from 20 kHz to 10 MHz.

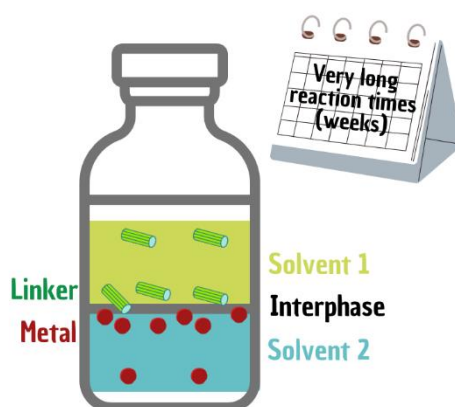
In this case, the energy is not delivered directly from the ultrasound to the molecules but takes advantage of a system of compression and rarefaction areas generated when the ultrasound is applied to a liquid. In areas of reduced pressure, the pressure is lower than the

vapor pressure of the solvent and of the reagents and this leads to the formation of bubbles. Meanwhile, vapor diffusion of the reactants into the bubbles volume occurs causing them to grow and accumulate energy. At some point the bubbles are unable to enlarge further and collapse releasing energy very quickly, reaching temperatures up to 5000K and pressures of 1000 bar. This phenomenon is called cavitation and depends on several parameters such as the intensity of the sound waves, the frequency, the temperature and the nature of the liquid medium. For instance, volatile solvents are not used in the sonochemical method because they result in lower energy associated with the cavitation phenomenon.

$[\text{Ag}(\text{mbih})(\text{BDC})\cdot 2\text{H}_2\text{O}]_n$ , where mbih = 1,6-bis(2-methylbenzimidazolyl)hexane, is 1D CP obtained both by solvothermal and sonochemical route.<sup>66</sup> Concerning with the second one, the mixture of metal salt and organic linkers was positioned in an ultrasonic bath at room temperature and atmospheric pressure for 90 minutes, with a set power of 120 W. The product obtained with the ultrasound-assisted technique shows nano-size particles. Then, tests have demonstrated that particle size decreases as sonication time rises and with increasing ultrasonic power.

Diffusion technique is another intriguing way to obtain CPs and MOFs.

The diffusion of the reactants can occur in liquid, gel, or gas phase. The diffusion in liquid phase, for example, involves the use of immiscible solvents in which solubilize separately the metal precursor and the organic linker. The formation of the extended network takes place because of the encounter of the two building blocks at the interphase between the two solvents (**Figure 25**).



**FIGURE 25** Scheme of diffusion in liquid phase method. The reaction occurs in the interphase between the two immiscible liquids.

The issue with this technique is mainly the extremely high reaction times, which can reach even weeks.

Another time-consuming technique for synthesizing CPs and MOFs is slow evaporation, which involves simple solubilization of the starting materials in a solvent or solvent mix and slow evaporation of it/them. Also with this technique, it is possible to work at room temperature.

Once the various techniques for the synthesis of CPs and MOFs have been presented, some clarifications are added regarding reaction solvents.

In addition to water, DMF, alcohols and all the other previously mentioned solvents, ionic liquids (ILs) and supercritical liquids have also been studied as reaction media in the synthesis of CPs.

The former ones are organic salts having very low melting points and vapor pressure and a modifiable solubilizing power. ILs are made of organic or inorganic positively or negatively charged ions and some of them are liquid at room temperature and for this reason indicated as RTILs. The advantage of using ILs lies in the possibility of easily recycling the medium and effectively solubilizing inorganic and organic reactants simultaneously.

Supercritical liquids are also designed for the synthesis of MOFs as they allow the solubilization of organic linkers that would otherwise be difficult to solubilize.

Of these, the most studied is certainly supercritical carbon dioxide ( $s\text{CO}_2$ ), given its low toxicity, moderate cost, and abundance, as well as the ability to be easily recycled.

## 1.5 Activation of MOFs

We have already mentioned several times that the peculiarity of MOFs is their porosity and high surface area. In the previous subchapter, we have listed various synthetic ways to obtain MOFs. Once the desired structures have been obtained, however, the cavities of MOFs turn out to be occupied: solvent molecules, organic linker molecules or metal salts that have not reacted or modulators can be found inside. It is clear that in order to use a MOF for any application it is necessary that the cavities be wiped clean of the various guest molecules inside, so that the MOF is ready to adsorb gases for gas storage, for the separation of pollutants from water or for drug delivery. The MOF is said to be "activated." In this subchapter we will look at the most common techniques used for activation, focusing on the different advantages in terms of preserving structural properties and in terms of green approach.

A summary diagram of all activation methods is shown in **Figure 26**.

Choosing the right activation method without compromising the crystallinity of the MOF is critical. It can generally be perceived that activation is suboptimal when there is much difference between the surface area value determined by porosimeter versus the theoretical value calculated from X-ray resolved structures.<sup>67</sup>

The classic method of activation is thermal activation, which involves heating the sample to a certain temperature for a certain time under vacuum condition and it has already been widely used for carbons and zeolites.

This method is simple and requires no additional reagents, but it often results in the loss of crystallinity resulting in a decrease in surface area.

This is due to the capillary action and surface tension of the imprisoned molecules housed in the MOF cavity, which as they come out of the pores as gases can break the crystals, during the activation process.

Before performing thermal activation, it is advisable to perform a thermogravimetric analysis so as to know the decomposition temperature of the MOF, and therefore select an activation temperature lower than it, usually half of it.

Solvent exchange is an activation mode that is often performed as it implies replacing reaction solvents with high boiling temperature and capillary tension such as DMF with low-boiling solvents with a lower vapor pressure such as chloroform or dichloromethane. The



solvent used for exchange, in fact, is usually an apolar solvent that establishes weak intermolecular bonds and therefore exerts less capillary forces.<sup>68</sup> *n*-hexane and perfluoropentane proved to be excellent exchange solvents as they have very low surface tension.<sup>69</sup>

After the MOF is obtained, it is usually washed several times with the reaction solvent to remove unreacted reactants. Then, the MOF is soaked in the exchange solvent, decanted or centrifuged, and again immersed in the exchange solvent. This operation is usually repeated several times. A thermal activation at moderate temperatures can be subsequently carried out to remove the exchange solvent from the MOF pores.

It has been furthermore observed that solvent exchange kinetics are very fast, so it is not necessary to keep the MOF immersed in the exchange solvent for long times; it is much more effective to perform several short washes (e.g., every 20 minutes).

In addition, one can also treat the dried MOF solvothermally with the exchange solvent.<sup>70</sup> and also Soxhlet extractions with the exchange solvent have been tested.<sup>71</sup>

Even if the solvent exchange method is very effective, its use on an industrial scale is impractical both because large quantities of solvent are used with their associated handling and exposure hazards and because these solvents are often halogenated and therefore have higher disposal costs.

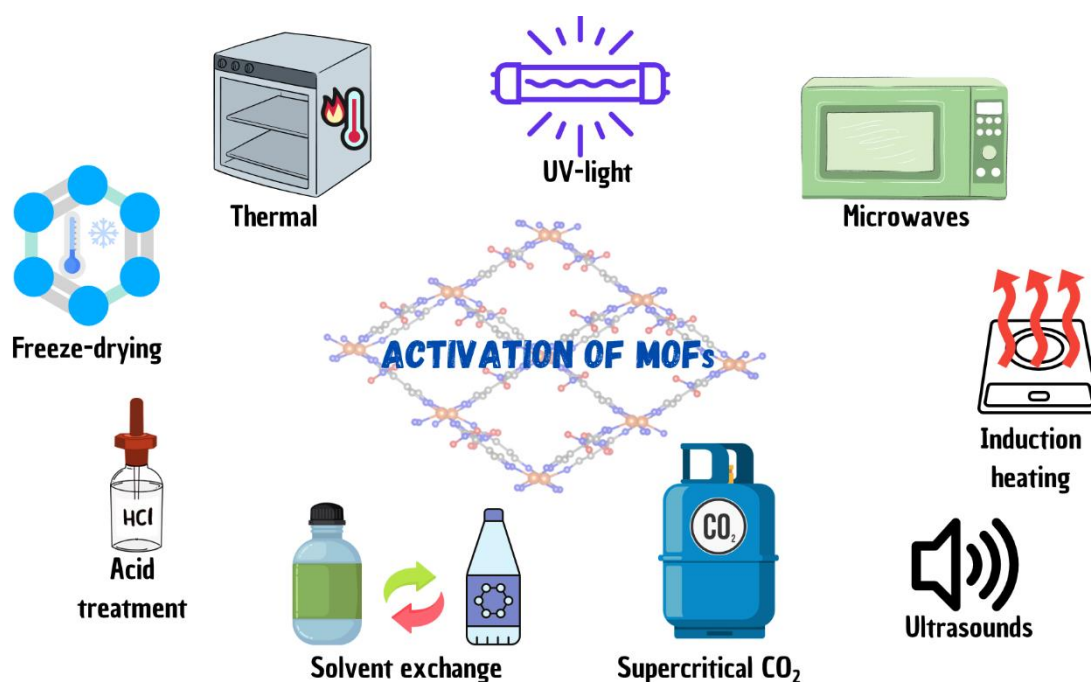


FIGURE 26 A summary of all activation methods of MOFs.

Activation of MOFs using supercritical carbon dioxide is a method that is increasingly gaining ground in the scientific literature, as several MOFs have shown a much higher surface area and pore volume when activated by this method,<sup>72</sup> and which I personally got to know and adopt experimentally during my six-month visiting period at Northwestern University in Evanston, Illinois, United States, hosted by Prof. Omar K. Farha.

The sCO<sub>2</sub> succeeds in gently activating MOFs because the supercritical phase does not generate surface tension and capillary forces, so it avoids crystal lattice disruption.

Before using the instrumentation for activation with supercritical CO<sub>2</sub>, the sample is immersed in an exchange solvent that is miscible with CO<sub>2</sub> in the liquid state, usually methanol and ethanol.

The sample is subsequently moved to a suitable vessel, leaving it soaked overnight in the selected solvent so that the MOF settles to the bottom. The next day, the excess solvent is removed, leaving only a thin layer to cover the solid.

At this point, the actual activation process can begin. The sample is placed in the sCO<sub>2</sub> dryer and several washes with liquid carbon dioxide are performed about every two hours, followed each time by purging and introducing new liquid CO<sub>2</sub>. The last step consists of using supercritical CO<sub>2</sub>. The system is brought to supercritical conditions (304 K and 73 atm), and the gaseous CO<sub>2</sub> is released out of the dryer. More information on the procedure, the equipment and a demonstration video are given as supplementary materials by *Howarth et al.*<sup>73</sup>

The safety, nontoxicity, and nonflammability of CO<sub>2</sub>, together with the excellent activation performance attested for various MOFs such as NU-1501-Al, UMCM-9, and SNU-70,<sup>74</sup> make this method an effective alternative that should be taken into account.

Freeze drying is another interesting MOF activation technique that involves the exchange of the reaction solvent for one with a high freezing point, such as benzene which freezes at 278.5 K. The sample is brought to 273 K and then to room temperature for several cycles. Finally, removal of the benzene is done by sublimation, placing MOF under vacuum and at a temperature lower than benzene freezing point. Given the toxicity and carcinogenicity of benzene, cyclohexane can be used instead.

For chemically stable MOFs, acid treatment is possible and sometimes necessary. This method of activation, which is then followed by common thermal activation, is used in cases where the guest molecules inside the MOF pores are coordinated to metal centers and

therefore difficult to remove only by conventional heating. For instance, benzoic acid molecules can be easily removed from zirconium nodes when treated with a HCl/DMF mixture, allowing the formation of Zr-OH bonds.<sup>75</sup>

Other, little-used activation techniques are reported in the literature<sup>68,76</sup> employing microwaves, UV light, ultrasounds and induction heating.

## 1.6 Determination of MOFs porosity

In the previous subchapters, we talked in detail about MOFs: we discussed the main topologies of these three-dimensional porous networks, then we outlined synthetic strategies for obtaining them and finally focused on how to activate MOFs so that they are ready for the designated application. But once the MOFs are activated, how do we determine their porosity and surface area? What is the most correct equation to describe the physical adsorption of gases in MOFs? What are the differences between microporous and mesoporous MOFs? What are the most correct gases to consider when evaluating the porosity of a MOF?

All these questions will be answered in this subchapter.

First of all, we need to define the correct terms to use when referring to the gas adsorption phenomenon, following the definitions and classifications reported in the 2015 IUPAC Technical Report on gases physisorption.<sup>77</sup>

The first distinction to be made deals with adsorption and absorption. The first one occurs when atoms, ions or molecules of adsorbate concentrate near the surface of the adsorbent material. We are particularly interested in systems in which the adsorbed molecules are gases, and the adsorbent material is a solid, the MOF. Absorption, on the other hand, requires that adsorbate molecules penetrate the surface of the adsorbent material reaching the bulk of the material. Often the two phenomena both occur, and for this reason the general term sorption is preferred to be used.

The other crucial distinction that cannot be neglected is between physisorption and chemisorption. The difference is based this time on the nature of the interactions that are established between the sorbent material and the sorbate: if they are intermolecular forces with an electrostatic nature such as hydrogen bonding, Van der Waals forces, and London dispersion forces, one will speak of physisorption; if, on the opposite, a chemical bond is established, as occurs for example when hydrogen bonds covalently to the surface of platinum,<sup>78</sup> at that time one will speak of chemisorption.

As we are interested in gases adsorption by MOFs, the discussion will focus exclusively on physisorption.

Depending on the pore size of the adsorbent material, we can have micropores if the pore size is less than 2 nm, mesopores if this size is in the range of 2-50 nm while we will call macropores pore sizes exceeding 50 nm.

Going even deeper with the discussion, it is also useful to define the concept of internal and external surface of the adsorbent material. Typically, the internal surface is the one related to the pores, while the external surface is the surface outside the pores. However, recently, there is a tendency to assign to the internal surface the meaning of microporous surface and then to the external surface the significance of meso- and macroporous surfaces.

The measurement of adsorption of a gas by an adsorbent material such as MOFs is performed with an instrument called porosimeter. For each measurement, a graph called isotherm is generated where the amount of adsorbed gas (expressed in millimoles per gram of adsorbent material: mmol/g, or in cubic centimeters over grams of gas under standard temperature and pressure conditions: cm<sup>3</sup>/gSTP) is plotted on the ordinates as a function of the relative pressure  $p/p^0$  on the abscissas. This relative pressure consists of the ratio between the measured equilibrium pressure  $p$  and the saturation pressure  $p^0$  of the probe gas at the established analysis temperature, which is constant and that is the reason why the graph is called an isotherm.

The adsorption isotherm is generated point by point by gradual dosing of the analysis gas by the porosimeter. In addition, the graph generally consists of an adsorption isotherm and a desorption isotherm, which do not always coincide, as we will see shortly.

IUPAC catalogues adsorption isotherms into six different types, depicted in **Figure 27**, indicated using Roman numerals.

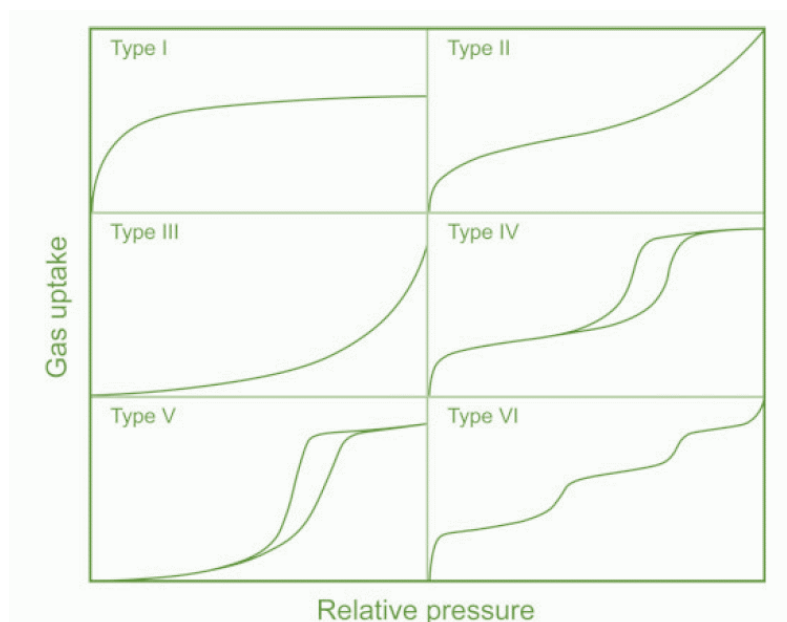


FIGURE 27 Representation of the six different isotherms individuated by IUPAC.<sup>15</sup>

Type I isotherms indicate exclusively microporous materials which exhibit high gas adsorption even at very low relative pressures reaching a plateau value. Type II, III and VI isotherms, on the other hand, describe macroporous or nonporous materials with sparse or no adsorption at very low relative pressures and higher values for very high relative pressures. What makes these three types different is the presence or absence of knees in the graph, which generally correspond to the completion of homogeneous adsorption layers: a single layer (monolayer) in type II, an undefined multilayer in type III, and a highly homogeneous and defined layer-by-layer adsorption in type VI.

Finally, type IV and V isotherms are not as reversible as the previous ones, as the adsorption and desorption isotherms do not coincide, and hysteresis occurs. The hysteresis phenomenon defines mesoporous MOFs and becomes apparent when there is condensation of the adsorbed gas in the pores at a lower pressure than the saturation pressure and depends on the pore geometry and MOF structural features.

**Figure 28** shows the various types of hysteresis that are obtained depending on the MOF texture. IUPAC has classified them into 5 classes that are indicated by a capital H followed by a number from 1 to 5. H1 is typical of MOFs with a very small range of uniform mesopores and has been observed mainly in MOFs whose pores are cylindrical. H2 hysteresis can be seen in MOFs with more complex networks, and which may have obstructed pores, structures resembling the shape of an ink bottle (in H2(b) is representative

of larger pores with respect to H2(a)). Hysteresis H3 concerns narrow-slit pores, while H4 is common to MOFs with wide-slit pores. Hysteresis H5 is uncommon and has been found in structures that simultaneously have totally open mesopores and blocked mesopores.<sup>15,77</sup>

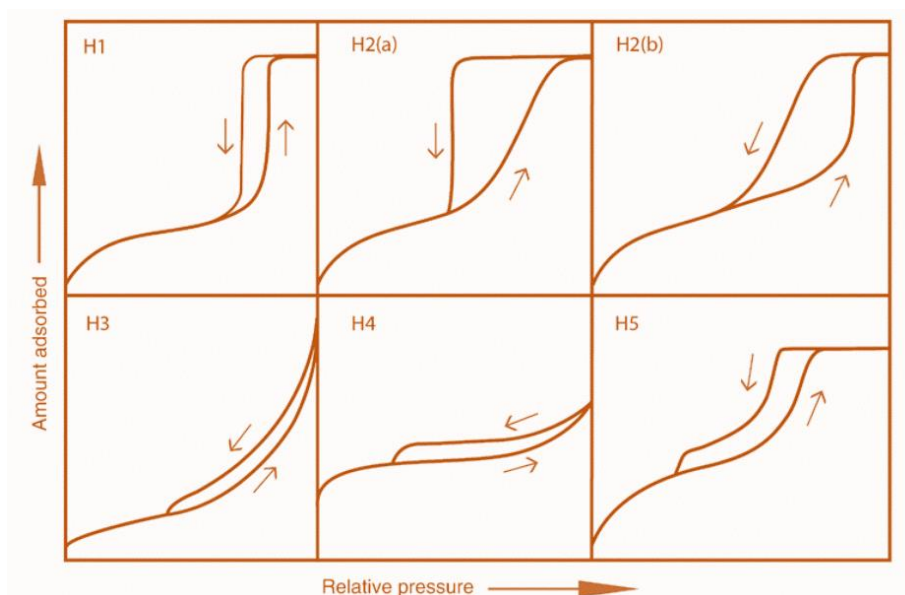


FIGURE 28 Representation of different hysteresis types.<sup>77</sup>

It has also been observed that the filling of the pores of networks having micro-, meso-, and macropores (type VI isotherms) with the probe gas is sequential according to this order, i.e., that all micropores are filled first, then all mesopores, and finally macropores and each fill corresponds to a different knee of the curve, as shown in **Figure 29**.

We reviewed the various isotherm morphologies that can be encountered by performing gas adsorption measurements with MOFs. At this point, however, we are interested in understanding how MOF porosity information can be derived. Once the isotherm related to an adsorption measurement of a gas has been obtained with the aid of the porosimeter, in fact, the values of surface area, pore volume, pore size distribution etc. can be derived through the application of mathematical models that best describe the phenomenon being studied.

Specifically, we define the specific surface area of MOF as the ratio between the total area expressed in square meters and the mass in grams of MOF, and for that reason its unit of measurement will be  $\text{m}^2/\text{g}$ . Similarly, the specific pore volume will be given by the total volume expressed in cubic centimeters divided by the mass of MOF expressed in grams, and the unit of measurement will be  $\text{cm}^3/\text{g}$ . Porosity, on the other hand, is expressed as a

percentage by dividing the pore volume of the MOF over the total volume of the MOF and multiplying by one hundred.

We are familiar with encountering in scientific publications concerning MOFs, two different values of specific surface area for each MOF, obtained from the corresponding two mathematical models by which they are calculated: Langmuir and BET (Brunauer, Emmett and Teller, which are the names of the creators of such model).

Langmuir's model is particularly well suited for monolayer adsorption systems with homogeneous surfaces and with very strong, covalent interactions between adsorbent and adsorbate and no interaction between the adsorbate molecules; in practice it is fine for describing chemisorption phenomenon and it is well represented by type I isotherms.<sup>79</sup>

The specific surface area value obtained with Langmuir's model is usually higher than the BET value and tends to overestimate the real value.

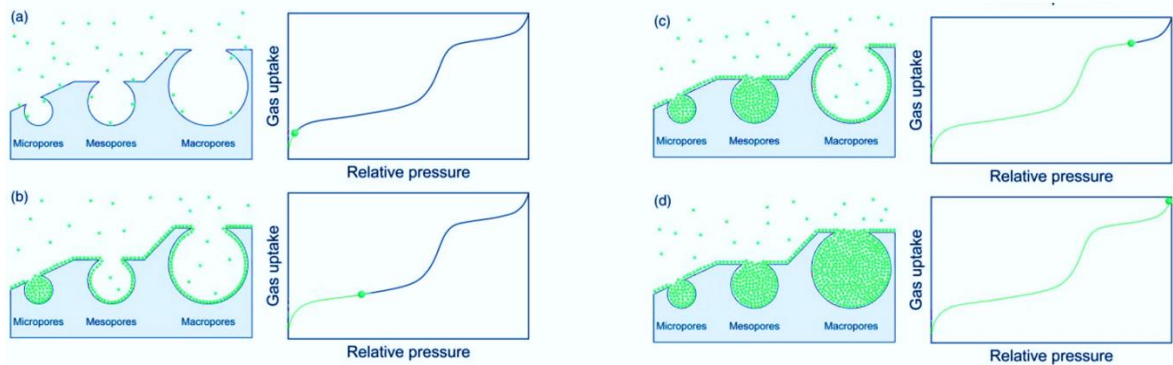


FIGURE 29 Outline of probe gas adsorption corresponding to a) surface area, b) micropores filling, c) mesopores filling and d) macropores filling.<sup>15</sup>

The BET model does not take into account the strong interaction between adsorbent and adsorbate and at the same time predicts a heterogeneous surface of infinite adsorption layers when the pressure equals the saturation pressure.<sup>80</sup> Weak intermolecular forces are established between the various adsorbate gas molecules, but only the vertical direction, while horizontal interactions aren't considered.<sup>81</sup>

The BET equation can be written in linear form as:

$$\frac{p/p^\circ}{n(1 - p/p^\circ)} = \frac{1}{W_{ml} \times C} + \frac{C - 1}{W_{ml} \times C} (p/p^\circ)$$



where  $n$  is the quantity of the adsorbed gas for a certain relative pressure  $p/p^\circ$  and a certain temperature,  $W_{ml}$  is called “monolayer capacity” of the probe gas, and  $C$  is a constant which affects the isotherms shape in the linear BET range ( $p/p^\circ = 0.05-0.30$ ) and depends exponentially on the energy corresponding to the monolayer adsorption.<sup>82</sup>

The value of specific surface area will be calculated from the following equation:

$$SSA = \frac{W_{ml}}{M \times m} \times N \times A$$

where  $SSA$  is the acronym for Specific Surface Area,  $N$  is the Avogadro number,  $A$  is the cross-sectional area of the probe gas (0.162 nm<sup>2</sup> for nitrogen N<sub>2</sub>),  $M$  is the molar mass of the probe gas and  $m$  is the mass of the sample.

Since the linearity of the BET equation is not always limited to the range 0.05-0.30, *Rouquerol et al.* proposed a set of consistency criteria<sup>83</sup> to ensure the validity of the obtained BET value and its reproducibility:

- i) consider the relative pressure range in which  $(1 - p/p^\circ)$  increases as  $p/p^\circ$  becomes higher.
- ii) the BET constant  $C$  must be  $>0$ .
- iii) the monolayer capacity  $W_{ml}$  calculated from BET equation must match with a relative pressure inside the range used for BET analysis.
- iv) the term  $\frac{1}{\sqrt{C+1}}$  must be the same of the pressure determined in criterion iii) with a maximum tolerance of 20%.

The pore size distribution is another useful piece of information that can be gleaned from other mathematical models, the DFT (Density Functional Theory) and the BJH (Barrett, Joyner and Halenda) which are not covered here. The pore distribution not only indicates the class which MOFs pore belong to (micropores, mesopores or macropores), but the morphology of the curve also reveals the network pristinity and the presence or absence of defects in the crystalline lattice.

A pore size distribution characterized by one or a few (depending on the topology of the network) sharp peaks can be attributed to a uniform and regular structure, while if the profile

of the distribution shows broad peaks, we are faced with a less crystalline and irregular network.

It is possible, in addition, to determine the isosteric heat of adsorption  $Q_{st}$ , that is an evaluation of the interactions between adsorbate and MOF, applying the Clausius-Clapeyron equation on at least two isotherms, carried out on the same sample and with same probe gas, measured at different temperatures.

$$Q_{st} = R \ln \left( \frac{P_1}{P_2} \right) = \frac{T_1 \times T_2}{T_2 - T_1}$$

At this point we only have to answer the question concerning which gaseous molecules can be used as probe to determine the MOF surface area and which analysis conditions must be adopted.

The pivotal gas is undoubtedly  $N_2$  gas, given the low costs required to obtain liquid nitrogen, and generally the structural properties of MOF (surface area, pore volume, pore size distribution) are determined with this gas at 77 K.<sup>84</sup>

In microporous materials, filling with nitrogen already starts at very low pressures,  $p/p^0$  less than  $10^{-6}$ , and is very slow. Nitrogen molecule has a kinetic diameter of 3.6 Å. The high quadrupole moment of molecular nitrogen must also be considered, as it may cause that at heterogeneous adsorption sites a certain orientation of gas molecules does not allow their entry into very narrow pores. This is especially true for ultramicroporous materials (with dimensions less than 0.7 nm). Nevertheless, the pore size distribution in MOFs under nitrogen analysis is usually in line with that expected.

Argon on the other hand is a monoatomic gas that does not possess quadrupole moment and is less prone to polarization than nitrogen. At the same time, it is an inert gas like nitrogen and has a slightly smaller kinetic diameter, 3.4 Å, making it suitable for the analysis of materials with very small pores. BET analyses in argon are performed at 87K.

In case of analysis of ultramicroporous materials or with many open metal sites (unoccupied metal coordination sites), it is advisable to choose argon gas probe and to increase the equilibration intervals, after each gas dosage, to 30 seconds, so as to provide time for the diffusion of that gas into the narrower pores.

$CO_2$  is another gas used as a probe in BET analysis. Unlike the previous two, it is not an inert gas, and it has an even lower kinetic diameter (3.30 Å) making it particularly suitable for

pores smaller than even 0.7 nm. CO<sub>2</sub> analyses are typically performed at 195K and 273K, but for textural investigations the former temperature is adopted.

Furthermore, since CO<sub>2</sub> under conditions temperature equal to 273 K and pressure of 1 bar does not condense, the absolute pressure is measured and then the saturation pressure of that gas at 273 K, which is 26200 torr, is used to convert the absolute one to relative pressure.

For this reason, the maximum  $p/p^\circ$  is 0.03 and in this case larger micropores and mesopores will not be filled at pressures lower than 1 bar.

Two other gases are used as probes in BET analysis: krypton, which is particularly popular for determining the surface area of nonporous materials with surface areas  $< 5 \text{ m}^2/\text{g}$ , and O<sub>2</sub>, which, presenting a saturation pressure one-fifth that of nitrogen, allows determination of the quantity of adsorbed gases with greater accuracy.

A resuming scheme of all gases employed as probe for surface area determination with their analysis temperature, kinetic diameter and main features are reported in **Figure 30**.

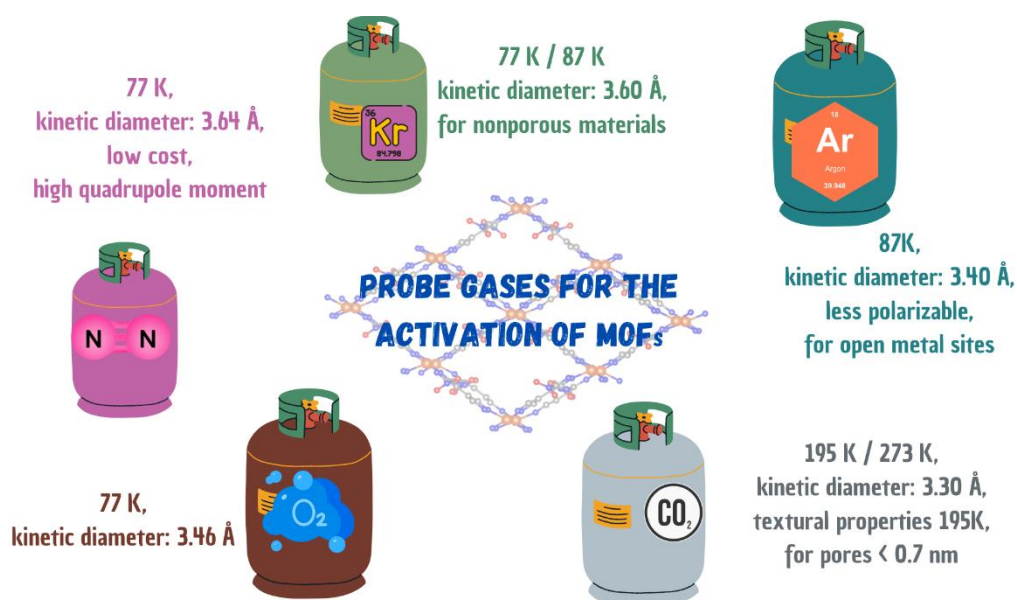


FIGURE 30 Scheme of the gases employed for the measure of the surface area with their main features.

## 1.7 Pyrazolate-based linker for the synthesis of CPs and MOFs

In this subchapter we are going to look specifically at the pyrazolate-based class of linkers, for the synthesis of 1D coordination polymers and MOFs. Though especially with regard to MOFs, the scientific literature is full of networks based on carboxylate ligands, there are some peculiarities and advantages in using azolate linkers for the construction of infinite structures.

Azoles are a family of very stable 5-membered aromatic rings containing one to four nitrogen atoms with  $sp^2$  hybridization.

In this discussion we will deal exclusively with the pyrazole ring, which still turns out to be one of the most studied heterocyclic rings as it is a recurring moiety in compounds of pharmaceutical and agrochemical interest,<sup>85</sup> and at the same time it is a pivotal ligand in coordination chemistry, as several of the metal complexes and CPs based on it and its derivatives have shown activity in a wide variety of fields: catalysis,<sup>86</sup> medicine,<sup>87</sup> microbiology,<sup>88</sup> magnetism.<sup>89</sup>

Pyrazole can be deprotonated to give the corresponding conjugated base called pyrazolate, in which the negative charge is delocalized throughout the ring by resonance. Compared with tetrazole, imidazole and triazole, pyrazole possesses a higher  $pK_a$  (14.2)<sup>90</sup>, resulting in stronger interactions with the metal center.

The pyrazolate anion can coordinate in three different ways, as shown in **Figure 31**: it can bind a single metal using a single nitrogen with a monodentate fashion; it can simultaneously bind two metal centers across the two nitrogen atoms with an exo-bidentate fashion, and finally it can take advantage of both adjacent nitrogen atoms to bind a single metal center with an endo-bidentate fashion. In coordination compounds, pyrazolates establish bent linkages with angles of  $70^\circ$  and for this reason, in exo-bidentate coordination mode the two metal centers are positioned at short distance, which varies from 3.5 to 4.7 Å, according to the metal ionic radius.<sup>91</sup>

Substituents on pyrazole ring in position 3- and 5- generate steric hindrance, whereas substituents in 4-position affect electronic properties due to conjugation effect.

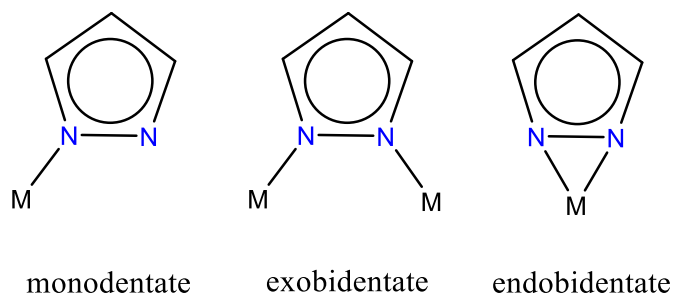


FIGURE 31 Different ways in which the pyrazolate ion can coordinate a metal center ( $M$ ).<sup>3</sup>

Taking into account Pearson's HSAB (hard and soft acids and bases) theory, pyrazolate, as a soft base, will tend to bind with stronger interactions soft metal centers, e.g.  $Zn^{2+}$ ,  $Co^{2+}$ ,  $Cu^{2+}$  and  $Ni^{2+}$ , rather than  $Ti^{4+}$ ,  $Zr^{4+}$ ,  $Fe^{3+}$ ,  $Al^{3+}$  or  $Cr^{3+}$  which are hard acids and therefore will prefer hard bases such as carboxylates.<sup>92</sup>

1D coordination polymers based on simple pyrazolate linker (pz) with  $Cd^{2+}$  and  $Zn^{2+}$  were reported by *Masciocchi et al.* in 1999.<sup>93</sup> The structures  $[M(\mu\text{-pz})_2]_n$  with  $M = Zn$  or  $Cd$  are analogues and show a tetrahedral coordination environment with bridging pyrazolate between two metal centers, as highlighted in **Figure 32**.



FIGURE 32  $Zn(pz)_2$  crystal structure. Zinc (filled circle) and carbon (empty circle) atoms are indicated. Hydrogen atoms are omitted for clarity.  $Cd(pz)_2$  crystal structure is analogous.<sup>93</sup>

$[Ag(\mu\text{-cdipz})]_n$ , where  $\text{cdipz} = 4\text{-chloride-}3,5\text{-diisopropyl-}1\text{-pyrazolate anion}$ , is instead an example of 1D coordination polymer obtained with a substituted pyrazolate linker. The linear coordination of  $Ag^+$  ion and steric hindrance by the two isopropyl groups in position 3,5 lead to a zigzag motif, as shown in **Figure 33**.<sup>94</sup>

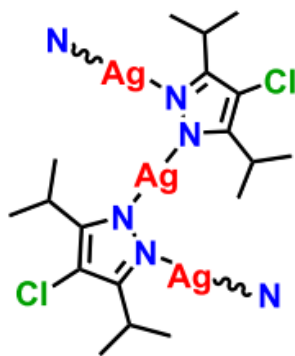


FIGURE 33 Representation of  $[Ag(\mu\text{-cdipz})]_n$  structure showing zigzag 1D chains.

In the research group at the University of Camerino where I conducted research during my three years as a Ph.D. student, the interest in the pyrazole molecule began many years ago, thanks to the possibility of obtaining an extraordinary variety of metal complexes of various alkali, alkaline-earth, transition and even lanthanide metal ions based on pyrazole and some of its derivatives, such as 4-acylpyrazolones, 4-diazo-5-pyrazolones, and 4-hydrazone-5-pyrazolones.<sup>95,96</sup>

At the same time, the research group began to study the eventuality of obtaining extended structures based on the pyrazolate linker. A major breakthrough occurred in 2005 when the coordination polymer  $Cu(pz)_2 \cdot H_2O$  by simple mixing of  $Cu(CH_3COO)_2$  and pyrazole in MeCN.<sup>97</sup>

This CP shows a pink color, due to square planar coordination environment of  $Cu^{2+}$  ion linked to four nitrogen atoms belonging to four different pyrazolate linkers and differently from the anhydrous 1D CP  $\alpha\text{-}Cu(pz)_2$ , reported by *Ehlert et al.* in 1991 which is green and with a tetrahedral coordination geometry of copper ions.<sup>98</sup>

A very rare feature of this coordination polymer lies in the position of the water molecule, weakly coordinated to two metal centers (Cu-O distance of 2.913 Å), without the possibility of establishing hydrogen bonds, as demonstrated by the two sharp and totally separated asymmetric and symmetric stretching vibration in the IR spectra at 3617 and 3546  $cm^{-1}$ , respectively.

By placing  $Cu(pz)_2 \cdot H_2O$  at reflux in water, another coordination polymer, with formula  $Cu(pz)OH$ , can be obtained in which a hydroxyl group replace one pyrazolate ion.

Other structures similar to  $Cu(pz)_2 \cdot H_2O$  can be obtained in DMF with the pyrazolate linker and with 4-X-pyrazolate where X=Cl, Br, I.<sup>99</sup> More details on these CPs are given in the

experimental section of this thesis, as these coordination polymers have been studied for their antibacterial activity.

In order to obtain three-dimensional porous structures, organic linkers containing multiple pyrazole rings (polypyrazolate) can be utilized.

Generally, MOFs based on poly-pyrazole linkers show higher stability in water with respect to carboxylate-based MOFs, which is especially useful for applications involving water adsorption or working conditions in water.<sup>100,101</sup>

In **Figure 34** several polypyrazolate linkers are reported.

Usually these are rigid linkers composed of multiple aromatic rings linked together or condensed rings as in the case of H<sub>2</sub>NDI-H.

In addition, in order to have longer linkers, benzene rings connected to each other in *para*-position (e.g., BDP and H<sub>2</sub>PBP), or triple C  $\equiv$  C bonds (e.g., H<sub>2</sub>BPE or H<sub>2</sub>BPEB) are chosen to ensure linearity and symmetry of the linker.

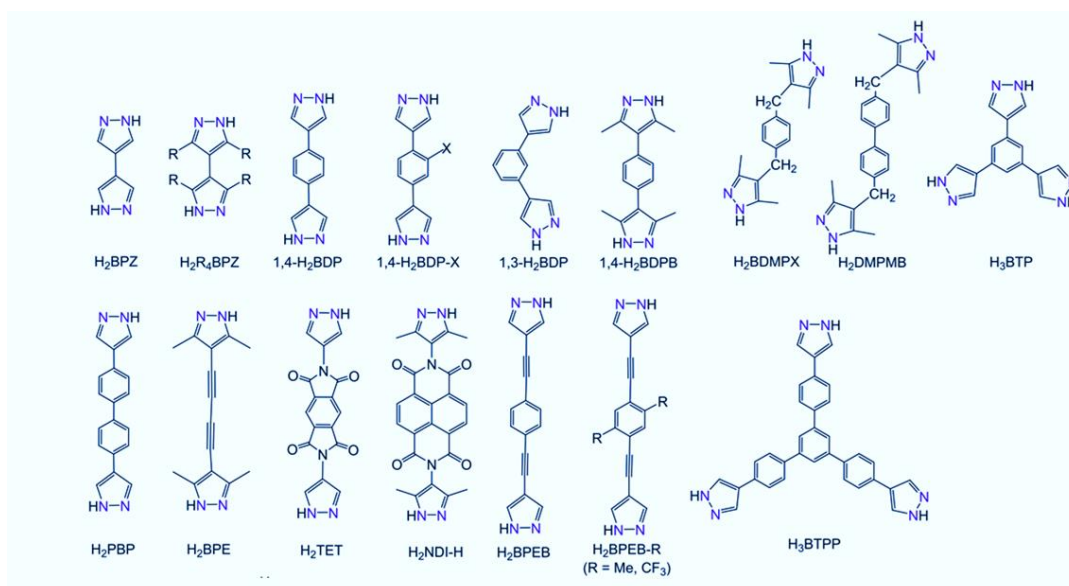


FIGURE 34 List of some bipyrazolate linkers employed for the synthesis of MOFs.<sup>102</sup>

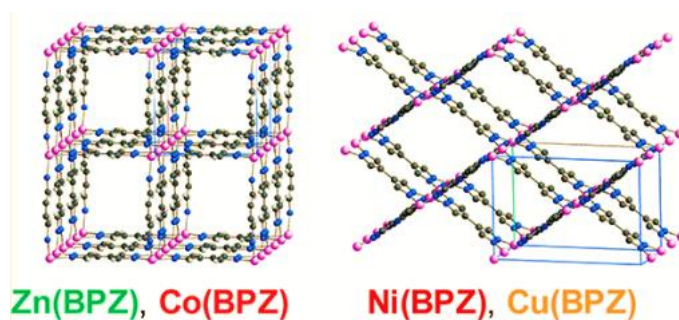
A longer linker usually corresponds to having MOFs with larger pores.

One can arrange the pyrazole groups at different angles, for example 120°, by exploiting the 1,3,5 positions of the benzene H<sub>3</sub>BTPP.

Finally, flexible linkers such as H<sub>2</sub>BDMPX e H<sub>2</sub>DMPMB have been employed too.

4,4'-bipyrazolate (BPZ) is the most simple polypyrazolate and has been used for the synthesis of MOFs with late transition metals such as Fe, Co, Ni, Pd, Cu, Zn, Cd and also Ga.<sup>103–105</sup>

Focusing on the metals Zn, Co, Cu and Ni, we obtain two isorecticular pairs. The first one is formed by the bipyrazole MOFs of Zn and Co, namely the ZnBPZ and CoBPZ structures, in which the metal ion  $M^{2+}$  exhibits a tetrahedral coordination geometry by binding four nitrogen atoms of four different bipyrazole linkers, leading to the formation square-shaped channels. The CuBPz and NiBPZ pair, on the other hand, shows the  $M^{2+}$  metal ion with a square planar coordination environment, conducting to porous structures with rhombic channels. All of the above can be visualized in **Figure 35**.



**FIGURE 35** *Different topologies displayed by Zn(BPZ)/Co(BPZ) and Ni(BPZ)/Cu(BPZ). The first pair exhibits square channels, while the second pair shows rhombic channels.*

Similar structures have been synthesized with Zn-, Co-, Cu- and Ni-MOFs based on 4,4'-bipyrazolates substituted at the 3,3' and/or 3,5 and/or 5,5' position or based on substituted 1,4- $H_2$ BDP linkers. Some of them are being studied in this dissertation so more information will be emphasized in the experimental section.<sup>106–114</sup>

An interesting case, however, is the CoBDP MOF obtained by J. F. Long's group.<sup>115–117</sup> The MOF was not only found to be able to adsorb methane, but it is the gas itself that induces a phase transition that causes the network to switch from a collapsed form to an expanded one where the density halves from the former while the pseudotetrahedral geometry is retained. This expansion phenomenon can also be observed in the BET analysis in methane where a pronounced hysteresis occurs.

What has just been said is shown in **Figure 36**.



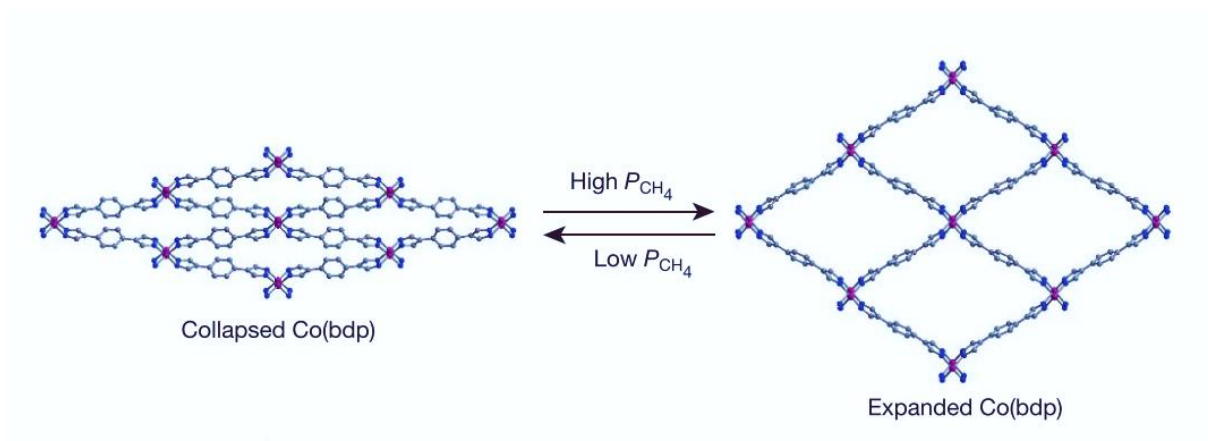


FIGURE 36 *Collapsed and expanded structures of Co(BDP) at different methane pressures.*<sup>115</sup>

## 1.8 Applications of MOFs: antibacterial activity and carbon dioxide capture and reutilization

If we were asked to describe MOFs in only two words, we could provide a general but convincing idea of their uniqueness and extraordinariness just by the terms "design" and "porosity".

Synthetic design allows one not only to think about a given network and choose the right building blocks to implement it, but also to introduce structural changes to modulate the properties and thus improve the performances of the porous material.

The easy tunability in this type of frameworks then makes the porosity of MOFs and COFs even more peculiar, as it enables the design and fabrication of materials with porosity never before achieved.

NU109E and NU110E are among the MOFs with largest surface area ever recorded arriving at values of 7010 and 7140 m<sup>2</sup>/g, respectively.

To realize the grandiosity of this, simply consider that an entire football field has a surface area of about 5300 m<sup>2</sup> and so that means that a single gram of these two porous materials has more area than a football field!

These MOFs were realized by exploiting 3,2,4-connected coordination units with a so-called **rht** topology that has the advantage of not allowing interpenetration of networks, a phenomenon that would undoubtedly tend to reduce the overall surface area.<sup>118</sup> The corresponding linkers used have six carboxylate moieties. What is more, computational calculations have been performed and for now it seems that the maximum theoretical BET surface area value obtainable for an MOF in which ethynyl groups are used in the expansion of the organic linker is 14600 m<sup>2</sup>/g.<sup>119</sup>

Given these premises, it is intelligible to state that all the applications of MOFs revolve around their porosity and thus the possibility of leveraging on cavities for adsorption and/or chemical conversion of guest molecules.

The literature on MOFs is now vast and it has been growing by leaps and bounds since 1995. Although in this subchapter we will cover specifically the applications inert to this PhD dissertation i.e. antimicrobials MOFs<sup>120-122</sup> and carbon dioxide capture and conversion,<sup>123,124</sup> a large number of reviews have been written on the most diverse applications of MOFs. Such applications further involve industry and process engineering,<sup>125,126</sup> biomedicine, biosensing and drug delivery,<sup>127-133</sup> electrochemical sensors, batteries and supercapacitors,<sup>134-137</sup> food

safety,<sup>138,139</sup> gas storage and separation,<sup>140,141</sup> catalysis, biocatalysis and photocatalysis,<sup>142–144</sup> analytical and green applications<sup>52,145,146</sup> and also more.<sup>147–151</sup>

Antimicrobial MOFs are all those MOFs that show activity against bacteria, fungi, viruses, and parasites. Focusing on the antibacterial aspects, these porous materials appear to be excellent contenders for this purpose because their dual organic/inorganic nature allows them to combine the characteristics of common inorganic antibacterial agents with long sterilization times required and with broad-spectrum activity and those of organic antimicrobials, which are less expensive, more selective in their activity, and rapid but also more toxic and more prone to drug resistance.

In addition, the presence of defined pores in extended frameworks allows the possibility of trapping biologically active species that are natural organic molecules or drugs already known in the literature or metal ions and nanoparticles and releasing them in a controlled manner.<sup>152,153</sup>

Antibacterial MOF activity can also be exerted by direct contact with the bacterial surface through depolarization of the bacterial wall and subsequent disruption of the entire cell.<sup>154</sup>

Also in the biological field, the synthetic design of MOFs plays a key role because it provides the way to choose a suitable metal node or to use bioactive organic compounds as linkers; for instance, metal centers activated by UV radiation can be employed to produce ROS, the active oxygen species. The various ways in which antibacterial activity of MOF is explicated are depicted in **Figure 37**.

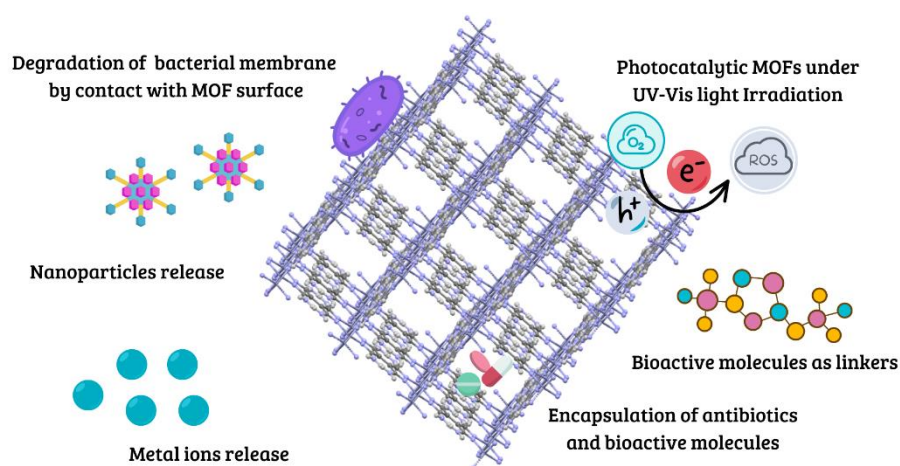


FIGURE 37 Scheme of how MOFs antimicrobial activity can be exerted.<sup>121</sup>

Generally speaking, scientific papers on antimicrobial MOFs mainly concern the use of Ag(I), Zn(II), Cu(II), Ni(II) and Co(II) metal centers but tests have also been conducted on Zr(IV) and Ti(IV) MOFs.<sup>155</sup>

The antibacterial activity is sometimes exerted by the release of metal ions that make up MOF, which slowly decomposes in an aqueous environment. The activity recorded is higher for those MOFs that decompose quickly but at the same time is less long-lasting. A proper balance between the chemical stability in water of MOF and its activity must necessarily be attained. This was observed in the study of three different MOFs (MOF-5, ZIF-8 and Ag(CB)(H<sub>2</sub>O) where CB = 4-cyanobenzoate with antibacterial activity against the oral bacteria *P. gingivalis*, *S. mutans* and *F. nucleatum*.<sup>156</sup> In this case, MOFs based on the Ag<sup>+</sup> ion exhibit higher antibacterial activity and longer sterilization time.

The drug nalidixic acid (HNDX) based on quinolone moiety has been used as organic linker to synthesize MgNO<sub>3</sub>(NDX)(H<sub>2</sub>O)<sub>3</sub> and MnCl(NDX)(H<sub>2</sub>O)<sub>3</sub> MOFs. The organic compound possesses bacteriostatic and bactericidal activity in different concentrations, along with an anti-inflammatory effect. Nevertheless, its poor solubility in water makes its oral assumption vain. For this reason, the possibility of incorporating the drug in MOFs enables an easier assumption and, at the same time, a better antibacterial activity against *E. faecalis*, *P. aeruginosa*, *E. coli* and *S. aureus*.<sup>157</sup>

A synergistic action of the guest molecules trapped in the MOFs can lead to increased antibacterial activity.

A convincing proof of that is given by the study of the two MOFs Co<sub>2</sub>(dhtp)(H<sub>2</sub>O)<sub>2</sub> and Ni<sub>2</sub>(dhtp)(H<sub>2</sub>O)<sub>2</sub> (H<sub>4</sub>dhtp = 2,5-dihydroxyterephthalic acid) and HKUST-1 loaded with the antibiotic metronidazole and NO molecules against *S. aureus* and *P. aeruginosa*.

The interesting aspect is that the MOFs loaded with only one of the two guest molecules are not very active, while the activity becomes much stronger when both are present resulting in synergic combination therapy.

This brief explanation is only intended to explain the reasons why MOFs are an excellent resource in the microbiological field. More details on antibacterial tests using CPs and MOFs will be provided in the experimental part (Chapter 2 and 3).

The capture of carbon dioxide and its conversion into useful products is another fundamental application that MOFs can fulfill.

It is well known that CO<sub>2</sub> levels have been increasing since the Industrial Revolution and continue to do so at an unsustainable rate. Urgent measures are needed to avoid that the emissions of the main greenhouse gas do not increase by 50% with a consequent rise in the global temperature of about 2 K by 2025.<sup>158</sup>

The high porosity and surface area of MOFs are very convenient for this kind of application. Even though carbon dioxide is an apolar molecule because of its linear geometry and overall dipole moment of 0, it exhibits a partial positive charge on the carbon atom and a partial negative electronic density on the two oxygen atoms. This makes it available to interactions of an electrostatic nature, hydrogen bonds and even the formation of chemical bonds.

MOFs allow the absorption of CO<sub>2</sub> on two fronts. MOFs metal nodes can be exploited as Lewis acids, especially in those structures where there are open metal sites. That is the case of Ni<sup>2+</sup> in the MOF Ni<sub>2</sub>(dhtp),<sup>159</sup> where the removal of a coordinated water molecule from an octahedral environment frees up a coordination site for CO<sub>2</sub> coordination.

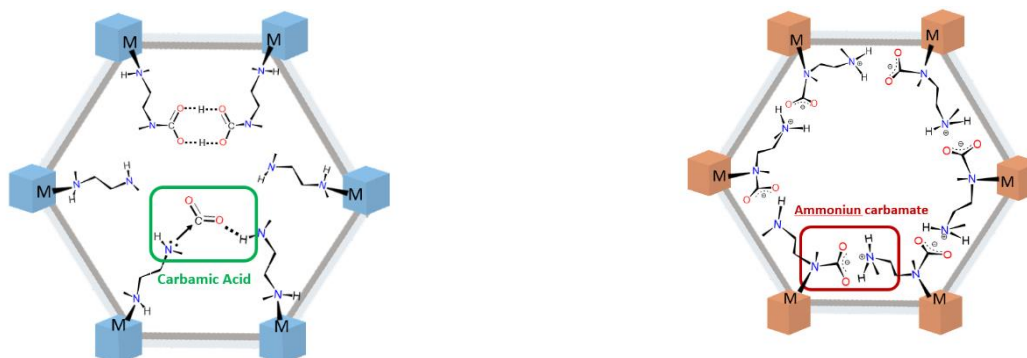
Another way is to use linkers with appropriate functional groups (already present or added via PSM) which can establish secondary interactions or covalently bind CO<sub>2</sub>.

Nitrogen-based functional groups are usually chosen because nitrogen lone pair can interact with carbon partial positive charge. In addition, hydrogen bonds between carbon dioxide and amines, amides or nitro-groups can occur, as shown in **Figure 38**. Interactions of the same type can also be observed with hydroxyl and carboxyl groups.



FIGURE 38 Representation of Lewis Base-Acid Interaction and Hydrogen Bond in the adsorption of CO<sub>2</sub> via amino group.<sup>124</sup>

When  $\text{CO}_2$  enters the pores, the interaction with the amino groups can lead to a chemical reaction with the formation of carbamic acid or an ammonium carbamate, as can be seen in **Figure 39**.



**FIGURE 39** Representation of carbamic acid or ammonium carbonate formation in the presence of an amino group and carbon dioxide.<sup>124</sup>

The capture of  $\text{CO}_2$  by the MOF can also take place directly from the air, at high pressures of  $\text{CO}_2$ , in pre- or post-combustion processes<sup>160</sup> or by combustion in a pure oxygen environment. However, such industrial processes are beyond this thesis and are therefore not covered here.

At this point, in any case, the question we can ask ourselves is the following. Once the carbon dioxide has been stored inside the MOF what do we do with it?

$\text{CO}_2$  can be captured and converted into other products either by chemical reaction with other guest substrates or it can be reduced to other compounds photochemically or electrochemically.

For example, in the presence of an epoxide and a Lewis base (LB), cycloaddition of carbon dioxide can occur to yield a cyclic carbonate, as shown in **Figure 40**.

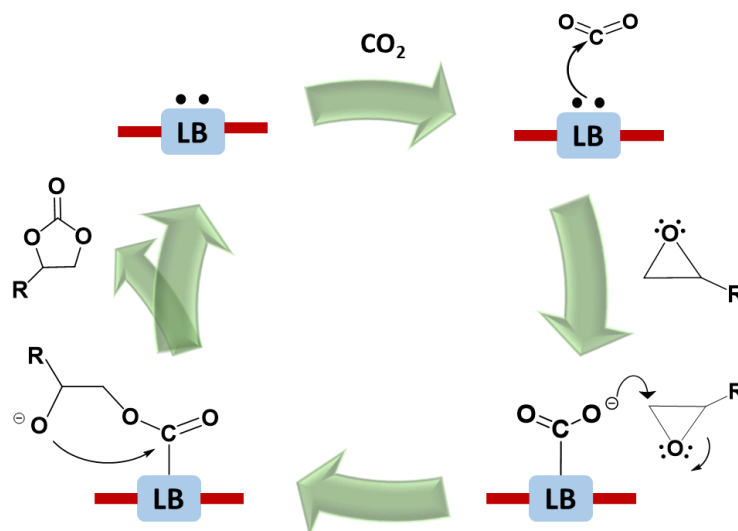


FIGURE 40 Scheme of cyclic carbonate formation in the presence of a Lewis Base (LB) such as an amino group.<sup>123</sup>

Hf-NU-1000, for instance, has been studied for the adsorption and the conversion of carbon dioxide via cycloaddition of styrene oxide, with the aid of a co-catalyst, the surfactant tetrabutylammonium bromide (TBAB).<sup>161</sup>

Another route is the activation of the aryl C-H bond and the subsequent insertion of CO<sub>2</sub>, as shown by *Wen-Yang Gao et al* for the UiO-67 MOF made of 2-phenylpyridine-5,4'-dicarboxylic acid (dcpyp) linkers and the SBU Zr<sub>6</sub>O<sub>4</sub>(OH)<sub>4</sub>.<sup>162</sup>

Alkyne moieties can also be exploited in the capture of CO<sub>2</sub> by carboxylation reactions of terminal alkynes. Cu(IN)-MOF where IN= pyridylcarboxylate, also called isonicotinic acid) has been studied for the carboxylation of a variety of terminal alkynes in the presence of Cs<sub>2</sub>CO<sub>3</sub>. The reaction requires the deprotonation of the alkyne group, the generation of copper acetylide and Cu<sup>2+</sup> reduction to Cu<sup>+</sup>.

Electrocatalytic reduction of carbon dioxide, instead, involves systems in which there are mobile protons that can be easily moved to the catalytic active site and that exhibit a redox-active site.

The idea of electrocatalytic reduction, just as with photochemical reduction, is to produce useful products that can then be reused in organic synthesis, such as CH<sub>4</sub>, CH<sub>3</sub>OH, CO, HCOOH.<sup>163</sup>

The main issue concerning this application deals with the large number of protons/electrons needed to transform carbon dioxide in other species. Moreover, the production of H<sub>2</sub> from water is a secondary and competitive reaction which must be taken into account.<sup>164</sup>

In order to solve these problems, high potentials must be applied, resulting in less selectivity and formation of unwanted species and energy waste.

In electrocatalytic tests, a layer of electrochemically active compounds is coated on the surface of the electrode as a thin film and the number of electrochemically active sites is directly related to the accessible surface area of the thin film deposited on the electrode. For this reason, to increase the electrocatalytic reaction rate, nanoporous materials with high surface area such as MOFs are a good choice.

Nevertheless, some limitations negatively affect the potential application of metal-organic frameworks in the electrochemical field: (i) the electrically insulating or low conducting feature of most MOFs; (ii) their poor thermal and water stability.<sup>165</sup>

The first issue can be solved through two different techniques: redox hopping or band transport.

Redox hopping deals with the motion of electrons via self-exchange reactions between redox centers coupled to the motion of counter-balancing ions;<sup>166</sup> band transport, instead, is based on the construction of the electrical conductivity by the introduction of both the electron-donating and electron-accepting moieties in a highly conjugated organic linker.<sup>167</sup>

On the other side, MOFs' low thermal and water stability can be improved by the employment of nitrogen-based ligands such as pyrazoles and pyridines; in fact, MOFs in which M-N bonds are formed, exhibit a better thermal and water stability compared to MOFs based on carboxylate linkers, as we have previously said.<sup>100</sup>

PCN-222 (Fe), a MOF based on porphyrin linker, has been investigated for the selective conversion of carbon dioxide into CO, leveraging on linker known activity and network porosity and stability.<sup>168</sup>

In the experimental part, two works are illustrated concerning the capture and conversion of CO<sub>2</sub>: the first one is based on the fixation of carbon dioxide with epoxy rings (Chapter 4), while the second one deals with the electrocatalytic reduction of CO<sub>2</sub> into CO and methane (Chapter 5). More details can be found in that section.



**CHAPTER 2:**  
**Antibacterial Activity of Cu(II)**  
**Pyrazolate-based Coordination Polymers**

## 2.1 Aim of the research work

Biomedical research has been very dedicated in recent years to the search for new substances with antibacterial activity to eliminate all those infections caused by bacteria that have become resistant to antibiotics over the years.

The use of metal species has proved successful, and it has been observed that the bactericidal activity is mainly expressed in the interaction that occurs between the cell membranes of the bacterium and the metal ions released by the antibacterial metal-based compound used.

However, the uncontrolled release of ions appears to be an obstacle to the use of these antibacterial species in medical devices and food packaging.

In this regard, the application of very stable and insoluble coordination compounds such as CPs and MOFs faces this problem, also allowing easier recycling of the compound.

As already mentioned in the introduction, the activity of the Cu(II) ion against various bacterial strains is known;<sup>169</sup> in addition various pyrazole derivatives have also shown antibacterial activity, including the well-known commercial anti-inflammatory Celecoxib.<sup>170</sup>

For this reason, eight copper(II) pyrazolate coordination polymers **1** [Cu( $\mu$ -pz)( $\mu$ -OH)]<sub>n</sub>, **2** [Cu( $\mu$ -NO<sub>2</sub>pz)<sub>2</sub>]<sub>n</sub>, **3** [Cu( $\mu$ -pz)<sub>2</sub>·H<sub>2</sub>O]<sub>n</sub> and **4-8** [Cu( $\mu$ -4-Xpz)<sub>2</sub>·DMF]<sub>n</sub> (**4** X=H, **5** X=NO<sub>2</sub>, **6** X=Cl, **7** X=Br, **8** X=I) were investigated as antibacterial materials in this work, with a view to understanding whether the eventual activity presented by the CPs is given exclusively by the metal center, by the organic linker or by a synergistic action, and to hypothesizing the action mechanism. In addition, the reported antibacterial, antiparasitic, herbicidal and antineoplastic activity of organic compounds possessing nitro functionality<sup>171</sup> prompted us to expand the Cu(4-X-pz) CPs series with two novel CPs based on the 4-nitropyrazole linker. The synthesis and the characterization of compounds **2** and **5**, in fact, are here reported.

The microbiological analyses were performed in the Research Centre for Hygienistic, Health and Environmental Sciences (School of Pharmacy) of the University of Camerino, under the supervision of Dr. Stefania Scuri.

The crystal structure of **2** was determined by Prof. Simona Galli at University of Insubria (Como).

A scheme of **1-8** CPs is illustrated in **Figure 41**.

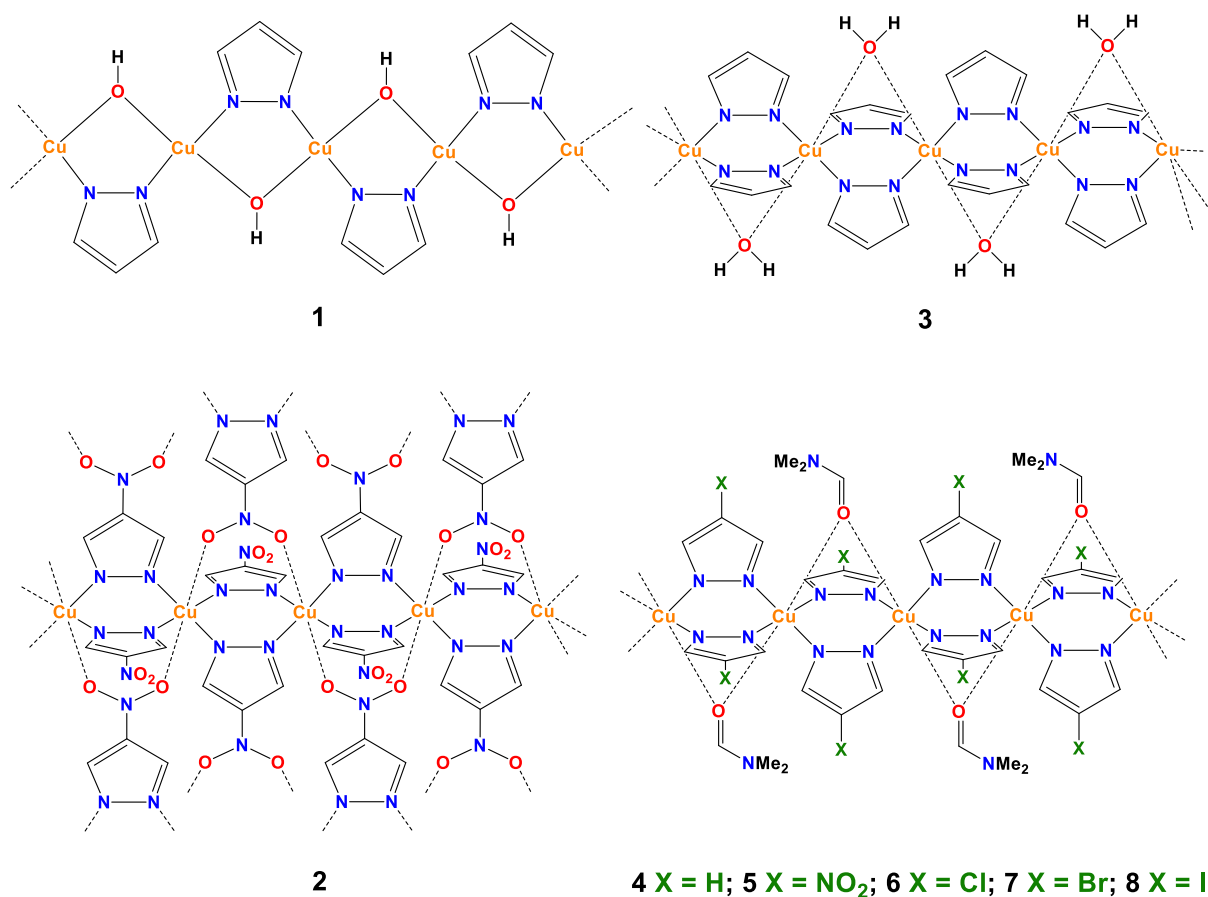


FIGURE 41 Scheme of 1-8 CPs tested as antibacterial materials in this work.

## 2.2 Experimental section

### 2.2.1 Material and methods

All reactions and manipulations were performed in air, but particular attention is paid to 4-nitropyrazole and the corresponding synthesized CPs, as nitrated compounds are potentially explosive. In all cases, however, no dangerous episodes occurred during their use and during the synthesis.

Infrared spectra were registered in the range 4000-650  $\text{cm}^{-1}$  with a Perkin Elmer Spectrum One model FTIR spectrometer working in ATR mode. Elemental analyses (% m/m C, H, N) were completed with a Fisons Instruments 1108 CHNS-O elemental analyser.

TGA and DTA thermal analyses (thermogravimetric and differential thermal analysis) were recorded with the aid of PerkinElmer STA6000 instrument. The setting temperature programme varied from 303K to 873K with a heating rate of 10 K/min under a  $\text{N}_2$  flow (30 mL/min). Indium (156.6, 0.2 K) and tin (232.0, 0.2 K) fusion temperatures were used as standards for the evaluation of instrument accuracy with heating/cooling dynamic segments.

Fluorescence analyses were performed with a BMG LABTECH FLUOstar Omega fluorescence cytometer. The CLSM images were registered with a confocal microscope (Nikon ECLIPSE Ti), fixing the samples between a slide and an 18 mm square coverslip. IKA KS 130 BASIC platform shaker was used for eppendorfs shaking in antibacterial rate (%) determination. Optical density measurements were carried out at 600 nm with a Bio-Tek  $\mu$ Quant microplate spectrophotometer. Powder X-ray diffraction (PXRD) qualitative analyses were performed with a Bruker D8 Advance diffractometer acquiring data at room temperature with  $2\theta$  range of 3–35°, steps of 0.02° and a time per step of 1 s. Magnetic susceptibilities were recorded at 293 K with a Sherwood Scientific magnetic balance MSB-Auto applying the Gouy method and the adequate Pascal constants to correct for diamagnetism. The instrument calibration was performed using HgCo(NCS)<sub>4</sub>. The magnetic moments (in Bohr Magnetons, B. M.) were calculated following the equation  $\mu_{eff} = 2.84(\chi_m^{corr}T)^{1/2}$  in which  $\chi_m^{corr}$  is the corrected mass magnetic susceptibility. ICP analyses were performed with an iCAP PRO Thermo Scientific.

### 2.2.2 Synthesis of CP 2, [Cu( $\mu$ -NO<sub>2</sub>-pz)<sub>2</sub>]<sub>n</sub>

In 30 mL of MeCN, 4-nitro-1*H*-pyrazole (2 mmol, 0.226 g) was solubilized. Copper acetate (CH<sub>3</sub>COO)<sub>2</sub>Cu·H<sub>2</sub>O (1.0 mmol, 0.199g) was added and the obtained reaction mixture was stirred at room temperature for 2 h. A bright purple solid was yielded after three 30 minutes-cycles of centrifugation at 6000 rpm. The solid was washed with fresh acetonitrile and centrifugated at 6000rpm twice and then finally dried at 333 K in an oven under vacuum. 0.240 g of compound **2** were obtained, yield of 83%. Elemental analysis calculated for: C<sub>6</sub>H<sub>4</sub>N<sub>6</sub>O<sub>4</sub>Cu: H, 1.40; C, 25.05; N, 29.21. found: H, 1.47; C, 25.33; N, 28.88. IR (cm<sup>-1</sup>): 3141w  $\nu$ (C-H<sub>arom</sub>), 1488vs  $\nu_{as}$ (N-O<sub>2</sub>), 1411s,  $\nu$ (C=C + C=N), 1283vs  $\nu_{sym}$ (N-O<sub>2</sub>), 1178m, 1039m, 1007m, 876m, 815m, 753m. Room-temperature magnetic susceptibility:  $\mu_{eff}$  (298 K) = 1.34 B.M.

### 2.2.3 Synthesis of CP 5, [Cu( $\mu$ -NO<sub>2</sub>-pz)<sub>2</sub>·DMF]<sub>n</sub>

In 25 mL of DMF, 4-nitro-1*H*-pyrazole (2 mmol, 0.226 g) was solubilized and then copper acetate (CH<sub>3</sub>COO)<sub>2</sub>Cu·H<sub>2</sub>O (1.0 mmol, 0.199g) was added to the reaction mixture. The reaction was performed at room temperature for 2 hours. A pale lilac precipitate was obtained. The precipitate was filtered, washed with fresh DMF and dried at air. 0.298 g, of

compound **5** (yield of 82%) were obtained. Elemental analysis calculated for:  $C_9H_{11}N_7O_5Cu$ : H, 3.07; C, 29.96; N, 27.18. found: H, 3.09; C, 29.79; N, 27.07. IR ( $cm^{-1}$ ): 3526br  $\nu(O-H)$ , 3137w  $\nu(C-H_{arom})$ , 2932wbr  $\nu(C-H_{alif})$ , 1653vs  $\nu(C=O)$ , 1498s  $\nu_{as}(N-O_2)$ , 1408s  $\nu(C=C + C=N)$ , 1382m, 1284vs  $\nu_{sym}(N-O_2)$ , 1181m, 1100s, 1037m, 1009m, 871m, 815s, 757s. Room-temperature magnetic susceptibility:  $\mu_{eff}(298\text{ K}) = 1.56\text{ B.M.}$

#### 2.2.4 Crystal structure of CP **2**, $[Cu(\mu-NO_2-pz)_2]_n$ and CP **5**, $[Cu(\mu-NO_2-pz)_2 \cdot DMF]_n$

Powdered samples of **2** and **5** (ca. 50 mg) were deposited in the hollow of a 0.2 mm deep silicon zero-background plate. Data acquisitions were performed on a Bruker AXS D8 Advance vertical-scan  $\theta:\theta$  diffractometer equipped with a sealed X-ray tube (Cu  $K\alpha$ ,  $\lambda = 1.5418\text{ \AA}$ ), a Bruker Lynxeye linear position-sensitive detector, a filter of nickel located in the diffracted beam and the following optical components: primary- and secondary-beam Soller slits ( $2.5^\circ$ ), fixed divergence slit ( $0.5^\circ$ ), antiscatter slit (8 mm). The generator was operated at 40 kV and 40 mA. After a preliminary acquisition to assess the feasibility of the crystal structure determination, performed in the  $3\text{--}35^\circ\ 2\theta$  range with step of  $0.02^\circ\ 2\theta$  and time/step of 1 s, diffraction data for the structure determination were collected from  $5^\circ$  up to  $105^\circ\ 2\theta$ , with steps of  $0.02^\circ\ 2\theta$ , and a time/step of 10 h. A manual peak search enabled us to estimate the maximum positions of twenty low-to-medium-angle peaks. Working on the maximum positions, the Singular Value Decomposition algorithm<sup>172</sup> implemented in TOPAS-R v. 3.0,<sup>173</sup> provided approximate unit cell parameters for both the compounds. The space groups were assigned based on the observed systematic absences. The unit cell parameters and space groups were preliminary confirmed by whole powder pattern refinements carried out with the Le Bail method as implemented in TOPAS-R v. 3.0. The structure determination was carried out with TOPAS-R v. 3 adopting the Simulated Annealing approach<sup>174</sup>. Rigid bodies were used to describe the crystallographically independent portion of the 4- $NO_2$ pz ligand and the DMF molecule, initially assigning idealized values to bond distances and angles. (Bond distances and angles for the rigid body describing the ligand: endocyclic C-C and C-N bonds = 1.36  $\text{\AA}$ ; exocyclic C-N bond = 1.40  $\text{\AA}$ ; N=O bonds = 1.25  $\text{\AA}$ ; C-H bonds = 0.95  $\text{\AA}$ ; pyrazolate ring internal and external bond angles =  $108^\circ$  and  $126^\circ$ , respectively; angles at the nitrogen atom of the  $NO_2$  group =  $120^\circ$ . Bond distances and angles for the rigid body describing the DMF molecule: C-N bonds = 1.40  $\text{\AA}$ ; C=O bond = 1.25  $\text{\AA}$ ; C-H bonds = 0.95  $\text{\AA}$ ; angles at the nitrogen and carbonyl carbon atoms =  $120^\circ$ ; angles at the methyl

carbon atoms = 109.5°) The position of their centre of mass and their orientation (when allowed by symmetry) were varied. The structure determination was successful in the case of **2**, while no attempt of disclosing the crystal structure of **5** was effective. Structure refinement for **2** was carried out with the so-called Rietveld method<sup>175</sup> as implemented in TOPAS-R v. 3.0. The background was modelled through a polynomial function of the Chebyshev type. A unique isotropic thermal factor ( $B_{\text{iso}}$ ) was attributed to the metal centre, while the other atoms were attributed an isotropic thermal factor amounting to  $B_{\text{iso}}' = B_{\text{iso}} + 2.0 \text{ (\AA}^2\text{)}$ . The instrumental contribution to the peak profile was described by the Fundamental Parameters Approach.<sup>176</sup> The anisotropic peak broadening was successfully described using second-order spherical harmonics convoluted to Lorentzian and Gaussian contributions.

Crystal data for  $[\text{Cu}(\mu\text{-4NO}_2\text{pz})_2]_n$ , **1**:  $\text{C}_6\text{H}_4\text{CuN}_6\text{O}_4$ , FW = 287.66 a.m.u., monoclinic,  $C2/m$ ,  $a = 20.058(3) \text{ \AA}$ ,  $b = 7.603(1) \text{ \AA}$ ,  $c = 7.3757(9) \text{ \AA}$ ,  $\beta = 115.018(7)^\circ$ ,  $V = 1019.2(2) \text{ \AA}^3$ ,  $Z = 8$ ,  $Z' = 4$ ,  $\rho = 1.87 \text{ g cm}^{-3}$ ,  $F(000) = 572$ ,  $R_{\text{Bragg}} = 0.68$ ,  $R_p = 1.5\%$  and  $R_{\text{wp}} = 2.0\%$ , for 4851 data and 41 parameters in the 8.0-105.0° ( $2\theta$ ) range.

### 2.2.5 Bacterial culture

Copper(II) pyrazolate coordination polymers **1-8** were investigated as antimicrobial agents against *Staphylococcus aureus* (*S. aureus*) ATCC 25923 as representative of Gram-positive bacteria and *Escherichia coli* (*E. coli*) ATCC 25922 and *Pseudomonas aeruginosa* (*P. aeruginosa*) ATCC 27853 as representative of Gram-negative bacteria.

For each bacterial strain, bacterial inocula were prepared by adding a monoclonal colony to Tryptone Soy Broth (TSB) nutritious medium and letting it grow at 310 K overnight. The bacterial culture was diluted to  $10^6 \text{ CFU mL}^{-1}$  concentration in physiological solution (CFU = colony-forming units; it is an estimation of the number of viable cells that can reproduce).

### 2.2.6 Antibacterial Rate (%) and Viable Cells (%)

In order to define the antibacterial rate (%) the number of CFU was determined transferring the treated sample into Petri dishes containing Plate Count Agar medium, according to the following procedure. For each bacterium strain, 4 mg of **1-8** Cu(II) pyrazolate polymers powder was separately added in 8 eppendorfs (one for each CP tested) containing the bacterial culture at  $10^6 \text{ CFU mL}^{-1}$  concentration in 1 mL of autoclaved physiological solution. All eppendorfs were put on a platform shaker and kept shaking for 24h at 160 rpm. At set

time intervals (0, 2, 4, 6, 8, 10, 12, 14, 16, 18, 20, and 24 h) 10  $\mu$ L of supernatant for each treated sample were withdrawn, diluted in physiological solution, and poured uniformly into Petri dishes containing Plate Count Agar (OXOID) and incubated overnight. For each bacterial strain, an untreated sample was prepared with the same procedure and was used as a blank.

CFUs were manually counted. Antibacterial Rate (%) expressing the bacterial growth inhibition was calculated using the following formula:

$$\left( \frac{CFU_{t_0} - CFU_{t_k}}{CFU_{t_0}} \right) \times 100$$

where  $t_0$  is the time zero at the beginning of the test and  $t_k$  is the specific interval in hours (0, 2, 4, 6, 8, 10, 12, 14, 16, 18, 20, and 24 h).

Similar procedures were used to evaluate the activity of free linkers (4-X-pyrazole with X= H, NO<sub>2</sub>, Cl, Br, or I) against *E. coli* and *S. aureus* at time intervals 0, 4, 8, 12, 16 and 20h. Antibacterial activity is reported as the number of Viable Cells (%) expressed by the following formula:

$$\left( \frac{CFU_{t_k}}{CFU_{t_0}} \right) \times 100$$

### 2.2.7 Bacterial Growth curve

The observation of bacteria growth as a function of time both in the blank (untreated sample) and in the samples treated with **1-8** was determined by optical density measurements at 600 nm (OD<sub>600</sub>) of the bacterial suspensions. Eppendorfs containing bacterial culture and Cu (II) pyrazolate CPs powder were prepared with the same concentrations of the previous tests and the same time intervals.

### 2.2.8 Detection Reactive Oxygen Species (ROS)

2',7'-Dichloro-dihydro-fluorescein diacetate (DCFH-DA) was chosen as oxidation probe for the evaluation of the production of ROS. For each bacterial strain, 1 mL of a bacterial culture at 10<sup>6</sup> CFU/mL concentration in PBS (phosphate buffer solution) using bacterial cells grown in nutritious medium TSB overnight, was incubated for 30 minutes with 20  $\mu$ L of 2',7'-Dichloro-dihydro-fluorescein diacetate solution at 310 K. 1 mL of **1-8** Cu(II) pyrazolate CPs

suspension in physiological solution was prepared for each CP adding 0,4 mg of CP into an eppendorf. 10  $\mu$ L of bacterial suspension were transferred in each eppendorf. The ROS production was evaluated at 1, 2, 3, and 4 hours of treatment and an untreated sample was prepared with the same procedure and was used as a blank.

For each interval time, 100  $\mu$ L of the sample from each eppendorf was transferred into 96 well plates, in triplicate. The fluorescence tests for each sample were carried out with the aid of a FLUOstar Omega fluorescence cytometer at 485/20 nm and 528/20 nm wavelengths for excitation and emission respectively. Also, the fluorescence of only medium sample and medium + bacteria strain (blank) was determined. The average of the three replications was plotted as the intensity of fluorescence in arbitrary unit (a.u). The statistical significance was determined by One-Way-Anova with Bonferroni's multiple comparisons test; \*  $p < 0.05$ .

#### **2.2.9 Propidium Iodide (PI) uptake**

Propidium Iodide (PI) was employed as fluorescent probe to observe the viability of bacteria treated with compounds **1-8**.

1 mL of **1-8** Cu(II) pyrazolate CPs suspension in physiological solution was prepared for each CP adding 0,4 mg of CP into an eppendorf. Bacterial culture was added to CPs suspensions with a final concentration of  $10^6$  CFU/mL.

After 4, 8, 24, and 48h, 100  $\mu$ L of the sample from each eppendorf was transferred into 96 well plates, in triplicate, and 1.5  $\mu$ L of Propidium Iodide (PI) solution was added to each eppendorf tube in the dark and incubated for 20 minutes at 310 K. After this, the fluorescence tests were carried out with the aid of a FLUOstar Omega fluorescence cytometer at 485/20 nm and 528/20 nm.

Also, the fluorescence of only medium sample and medium + bacteria strain (blank) was determined. The average of the three replications was plotted as the intensity of fluorescence in arbitrary unit (a.u). The statistical significance was determined by One-Way-Anova with Bonferroni's multiple comparisons test; \*  $p < 0.05$ .

#### **2.2.10 Metal ions release test**

To assess  $\text{Cu}^{2+}$  ion release in physiological solution after 24 h, 4 mg of **1**, **2** and **5** were each suspended in 10 mL of physiological solution. After 1 day, the supernatants were filtered through a 0.45  $\mu$ m filter and 9 mL of each solution were combined with 1 mL of  $\text{HNO}_3$  1%



w/w in physiological solution and the three obtained samples analyzed by ICP. The concentration values of  $\text{Cu}^{2+}$  ion detected (in ppm) are associated with the copper absorption at 219.958 nm.

## 2.3 Results and discussions

### 2.3.1 Synthetic procedures

The coordination polymers **1**, **3**, **4**, **6**, **7** and **8** were reprepared following the synthetic procedures reported in literature.<sup>97,99</sup>

**1** was obtained dissolving copper (II) acetate ( $\text{Cu}(\text{CH}_3\text{COO})_2 \cdot \text{H}_2\text{O}$ ) and pyrazole in 1:2 ratio in two separate flask containing MeCN and mixing the two solutions. As a result, a pale pink solid is yielded.

**3** was prepared by refluxing **1** in water for about 2h, until a dark violet solid is observed.

**4**, **6**, **7** and **8** were prepared via microwaves-assisted reaction, heating at 413 K for 0.5h and at 393 K for 2 h. Lastly, the samples are slowly cooled to room temperature at 8 K/min.

**2** and **5** were prepared in similar ways, by dissolving pyrazolate linker in MeCN and DMF respectively and subsequently adding  $\text{Cu}(\text{CH}_3\text{COO})_2 \cdot \text{H}_2\text{O}$  with a metal:linker ratio of 1:2, stirring for 2h. A bright purple solid is yielded for **2**, whereas **5** shows a pale lilac color.

It should be added that **2** solid requires three 30 minutes-cycles of centrifugation at 6000 rpm because even with filter paper for compounds with particle sizes of 2-4  $\mu\text{m}$ , which is the one with the smallest particle size available to us, it was not possible to filter as the solid passed through the filter.

IR, TGA and PXRD analyses confirm that **2** can also be obtained by heating **5** at 433 K for 1h.

An attempt to synthesize **5** with the microwave reactor has been performed in the same conditions used for **4**, **6**, **7** and **8**. However, the formation of a dark red gas at the opening of the microwave vial suggests that the nitro group of 4-nitropyrazole has disengaged from the pyrazole ring as gaseous  $\text{NO}_2$ .

### 2.3.2 Infrared characterization

FT-IR spectra of **2** and **5** show weak signals at 3141  $\text{cm}^{-1}$  and 3137  $\text{cm}^{-1}$  respectively, corresponding to the  $\nu(\text{C-H})$  of aromatic hydrogen atoms. The very sharp and very strong

peaks at  $1488\text{ cm}^{-1}$  and  $1283\text{ cm}^{-1}$  for **2** and at  $1498\text{ cm}^{-1}$  and  $1284\text{ cm}^{-1}$  for **5** can be assigned to the  $-\text{NO}_2$  asymmetric and symmetric vibrations. In addition, the sharp band at  $818\text{ cm}^{-1}$ , present in both the spectra of **2** and **5**, can be attributed to the  $\nu(\text{C}-\text{NO}_2)$  vibration.<sup>177</sup> For the CP **5** the weak-broad band observable in the range  $3550\text{--}3250\text{ cm}^{-1}$  can be ascribed to the  $\nu(\text{O}-\text{H})$  stretching vibration of water molecules, indicating a certain hygroscopicity of **5** also proved by the TGA profile. Furthermore, in CP **5** an intense band at  $1653\text{ cm}^{-1}$  is present and confirms the presence of coordinated DMF molecules, as the band corresponds to the  $\nu(\text{C}=\text{O})$  stretching and it is shifted slightly towards lower wavenumbers with respect to free DMF ( $1661\text{ cm}^{-1}$ ). In **Figure 42** IR spectra of **2** and **5** are reported. The presence of many well-defined, sharp, and intense peaks is typical of ordered and extended structures in which the positions of the various functional groups are regularly repeated and therefore molecular vibrations all occur with the same energy. **Figure 43** compare **2** with **5** after thermal treatment at  $433\text{ K}$  for  $1\text{ h}$ . Loss of water molecules and also coordinated DMF molecules is observed as peaks in the  $3550\text{--}3250\text{ cm}^{-1}$  region and the peak at  $1653\text{ cm}^{-1}$  are absent. The two IR spectra are superimposable, confirming that once compound **5** has released the coordinated DMF molecules bridged to two  $\text{Cu}^{2+}$  ions, the nitro groups of the adjacent chain have a chance to interact with the metal centers in which a coordination site has become available.

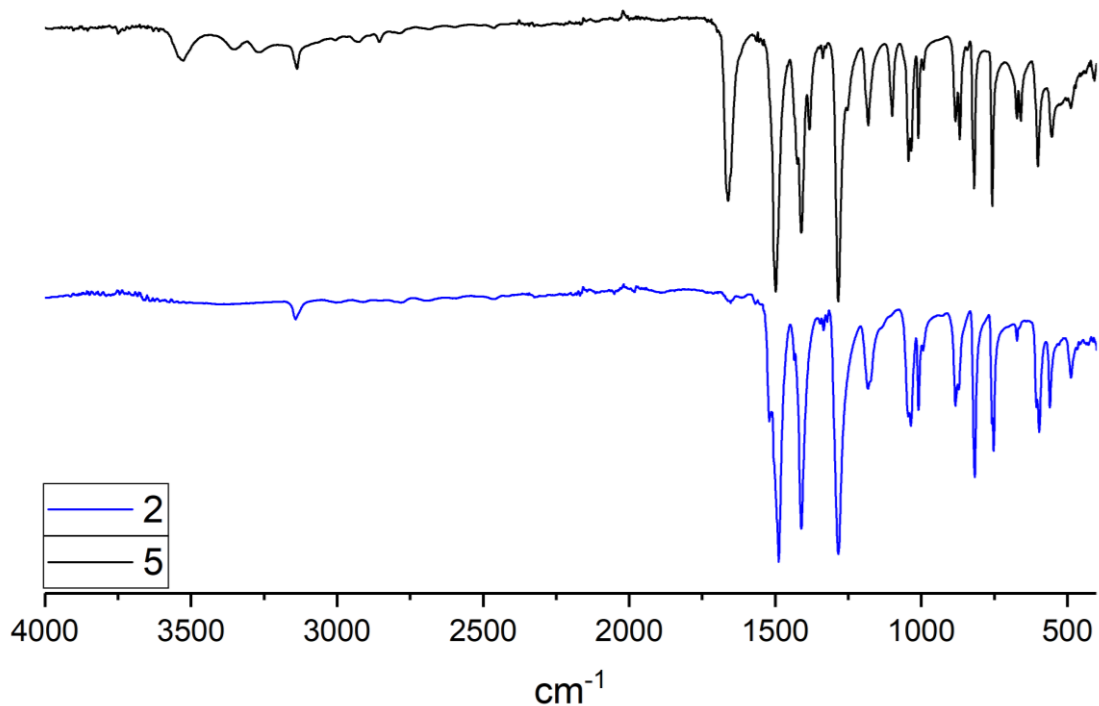


FIGURE 42 **2** (blue) and **5** (black) IR spectra (4000-400  $\text{cm}^{-1}$ ).

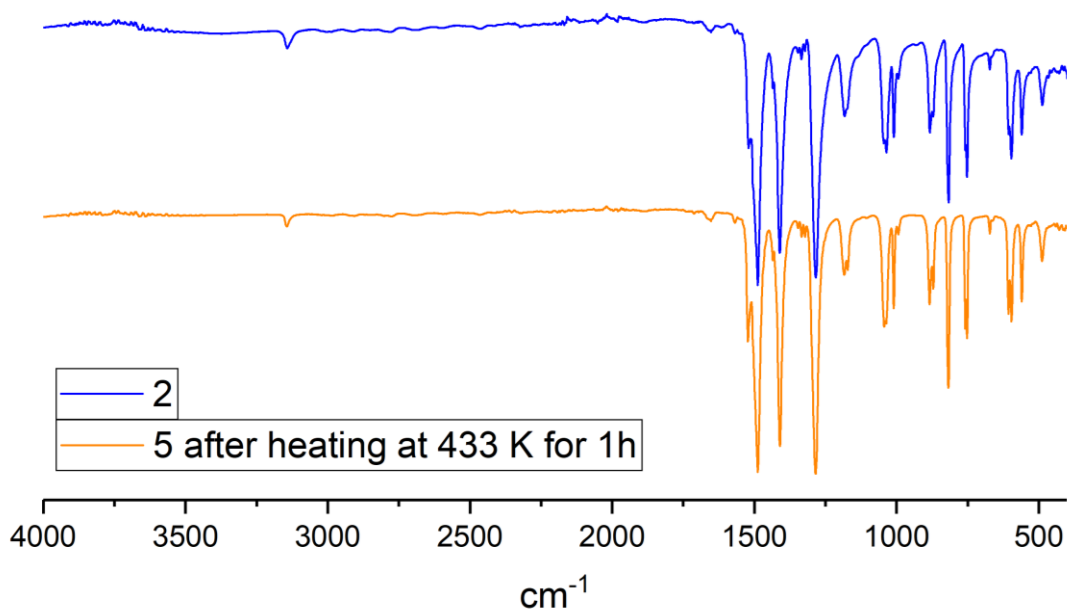


FIGURE 43 **2** (blue) and **5** after heating at 433 K for 1h (orange) IR spectra. The two spectra are superimposable, confirming the transformation of **5** in **2** after the thermal treatment.

### 2.3.3 Thermogravimetric analyses

The thermal profile of **1**, **3**, **4** and **6-8** has been already explored.

CP **1** is stable until 503 K and it starts losing the bridging -OH group, achieving  $\text{Cu}(\text{pz})_2$  species, which is the same obtained after removal of water molecules from CP **3**. In addition,

**4** and **6-8** show thermal stability up to 513-543 K, after the removal of a DMF molecule for formula unit in the range 363-533 K.<sup>99</sup>

**Figure 44** describes the thermal behaviour of **2** and **5**. CP **2** shows thermal stability up to 553 K. A rapid exothermic decomposition associated with a 50% loss of weight occurs in the temperature range of 563–623 K, followed by another rapid decomposition corresponding to a 15% loss of weight until 673 K. No further transformations are observed until 873 K. CP **5** exhibits two weight losses highlighting the presence of clathrate solvent molecules: the first loss of 4.3% starts at 343 K and ends at 373 K and can be attributed to the release of water molecules due to **5** hygroscopicity, whereas the second loss of 17.9% in the temperature range 393– 478 K is due to the release of coordinated DMF molecules, occurring at temperatures higher than DMF boiling point (425 K) and thus indicating a strong interaction of the solvent molecule with the metal centers. The unsolvated compound remains stable up to 553 K, then a rapid decomposition happens in the temperature range of 573–653 K associated with a 45% weight loss. The TGA profile of **5** after the thermal treatment at 433 K for about 1 h is also reported. In all the three curves, the stability of CPs end at the same point (~553 K), indicating that after the loss of clathrate molecules, **2** and **5** CPs correspond to the same compound. However, for compound **5** after treatment, no further decomposition occurs after 623 K as for **2**, probably suggesting a higher purity of the CP obtained by this method.

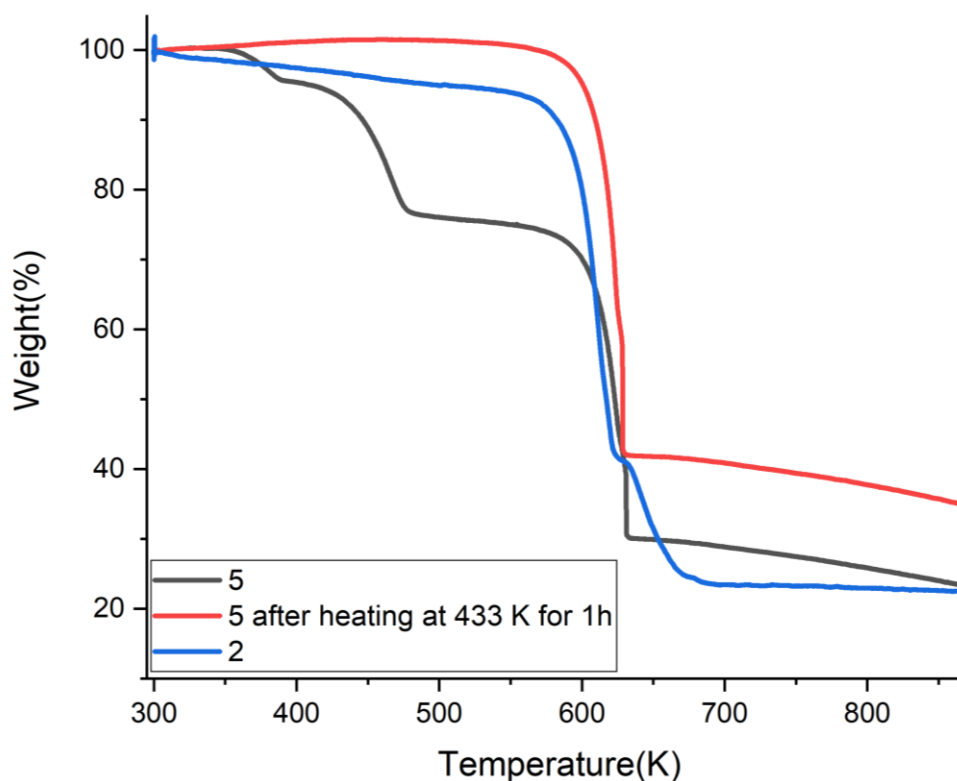


FIGURE 44 TGA curves of **2** (blue), **5** (black) and **5** after thermal treatment at 433 K for 1 h (red).

#### 2.3.4 Crystal structure of **2** $[\text{Cu}(\mu\text{-NO}_2\text{-pz})_2]_n$

CPs **2** and **5** were obtained as microcrystalline powders. Unfortunately, the molecular structure of **5** could not be solved and only potential space group and unit cell parameters are here reported: (triclinic,  $P-1$ ,  $a = 10.1379(7) \text{ \AA}$ ,  $b = 7.3247(9) \text{ \AA}$ ,  $c = 10.6400(7) \text{ \AA}$ ,  $\alpha = 87.78(1)^\circ$ ,  $\beta = 112.461(4)^\circ$ ,  $\gamma = 87.904(9)^\circ$ ,  $V = 728.5(1) \text{ \AA}^3$ ). On the contrary, the crystal structure of **2** was successfully determined and is depicted in **Figure 45**. The CP crystallizes in the monoclinic space group  $C2/m$ . The asymmetric unit features half of a copper(II) ion on an inversion center and two halves of 4- $\text{NO}_2\text{pz}$  ligands on mirror planes. The metal centers are hexa-coordinated with a  $\text{trans-CuN}_4\text{O}_2$  octahedral stereochemistry. The  $\mu$ -bridging by the distinct pyrazolate nitrogen atoms leads to the formation of 1D chains running along the crystallographic  $b$ -axis with a pace of about  $3.80 \text{ \AA}$ . The oxygen atoms of the  $\mu\text{-NO}_2$  group belonging to a pyrazolate lying approximately on the (100) plane coordinate the  $\text{Cu}^{2+}$  ions of an adjacent chain, thus producing 2D slabs extending parallel to this plane and piling along the crystallographic  $a$ -axis. The other independent linker lies in the (10-1) plane occupying the empty space among consecutive slabs. Its oxygen atoms establish weak

C-H...O non-bonding interactions ( $C\cdots O = 3.2 \text{ \AA}$ ). The crystal structure features a residual empty volume of  $\approx 12\%$ . PXRD pattern after Rietveld refinement is evidenced in **Figure 46**.

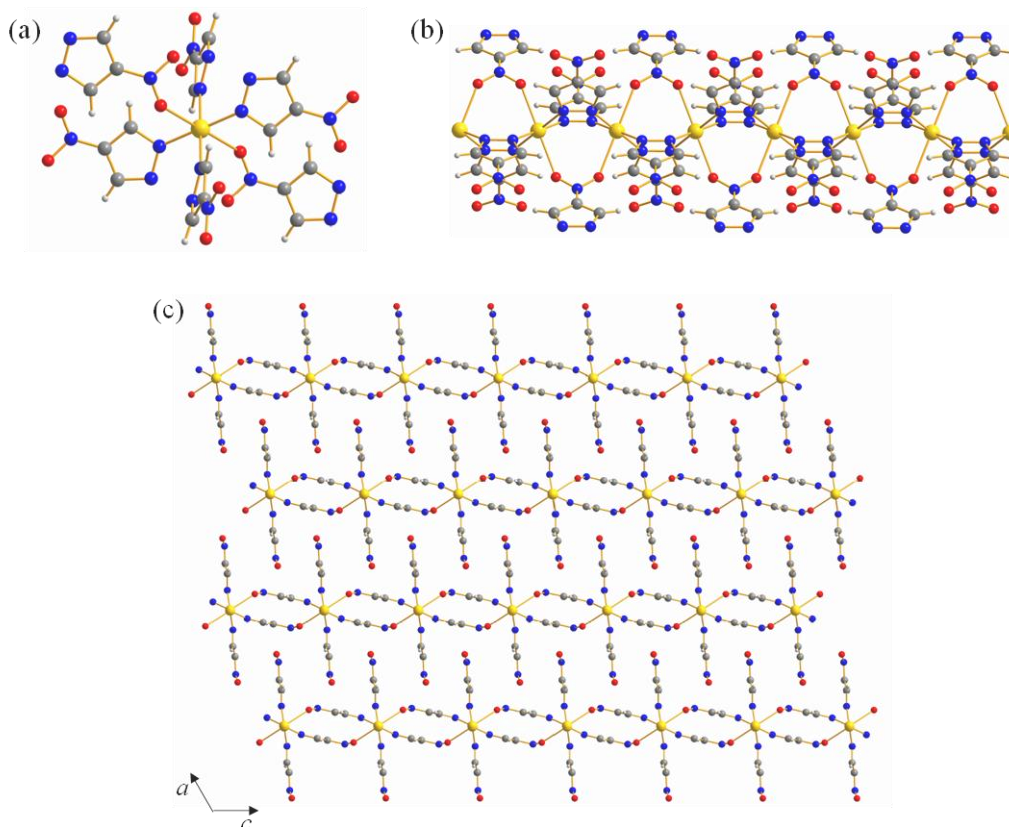


FIGURE 45 Representation of the crystal structure of CP 2: (a) the coordination geometry and the stereochemistry of Cu(II) metal center; (b) the 1D chain of metal ions running along the b-axis; (c) packing of the 2D slabs viewed along the [010] direction. Carbon (grey), hydrogen (white), nitrogen (blue), oxygen (red) and copper (yellow) atoms are indicated.

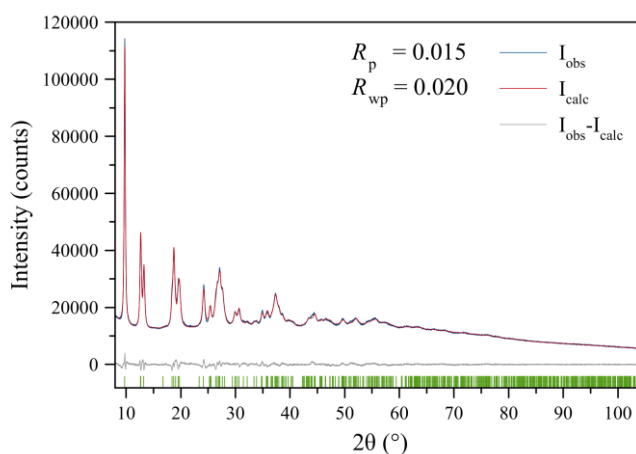


FIGURE 46 PXRD pattern of 2. The structure refinement carried out with the Rietveld method is shown through experimental, calculated and difference traces (in blue, red and grey, respectively). The green markers at the bottom indicate the positions of the Bragg reflections.

### 2.3.5 Antibacterial activity: bacterial growth curve and antibacterial rate

Initially, the antibacterial activity of pyrazole linkers (4-X-pyrazole with X= H, NO<sub>2</sub>, Cl, Br, or I) was tested on *E. coli* and *S. aureus* as representatives of Gram- and Gram+ bacteria respectively and the results are depicted in **Figure 47**.

By placing the number of viable bacterial cells of the blank (*E. coli* or *S. aureus*) at time 0 equal to 100%, the activity of the free linkers is reported in comparison to it. As can be seen, simple pyrazole and the various substituted pyrazoles show an antibacterial activity, effectively decreasing the number of viable bacterial cells in the first few hours, but this activity is not maintained over time. Exceptions are 4-NO<sub>2</sub>-pyrazole, which after 20h reduces the number of viable cells of *E. coli* to about 35% and the viable cells of *S. aureus* to 67%, and 4-Br-pyrazole, which reduces the number of viable cells of *E. coli* to 68% after the same time of treatment.

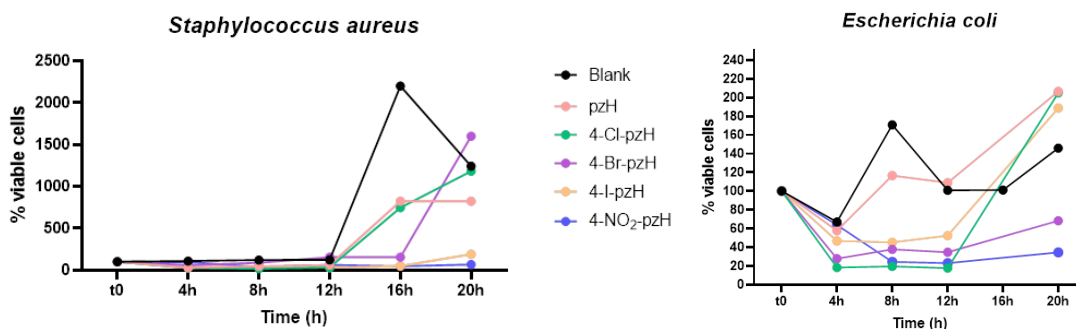


FIGURE 47 Antibacterial activity of the free linkers, reported in % of viable bacterial cells as a function of time, against *S. aureus* and *E. coli*.

These results confirm antibacterial activity of the nitro group as a substituent on the pyrazole ring. However, the general low activity of the free linkers has led to focus mainly on the antibacterial properties of the corresponding CPs, so all the following discussion in this chapter will only deal with them.

The bacterial growth curve and the antibacterial rate of the samples treated with CPs **1-8** were determined against two Gram- bacterial strains, *E. coli* and *P. aeruginosa*, and the Gram+ *S. aureus*, while the growth inhibition was evaluated by the OD<sub>600</sub> value. **Figure 48** and **Figure 49** represent respectively the bacterial growth curve and the antibacterial rate after the treatment with CPs **1-8** in 24h.

All CPs showed pronounced antibacterial activity. The number of viable cells was applied to calculate the kill rate, and it denotes a useful parameter for the determination of a bactericidal or bacteriostatic action. Bactericidal activity is defined as the decrease in the

number of viable bacterial cells  $\geq 99.9$  percent of the inoculum within 18 to 24 hours, whereas bacteriostatic activity is expressed as a reduction in bacterial growth maintained stable between 90 and 99%, again within 18 and 24 h of inoculation.

In general, when analysing the antibacterial activity of the compounds against each bacterial strain tested, all compounds showed more homogeneous performance against *P. aeruginosa* and *S. aureus*. Some compounds, however, were less effective against *E. coli*, both in terms of time and rate.

In particular, as highlighted in **Figure 48**, in the bacterial growth curves showed a strong activity against *P. aeruginosa* and *S. aureus* as early as the first 4 hours. For what concerns *E. coli*, CPs 1-4 exhibited a pronounced activity in 4h, while 5 and 8 showed the best action with more than 95% bacterial death about 8 hours after inoculation. Moreover, CP 8 could not maintain the performance achieved during all treatment periods.

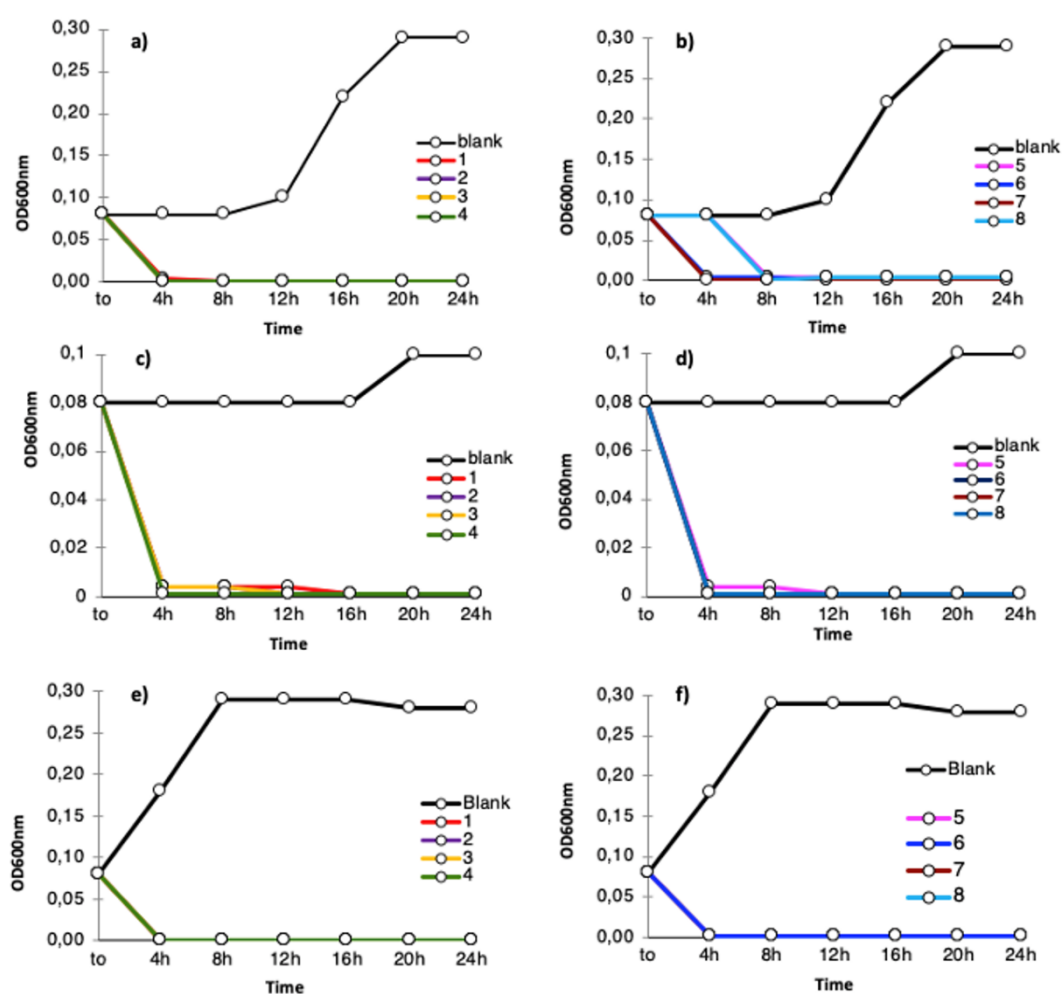


FIGURE 48 Bacterial growth curve of 1-8 CPs against *E. coli* (a and b), *S. aureus* (c and d), and *P. aeruginosa* (e and f) as a function of treatment time.



Antibacterial rate (%) (**Figure 49**) confirm antibacterial rate trend. An evident bacteriostatic activity (95% growth inhibition) of *P. aeruginosa* and *S. aureus* was observed just after 8h of treatment for all CPs (except for **1**), while the bactericidal activity against the two strains is achieved within 12 hours of treatment, with a 99.99% growth inhibition kept stable also after 24 hours. As already emphasised in the growth curves, a less marked activity was detected for certain CPs against *E. coli*. In particular, compounds **1-4** and **6** showed a bacteriostatic activity of more than 95% within 4h. On the contrary, the other CPS reached the same performance after longer inoculation times. A bactericidal activity (99.9% of inhibition) has been achieved very fast by **3** and **4** within 4h, while **1** within 8 h, **5** and **7** within 12h and finally **2** only after 24h. **6** and **8**, on the other side, do not show a bactericidal activity even after 24h of treatment.

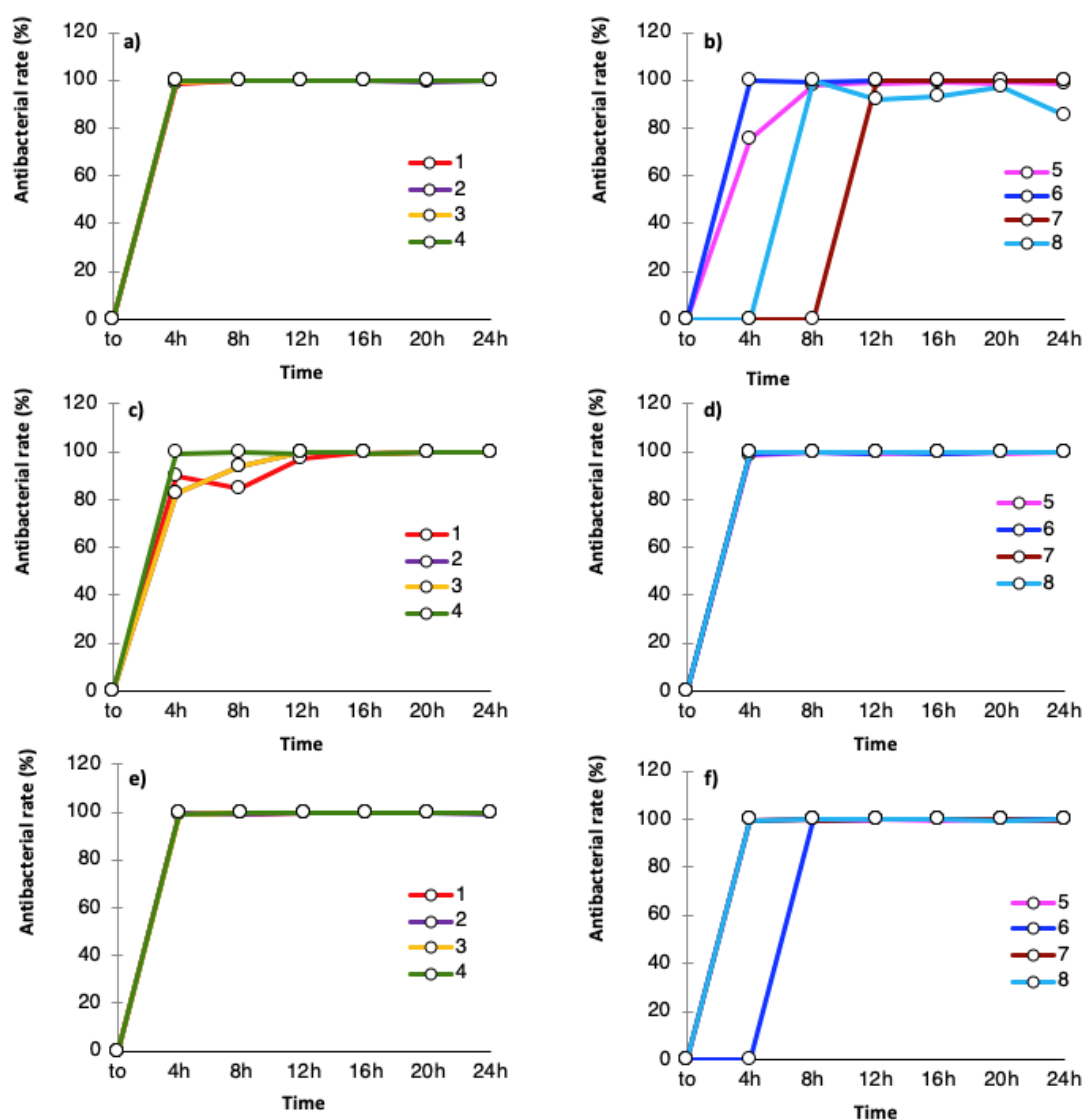


FIGURE 49 Antibacterial rate (%) of *E. coli* (a and b), *S. aureus* (c and d), and *P. aeruginosa* (e and f) treated with CPs 1-8.

Structural considerations on the eight CPs may suggest an explanation for this trend.

Since organic linkers do not exhibit long-lasting activity, the activity is reasonably mainly exerted by the copper(II) ion electrostatic interaction with the negatively charged bacterial membranes. For this to occur, the exposure of at least one free copper(II) ion coordination site is paramount.

The substitution of the hydrogen in position 4 in the pyrazole molecule with more or less bulky atoms or groups, as well as the strong bridging coordination exerted by the DMF molecule occupying the Cu(II) axial coordination position, could hinder the interaction between the metal ion and the bacterial surface.

Given these premises, it is perhaps for this reason that the structures that achieve bactericidal activity faster are the least crowded **3** and **4** (4h), and **1** (8h) while for the other ones 12 or 24 hours are required or even **6** and **8** never reach the maximum percentage of inhibition.

Based on the same reason, CP **2**, which is the only 2D coordination polymer, takes a longer time to perform its bactericidal action because the coordination of the nitro groups on the copper ions of the adjacent chains also could reduce the interaction space of the metal center with the bacteria (See **Figure 41** for a comparison among the different structures).

In addition, the activity contribution due to the release of metal ions, which will be discussed in the next subchapter, should also be considered.

The fact that CPs based on copper(II) ion and pyrazolate linkers were generally found to be less effective on *E. coli* in terms of time of activity and percentage of growth inhibition than on *S. aureus* and *P. aeruginosa* should not surprise us.

There are two main factors to take into account. The first one is the structural difference in cell walls that characterizes Gram-positive bacteria such as *S. aureus* with respect to Gram-negative bacteria such as *E. coli* and *P. aeruginosa*. Gram-negative bacteria have a thinner peptidoglycan layer than the multilayer layer observed for Gram-positive bacteria, but at the same time, they possess an outer membrane consisting mainly of lipopolysaccharides that makes the bacteria less susceptible to attack by antimicrobial agents.<sup>178,179</sup> A representation of what has just been said can be found in **Figure 50**.

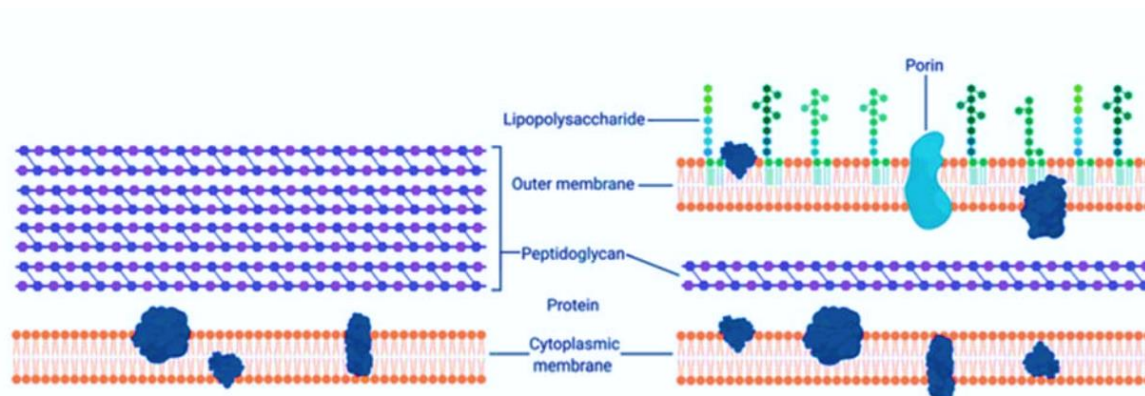


FIGURE 50 Representation of Gram-positive (left) and Gram-negative (right) bacteria cell walls.<sup>178</sup>

Copper(II) CPs would then have more difficulty in electrostatically interacting with the Gram-negative cell wall and thus produce the ROS that lead to membrane rupture and destruction of cellular material essential for the bacterium's life, as is described and demonstrated in the tests in the next section.

The second point to consider, in addition, concerns the specific adaptive mechanisms that both Gram-positive and Gram-negative bacteria have developed for regulating copper homeostasis, an element that would result toxic for the biochemistry bacteria at high concentrations and for that reason to be regulated.<sup>180</sup> Even within the same type of bacteria, these adaptive mechanisms vary, and for this reason, *P. aeruginosa* and *E. coli*, while both being Gram-negative, have distinct channels or proteins<sup>181–183</sup>.

### 2.3.6 Antibacterial mechanism: ROS production test, PI uptake and metal ions release test

To elucidate the antibacterial mechanism of **1-8**, three tests were performed in order to investigate their ROS production against Gram- and Gram+ tested bacteria, the severity of damage on the permeabilization of cell membrane and the eventual release of  $\text{Cu}^{2+}$  ions. In fact, the antibacterial mechanism could be related to the damage of the bacterial cell in terms of disintegration of the cell membrane due to the interaction with CPs surface and/or metal ions release, and generation of reactive oxygen species (ROS) resulting in increasing stress to the bacterial cell.

Metal ions release tests were conducted with the help of an ICP, and the  $\text{Cu}^{2+}$  ion concentration values (in ppm) detected after 24h are provided in the following table:

CPs	Cu <sup>2+</sup> released (ppm)
1	0.930
2	0.220
5	0.646

The results demonstrate high stability of the selected CPs, given the release values of less than 1 ppm for each CP. These concentration values are lower than those reported for release tests with MOFs based on copper(II) metal centers and carboxylate linkers.<sup>152,169</sup> This can be attributed to a higher bond strength that the soft acid Cu<sup>2+</sup> establishes with the soft base pyrazolate, according to Pearson's HSAB theory.<sup>184</sup>

The low concentration values of Cu<sup>2+</sup> released suggests that the mechanism of antibacterial action of CPs occurs by the combined action of electrostatic interaction of the CP with the bacterial cell and through the release of Cu<sup>2+</sup> ions.

The ROS assay was performed using dichlorofluorescein diacetate (DCFH-DA) as a fluorescent probe. A greater ROS generation means more stressed bacterial cells. After incubation with CPs **1-8**, the amount of ROS was detected by emission at the wavelength of 523 nm.

The results reported in **Figure 51** confirm the generation of free radicals in all bacterial strains. However, some differences occur and are here commented. A significant fluorescence signal was observed for all samples treated with **1-8** corresponding to the free radicals in *E. coli*, *P. aeruginosa*, and *S. aureus* cells during the first 4h of treatment, while the fluorescent signal of the untreated bacterial suspension (C-) was negligible. A very high production of ROS in the samples treated with **5** was confirmed by the intensity of fluorescence post-treatment for all bacteria tested just after 1h. Whereas **4** showed the highest ROS production in *P. aeruginosa*, **1** displayed the lowest intensity of fluorescence for all bacteria tested.

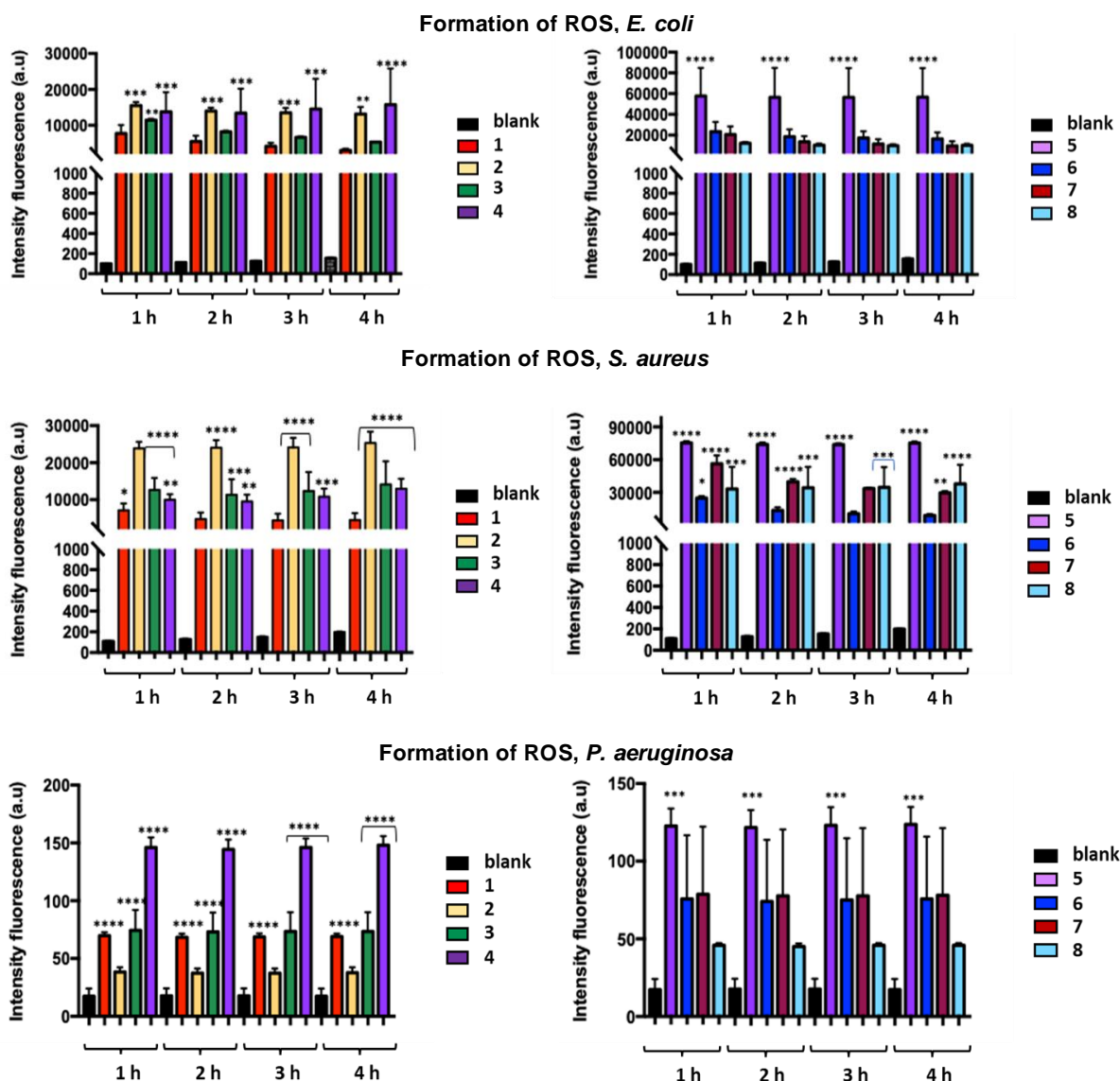


FIGURE 51 Formation of ROS in *E. coli*, *S. aureus*, and *P. aeruginosa* bacteria cells exposed to 1-8 for 4 hours. The data are represented as the mean  $\pm$  SD of at least three separate experiments; statistical significance\*  $p < 0.05$ .

The damage on the membrane caused by 1-8 was further investigated through Propidium iodide (PI) assay with the aim of assessing the cellular damage of bacteria (Figure 52). The red fluorescence emission was determined and compared with the untreated bacterial suspension. A similar trend towards all cultured bacterial strains treated with CPs 1-8 was appreciated, with a moderate increase in the fluorescence emission as a function of time.

Associated with the measurement of fluorescence intensity of PI, the confocal laser scanning microscopy (CLSM) allows a visible evaluation of live and dead bacteria cells thanks to the the LIVE/DEAD BacLight Bacterial Viability Kit. The SYTO 9 dye is able to label all bacteria

in a population, whereas PI penetrates only in those bacterial cells with a compromised membrane.

In **Figure 53a** and **b**, untreated *E. coli* and *S. aureus* are depicted in green color due to the SYTO9 dye. In the case of dead *E. coli* and *S. aureus*, PI penetrated through bacteria with disrupted cell membranes and stained them with red color (**Figure 49c** and **d**). For instance, CLSM image of CP **2** after 4 hours of treatment (under the same conditions adopted for the growth inhibition curve) underlined a significant antibacterial activity of copper(II) CPs. By comparing the picture of the untreated *E. coli* **49a** with the treated one **49c**, a distinct reduction of live cells (green) and the appearance of dead cells (red) is appreciable. Once again, in the case of *S. aureus*, the treatment is even more efficient as only dead cells in red are observed, reiterating the trend seen in the other antibacterial tests.

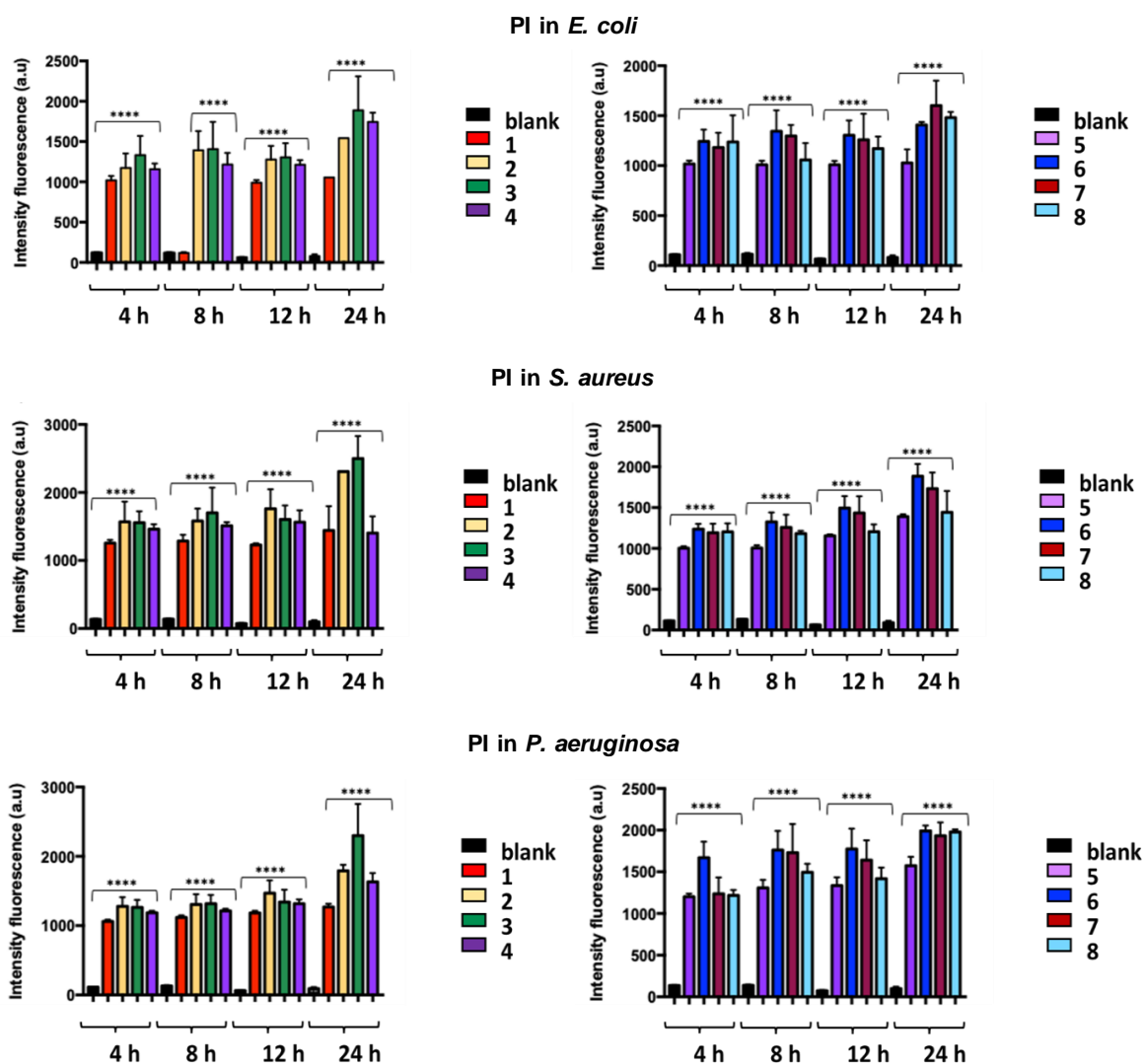


FIGURE 52 PI fluorescent emission for *E. coli*, *S. aureus*, and *P. aeruginosa* cells exposed to CPs 1-8. The data are represented as the mean  $\pm$  SD of at least three separate experiments; statistical significance\*  $p < 0.05$ .

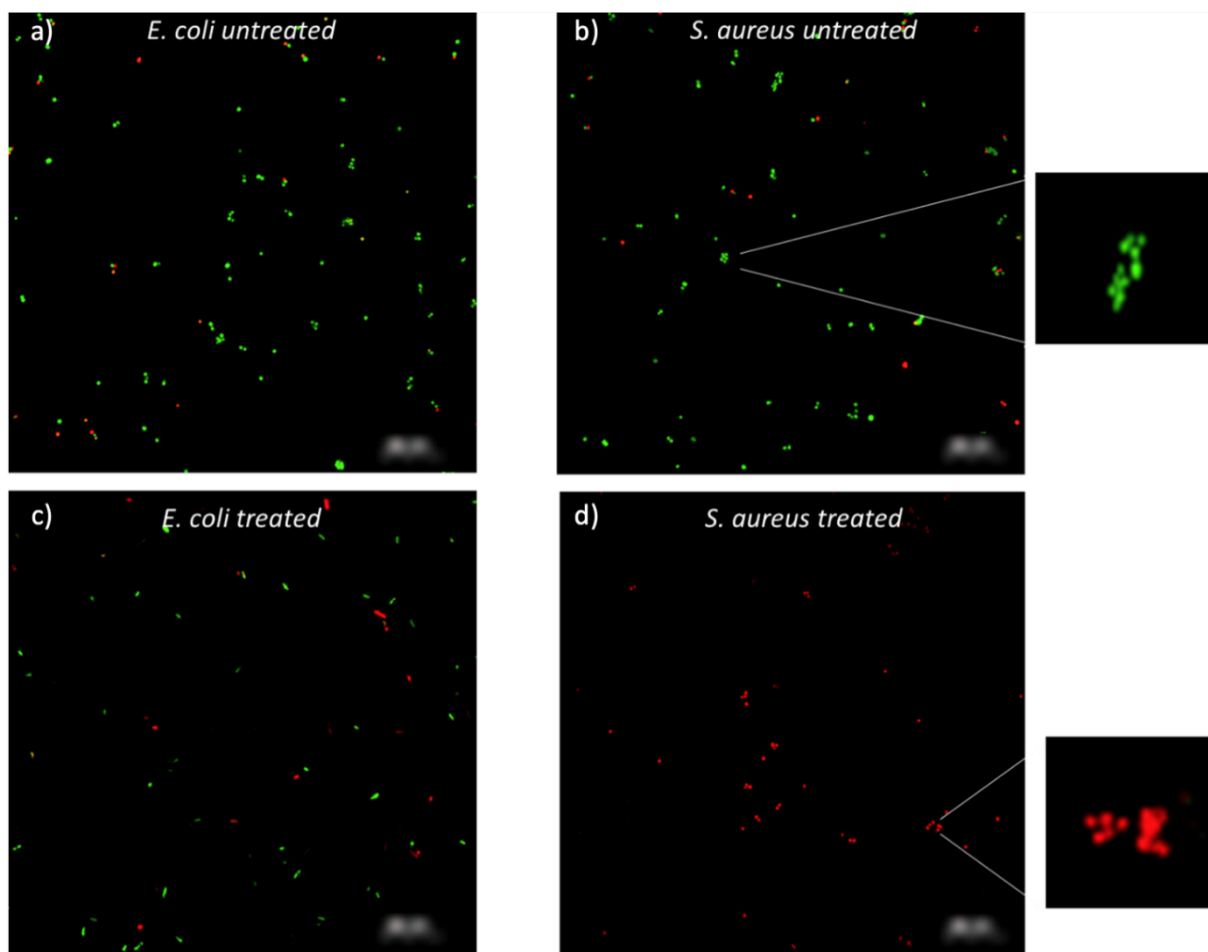


FIGURE 53 Live *E. coli* and *S. aureus* in green color and dead *E. coli* and *S. aureus* in red color due to the SYTO9 dye of LIVE/DEAD<sup>®</sup> BacLight Kit, before a), b) and after CP 2 treatment c), d).

## 2.4 Conclusions

In summary, eight CPs based on Cu(II) ions and simple or substituted pyrazolate linkers have been investigated as novel antibacterial materials against three different bacterial strains: *S. aureus*, *E. coli* and *P. aeruginosa*. CP 2 and 5 in which the organic linker is 4-nitropyrazole are novel structures and for this reason they have been characterised with several techniques including IR, TGA and PXRD. 2 resulted in a 2D CP due to the coordination for each nitro group on two copper ions of the adjacent chain, while 5 shows a structure analogue to 4 and 6-8.

The eight CPs have shown marked antibacterial activity and the investigation of the mechanism seems to confirm that all the CPs are able to stimulate ROS production and formation of highly reactive radicals. As a result, the cellular microenvironment is disrupted

by binding to the membrane lipids or by leaching of  $\text{Cu}^{2+}$  ions that can electrostatically interact with the phospholipidic or peptidoglycan cell membrane and penetrate the outer wall of the bacterial surface. Such an interaction can deactivate vital enzymes and damage the cell membrane integrity and permeability.

A bactericidal activity against *S. aureus* and *P. aeruginosa* have been recorded for all CPs, whereas a little lower activity in terms of treatment time and antibacterial rate (%) was observed towards *E. coli*.



**CHAPTER 3:**  
**Antibacterial Activity of zinc and copper**  
**bis(pyrazolate)-based MOFs**

### 3.1 Aim of the research work

The antibacterial activity of copper(II) coordination polymers in the previous work prompted us to evaluate the antibacterial activity of MOFs based on two different metal centers: zinc and copper.

With regard to the use of organic linkers, the following three compounds were chosen: 1) H<sub>2</sub>BPZ, 4,4'-bipyrazole; 2) H<sub>2</sub>Me<sub>4</sub>BDP, 1,4-bis(1H-pyrazol-4-yl-3,5-dimethyl)benzene and 3) H<sub>2</sub>BPZNH<sub>2</sub>, 3-amino-4,4'-bipyrazole, reported in **Figure 54**.

Consequently, six MOFs were obtained and named **Zn1**, **Zn2**, **Zn3**, **Cu1**, **Cu2** and **Cu3**, so as to specify the metal center and organic linker according to the corresponding number.

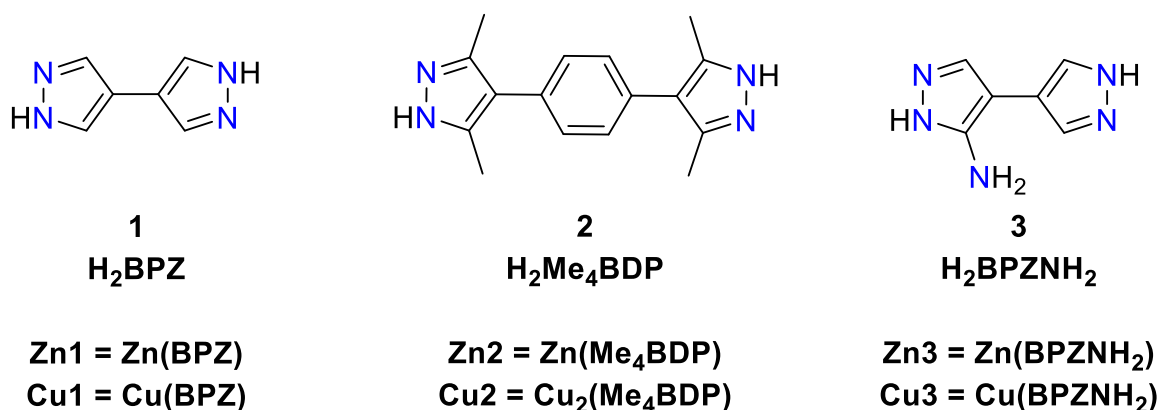


FIGURE 54 Representation of the three linkers employed in this work and the corresponding MOFs unit formula.

In this case, MOFs were synthesized according to the procedures reported in the literature or by making some variations to them.

The purpose of this work lies in evaluating the different antibacterial activity of the two different metal centers (copper and zinc) and testing whether the variation of the organic linker in the framework can affect the activity of MOF with the same metal used.

The microbiological analyses were performed in the Research Centre for Hygienistic, Health and Environmental Sciences (School of Pharmacy) of the University of Camerino, under the supervision of Dr. Stefania Scuri.

## 3.2 Experimental section

### 3.2.1 Materials and methods

Solvothermal reactor ТЕРМОДАТ was used to prepare MOFs at 393K.

Fluorescence analyses were performed with a BMG LABTECH FLUOstar Omega fluorescence cytometer. IKA KS 130 BASIC platform shaker was used for eppendorfs shaking in antibacterial rate (%) determination. Optical density measurements were carried out at 600 nm with a Bio-Tek  $\mu$ Quant microplate spectrophotometer.

### 3.2.2 Bacterial culture

Copper and Zinc bis(pyrazolate)-based MOFs **Zn1**, **Zn2**, **Zn3**, **Cu1**, **Cu2** and **Cu3**, were investigated as antimicrobial agents against *S. aureus* ATCC 25923 as representative of Gram-positive bacteria and *E. coli* ATCC 25922 as representative of Gram-negative bacteria. For each bacterial strain, bacterial inocula were prepared by adding a monoclonity to Triptone Soy Broth (TSB) nutritious medium and letting it grow at 310 K overnight. The bacterial culture was diluted to  $10^6$  CFU mL<sup>-1</sup> concentration in physiological solution.

### 3.2.3 Antibacterial rate (%)

In order to define the antibacterial rate (%) the number of CFU was determined transferring the treated sample into Petri dishes containing Plate Count Agar medium, according to the following procedure. For each bacterium strain, 0.4 mg of each MOF was separately added in 6 eppendorfs (one for each MOF tested) containing the bacterial culture at  $10^6$  CFU mL<sup>-1</sup> concentration in 1 mL of autoclaved physiological solution. All eppendorfs were put on a platform shaker and kept shaking for 24h at 160 rpm. At set time intervals (0, 3, 10 and 24 h) 10  $\mu$ L of supernatant for each treated sample were withdrawn, diluted in physiological solution, and poured uniformly into Petri dishes containing Plate Count Agar (OXOID) and incubated overnight. For each bacterial strain, an untreated sample was prepared with the same procedure and was used as a blank.

CFUs were manually counted. Antibacterial Rate (%) expressing the bacterial growth inhibition was calculated using the following formula:

$$\left( \frac{CFU_{t_0} - CFU_{t_k}}{CFU_{t_0}} \right) \times 100$$

where  $t_0$  is the time zero at the beginning of the test and  $t_k$  is the specific interval in hours (0, 3, 10 and 24h).

### 3.2.4 Detection Reactive Oxygen Species (ROS)

2',7'-Dichloro-dihydro-fluorescein diacetate (DCFH-DA) was chosen as oxidation probe for the evaluation of the production of ROS. For each bacterial strain, 1 mL of a bacterial culture at  $10^6$  CFU/mL concentration in PBS (phosphate buffer solution) using bacterial cells grown in nutritious medium TSB overnight, was incubated for 30 minutes with 20  $\mu$ L of 2',7'-Dichloro-dihydro-fluorescein diacetate at 310 K. 1 mL of **Zn1**, **Zn2**, **Zn3**, **Cu1**, **Cu2** and **Cu3** suspension in physiological solution was prepared for each MOF with a final concentration of 6  $\mu$ g/mL for Cu-based MOFs and 125  $\mu$ g/mL for Zn-based MOFs. 10  $\mu$ L of bacterial suspension were transferred in each eppendorf. The ROS production was evaluated after 2 and 4 hours of treatment and an untreated sample was prepared with the same procedure and was used as a blank.

For each interval time, 100  $\mu$ L of the sample from each eppendorf was transferred into 96 well plates, in triplicate. The fluorescence tests for each sample were carried out with the aid of a FLUOstar Omega fluorescence cytometer at 485/20 nm and 528/20 nm wavelengths for excitation and emission respectively. Also, the fluorescence of only medium sample and medium + bacteria strain (blank) was determined. The average of the three replications was plotted as the intensity of fluorescence in arbitrary unit (a.u). The statistical significance was determined by One-Way-Anova with Bonferroni's multiple comparisons test; \*  $p < 0.05$ .

### 3.2.5 Propidium Iodide (PI) uptake

Propidium Iodide (PI) was employed as fluorescent probe to observe the viability of bacteria treated with **Zn1**, **Zn2**, **Zn3**, **Cu1**, **Cu2** and **Cu3**.

1 mL of **Zn1**, **Zn2**, **Zn3**, **Cu1**, **Cu2** and **Cu3** suspension in physiological solution was prepared for each MOF with a final concentration of 6  $\mu$ g/mL for Cu-based MOFs and 125  $\mu$ g/mL for Zn-based MOFs. Bacterial culture was added to MOFs suspensions with a final concentration of  $10^6$  CFU/mL.

After 2h and 4h, 100  $\mu$ L of the sample from each eppendorf was transferred into 96 well plates, in triplicate, and 1.5  $\mu$ L of Propidium Iodide (PI) solution was added to each

ependorff tube in the dark and incubated for 20 minutes at 310 K. After this, the fluorescence tests were carried out with the aid of a FLUOstar Omega fluorescence cytometer at 485/20 nm and 528/20 nm.

Also, the fluorescence of only medium sample and medium + bacteria strain (blank) was determined. The average of the three replications was plotted as the intensity of fluorescence in arbitrary unit (a.u). The statistical significance was determined by One-Way-Anova with Bonferroni's multiple comparisons test; \*  $p < 0.05$ .

### 3.3 Results and discussions

#### 3.3.1 Preparation of Zinc and Copper bis(pyrazolate)-based MOFs

The synthesis of the six MOFs were performed as reported in the literature<sup>103,110,112</sup> or by making some variations to them.

Zn(BPZ) (**Zn1**) was synthesized starting from 0.2 mmol of  $\text{Zn}(\text{CH}_3\text{COO})_2 \cdot 2\text{H}_2\text{O}$  and 0.2 mmol of linker **1**, by dissolving the two reagents in 30 mL of MeOH and keeping the reaction at 318 K for 24h.

Cu(BPZ) (**Cu1**) was obtained in similar way, starting from 0.2 mmol of  $\text{Cu}(\text{CH}_3\text{COO})_2 \cdot \text{H}_2\text{O}$  and 0.2 mmol of linker **1**, by dissolving the two reagents in 30 mL of MeCN and keeping the reaction at 318 K for 24h.

Zn(Me4BDP) (**Zn2**) and Cu<sub>2</sub>(Me4BDP) (**Cu2**) were synthesized in a solvothermal reactor by dissolving 0.25 mmol of the metal precursor (respectively  $\text{Zn}(\text{CH}_3\text{COO})_2 \cdot 2\text{H}_2\text{O}$  and  $\text{Cu}(\text{CH}_3\text{COO})_2 \cdot \text{H}_2\text{O}$ ) in 5 mL of MeOH whereas 0.25 mmol of linker **2** are solubilized in 5 mL of DMF.

Zn(BPZNH<sub>2</sub>) (**Zn3**) was obtained by dissolution of 0.2 mmol of  $\text{Zn}(\text{CH}_3\text{COO})_2 \cdot 2\text{H}_2\text{O}$  and 0.2 mmol of linker **3** in 8 mL of water and keeping the reaction at room temperature for 24h.

Finally, Cu(BPZNH<sub>2</sub>) (**Cu3**) was prepared starting from 0.2 mmol of  $\text{Cu}(\text{CH}_3\text{COO})_2 \cdot \text{H}_2\text{O}$  and 0.2 mmol of linker **3** dissolved in 8 mL of DMF, keeping the reaction at 393K for 24h.

#### 3.3.2 Zinc and Copper bis(pyrazolate)-based MOFs structures and BET Surface Area

As anticipated in the introduction, Zn(II) MOFs with bis(pyrazolate) ligands tend to crystallize with a  $P4_2/mmc$  space group, resulting in a network with square channels extending along the

[001] crystallographic direction due to the tetrahedral coordination geometry of the metal node, as highlighted in **Figure 55**, where the isorecticular structures of **Zn1** and **Zn3** are shown. **Cu1** and **Cu3**, in contrast, crystallize in the orthorhombic space group *Imma*. A 3D (4,4)-connected porous network is formed thanks to the square planar coordination geometry of  $\text{CuN}_4$  nodes, having 1D rhombic channels which extend parallel to the [010] crystallographic direction. **Figure 56** represents **Cu1** and **Cu3** crystal structures and their isorecticularity.

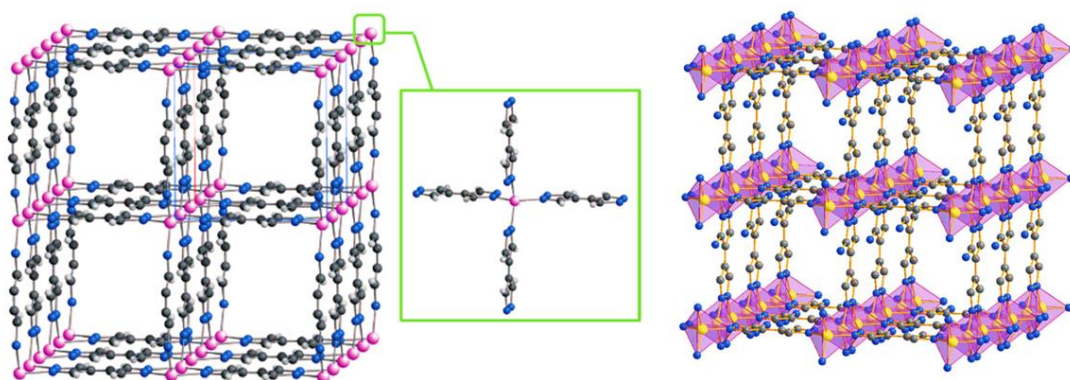


FIGURE 55 Crystal structure of **Zn1** (left) and **Zn3** (right). Carbon (black), Nitrogen (blue) and Zinc (pink or yellow) atoms are highlighted. The tetrahedral coordination geometry of the metal node is emphasized in the green box.

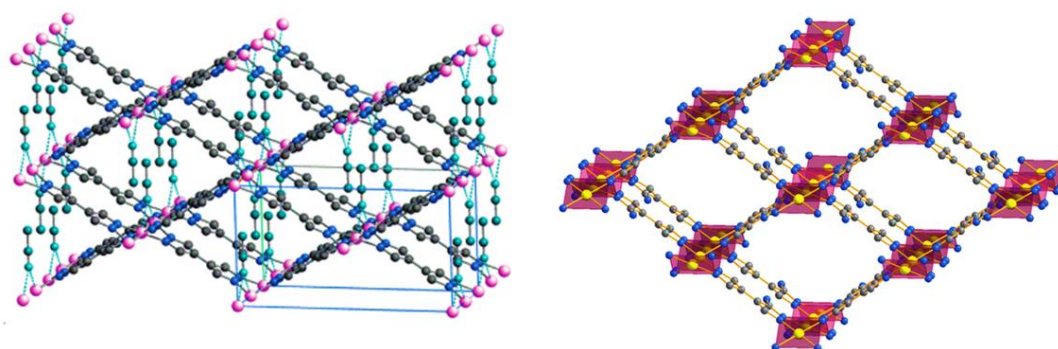


FIGURE 56 Crystal structure of **Cu1** (left) and **Cu3** (right). Carbon (black), Nitrogen (blue) and Copper (pink or yellow) atoms are highlighted, and the square planar coordination geometry is appreciable. Weak coordinating MeCN molecules are shown in cyan at left.

Crystal structures of **Zn2** and **Cu2** haven't been solved yet, but tests are ongoing.

In order to enrich the description of these six MOFs, the BET surface area values reported in literature for each of them is given as follows.

MOF	BET Surface Area (m <sup>2</sup> /g)
Zn1	778
Zn2	647
Zn3	395
Cu1	314
Cu2	939
Cu3	100

The trend in surface area observed for the three copper MOFs is consistent with the fact that linker **2** is longer than the other two linkers and therefore should lead to networks with higher surface area,<sup>185</sup> while the fact that the copper-based MOF with linker **3** having the amino group shows less surface area than the corresponding MOF with linker **1**, lies in the bulkiness of that functional group, which reduces the available volume of the pores.<sup>186</sup> However, this trend is not observed for Zinc-based MOFs for which **Zn1** exhibits the highest surface area. This should not surprise us: the surface area value is certainly related to geometrical considerations about the metal node and the nature and length of the organic linker, but it also depends significantly on the activation conditions applied. The optimal conditions, in fact, differ for each MOF and are often difficult to achieve or otherwise time-consuming.

### 3.3.3 Antibacterial activity: antibacterial rate

Bacterial culture (*E. coli* or *S. aureus* at 10<sup>6</sup> UFC/mL) was treated at t<sub>0</sub>, 3h, 10h, and 24h, with **Zn1**, **Zn2**, **Zn3**, **Cu1**, **Cu2** and **Cu3** at different concentrations (125 µg/mL and 6 µg/mL respectively). The chosen concentrations are the result of previous optimizations in which it was observed that zinc MOFs at 6 µg/mL is not active at all.

The number of colonies after incubation period, in the treatment and positive control plates, was counted to evaluate the % of viable cells.

**Figure 57** shows the antibacterial rate (%) calculated for the six MOFs.

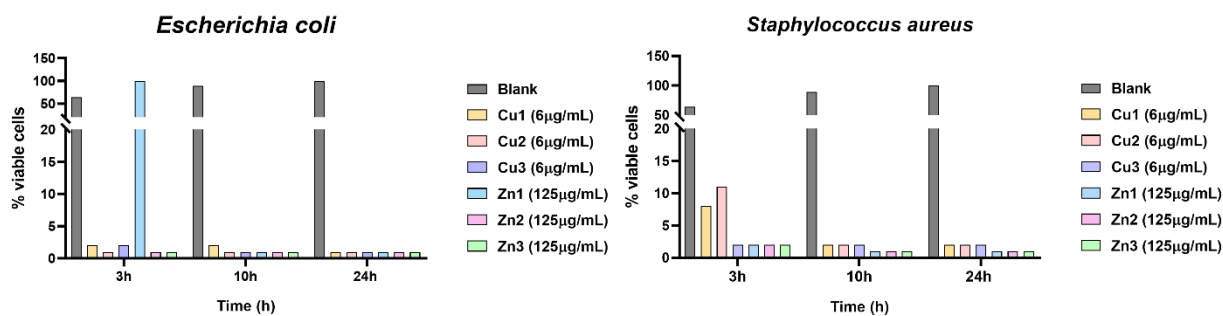


FIGURE 57 Evaluation of antibacterial rate (%) for each MOF against *E. coli* (left) and *S. aureus* (right).

CuMOFs achieve within the first 3 hours of exposure the 90-99% of viable cells reduction against *S. aureus* (a lower activity is performed by **Cu1** and **Cu2** after 3h), whereas a bacteriostatic activity is observed in the first three hours against *E. coli* that increase until the accomplishment of a bactericidal activity after 10 hours for both bacterial strains tested. Concerning with ZnMOFs, they show an analogue antibacterial activity in terms of time, but an higher concentration of compounds is required to exert their activity. An exception is **Zn1** which does not show any activity after 3h of treatment against *E. coli*, even if it results bactericidal after 10h and keep its performance after 24h of treatment.

Greater surface area does not imply greater antibacterial activity, although there is a greater exposed area of Cu(II) or Zn(II) ions that can interact with the bacterial cell and destroy it. On the contrary, **Zn1** and **Cu2** MOFs result in the first 3 hours of treatment being the least effective (against *E.coli* and *S. aureus*, respectively).

### 3.3.4 Antibacterial mechanism: ROS production test and PI uptake

ROS testing was performed to verify the mechanism of antibacterial action of the six MOFs. In my research group, after verifying the activity of the eight Copper Coordination Polymers of the previous work and of zinc complexes with substituted hydrazones,<sup>187</sup> we were hopeful to observe ROS production also for the six Copper and Zinc based MOFs.

**Figure 58** shows the ROS production of treated samples with the six MOFs in comparison with the blank (the untreated sample).



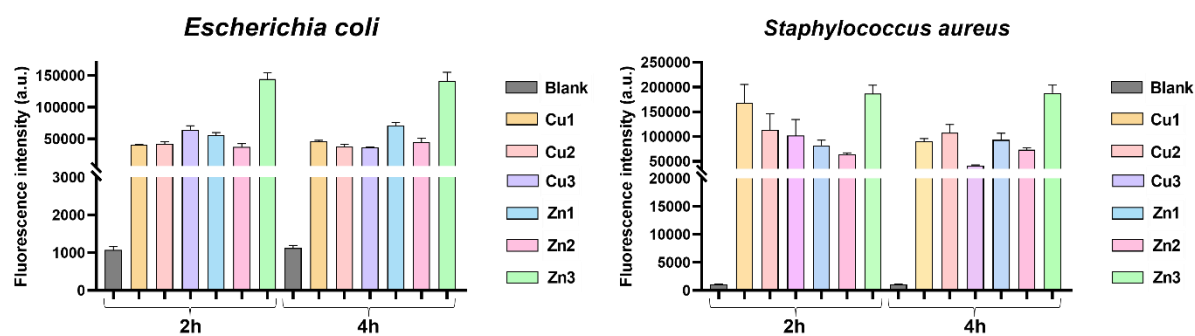


FIGURE 58 ROS production test of the samples treated with the six MOFs against *E. coli* and *S. aureus* after 2h and 4h of treatment.

A high production of radical species is observed in all cases comparing with the untreated sample. **Zn3** emerges among all by presenting an elevated ROS generation already at 2h of treatment against both bacterial strains.

Also in this work, the PI permeability assay was then performed to observe the fluorescence of dead cells labeled with the red probe.

In **Figure 59** the measure of the intensity of fluorescence due to PI probe for all treated samples is shown.

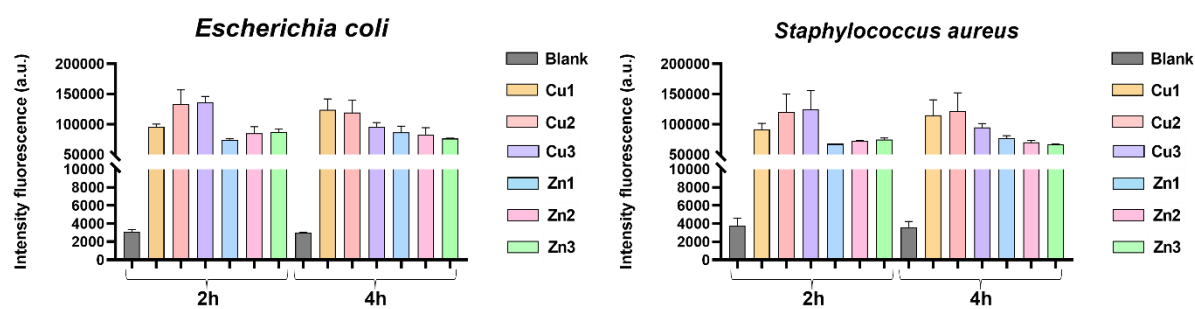


FIGURE 59 PI uptake of all treated samples with the six MOFs after 2h and 4h of test.

The activity of **Zn1**, **Zn2**, **Zn3**, **Cu1**, **Cu2** and **Cu3** is confirmed by the high fluorescence intensity recorded for the treated samples compared with the blank. Note in this case an almost completely similar trend between *E. coli* and *S. aureus*.

### 3. 4 Conclusions

Six MOFs based on two different metal nodes (copper and zinc) and on three different organic linkers (1, 2 and 3) were prepared according to literature and tested as antibacterial compounds against *E. coli* and *S. aureus*.

The tests did not show a clear influence of the nature of the organic linker on the antibacterial activity as well as the surface area value does not seem to be a discriminating factor from these preliminary tests.

However, the different efficiency of CuMOF and ZnMOF in terms of concentrations required to express their activity should be highlighted (6 against 125  $\mu\text{g}/\text{mL}$ ).

Also in this work, it can be hypothesized that the antibacterial activity is carried out by the interaction between the MOF and the surface of the bacterium wall and by metal ions release. Therefore, metal ions release tests will be performed to clarify this aspect. At the same time, the production of radical species destroys the cellular content leading to the death of the bacterium.

The research on these MOFs is also moving towards the evaluation of fungal activity and the first tests, which are outside this thesis work and therefore not reported in this chapter, look promising.

**CHAPTER 4:**  
**Carbon dioxide capture and conversion**  
**through fixation with epoxides in**  
**diamino-decorated Zn(II)-bipyrazolate MOFs**

## 4.1 Aim of the research work

Since the onset of the Industrial Revolution, anthropogenic activities have been causing an increase in atmospheric carbon dioxide emissions. It is widely acknowledged that this gas is responsible for global warming, and indirectly contributes to the depletion of the stratospheric ozone layer. Furthermore, carbon dioxide causes ocean acidification with catastrophic consequences for marine life.<sup>188</sup> For this reason, the scientific community is urgently seeking new strategies to address this disproportionate increase in emissions, with a focus on systems that are not only capable of capturing this gas, but also converting it into value-added products. Metal-Organic Frameworks have emerged as a viable solution to counteract the rapid growth of carbon dioxide emissions, owing to their remarkable ability to selectively adsorb, store and convert CO<sub>2</sub> into other valuable products (Carbon Dioxide Capture and Reuse, CCR). As previously described in the introduction of this thesis, the incorporation of functional groups on the organic linker able to establish Lewis acid / base and hydrogen bond interactions with CO<sub>2</sub> (such as amino groups) results in highly performing CO<sub>2</sub> capture MOFs.

Given these premises, in this study, two isomeric forms of diamino-decorated zinc bipyrazolate MOFs, namely **Zn(3,3'-L)** and Zn(3,5-L) (where L = diamino-4,4'-bipyrazolate, **Figure 60**), were synthesized by refluxing in DMF, and characterized through IR, TGA/DTA, EA analyses, whereas the structures have been solved through XRPD analysis. Besides, the textural properties, including BET surface area and pore size distribution, as well as their CO<sub>2</sub> adsorption ability, were investigated through N<sub>2</sub> and CO<sub>2</sub> adsorption, in addition to the potential of such MOFs as heterogeneous catalysts for the solvent-free conversion of epichlorohydrin or epibromohydrin and carbon dioxide into the corresponding cyclic carbonates at 393K and pCO<sub>2</sub> = 5 bar.

The synthesis of the organic linkers has been realized in University of Kyiv, Ukraine, by Prof. Domasevitch's group; PXRD analyses and structures determination were conducted by Prof. Galli's research group in University of Insubria, Como; the catalytic tests were performed by Dr. Rossin's group in CNR Institute of Sesto Fiorentino.

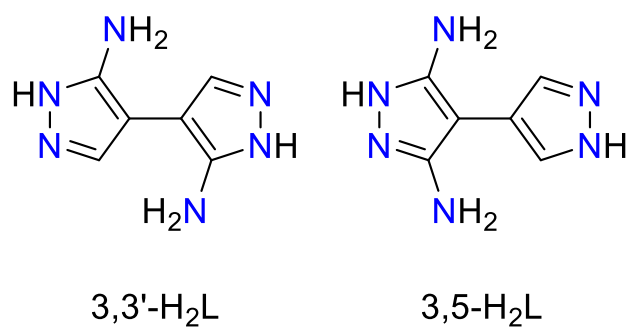


FIGURE 60 Molecular structures of the two isomeric forms 3,3'-diamino-4,4'-bipyrazole (**3,3'-H<sub>2</sub>L**) and 3,5-diamino-4,4'-bipyrazole (**3,5-H<sub>2</sub>L**) employed as linkers for the synthesis of the corresponding MOFs.

## 4.2 Experimental section

### 4.2.1 Material and methods

3,3'-diamino-4,4'-bipyrazole and 3,5-diamino-4,4'-bipyrazole (**3,5-H<sub>2</sub>L**) were synthesized according to the previous literature.<sup>189,190</sup> The syntheses utilized chemicals and reagents that were procured from commercial suppliers, and were used without additional purification. However, for the epoxides used in the catalytic tests, they were distilled before use and stored over 4 Å molecular sieves under nitrogen. IR spectra were recorded from 4000 to 600 cm<sup>-1</sup> with a PerkinElmer Spectrum One System instrument. Thermal analysis (TGA-DTA) was performed with a PerkinElmer STA 6000 Simultaneous Thermal Analyzer. The samples were heated from 303 to 923 K at a heating rate of 10 K min<sup>-1</sup> under a nitrogen flow (20 mL min<sup>-1</sup>). The <sup>1</sup>H NMR spectrum of 3,3'-diamino-4,4'-bipyrazole was obtained in deuterated dimethylsulfoxide ([D<sub>6</sub>]DMSO) on a Bruker Ascend 400 instrument operating at 400 MHz and 298 K. The chemical shifts are reported in parts per million and SiMe<sub>4</sub> was used as internal standard. Elemental analyses (C, H, N %) were performed with a Fisons Instruments 1108 CHNS-O elemental analyzer. Powder X-ray diffraction (PXRD) qualitative analysis was carried out with a Bruker AXS D8 Advance diffractometer, acquiring data at room temperature in the 3–35° 2θ range, with steps of 0.02°, and time per step of 1 s. GC/MS analyses of the reaction mixtures after the catalytic runs were determined on a Shimadzu QP2010S apparatus equipped with a flame ionization detector and a Supelco SPB-1 fused-silica capillary column (30 m length, 0.25 mm internal diameter, 0.25 μm film thickness). For zinc determination, Graphite Furnace Atomic Absorption Spectroscopy (GF-AAS) on a GBC 908AA instrument was performed.

#### 4.2.2 Synthesis of 3,3'-H<sub>2</sub>L

Care must be taken when handling nitro compounds because they are explosive. No hazards have occurred during their synthesis and handling, but it is suggested to wear a face shield in addition to common laboratory protective tools. This family of compounds also exhibit low sensitivity toward impact (30 J), friction (>360 N) and electrostatic discharge (>0.50 J).

3,3'-dinitro-4,4'-bipyrazole (24.64 g, 0.11 mol) was suspended in 2 L of water at 343 K. An aliquot corresponding to 1 mL of a Raney 2800 nickel aqueous slurry was then added, followed by the dropwise addition of an aqueous solution of hydrazine hydrate, obtained by dissolution of such compound (48.5 mL, 1 mol) in 200 mL of water for 4h at 343 K under energetic stirring. Fresh portions (1 mL) of nickel catalyst were systematically added each 1h. After the first 2h, 3,3'-dinitro-4,4'-bipyrazole dissolution was achieved and observable because of the orange coloration of the mixture attributable to nitropyrazolate anion in solution. The reduction reaction was easily monitored by the gradual fading of the solution color over the following 2 h. After the complete addition of hydrazine, the mixture was further stirred for 2 h. Then, it was filtered while hot and the precipitate was washed with 1.5 L of hot water (temperature range: 343–353 K). The colorless filtrates were combined and reduced to 150 mL on a rotary evaporator. Colorless crystals of the product were filtered, washed with small portions of cold water and air-dried. Yield: 17.11 g (95 %). Single crystals suitable for an X-ray diffraction analysis were obtained after recrystallization from water. Elem. anal. calcd. for C<sub>6</sub>H<sub>8</sub>N<sub>6</sub> (MW = 164.2 g mol<sup>-1</sup>): C, 43.89; H, 4.91; N, 51.20 %. Found: C, 43.64; H, 5.03; N, 50.94 %. <sup>1</sup>H NMR (400 MHz, 298 K, [D<sub>6</sub>]DMSO): δ (ppm) = 7.99 (2 H, CH), 7.75 (4 H, NH<sub>2</sub>), 12.80 (2 H, NH).

#### 4.2.3 Synthesis of Zn(3,3'-L)

3,3'-H<sub>2</sub>L (0.164 g, 1 mmol) was dissolved in 15 mL of DMF inside a 50 mL reaction flask equipped with a reflux condenser. After a stirring period of ten minutes, Zn(CH<sub>3</sub>COO)<sub>2</sub>·2H<sub>2</sub>O (0.220 g, 1 mmol) was added to the mixture. The reaction was kept under stirring at 393 K for 3 h and then slowly cooled to room temperature. A white precipitate was obtained, filtered off, washed twice with DMF and dried under vacuum. Yield: 86 %. Elem. anal. calcd. for Zn(3,3'-L)·DMF, C<sub>9</sub>H<sub>13</sub>N<sub>7</sub>OZn (MW = 300.6 g mol<sup>-1</sup>): C, 35.96; H, 4.36; N, 32.61 %. Found: C, 35.79; H, 4.31; N, 32.55 %. IR (ν, cm<sup>-1</sup>): 3388(w), 3322(w) [ν (N-H)], 3097–2926 [ν (C-

H<sub>aromatic</sub>) +  $\nu$  (C-H<sub>aliphatic</sub>), 1662(s) [ $\nu$  (C=O)], 1615(m), 1526(m) [ $\nu$  (C=C) +  $\nu$  (C=N)], 1489(s), 1384(s), 1293(w), 1254(w), 1096(s), 979(s), 660(s), 636(m), 467(s).

#### 4.2.4 Synthesis of Zn(3,5-L)

The synthesis is analogue to the previous one, except for the use of **3,5-H<sub>2</sub>L** (0,164 g, 1 mmol) in place of **3,5-H<sub>2</sub>L**. Yield: 84 %. Elem. anal. calcd. for **Zn(3,5-L)·DMF**, C<sub>9</sub>H<sub>13</sub>N<sub>7</sub>OZn (MW = 300.6 g mol<sup>-1</sup>): C, 35.96; H, 4.36; N, 32.61 %. Found: C, 36.11; H, 4.42; N, 32.57 %. IR ( $\nu$ , cm<sup>-1</sup>): 3324(w) [ $\nu$  (N-H)], 3096–2927 (w) [ $\nu$  (C-H<sub>aromatic</sub>) +  $\nu$  (C-H<sub>aliphatic</sub>)], 1662(s) [ $\nu$  (C=O)], 1615(s), 1514(s) [ $\nu$  (C=C) +  $\nu$  (C=N)], 1436(m), 1383(s), 1256(m), 1133(s), 1095(s), 1010(w), 954(s), 843(m), 754(m), 657(s).

#### 4.2.5 Preparation of [epibromohydrin@Zn(3,3'-L)]

**Zn(3,3'-L)** (60 mg) was thermally activated at 473 K for 12h, at 10<sup>-6</sup> torr, with the aid of a ASAP 2020 porosimeter. The activated MOF was then suspended in dry and degassed epibromohydrin (5 mL) under a nitrogen atmosphere in a Schlenk flask. The suspension was gently stirred and kept at 393 K for 24 h, in order to promote the epoxide diffusion into the MOF cavities. After one day, the flask was brought back to room temperature, the solid was left to decant, and the liquid supernatant removed. [epibromohydrin@Zn(3,3'-L)] was finally recovered in quantitative yield, washed three times with 10 mL of petroleum ether and dried under nitrogen atmosphere.

#### 4.2.6 Powder X-ray diffraction (PXRD) structure determination

About 50 mg of microcrystalline **Zn(3,3'-L)** and [epibromohydrin@Zn(3,3'-L)] were placed in the cavity of a silicon free-background sample-holder 0.2 mm deep (Assing Srl, Monterotondo, Italy) and analyzed by powder X-ray diffraction (PXRD) with a Bruker AXS D8 Advance vertical-scan  $\theta : \theta$  diffractometer, provided with a sealed X-ray tube (Cu K $\alpha$ ,  $\lambda = 1.5418 \text{ \AA}$ ), a Bruker Lynxeye linear position-sensitive detector, a filter of nickel in the diffracted beam and the following optical components: primary beam Soller slits (aperture = 2.5°), fixed divergence slit (aperture = 0.5°), antiscatter slit (aperture = 8 mm). The generator was operated at 40 kV and 40 mA. After preliminary PXRD acquisitions to verify the samples purity and crystallinity as described above, data acquisitions for a deeper data treatment were performed in the  $2\theta$  range 5–105°, with steps of 0.02° and an overall scan time of

about 12 hours. A standard peak search on the **Zn(3,3'-L)** PXRD pattern allowed for the estimation of the maximum positions of the first 20 low-to-medium angle peaks that were analyzed with the software TOPAS-R V3.0<sup>173</sup> through the Singular Value Decomposition algorithm,<sup>172</sup> to retrieve the unit cell parameters. The space group was assigned based on the systematic absences. The space group and unit cell parameters were then confirmed by a whole powder pattern refinement carried out with TOPAS-R V3.0 employing the Le Bail method. Based on the space group and unit cell values, **Zn(3,3'-L)** is isostructural with Zn(BPZNO<sub>2</sub>), where H<sub>2</sub>BPZNO<sub>2</sub> is 3-nitro-4,4'-bipyrazole,<sup>191</sup> so that the crystal structure characterization was carried out only for [**epibromohydrin@Zn(3,3'-L)**]. The latter shares the same space group and unit cell parameters of the parent **Zn(3,3'-L)** MOF. Hence, the structure refinement of the framework was achieved with TOPAS-R V3.0 applying the Rietveld method starting from the crystal structure of Zn(BPZNO<sub>2</sub>). Then, the position and orientation of epibromohydrin were retrieved through the Simulated Annealing approach.<sup>174</sup> The crystallographically independent portion of the ligand and epibromohydrin were described through a rigid body built up using the z-matrix formalism, initially setting bond lengths and angles to average values. The center of mass of the ligand was located on a 2/m symmetry element, occurrence which implies that the two -NH<sub>2</sub> groups and the two hydrogen atoms share the four crystallographically equivalent positions (the four carbon atoms) with 50 % probability each. The ligand orientation was allowed to vary along the crystallographic c-axis. During the final Rietveld refinement stages, pyrazole C-C and C-N bond lengths were refined in restrained ranges (1.34–1.38 Å), retrieved with a search in the Cambridge Structural Database (v. 2020) for room-temperature crystal structures containing the M(pyrazolate) (M = 3d transition metal ion) moiety. The torsion angle among the two pyrazolate rings was free to refine, but no sensible variation from planarity or significant lowering of the figures of merit were observed, so that the ligand was eventually kept planar. The background curve was modelled using a polynomial function of the Chebyshev-type. An isotropic thermal factor [Biso(M)] was refined for the metal ion, while for the ligand and epoxide atoms the isotropic thermal factor was calculated as Biso(L) = Biso(M) + 2.0 (Å<sup>2</sup>). The peak profile was described using the Fundamental Parameters Approach.<sup>176</sup> The anisotropic peak broadening was described using second-order Lorentzian and fourth-order Gaussian spherical harmonics, modulating their contribution based on the reflections Miller indices.



Crystal data for [epibromohydrin@Zn(3,3'-L)], Zn(3,3'-L)·0.7 (C<sub>3</sub>H<sub>5</sub>OBr): C<sub>8.1</sub>H<sub>9.5</sub>Br<sub>0.7</sub>N<sub>6</sub>O<sub>0.7</sub>Zn, MW = 323.4 g mol<sup>-1</sup>, orthorhombic, Cccm, a = 12.566(2) Å, b = 12.681(2) Å, c = 7.2365(7) Å, V = 1153.2(3) Å<sup>3</sup>, Z = 16, Z' = 4, ρ = 1.855 g cm<sup>-3</sup>, F(000) = 629.2, R<sub>Bragg</sub> = 0.007, R<sub>p</sub> = 0.020 and R<sub>wp</sub> = 0.025, for 4851 data and 76 parameters in the 8.0–105.0° (2θ) range. CCDC Deposition number: 2045969.

#### 4.2.7 Variable-temperature powder X-ray diffraction

A variable-temperature PXRD experiment was performed with the diffractometer described above on about 20 mg sample of Zn(3,3'-L) heating in air with a custom-made sample heater (Officina Elettrotecnica di Tenno, Ponte Arche, Italy), in the temperature range 303–763 K with steps of 20 K. At each step, the data were acquired in isothermal conditions in the 2θ range 8.5–27.5°, with steps of 0.02° and a time per step of 1 s. The persistence of the room-temperature porous framework was assessed through whole powder pattern refinements performed with the Le Bail method, as implemented in TOPAS-R V3.0.

#### 4.2.8 Water vapor stability test

After activation (423 K, 10<sup>-3</sup> bar, 24 h) to remove the guest solvent and preliminary PXRD data acquisitions, about 10 mg samples of Zn(3,3'-L) and Zn(3,5-L), left deposited on the PXRD aluminum sample-holders, were introduced into an air-tight cell saturated with moisture. Their behavior towards water vapor was monitored at given time intervals by measuring PXRD diffraction patterns with the same conditions applied for the preliminary acquisitions. All the acquired data were treated through a whole powder pattern refinement with the Le Bail method using the software TOPAS-R V3.0.

#### 4.2.9 N<sub>2</sub> and CO<sub>2</sub> adsorption and BET Surface Area determination

Both MOFs (about 40 mg) were activated at 473 K under high vacuum (10<sup>-6</sup> torr) for 12 h before each measurement. The Brunauer–Emmett–Teller (BET) specific surface area (SSA) and porosity were estimated through volumetric N<sub>2</sub> adsorption at 77 K with an ASAP 2020 (Micromeritics) instrument. For the BET specific surface area calculation, the 0.01–0.1 p/p° pressure range of the isotherm was used for data fitting to satisfy all the Rouquerol consistency criteria (read the paragraph “Determination of MOFs porosity”, Chapter 1). The materials porosity was determined based on the BJH method (Halsey thickness equation) for

the mesopores and with the non-local density functional theory method (Tarazona NLDFT—cylinder-like pore shape typical of inorganic oxide materials) for the micropores. CO<sub>2</sub> and N<sub>2</sub> adsorption isotherms were also recorded at 273 and 298 K at a maximum pressure of 1.2 bar. The isosteric heat of adsorption (Q<sub>st</sub>) was calculated from the CO<sub>2</sub> isotherms measured at 273 and 298 K according to the following variant of the Clausius–Clapeyron equation:

$$\ln\left(\frac{p_1}{p_2}\right) = Q_{st} \frac{T_2 - T_1}{R \cdot T_1 \cdot T_2}$$

where P<sub>n</sub> (n = 1 or 2) is the pressure value for isotherm n; T<sub>n</sub> (n = 1 or 2) is the temperature value for isotherm n; R is the gas constant (8.315 J K<sup>-1</sup> mol<sup>-1</sup>). The CO<sub>2</sub>/N<sub>2</sub> selectivity at 298 K was calculated based on the Henry method as the ratio of the initial slopes of the adsorption isotherms. The IAST selectivity for an equimolar CO<sub>2</sub>/N<sub>2</sub> mixture at a total pressure of 1 bar was determined as the ratio of the (adsorbed) molar fractions of the two gases<sup>192</sup> as derived from the application of the free software pyIAST (<https://github.com/CorySimon/pyIAST>) to the experimental N<sub>2</sub> and CO<sub>2</sub> isotherms of **Zn(3,3'-L)** and **Zn(3,5-L)** collected at 298 K. A BET (CO<sub>2</sub>) and a Henry (N<sub>2</sub>) model were employed for the isotherms fitting, with root mean square deviations = 0.0040 (K<sub>a</sub> = 4.40; K<sub>b</sub> = 0.13; M = 4.12)/0.0013 (K<sub>H</sub> = 0.602) and 0.0039 (K<sub>a</sub> = 4.26; K<sub>b</sub> = 0.13; M = 3.80)/0.0021 (K<sub>H</sub> = 0.344) for **Zn(3,3'-L)** and **Zn(3,5-L)**, respectively. For a detailed explanation of these parameters, see the pyIAST webpage and documentation.

#### 4.2.10 Catalytic CO<sub>2</sub> epoxidation with **Zn(3,3'-L)** and **Zn(3,5-L)**

For a comparative analysis with Zn(BPZNH<sub>2</sub>),<sup>112</sup> the reaction temperature and pressure were kept identical to our previous trials. The two MOF catalysts were activated at 473 K under high-vacuum (10<sup>-6</sup> torr) for 12 h before running the catalytic tests, keeping them under N<sub>2</sub> atmosphere after activation. The MOF catalyst (0.05 mmol, 11.4 mg) and the epoxide substrate (10 mmol, about 800 μL for epichlorohydrin, MW = 92.52 g mol<sup>-1</sup> and about 860 μL for epibromohydrin, MW = 136.98 g mol<sup>-1</sup>) were placed in a Teflon sample holder inside a stainless-steel reactor under an inert atmosphere. The reactor was then pressurized with 5 bar CO<sub>2</sub> and kept at 393 K for 24 h under stirring, in a closed system. The limiting reagent was CO<sub>2</sub> (about 7 mmol against 10 mmol of epoxide), because of the reactor volume

limitations. At the end of the reaction, the reactor was cooled in an ice/water bath and bis(2-chloroethyl) ether (10 mmol) was added to the mixture as internal standard. The as-obtained suspension was finally filtered over a Celite pad and analyzed by gas chromatography. For the recycling tests, after the first catalytic run the supernatant liquid was carefully removed under an inert atmosphere. The solid catalyst was washed with dry and degassed acetone (3×5 mL) and it was then dried under vacuum for 1 h to remove all volatile compounds before re-using it for further catalytic cycles. The amount of zinc leached in solution after catalysis was determined by Graphite Furnace Atomic Absorption Spectroscopy (GF-AAS) on a GBC 908AA instrument.

## 4.3 Results and discussions

### 4.3.1 Synthetic procedures

**3,3'-H<sub>2</sub>L** was obtained in high yield similarly to the **3,5-H<sub>2</sub>L** linker already reported in the literature,<sup>190</sup> with some differences described here. The reaction involves two synthetic steps: the dinitration of 4,4'-bipyrazole and the subsequent catalytic reduction of the 3,3'-dinitro-4,4'-bipyrazole intermediate to the corresponding diamino compound. It is paramount to take into account that the dinitration pathways are strongly affected by the acidity of the reaction medium. This is due to the low basicity of mononitropyrazolyl intermediate which is more reactive than the pyrazolium cation and for this reason the conventional dinitration of 4,4'-bipyrazole in HNO<sub>3</sub>/H<sub>2</sub>SO<sub>4</sub> mixtures leads to the substitution at the same ring yielding the 3,5-dinitro isomer only. A less acidic medium (80 % v/v phosphoric acid as high-boiling inert solvent) promotes on the other hand the substitution on the free base 4,4'-bipyrazole, ensuring that each pyrazole ring is mononitrated. At this point, 3,3'-dinitro-4,4'-bipyrazole can be reduced to 3,3'-diamino-4,4'-bipyrazole using hydrazine hydrate in the presence of a Raney 2800 nickel aqueous slurry. The solvent of this second step is water differently from the reduction of 3,5-dinitro-4,4'-bipyrazole which has been conducted in a mixture 96% EtOH and H<sub>2</sub>O. **Figure 61** represents the two different routes that from simple bipyrazole lead to the formation of the two diamino isomers **3,3'-H<sub>2</sub>L** and **3,5-H<sub>2</sub>L**.

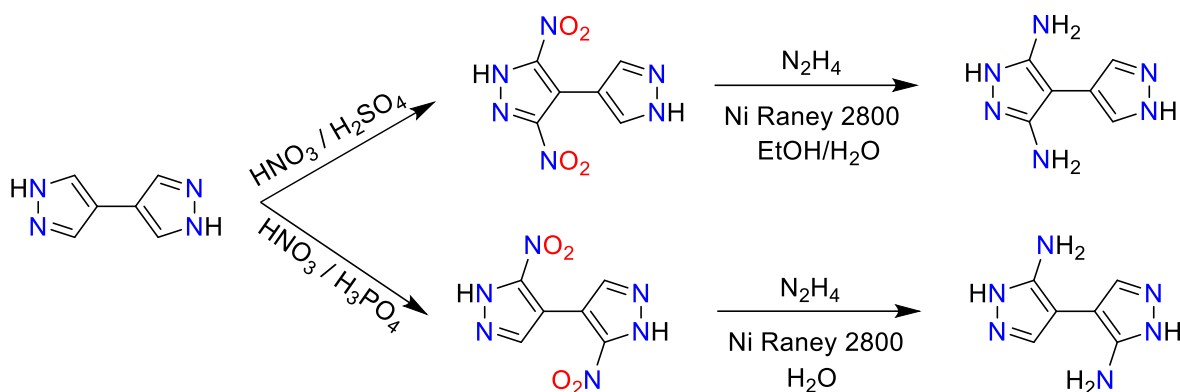


FIGURE 61 Selective dinitration pathways of 4,4'-bipyrazole to yield either 3,5-dinitro-4,4'-bipyrazole or 3,3'-dinitro-4,4'-bipyrazole, with subsequent reduction to 3,3'-H<sub>2</sub>L and 3,5-H<sub>2</sub>L.

Zn(3,3'-L) and Zn(3,5-L) were synthesized in DMF at 393 K following the method previously reported for Zn(3,5-L).<sup>190</sup> In this case, the reaction time was reduced from 8 to 3 hours, maintaining a comparable yield (83 vs. 84 % in this work).

#### 4.3.2 Infrared characterization

IR spectra were registered in the range 4000–400 cm<sup>-1</sup> and are reported in Figure 62. In both MOFs, it is possible to distinguish a broad peak corresponding to the stretching vibration frequency of the two diamino groups at 3324 cm<sup>-1</sup> for Zn(3,5-L) and 3322 cm<sup>-1</sup> for Zn(3,3'-L). In the range 3097–2926 cm<sup>-1</sup> the stretching frequencies attributable to aromatic and aliphatic C-H are found. The strong bands at 1662 cm<sup>-1</sup> reveal the presence of clathrate solvent molecules, due to the stretching mode of the carbonyl group in DMF. Finally, at 1514 and 1526 cm<sup>-1</sup> for Zn(3,5-L) and Zn(3,3'-L) respectively it is possible to observe the stretching vibration frequency of C=C and C=N bonds of the pyrazole rings.

#### 4.3.3 Thermal behavior

The thermogravimetric analysis was performed on Zn(3,3'-L) and it is shown in Figure 63a. However, thermal behavior of Zn(3,5-L) already reported in literature is here commented to make a comparison between the two MOFs. Both zinc(II) MOFs show initially a weight loss of ≈24 % for Zn(3,5-L) and ≈22 % for Zn(3,3'-L) below 610K and 583 K respectively, corresponding to the loss of 1.0 or 0.85 moles of clathrate DMF solvent per formula unit (calculated weight loss = 24.3 % and 22.6 %). After the removal of DMF molecules inside MOFs cavities, the activated zinc(II) MOFs show the same decomposition temperature (≈ 723K), suggesting that the two amino substituents exert a similar action on the strength of the

Zn–N coordinative bonds, independently from their position on the bipyrazolate ring. It should also be taken into account that the decomposition temperatures are slightly higher than mono-decorated Zn(BPZNH<sub>2</sub>),<sup>112</sup> which is 703 K. What has been just said reveal a stabilizing effect of the amino groups on the metal-pyrazolate bond. The variable-temperature PXRD experiment (**Figure 63b**) performed on Zn(3,3'-L), in addition, further confirmed its elevated thermal stability, maintaining the room-temperature detected crystal structure up to 763 K, the highest temperature the heating chamber can achieve.

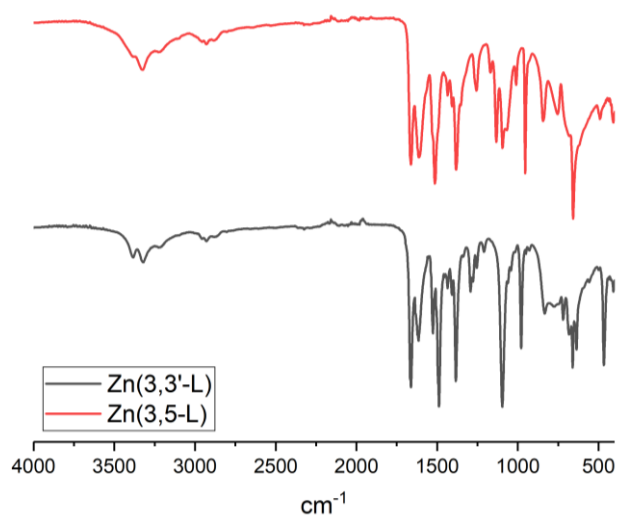


FIGURE 62 IR spectra of Zn(3,3'-L) and Zn(3,5-L).

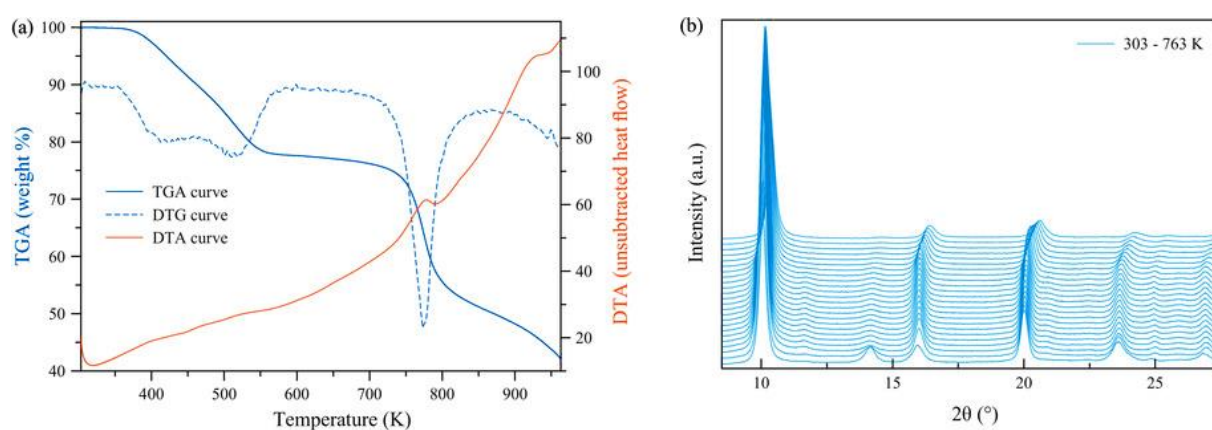


FIGURE 63 a) TGA (light blue), DTG (dotted, light blue) and DTA (orange) profile of Zn(3,3'-L); b) Variable-temperature PXRD analysis on Zn(3,3'-L) in the temperature range 303-763 K.

#### 4.3.4 Crystal structure of 3,3'-H<sub>2</sub>L and Zn(3,3'-L)

3,3'-H<sub>2</sub>L crystallizes in the monoclinic space group P2<sub>1</sub>/c and its structure is shown in **Figure 64**. The asymmetric unit contains half of a molecule, lying about an inversion center. For this

reason, the thermodynamically favored conformation for the free linker is the anti-relative disposition of the two amino groups. The presence of N-H...N hydrogen bonds attributable to the pyrazole N1-H and N2 sites as hydrogen donors and acceptors generate a supramolecular plane square net parallel to the ab plane, in which each bipyrazole molecule is a four-connected net node. In this case, the substitution of the hydrogens in position 3 of the pyrazole rings with amino groups introduce further hydrogen bonds, eliminating the weak C-H... $\pi$  and  $\pi$ ... $\pi$  interactions present in the crystal structure of unsubstituted 4,4'-bipyrazole.<sup>193</sup> Pyrazole N2 atom serves as double acceptor, by supporting also the N3-H...N2 hydrogen bond, which adds the N1-H...N2 hydrogen bond and interconnects the supramolecular layers. This type of secondary interactions is directional. The second kind of non-bonding interaction involving the amino groups [N3-H... $\pi$  interactions] are intra-layer and assemble the molecules into strips along the crystallographic b-axis, as reported for the crystal structure of 3-amino-4,4'-bipyrazole.

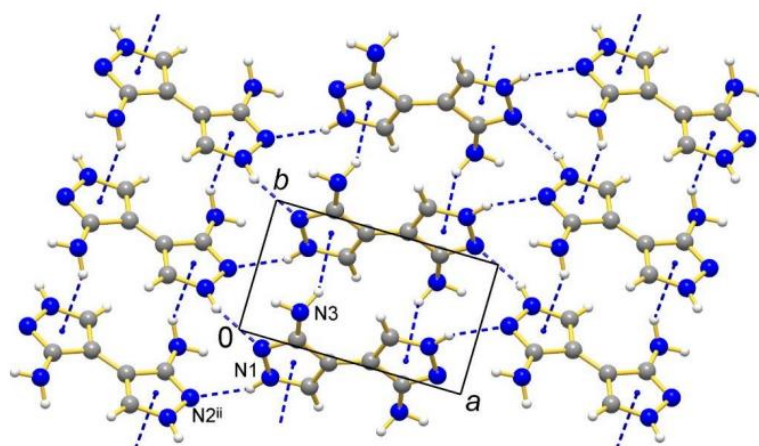


FIGURE 64 *Crystal structure of the linker 3,3'-H<sub>2</sub>L. Hydrogen bonds are highlighted with blue dashes.*

The crystal structure of **Zn(3,3'-L)** and [**epibromohydrin@Zn(3,3'-L)**] has been subsequently determined. This MOF crystallizes in the orthorhombic space group *Cccm* and shares the same structural motif of other Zn bipyrazolate MOFs known from the literature like the monoamino-tagged analogue **Zn(BPZNH<sub>2</sub>)**,<sup>112</sup> the isomeric **Zn(3,5-L)**,<sup>190</sup> the MIXMOF **Zn<sub>2</sub>(BPZ)(BPZNH<sub>2</sub>)**<sup>194</sup> and the longer-linker analogue **Zn(BDPNH<sub>2</sub>)** (**H<sub>2</sub>BDPNH<sub>2</sub>** = 2-amino-1,4-bis(1H-pyrazol-4-yl)benzene).<sup>113</sup> Tetrahedral ZnN<sub>4</sub> nodes and exo-tetradentate linkers determine the formation of a 3D (4,4)-connected network with **sra** network topology,<sup>195</sup> with 1D square channels running along the [001] crystallographic direction and hosting epibromohydrin molecules. **Figure 65** show the MOF crystal structure and the disposition of

epibromohydrin molecule inside the cavities. N–H···Br and N–H···O nonbonding interactions between the amino groups and the guest epoxide molecules are present [d(N···Br) and d(N···O) = 3.03 and 3.02 Å, respectively]. Main bond distances and angles: Zn–N, 2.028(2) Å; Zn···Zn, 3.6182(7) Å; N–Zn–N, 112.34(7)–120.4(4)°. To the best of our knowledge, this kind of structural characterization is rare and unprecedented for halogenated epoxides. The few literature cases reported so far concern with the structure determination of propylene<sup>196</sup> or styrene oxide<sup>197,198</sup> entrapped in MOF cavities.

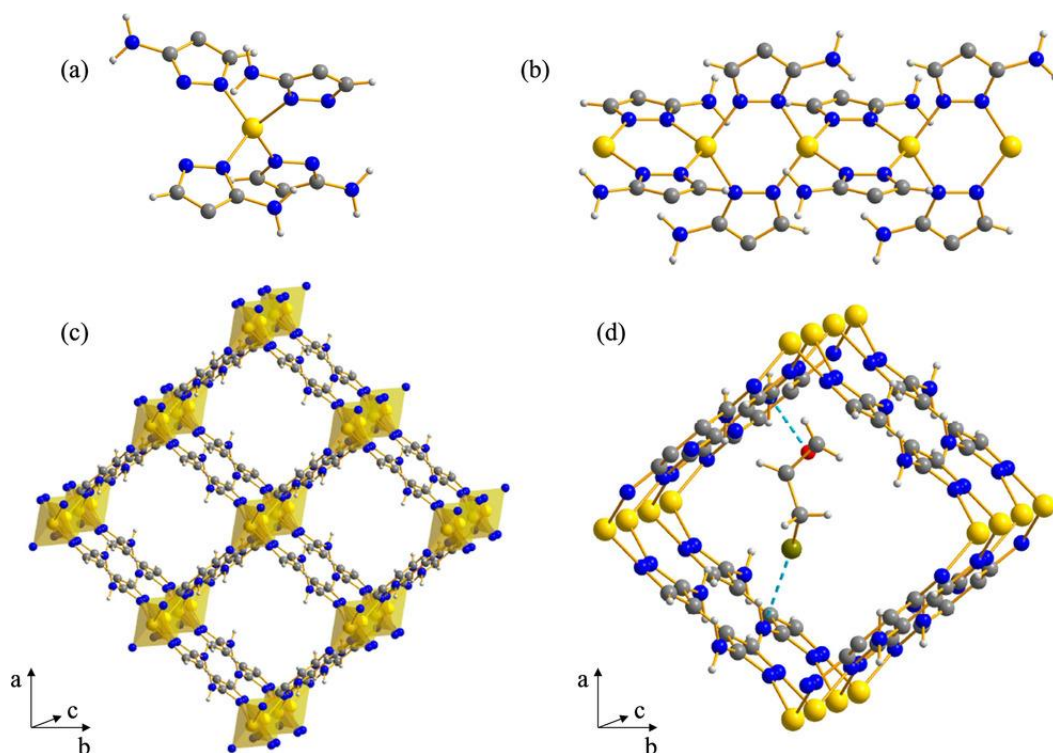


FIGURE 65 Representation of the crystal structure of **Zn(3,3'-L)** and **[epibromohydrin@Zn(3,3'-L)]**: (a) the tetrahedral coordination geometry of the ZnN<sub>4</sub> node; (b) the 1D chain running along the crystallographic c-axis; (c) the packing, viewed in perspective along the crystallographic c-axis. The epibromohydrin molecules have been omitted for sake of clarity. (d) A guest epoxide molecule in the 1D channel. Carbon (gray), hydrogen (light grey), bromine (brown), nitrogen (blue), oxygen (red) and zinc (yellow) atoms are indicated. The N–H···Br and N–H···O interactions are illustrated with cyan dashed lines.

#### 4.3.5 N<sub>2</sub> adsorption and BET Surface Area determination

The textural properties of the two isomeric MOFs were investigated through N<sub>2</sub> adsorption at 77 K on activated samples. As displayed in **Figure 66a**, the two zinc(II) MOFs show a type IV isotherm, peculiar of micro-mesoporous materials. They have comparable BET areas (463 and 504 m<sup>2</sup>g<sup>-1</sup> for **Zn(3,3'-L)** and **Zn(3,5-L)** respectively) and also similar to those measured for Zn(BPZNH<sub>2</sub>) (395 m<sup>2</sup>g<sup>-1</sup>) and for the MIXMOF Zn<sub>2</sub>(BPZ)(BPZNH<sub>2</sub>) (502

$\text{m}^2\text{g}^{-1}$ ). The t-plot analysis esteems the microporosity percentage and in this case that the main contribution to the total surface area is due to micropores for both MOFs: 77% and 57% for **Zn(3,3'-L)** and **Zn(3,5-L)**, respectively). However, a mesoporous component (mesopores can be seen as interparticle voids among the crystallites) is also evident in both MOFs, as witnessed by a certain adsorption at relative pressures higher than  $p/p^\circ \approx 0.1$  and the presence of hysteresis loops at high  $p/p^\circ$ . In **Zn(3,3'-L)**, the micropore size estimated from the NLDFT analysis (Tarazona approximation with cylindrical pore shape) is 13 Å, in line with the Zn···Zn distance observed in the crystal structure between opposite vertices of the square channels, which is 13.2 Å. The mesopore size was calculated through the BJH model applied to the desorption branch of the isotherm and is approximately 34 nm. As expected, in **Zn(3,5-L)**, the micropore size is very similar to that of **Zn(3,3'-L)** (1.2 nm) while the mesopore size is 13 nm. The total pore volume is 0.53 and  $0.47\text{ cm}^3\text{ g}^{-1}$  for **Zn(3,3'-L)** and **Zn(3,5-L)**, respectively.

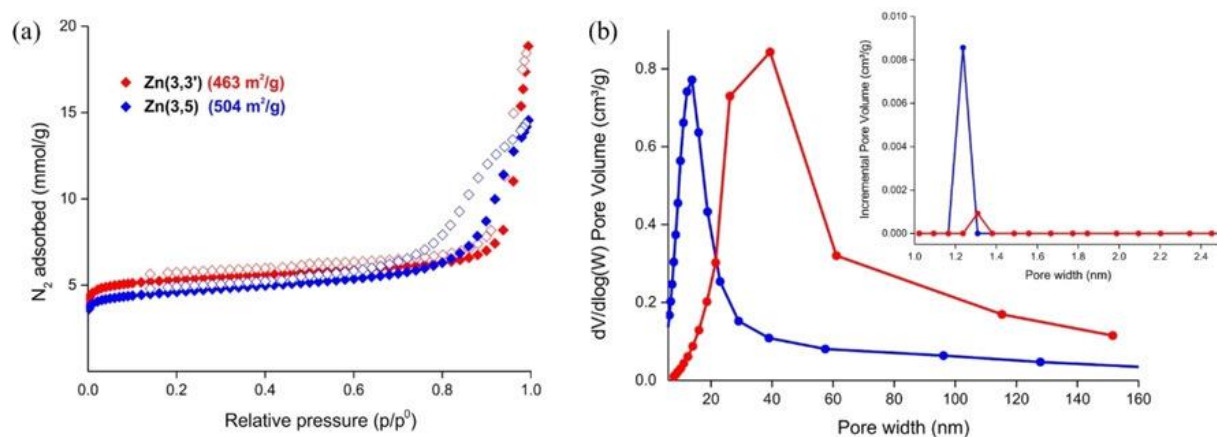


FIGURE 66 (a)  $N_2$  (77 K) adsorption isotherms of **Zn(3,3'-L)** (red diamonds) and **Zn(3,5-L)** (blue diamonds) and BET Surface Area values for both. Empty symbols represent the desorption branches. (b) BJH mesopore size distribution curves for **Zn(3,3'-L)** (red circles) and **Zn(3,5-L)** (blue circles). Inset: NLDFT micropore size distribution curves.

#### 4.3.6 $\text{CO}_2$ adsorption at 273 and 298 K

Before evaluating the catalytic activity of **Zn(3,3'-L)** and **Zn(3,5-L)** in the conversion of carbon dioxide into cyclic carbonates, the  $\text{CO}_2$  adsorption of the two MOFs was measured with the aid of an ASAP 2020 porosimeter at  $T = 273$  and 298 K and  $p_{\text{CO}_2}$  up to 1.2 bar. The  $\text{CO}_2$  adsorption isotherms are reported in **Figure 67**. The amount of gas stored by **Zn(3,3'-L)** at 273 K and 1 bar is  $4.5\text{ mmol g}^{-1}$  (19.7 wt. %  $\text{CO}_2$ ), whereas **Zn(3,5-L)** captures  $4.4\text{ mmol g}^{-1}$  (19.3 wt. %  $\text{CO}_2$ ), under the same conditions. As a result, it is conceivable to



state that the influence of the amino groups disposition in the organic linker on the carbon dioxide adsorption is negligible. In addition, the adsorption capacity of the two MOFs is slightly lower than mono(amino) analogue Zn(BPZNH<sub>2</sub>) (21.0 wt. % CO<sub>2</sub>, 4.8 mmol g<sup>-1</sup>) and of the MIXMOF Zn<sub>2</sub>(BPZ)(BPZNH<sub>2</sub>) (22.3 wt. % CO<sub>2</sub>, 5.1 mmol g<sup>-1</sup>), but higher than the value encountered for the longer analogue Zn(BDPNH<sub>2</sub>) (≈11 wt. % CO<sub>2</sub>, 2.5 mmol g<sup>-1</sup> at T = 273 K). This trend would indicate that although the introduction of one amino group for each linker is beneficial for CO<sub>2</sub> adsorption amount, the presence of two groups is not, probably because of the formation of more N-H...N weak interactions that reduce the affinity for CO<sub>2</sub> and/or because of greater steric hindrance generated by more substituents in the cavities.

In addition, the values of CO<sub>2</sub> adsorbed for **Zn(3,3'-L)** and **Zn(3,5-L)** are comparable with other amino-functionalized MOFs, such as MIL-101(Cr)-NH<sub>2</sub> which adsorbs 5.08 mmol g<sup>-1</sup> of CO<sub>2</sub> at 273 K, corresponding to 22.2 wt. %.<sup>199</sup>

In order to establish the strength of the adsorbent-adsorbate (host-guest) interactions in **Zn(3,3'-L)** and **Zn(3,5-L)**, the isosteric heat of adsorption (Q<sub>st</sub>) of CO<sub>2</sub> was determined from the CO<sub>2</sub> isotherms recorded at 273 and 298 K applying a variant of the Clausius–Clapeyron equation. The isosteric heat of adsorption represents the interaction strength between CO<sub>2</sub> and the cavities at zero coverage. The values of 24.8 and 25.4 kJ mol<sup>-1</sup> observed for **Zn(3,3'-L)** and **Zn(3,5-L)**, respectively, are higher than that of their untagged isostructural analogue [Zn(BPZ); Q<sub>st</sub> = 23.7 kJ mol<sup>-1</sup>] but lower than the values registered for Zn(BPZNH<sub>2</sub>) (Q<sub>st</sub> = 35.6 kJ mol<sup>-1</sup>), Zn<sub>2</sub>(BPZ)(BPZNH<sub>2</sub>) (Q<sub>st</sub> = 30.8 kJ mol<sup>-1</sup>) and Zn(BDPNH<sub>2</sub>) (Q<sub>st</sub> = 28.1 kJ mol<sup>-1</sup>). This further demonstrates that less amino groups assure a more efficient thermodynamic response towards guest CO<sub>2</sub> molecules. The values of Q<sub>st</sub> are in agreement with the typical heat of adsorptions registered for physisorption: 25-50 KJ/mol.<sup>200</sup> Lower values indicate systems in which the adsorbent/adsorbate interaction is negligible. On the other hand, a too strong interaction (> 50 KJ /mol) with CO<sub>2</sub> is not useful for the purpose of recycling the adsorbent material for multiple catalytic cycles because it becomes more expensive to regenerate it.

Lastly, the CO<sub>2</sub>/N<sub>2</sub> adsorption selectivity was calculated using the ratio of the initial slopes in the Henry region of the two different gases adsorption isotherms measured at 298 K. For what concerns selectivity, it seems that two tags are better than one: **Zn(3,3'-L)** and **Zn(3,5-L)** exhibit Henry CO<sub>2</sub>/N<sub>2</sub> selectivity of 20 and 32, respectively, higher than that measured for their mono(amino) analogue Zn(BPZNH<sub>2</sub>) and for the MIXMOF Zn<sub>2</sub>(BPZ)(BPZNH<sub>2</sub>). The

IAST  $\text{CO}_2/\text{N}_2$  selectivity values for an equimolar mixture measured at  $p = 1$  bar are 16 and 24 for  $\text{Zn}(3,3'\text{-L})$  and  $\text{Zn}(3,5\text{-L})$ , respectively. The better selectivity provided by the presence of two amino groups per linker can be justified by a larger bulk that causes  $\text{N}_2$  to have more difficulty than  $\text{CO}_2$  in entering the MOFs cavities ( $\text{N}_2$  has a larger kinetic radius than  $\text{CO}_2$ , 3.61 vs. 3.30 Å, **Figure 30**).

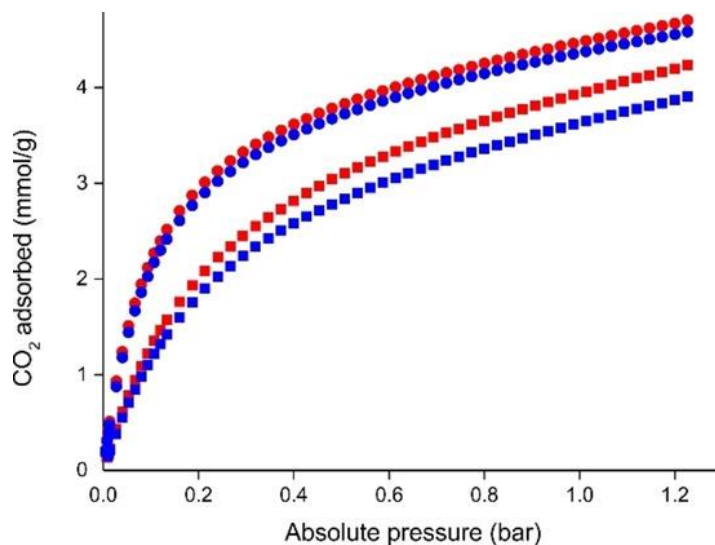


FIGURE 67  $\text{CO}_2$  adsorption isotherms of  $\text{Zn}(3,3'\text{-L})$  (red) and  $\text{Zn}(3,5\text{-L})$  (blue) at 273 K (circles) and 298 K (squares).

#### 4.3.7 $\text{Zn}(3,3'\text{-L})$ and $\text{Zn}(3,5\text{-L})$ catalytic activity in $\text{CO}_2$ cycloaddition to halogenated epoxides

The water stability of the two zinc(II) derivatives was tested through PXRD analyses on the samples kept into a water-vapor saturated environment for 120 days, revealing no phase transitions and no loss of crystallinity for both samples in such period (**Figure 68**).

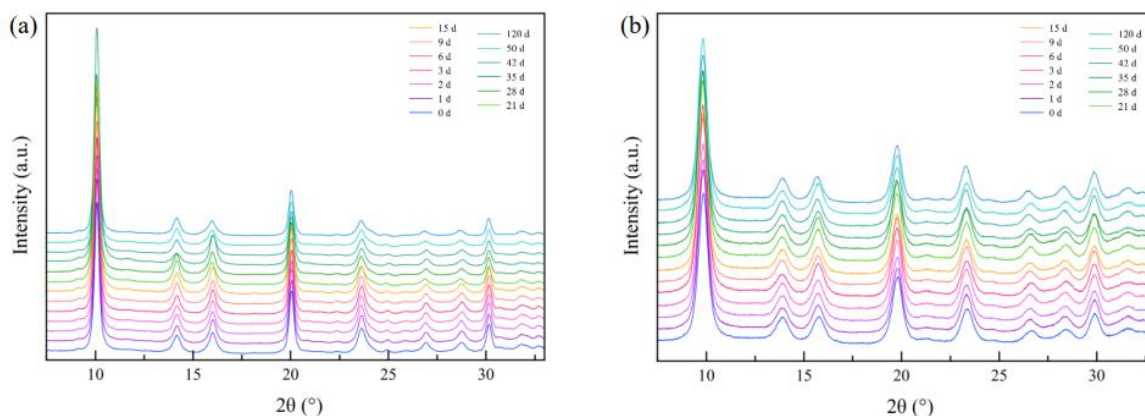


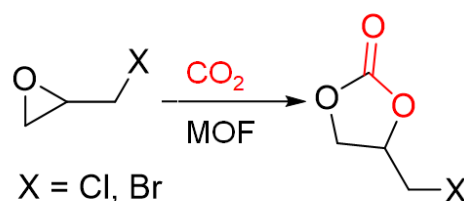
FIGURE 68 Water stability tests performed on  $\text{Zn}(3,3'\text{-L})$  and  $\text{Zn}(3,5\text{-L})$  for 120 days.

The MOFs were thermally activated and subsequently tested as heterogeneous catalysts for

the CO<sub>2</sub> addition to halogenated epoxides (e.g. epichlorohydrin and epibromohydrin) to yield the corresponding cyclic carbonates in solvent-free conditions, following the same procedure adopted for Zn(BPZNH<sub>2</sub>), as depicted in **Figure 69**. No co-catalysts were added in this catalysis to further activate the two epoxides. This makes the catalytic process greener and more sustainable and at the same time it allows a better understanding of the reaction mechanism in the absence of free halide ions, which are known as promoters of CO<sub>2</sub> cycloaddition with epoxides. Catalytic tests are here resumed:

Entry	Catalyst	X	Yield [%]	TOF <sup>[a]</sup>	Ref.
1	Zn(3,3'-L)	Cl	49	4.0	this work
2	Zn(3,5-L)	Cl	64	5.3	
3	Zn(3,3'-L)	Br	41	3.4	
4	Zn(3,5-L)	Br	49	4.0	
5	Zn(BPZNH <sub>2</sub> )	Cl	32	2.6	112

Reaction conditions: mmol catalyst = 0.05; mmol epichlorohydrin or epibromohydrin = 10; pCO<sub>2</sub> = 5 bar; T = 393 K; reaction time = 24 h. [a] Calculated as (mmol carbonate)·(mmol Zn)<sup>-1</sup> h<sup>-1</sup>.



**FIGURE 69** Scheme of carbon dioxide cycloaddition with epichlorohydrin or epibromohydrin to yield the corresponding cyclic carbonate.

Tests reveal that the presence of two amino groups improves CO<sub>2</sub> conversion compared with the mono(amino) analogue Zn(BPZNH<sub>2</sub>) (Entry 5), regardless of the position of the two amino groups and the nature of the epihalohydrin. This proves the mechanism previously hypothesized for Zn(BPZNH<sub>2</sub>) and shown in **Figure 70**, revealing an effective role to the aniline nitrogen at the organic linkers in MOF's cavities.

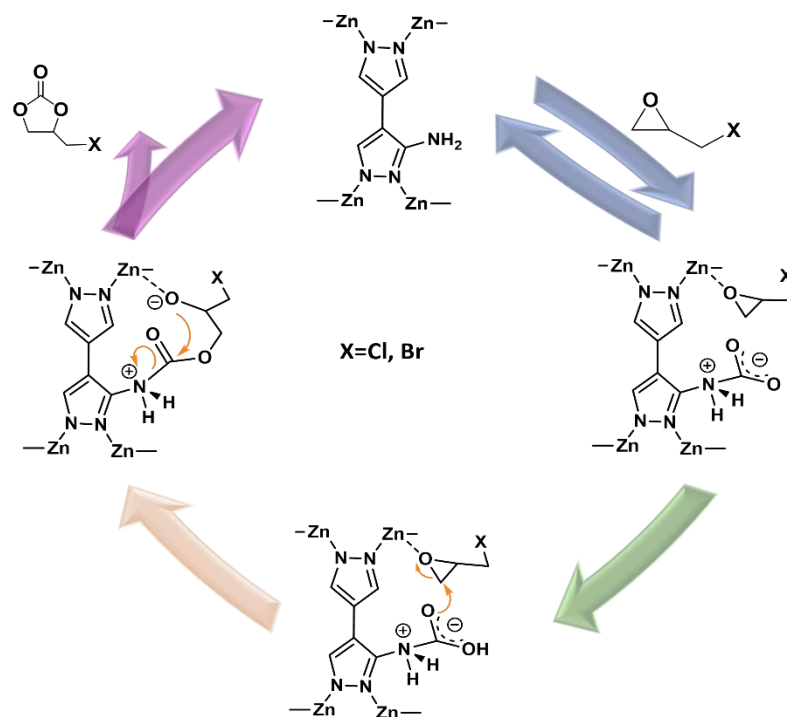


FIGURE 70 Proposed reaction mechanism of  $\text{CO}_2$  conversion in cyclic carbonates in the presence of halogenated epoxides, catalyzed by  $\text{Zn}(\text{BPZNH}_2)$ .

In general,  $\text{Zn}(3,5\text{-L})$  is more active than  $\text{Zn}(3,3'\text{-L})$  both for epichlorohydrin and epibromohydrin conversion. Such different trend can be affected by the two amino groups relative disposition in the MOFs pores.  $3,3'\text{-H}_2\text{L}$  can establish intramolecular  $\text{NH}_2 \cdots \text{NH}_2$  hydrogen bonds (2.5–3.2 Å according to the crystal structure) when the two tags are disposed in *syn*-orientation (even if that is the less probable as *anti*-conformation is the thermodynamically favored) and this could partially inhibit the interaction with  $\text{CO}_2$  molecules and consequently the catalytic activity. Dealing with the same MOF catalyst, the conversion of epichlorohydrin is higher than the conversion of epibromohydrin (Entries 1 vs. 3 and 2 vs. 4). This is due to the higher electronegativity of chlorine which is responsible for stronger hydrogen bonding interactions with the amino groups and its harder nature compared to bromine towards electrophilic sites such as  $\text{Zn}(\text{II})$ .

According to the crystal structure solved for [ $\text{epibromohydrin}@\text{Zn}(3,3'\text{-L})$ ], there is no interaction between the epoxide and the metal node. Nevertheless, one could speculate that in reality there are defects in the crystal structure, which could relate to the lack of some organic linkers and thus in the coordination of the zinc(II) ion to acetate or  $-\text{OH}$  groups due to hydrolysis, as already verified in the literature for other zinc(II) MOFs.<sup>201,202</sup> Such defects could constitute an additional site of MOF activity toward  $\text{CO}_2$  conversion. In addition, the

ability of the zinc ion to expand its coordination from 4 to 5 or 6 in the catalytic processes is certainly the basis of the activity of MOFs.

The recyclability of the catalyst **Zn(3,3-L)** has been defined. The activity is retained for almost three cycles with a percentage of activity equal to 92 and 90% for the second and the third runs respectively, normalizing the first cycle at 100%. Leaching of the metal into the reaction supernatant was directly quantified thanks to GF-AAS analysis after each catalytic cycle and it is negligible in all cases.

Further confirmation of the stability of **Zn(3,3-L)** MOF as a catalyst is provided by the PXRD profile after a catalytic run with epibromohydrin. As can be seen in **Figure 71**, no significant changes are depictable before and after the catalysis.

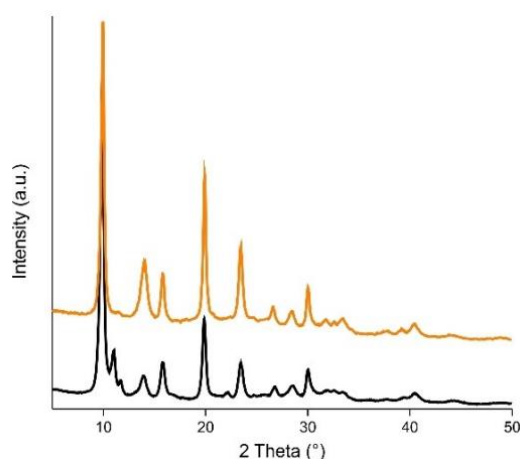


FIGURE 71 PXRD profile of **Zn(3,3'-L)** before (black) and after (orange) a catalytic run.

## 4.4 Conclusions

The catalytic activity of amino-decorated bipyrazolate zinc(II) MOFs in CO<sub>2</sub> epoxidation has been improved by introducing two -NH<sub>2</sub> groups on the bipyrazolate linker. The newly formed isomeric bis(amino)-tagged bipyrazolate MOFs, **Zn(3,3'-L)** and **Zn(3,5-L)**, showed excellent performance in converting halogenated epoxides epichlorohydrin and epibromohydrin into their respective cyclic carbonates under solvent-free and co-catalyst-free conditions. The maximum conversion achieved with the bis(amino)-tagged MOFs was 64%, which is twice the conversion rate achieved with their mono(amino) analogue Zn(BPZNH<sub>2</sub>). Despite this improvement in catalytic activity, the CO<sub>2</sub> adsorption capacity of the bis(amino)-tagged MOFs remained almost identical to that of Zn(BPZNH<sub>2</sub>). Structural evidence of direct CO<sub>2</sub> interaction with amino tags in MOFs has been previously reported,

but this work represents the first example of a crystal structure determination of an adduct between an amino-MOF and a halogenated epoxide. The crystal structure of the [epibromohydrin@Zn(3,3'-L)] adduct showed nonbonding interactions  $\text{Br}\cdots(\text{H})\text{-N}$ , providing proof of epoxide activation. Ongoing research aims to develop novel and effective MOF catalysts for this reaction.

The results described in this chapter have been published in the following paper: “Carbon Dioxide Capture and Utilization with Isomeric Forms of Bis(amino)-Tagged Zinc Bipyrazolate Metal–Organic Frameworks”, Chem. Eur.J. 2021,27,4746 –4754.<sup>203</sup>

**CHAPTER 5:**  
**Carbon dioxide capture and electroreduction**  
**with mixed Cu(II)/Ni(II) bipyrazolate MOFs**

## 5.1 Aim of the research

We have already discussed in the previous chapter the importance of finding new systems not only capable of adsorbing carbon dioxide but also of converting it into useful products in order to reduce emissions of this greenhouse gas, and the fact that MOFs perform well in doing this.

In this work, I focused on an additional technique for CO<sub>2</sub> conversion, which is electroreduction. It permits the formation of C<sub>1</sub> C<sub>2</sub> or C<sub>2+</sub> compounds, exploiting electric current with a greener approach if derived from renewable sources, such as biomass, wind and solar.<sup>204–206</sup>

The literature has recently been enriched with papers dealing with MOFs for CO<sub>2</sub> electroreduction based on transition metals Ni, Cu, Co and Fe, mainly for the production of carbon monoxide (CO), alcohols (CH<sub>3</sub>OH, CH<sub>3</sub>CH<sub>2</sub>OH), formic acid (HCOOH) and methane (CH<sub>4</sub>).<sup>207–214</sup>

Copper-based MOFs have been observed to be more efficient in hydrocarbons production, while Ni-containing MOFs promote the conversion of CO<sub>2</sub> to CO.<sup>215,216</sup>

Previous tests have shown that [Cu(BPZ)] does not withstand the harsh working conditions, resulting in the formation of metallic Cu nanoparticles during electroreduction of CO<sub>2</sub>, with irreversible catalyst decomposition.

Given these premises, in this work four Cu/Ni Mixed MOFs based on the organic linker 3,5-diamino-4,4'-bipyrazole (the same used for the previous work which has been abbreviated in 3,5-H<sub>2</sub>L) showing the following molar percentage: **Cu<sub>0.05</sub>Ni<sub>0.95</sub>**, **Cu<sub>0.1</sub>Ni<sub>0.9</sub>**, **Cu<sub>0.2</sub>Ni<sub>0.8</sub>** and **Cu<sub>0.5</sub>Ni<sub>0.5</sub>**.

This work was carried out in collaboration with: Dr. Rossin (CNR Institute, Sesto Fiorentino, Firenze) who helped me in the interpretation of the BET isotherms and of the isostatic adsorption heats; Prof. Galli (University of Insubria, Como) who determined the crystal structure of the MOF **Cu<sub>0.5</sub>Ni<sub>0.5</sub>** by PXRD; the research group of Prof. Hupp (Northwestern University, Evanston, Illinois, USA) who performed all the electroreduction tests, and recorded PXRD, XPS and TEM after the catalytic tests.



## 5.2 Experimental section

### 5.2.1 Materials and methods

3,5-diamino-4,4'-bipyrazole (3,5-H<sub>2</sub>L) was synthesized as reported previously.<sup>190</sup> All the chemicals and reagents employed in the syntheses purchased from commercial suppliers were used as received without further purification. IR spectra were recorded as neat from 4000 to 600 cm<sup>-1</sup> with a PerkinElmer Spectrum One System with ATR mode. Elemental analyses (C, H, N %) were performed with a Fisons Instruments 1108 CHNS-O elemental analyser. ICP analyses were performed with an iCAP PRO Thermo Scientific, by dissolving 1.8 mg of sample in 25 mL of an aqueous solution 1.5% w/w HNO<sub>3</sub> and 2N HCl. Powder X-ray diffraction (PXRD) qualitative analysis was carried out with a Bruker AXS D8 Advance diffractometer, acquiring data at room temperature in the 2θ range 3.0-35.0°, with steps of 0.02° and time per step of 1 s. The nature and purity of all the batches employed for the functional characterization were assessed by elemental analysis, IR spectroscopy and PXRD. Thermogravimetric analysis (TGA) was performed simultaneously was performed under a flow of N<sub>2</sub> over the temperature range 303-1073 K and with a heating rate of 10 K/min employing a PerkinElmer Pyris-1 thermogravimetric analyzer. X-ray fluorescence (XRF) qualitative elemental analyses were performed in air on a powdered batch (ca. 10 mg) of the four MOFs with a Panalytical MINIPAL 2 instrument equipped with a Cr X-ray source. SEM-EDX analysis was performed on a ZEISS SIGMA 300 FESEM (field emission scanning electron microscope) fitted with a Gemini column, achieving a maximum resolution of 1.2 nm, and with three electron detectors: high definition back scattered detector with 4 independent sectors, high efficiency secondary “in-lens” electron detector and Everhart–Thornley secondary electron detector.

### 5.2.2 Synthesis of [Cu<sub>0.05</sub>Ni<sub>0.95</sub>(3,5-L)] (Cu<sub>0.05</sub>Ni<sub>0.95</sub>)

Drawing inspiration from the previous preparations of Cu- and Ni-based MOFs with bipyrazolate linkers,<sup>103,112</sup> the synthesis was carried out in the following manner. Cu(CH<sub>3</sub>COO)<sub>2</sub>·H<sub>2</sub>O (0.025 mmol), Ni(CH<sub>3</sub>COO)<sub>2</sub>·4H<sub>2</sub>O (0.475 mmol) and 3,5-H<sub>2</sub>L (MW = 164.2 g mol<sup>-1</sup>, 0.5 mmol) were solubilized in a closed vessel containing N,N-dimethylformamide (DMF, 6 mL). The reaction was kept for 2 hours at 120°C. The resulting powder was washed 3 times with fresh DMF and 5 times with CH<sub>2</sub>Cl<sub>2</sub> with a soaking time of

30 minutes for each wash. Elem. Anal. Calcd. for  $C_6H_6N_6Cu_{0.05}Ni_{0.95}$  (FW = 221.1 g/mol): C, 32.60; H, 2.74; N, 38.01% and for  $C_6H_6N_6Cu_{0.05}Ni_{0.95}(CH_2Cl_2)_{0.80}$  (FW = 289.0 g/mol): C 28.03; H 2.64; N 28.63. Found: C, 28.70; H, 3.72; N, 28.96%. The phase purity was checked through PXRD. IR bands ( $cm^{-1}$ ): 3332 (m,br) [ $\nu(N-H)$ ]; 1618 (s,sh); 1558 (m,br); 1518 (s, sh) [ $\nu(C=N)$ ]+ $\nu(C=C)$ ]; 1391 (m,sh); 1139 (m,sh); 1071 (m,br); 958 (s, vsh); 925 (w, sh); 656 (s, sh).

### 5.2.3 Synthesis of $[Cu_{0.1}Ni_{0.9}(3,5-L)] (Cu_{0.1}Ni_{0.9})$

The synthetic procedure is analogue to the previous one adopted for  $Cu_{0.05}Ni_{0.95}$ , except for a different stoichiometric molar ratio of the starting copper and nickel metal salts respectively equal to 1:9 (0.050 mmol: 0.450 mmol). Elem. Anal. Calcd. For  $C_6H_6N_6Cu_{0.1}Ni_{0.9}$  (FW = 221.3 g/mol): C, 32.56; H, 2.73; N, 37.97% and for  $C_6H_6N_6Cu_{0.1}Ni_{0.9}(CH_2Cl_2)_{0.85}$  (FW = 293.5 g/mol): C, 28.03; H, 2.64; N, 28.63%. Found: C, 28.11; H, 3.56; N, 28.69%. The phase purity was checked through PXRD. IR bands ( $cm^{-1}$ ): 3325 (m,br) [ $\nu(N-H)$ ]; 1620 (s,sh); 1554 (m,br); 1518 (s, sh) [ $\nu(C=N)$ ]+ $\nu(C=C)$ ]; 1393 (m,sh); 1134 (m,sh); 1062 (m,br); 958 (s, vsh); 919 (m,sh); 658 (s, sh).

### 5.2.4 Synthesis of $[Cu_{0.2}Ni_{0.8}(3,5-L)] (Cu_{0.2}Ni_{0.8})$

The synthetic procedure is analogue to the one adopted for  $Cu_{0.05}Ni_{0.95}$ , except for a different stoichiometric molar ratio of the starting copper and nickel metal salts respectively equal to 1:4 (0.100 mmol : 0.400 mmol). Elem. Anal. Calcd. For  $C_6H_6N_6Cu_{0.2}Ni_{0.8}$  (FW = 221.8 g/mol): C, 32.49; H, 2.73; N, 37.89% and for  $C_6H_6N_6Cu_{0.2}Ni_{0.8}(CH_2Cl_2)_{0.55}$  (FW = 268.5 g/mol): C, 29.30; H, 2.67; N, 31.30%. Found: C, 28.38; H, 3.59; N, 28.40%. The phase purity was checked through PXRD. IR bands ( $cm^{-1}$ ): 3325 (m,br) [ $\nu(N-H)$ ]; 1618 (s,sh); 1557 (s,br); 1519 (s, sh) [ $\nu(C=N)$ ]+ $\nu(C=C)$ ]; 1391 (m,sh); 1138 (m,sh); 1056 (m,br); 958 (s, vsh); 924 (w, sh); 658 (s, sh).

### 5.2.5 Synthesis of $[Cu_{0.5}Ni_{0.5}(3,5-L)] (Cu_{0.5}Ni_{0.5})$

The synthetic procedure is analogue to the one adopted for  $Cu_{0.05}Ni_{0.95}$ , except for a different stoichiometric molar ratio of the starting copper and nickel metal salts respectively equal to 1:1 (0.250 mmol : 0.250 mmol). Elem. Anal. Calcd.  $C_6H_6N_6Cu_{0.5}Ni_{0.5}$  (FW = 223.3 g/mol): C, 32.28; H, 2.71; N, 37.64% and for  $C_6H_6N_6Cu_{0.5}Ni_{0.5}(CH_2Cl_2)_{0.75}$  (FW = 287.0 g/mol): C, 28.25; H, 2.63; N, 29.29%. Found: C, 28.94; H, 3.31; N, 28.07%. The phase purity was checked

through PXRD. IR bands ( $\text{cm}^{-1}$ ): 3326 (m,br) [ $\nu(\text{N-H})$ ]; 1620 (s,sh); 1553 (s,br); 1513 (s, br) [ $\nu(\text{C=N})$ ]+  $\nu(\text{C=C})$ ]; 1387 (m,sh); 1237 (w,br); 1134 (m,br); 1058 (m,br); 957 (s, vsh); 921 (w,sh) 657 (s, sh).

### 5.2.6 Crystal structure of $\text{Cu}_{0.5}\text{Ni}_{0.5}$

A powdered sample (about 50 mg) of  $\text{Cu}_{0.5}\text{Ni}_{0.5}$  was placed in the cavity of a 0.2 mm deep silicon free-background sample holder (Assing Srl, Monterotondo, Italy). PXRD data acquisitions were carried out at room temperature on a Bruker AXS D8 Advance vertical-scan  $\theta : \theta$  diffractometer, equipped with a sealed X-ray tube (Cu  $\text{K}\alpha$ ,  $\lambda = 1.5418 \text{ \AA}$ ), a Bruker Lynxeye linear position-sensitive detector, a filter of nickel in the diffracted beam and the following optical components: primary- and diffracted-beam Soller slits (aperture  $2.5^\circ$ ), fixed divergence slit (aperture  $0.5^\circ$ ), antiscatter slit (aperture 8 mm). The generator was operated at 40 kV and 40 mA. The data acquisition for the structure characterization was performed in the  $2\theta$  range  $5.0$ - $105.0^\circ$ , with steps of  $0.02^\circ$  and an overall scan time of about 12 hours. Comparison of the PXRD pattern of  $\text{Cu}_{0.5}\text{Ni}_{0.5}$  with those of Ni(BPZ) and Cu(BPZ)<sup>103</sup> suggested that the three compounds are isomorphous. Hence, the space group and unit cell parameters of  $\text{Cu}_{0.5}\text{Ni}_{0.5}$  were preliminary confirmed starting from those of Ni(BPZ) by means of a whole powder pattern refinement with the so-called Le Bail method<sup>217</sup> available in TOPAS-R v.3.<sup>173</sup> To describe the crystallographically independent portion of the 3,5- $\text{H}_2\text{L}$  ligand, a rigid body was built up using the z-matrix formalism, assigning idealized values to bond distances and angles. The metal ion and the centre of mass of the ligand were located according to the crystal structure of Ni(BPZ). The molar ratio of the Ni(II) and Cu(II) ions was imposed as 0.5:0.5, approximating the results of the EDX and ICP elemental analyses. Given the location of the ligand centre of mass ( $2/m$ , Whyckoff position c), the  $\text{NH}_2$  moieties are distributed (vicariant with hydrogen atoms) over the 3,3',5,5' positions of the rings, with site occupancy factor amounting to 0.25. Given the difficulty of detecting the position of hydrogen atoms through X-ray diffraction, the  $\text{NH}_2$  moieties were modelled as planar and positioned coplanar to the ligand skeleton. For the sake of simplicity, the clathrated solvent was modelled by means of dummy oxygen atoms describing the electron density smeared within the pores. The position of the dummy atoms, whose site occupation factor was refined, was assessed using the Simulated Annealing approach<sup>174</sup> available in TOPAS-R v.3. After the structure determination, instrumental and  $\text{Cu}_{0.5}\text{Ni}_{0.5}$  structural parameters were

collectively refined through the so-called Rietveld method<sup>218</sup> with TOPAS-R v.3. During the final Rietveld structure refinement stages, the ligand bond distances (except for the C-H and N-H ones) were refined in restrained ranges of values defined through a search in the Cambridge Structural Database (v. 2022) for room-temperature single-crystal structures containing the M(pyrazolate) (M = 3d metal ion) moiety. The background was modelled through a Chebyshev-type polynomial function. An isotropic thermal factor (Biso) was refined for the metal centre; the isotropic thermal factor of the other elements was calculated as  $Biso(L) = Biso + 2.0 \text{ \AA}^2$ . The instrumental contribution to the peak profile was modelled by means of the Fundamental Parameters Approach.<sup>176</sup> The sample contribution to the anisotropic peak broadening was accounted for using spherical harmonics.

Crystal data for **Cu<sub>0.5</sub>Ni<sub>0.5</sub>**, FW = 223.3 g mol<sup>-1</sup>: orthorhombic, Imma, a = 15.032(3) Å, b = 7.061(1) Å, c = 9.849(1) Å, V = 1045.3(3) Å<sup>3</sup>, Z = 16, Z' = 4, ρ = 1.99 g/cm<sup>3</sup>, F(000) = 629.84, R<sub>Bragg</sub> = 0.08, R<sub>p</sub> = 0.60% and R<sub>wp</sub> = 0.78%, for 4851 data and 75 parameters in the 8.0-105.0° (2θ) range.

### 5.2.7 N<sub>2</sub> and CO<sub>2</sub> adsorption and BET Surface Area determination

Before evaluating the BET surface area, about 40 mg of all Ni/Cu MOFs were thermally activated at 393 K under high vacuum (10<sup>-6</sup> Torr) for 5 h (after the solvent exchange washes with CH<sub>2</sub>Cl<sub>2</sub>). BET specific surface area and pore volume were calculated with the aid of an ASAP 2020 Micromeritics instrument, using N<sub>2</sub> as adsorbate at 77K, the 0.01-0.1 p/p° pressure range was used for BET specific surface area estimation, in order to satisfy all the Rouquerol consistency criteria. Also, the materials pore size distribution and pore volume (V<sub>tot</sub>, V<sub>micro</sub>) can be calculated from the same isotherm. Three different CO<sub>2</sub> adsorption isotherms were measured at T = 195, 273 and 298 K up to the maximum pressure of 1.2 bar. For each mixed Cu/Ni MOF, the isosteric heat of adsorption (Q<sub>st</sub>) was calculated at zero coverage together with the energy of adsorbate/adsorbent interactions as a function of mmol of CO<sub>2</sub> adsorbed.

### 5.2.8 CO<sub>2</sub> electroreduction tests with Cu/Ni mixed MOFs

All the electroreduction tests were carried out with a three-electrode setup on a Gamry 1010E potentiostat: Ag/AgCl/sat. KCl (BASi) is the reference, a BASi platinum wire is used as the counter electrode, whereas the working electrode is made of MOFs powder

suspended and dropped on carbon paper. LiClO<sub>4</sub> solution 0.1 M in acetonitrile was chosen as electrolyte. A H-cell in which the reference and the working electrode are positioned in one side while the counter electrode in the other part was filled with solvents. A rubber stopper was employed to seal the system. In order to conduct baseline cyclic voltammetry (CV), N<sub>2</sub> was purged for 15 min, while CO<sub>2</sub> was purged for 15 minutes to carry out the reaction CV. The CV was performed with a 50 mV/s scan rate from 0 to -1.8 V vs Ag/AgCl. Faraday efficiency was estimated with the help of chronoamperometry (CA) at desired potential and reaction was hold for 15 min, alternating 15 min of CO<sub>2</sub> purging between test. Headspace gas (200 μ L) was injected into Shimadzu Nexis GC-2030 for product analysis. Powder X-ray diffraction (PXRD) patterns of films were collected with STOE-STADI-MP (CuKα 1 radiation, λ = 1.54056 Å) in reflection mode to investigate the crystallinity of the material after the electroreduction tests. Before the measurement, the instrument was calibrated against an NIST silicon standard (640d).

## 5.3 Results and discussions

### 5.3.1 Synthesis of the mixed Cu/Ni MOFs

The mixed-metal MOFs Cu<sub>0.05</sub>Ni<sub>0.95</sub>, Cu<sub>0.1</sub>Ni<sub>0.9</sub>, Cu<sub>0.2</sub>Ni<sub>0.8</sub> and Cu<sub>0.5</sub>Ni<sub>0.5</sub> were all synthesized in DMF at 393 K, varying the molar ratios of copper(II) and nickel(II) acetate which are respectively 1:19, 1:9, 1:4 and 1:1. Metal acetates were chosen precursors mostly for three reasons: i) acetate anion as a weak base is able to encourage the organic linker deprotonation and the following coordination to the metal node; ii) the starting metal salt affects MOFs crystallinity and porosity<sup>219</sup> and previously other Ni(II) and Cu(II) MOFs based on bipyrazolate linkers have been reported in which the metal precursor is really the corresponding metal acetate<sup>102</sup>; iii) finally, the handling of acetates is less dangerous than other counterions such as nitrates or chlorides.<sup>220</sup>

Each mixed MOF was preactivated by solvent exchange method before the thermal activation at 393 K at 10<sup>-6</sup> Torr: five washes were conducted in CH<sub>2</sub>Cl<sub>2</sub> by soaking for about 30 minutes. The effectiveness of solvent exchange depends on the choice of low capillary tension solvents and the exchange kinetics are very rapid. For this reason, it is more effective to soak the MOF for minutes rather than hours or days.<sup>69</sup>

### 5.3.2 Preliminary characterization of the mixed Cu/Ni MOFs

The four Cu/Ni mixed MOFs were initially characterized by IR spectroscopy and the IR spectra are shown in **Figure 72**. In all samples, a very broad band at 3332-3325  $\text{cm}^{-1}$  can be observed ascribable to the stretching vibration frequency of the two amino groups belonging to the same pyrazole ring. In the range 1513-1519  $\text{cm}^{-1}$ , aromatic C=C and C=N stretching frequencies are noted, as occurs for the MOF Zn(3,5-L) consisting of the same organic linker, described in the previous chapter. The solvent exchange was found to be effective in removing the reaction solvent (DMF) as no peaks are observed in the IR spectra at about 1660  $\text{cm}^{-1}$ , where the carbonyl stretching of DMF is typically seen.

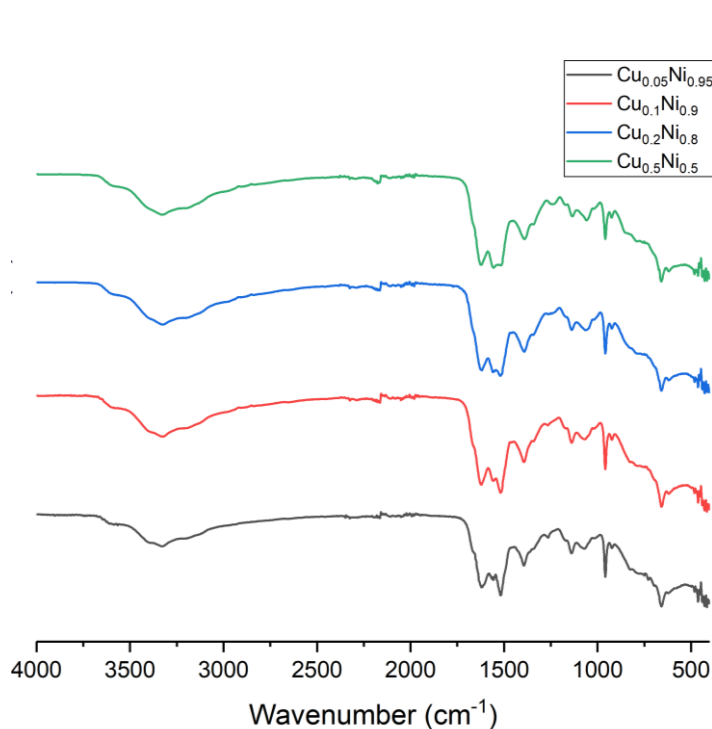


FIGURE 72 IR spectra of the four Cu/Ni mixed MOFs recorded at 4000-400  $\text{cm}^{-1}$ .

With the aim of confirming the actual molar ratio between copper and nickel in the four mixed MOFs, ICP and EDX analyses were performed. For all ICP tests, the absorption of Cu at 324.754 nm and of Ni at 221.647 nm was considered.

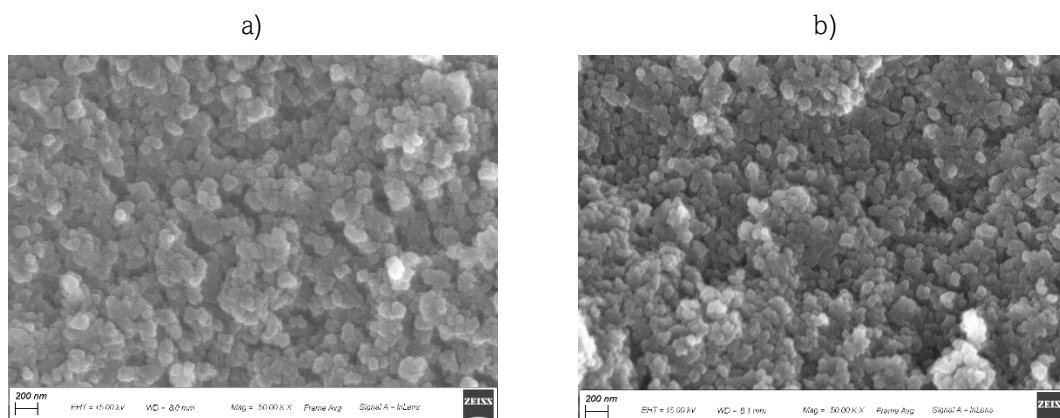
The following table resumes the molar Cu/Ni ratio values for **Cu<sub>0.05</sub>Ni<sub>0.95</sub>**, **Cu<sub>0.1</sub>Ni<sub>0.9</sub>**, **Cu<sub>0.2</sub>Ni<sub>0.8</sub>** and **Cu<sub>0.5</sub>Ni<sub>0.5</sub>** estimated by ICP and EDX techniques, and the expected values with respect to the reaction stoichiometry. Molar ratio percentage has also been reported for both techniques and compared with the corresponding expected value, for better understanding and easy comparison. What can be inferred from the reported data is that the values

determined by the two different techniques are in agreement with each other and in general agreement with the expected values for all four MOFs. Nevertheless, in all cases there is a slight lower molar content of copper (and consequently higher molar content of Ni) than the desired value. In detail, this discrepancy increases as the copper content in the framework increases.

Sample	Cu/Ni ratio ICP	Cu/Ni ratio EDX	Cu/Ni ratio expected	Cu/Ni Molar ratio (%) ICP	Cu/Ni Molar ratio (%) EDX	Cu/Ni Molar ratio (%) expected
<b>Cu<sub>0.05</sub>Ni<sub>0.95</sub></b>	0.052	0.050	0.053	5:95	5:95	5:95
<b>Cu<sub>0.1</sub>Ni<sub>0.9</sub></b>	0.093	0.100	0.111	9:91	9:91	10:90
<b>Cu<sub>0.2</sub>Ni<sub>0.8</sub></b>	0.213	0.221	0.250	18:82	18:82	20:80
<b>Cu<sub>0.5</sub>Ni<sub>0.5</sub></b>	0.820	0.863	1.000	45:55	46:54	50:50

SEM images were recorded to examine the MOFs morphology, while the distribution of Cu<sup>2+</sup> and Ni<sup>2+</sup> within the samples was checked by EDX technique.

Images with a magnification of 50000-fold are reported for all the Cu/Ni mixed MOFs in **Figure 73**. Some recurrent structural organization is highlighted.



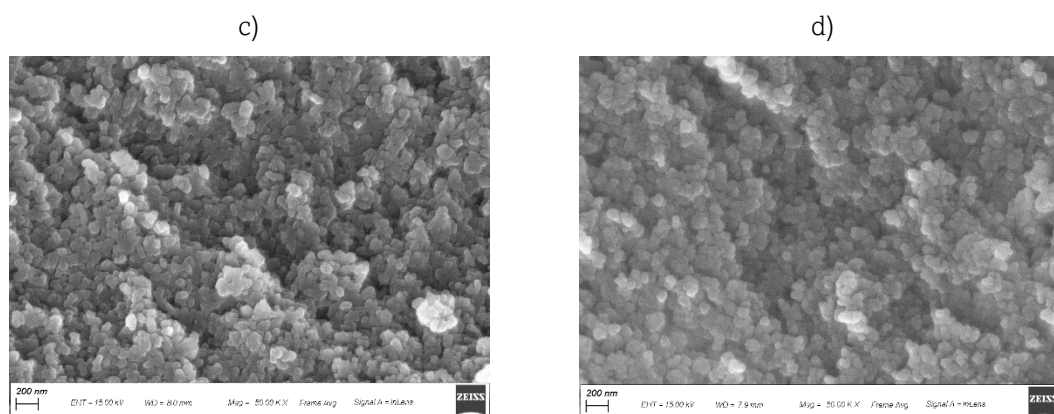


FIGURE 73 SEM images acquired with a 50000-fold magnification of a)  $\text{Cu}_{0.05}\text{Ni}_{0.95}$ , b)  $\text{Cu}_{0.1}\text{Ni}_{0.9}$ , c)  $\text{Cu}_{0.2}\text{Ni}_{0.8}$  and d)  $\text{Cu}_{0.5}\text{Ni}_{0.5}$ .

As an example, the distribution of  $\text{Cu}^{2+}$  and  $\text{Ni}^{2+}$  ions estimated via EDX within the  $\text{Cu}_{0.2}\text{Ni}_{0.8}$  framework is evidenced in **Figure 74**. A homogeneous distribution emerges for both ions, and a major content of nickel is visibly observable.

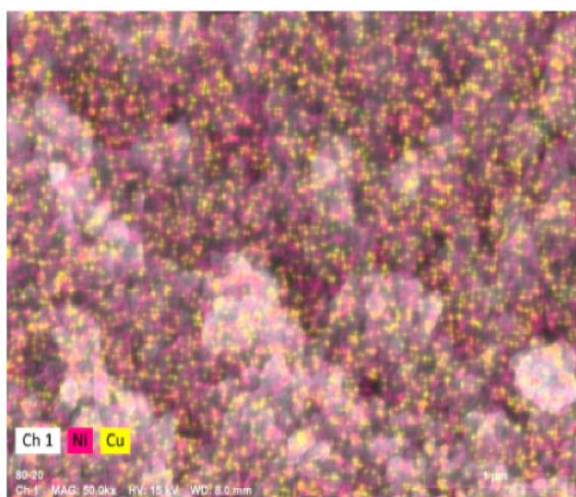


FIGURE 74 Copper(II) (yellow) and nickel (II) (pink) ions distribution revealed by EDX for  $\text{Cu}_{0.2}\text{Ni}_{0.8}$ .

### 5.3.3 Thermal behavior

Thermogravimetric profile of  $\text{Cu}_{0.05}\text{Ni}_{0.95}$ ,  $\text{Cu}_{0.1}\text{Ni}_{0.9}$ ,  $\text{Cu}_{0.2}\text{Ni}_{0.8}$  and  $\text{Cu}_{0.5}\text{Ni}_{0.5}$  was determined and depicted in **Figure 75**. For all MOFs, an initial weight loss of 9-11 % in the range of 303-293K associable to clathrate solvent inside the cavities occurs. The decomposition of the samples is observed in the range 503-713 K and, after that, a further decomposition at 973 K produce a residue with a relative mass of: 41% ( $\text{Cu}_{0.05}\text{Ni}_{0.95}$ ), 45% ( $\text{Cu}_{0.1}\text{Ni}_{0.9}$ ), 45% ( $\text{Cu}_{0.2}\text{Ni}_{0.8}$ ) and 38%.



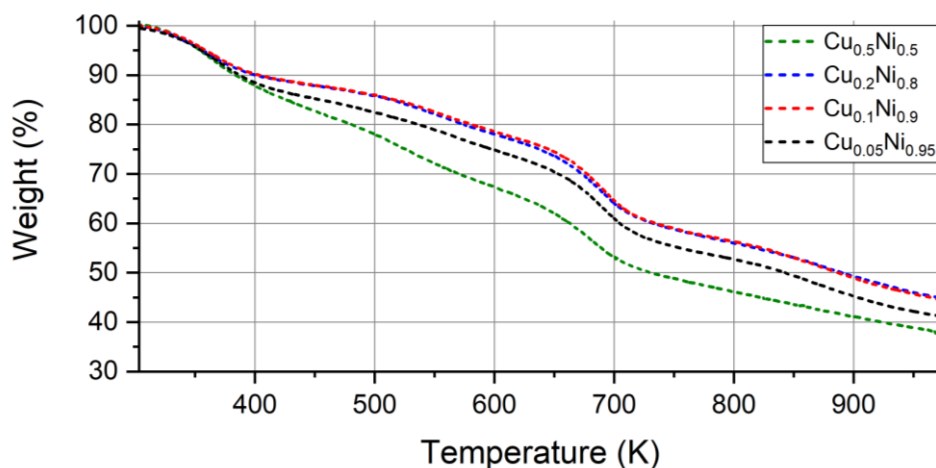


FIGURE 75 TGA curves of the four Cu/Ni mixed MOFs performed in the range 303-1073 K.

### 5.3.4 Crystal structure of Cu<sub>0.5</sub>Ni<sub>0.5</sub>

The crystal structure of **Cu<sub>0.5</sub>Ni<sub>0.5</sub>** has been solved via PXRD as representative of all four Cu/Ni mixed MOFs. The network is isostructural with the Cu(BPZ) and Ni(BPZ): **Cu<sub>0.5</sub>Ni<sub>0.5</sub>** crystallizes in the orthorhombic space group Imma. The coordination geometry of the metal node is square planar, with the metal centers linked with four nitrogen atoms deriving from four different bipyrazolate molecules, yielding a porous 3D framework with **pts** topology. Diamond-shaped 1D channels run along the crystallographic b-axis (**Figure 76**). The activated MOFs at room temperature and pressure show an empty volume of 42.5%, similar to Ni(BPZ) Cu(BPZ), Ni(BPZNH<sub>2</sub>) and Cu(BPZNH<sub>2</sub>) which is 40, 42, 44.5 and 45.4%, respectively.

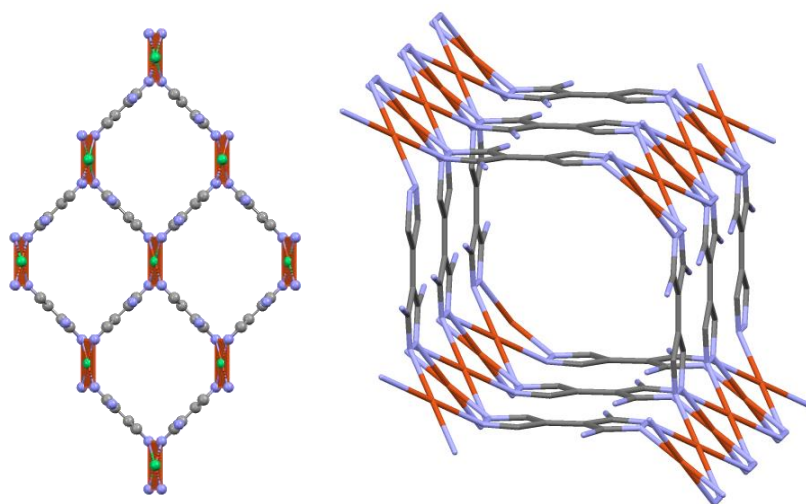


FIGURE 76 Representation of a portion of **Cu<sub>0.5</sub>Ni<sub>0.5</sub>** crystal structure, on the left. Carbon (grey), nitrogen (blue) and copper/nickel (green) atoms are indicated. Hydrogen atoms are omitted for clarity. The square planar coordination geometry of the metal centers is highlighted. On the right, a single pore display is reported.

### 5.3.5 N<sub>2</sub> and CO<sub>2</sub> adsorption and BET Surface Area determination

The MOFs specific surface area was determined by volumetric N<sub>2</sub> adsorption isotherm at 77 K on preactivated powders. In all cases, the isotherms are classifiable as Type II, corresponding to macroporous/non-porous materials. The four mixed Cu/Ni MOFs exhibit BET specific surface areas of 140-240 m<sup>2</sup>/g range, lower than the values obtained for the zinc analogue (504 m<sup>2</sup>/g) or for [M(BPZ)] (M = Cu: 314 m<sup>2</sup>/g; M = Ni: 767 m<sup>2</sup>/g) but similar to those registered for Cu(BPZNH<sub>2</sub>)](100 m<sup>2</sup>/g) and Ni(BPZNH<sub>2</sub>)](182 m<sup>2</sup>/g).

The micropore volume estimated with t-plot analysis is negligible (0.2-2% of the total pore volume at  $p/p^\circ = 0.95$ ) for all samples, whereas BJH method applied on the isotherm desorption branch do not distinguish mesopores. What has just said confirms that the samples are mainly macroporous.

In order to evaluate CO<sub>2</sub> adsorption and affinity of the four mixed Cu/Ni MOFs, CO<sub>2</sub> adsorption isotherms at T = 195, 298 and 273 K were recorded on activated samples (solvent exchange with CH<sub>2</sub>Cl<sub>2</sub> + thermal activation at 393 K and 10<sup>-6</sup> Torr) up to  $p_{\max} = 1.2$  bar.

Figure 77a show N<sub>2</sub> adsorption isotherms at 77K and Figure 77b CO<sub>2</sub> adsorption isotherms at 298 K of Cu<sub>0.05</sub>Ni<sub>0.95</sub>, Cu<sub>0.1</sub>Ni<sub>0.9</sub>, Cu<sub>0.2</sub>Ni<sub>0.8</sub> and Cu<sub>0.5</sub>Ni<sub>0.5</sub>. In Figure 78, instead, the CO<sub>2</sub> adsorption isotherms at 273 K (a) and 195 K (b) are reported.

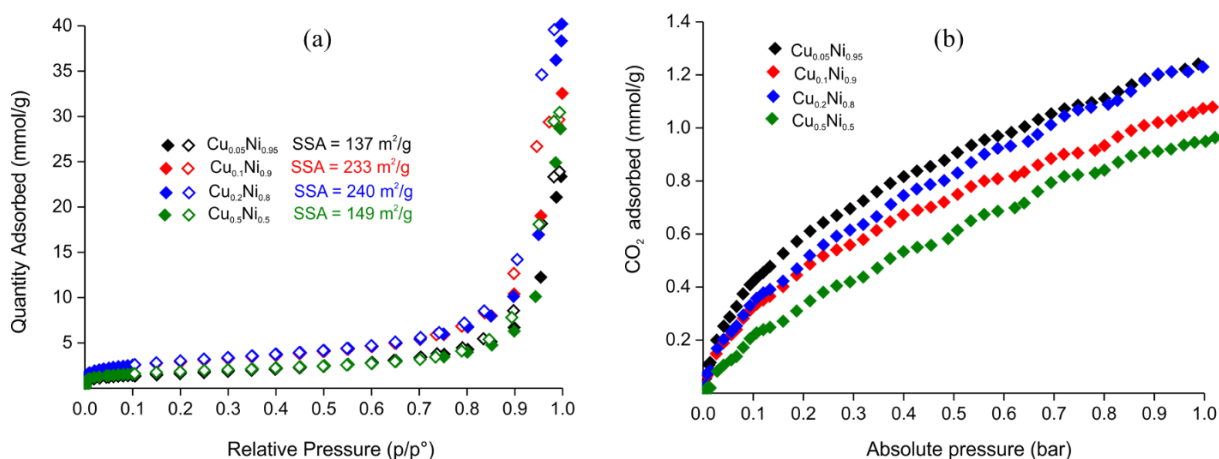


FIGURE 77 a) N<sub>2</sub> adsorption isotherms at 77 K and b) CO<sub>2</sub> adsorption isotherms at 298 K of the four Cu/Ni mixed MOFs. Empty symbols indicate the desorption branch.

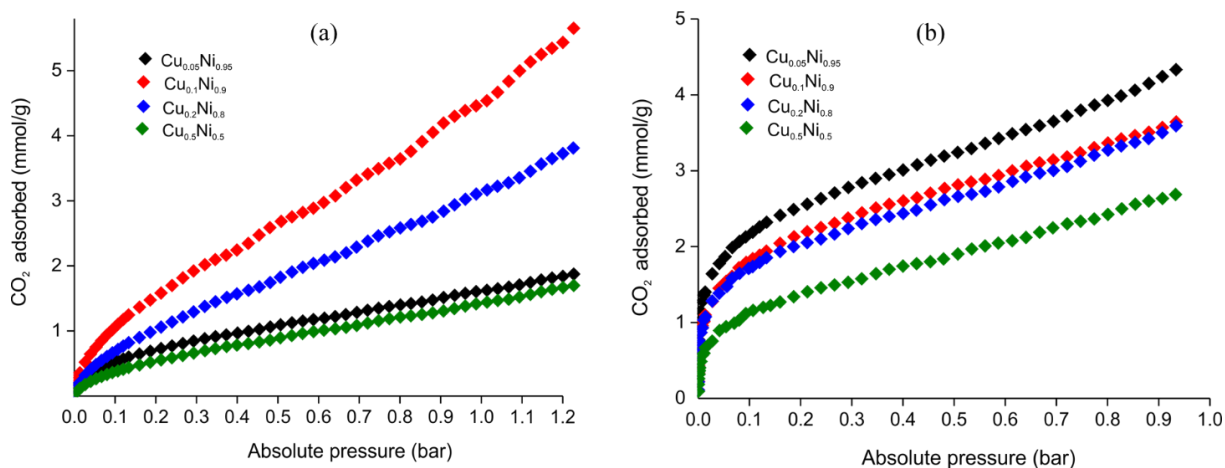


FIGURE 78 a)  $\text{CO}_2$  adsorption isotherms at 273 K and b) 195 K of the four Cu/Ni mixed MOFs.

In the following table, BET surface area and heats of adsorption values and  $\text{CO}_2$  adsorption in terms of mmol of gas per gram of MOF at 195, 273 and 298 K are resumed.

Sample	BET area [ $\text{m}^2/\text{g}$ ]	$Q_{st}(\text{CO}_2)$ [kJ/mol]	$\text{CO}_2$ quantity adsorbed ( $p = 1$ bar) [mmol/g]		
			T = 195 K	T = 273 K	T = 298 K
$\text{Cu}_{0.05}\text{Ni}_{0.95}$	137	24.0	4.3 (19.1 wt.%)	1.6 (7.1 wt.%)	1.3 (5.6 wt.%)
$\text{Cu}_{0.1}\text{Ni}_{0.9}$	233	25.7	3.6 (16.0 wt.%)	4.5 (20.0 wt.%)	1.0 (4.5 wt.%)
$\text{Cu}_{0.2}\text{Ni}_{0.8}$	240	26.2	3.6 (15.8 wt.%)	3.2 (14.0 wt.%)	1.3 (5.6 wt.%)
$\text{Cu}_{0.5}\text{Ni}_{0.5}$	149	24.5	2.7 (11.8 wt.%)	1.4 (6.3 wt.%)	0.9 (4.0 wt.%)

The data here reported show a conventional trend for which increasing the temperature of  $\text{CO}_2$  adsorption isotherm, the amount of adsorbate decreases, except for MOF  $\text{Cu}_{0.1}\text{Ni}_{0.9}$  that exhibit a higher adsorption of carbon dioxide at 273 K (4.5 mmol) and not at 195 K (3.6 mmol). This fashion can be reasonably explained considering that as the temperature rises, the kinetic energy of the adsorbate particles too become higher, allowing the adsorbate particles to “escape” from the interaction with the adsorbent material. The  $\text{CO}_2$  adsorption

values at 298 K (the working conditions employed for electroreduction) are included in the 4.0-5.6 wt.% range and are close to the values observed in Cu(BPZNO<sub>2</sub>) (9.4 wt.%; H<sub>2</sub>BPZ-NO<sub>2</sub> = 3-nitro-4,4'-bipyrazole).<sup>191</sup>

Adsorption heat values were calculated for each mixed MOF by performing Clausius-Clapeyron differential equation fitting and are displayed in **Figure 79**. The values fall in the range 24.0-26.2 KJ/ mol, with **Cu<sub>0.2</sub>Ni<sub>0.8</sub>** exhibiting the highest interaction with carbon dioxide at zero coverage. Such results represent typical values for physisorption systems.

The study on the variation of heat of adsorption as a function of the amount of carbon dioxide captured has also been carried out. This aspect is of considerable interest because it provides a way to observe the behavior of the adsorbent material (the MOF in our case) toward the adsorbate (CO<sub>2</sub>) as the latter is captured. In order to perform that, a range of captured CO<sub>2</sub> amount (expressed in mmol/g) common to all CO<sub>2</sub> adsorption isotherms at the three different temperatures and for the four different samples was selected. Therefore, the chosen range is 0.12-0.91 mmol/g, which has been divided into 10 points. The trends for all Cu/Ni mixed MOFs are reported in **Figure 80**. **Cu<sub>0.5</sub>Ni<sub>0.5</sub>** shows decreasing values of heat of adsorption when the amount of carbon dioxide decreases achieving a value of ≈13.6 KJ/mol when 0.91 mmol/g of CO<sub>2</sub> are adsorbed. **Cu<sub>0.2</sub>Ni<sub>0.8</sub>** and **Cu<sub>0.1</sub>Ni<sub>0.9</sub>**, on the other hand, exhibit increasing values of heat of adsorption up to 26.6 KJ/mol (at 0.38 mmol/g) and 25.5 KJ/mol (at 0.21 mmol/g), respectively, and then decreasing to 19.6 and 19.8 KJ/mol (at 0.91 mmol/g), respectively. Interesting is the case of **Cu<sub>0.05</sub>Ni<sub>0.95</sub>**, for which the heat of adsorption values increases to 29.3 KJ/mol (at 0.56 mmol/g) and then slowly decrease to 27.3 KJ/mol when 0.91 mmol/g of carbon dioxide are adsorbed. **Cu<sub>0.05</sub>Ni<sub>0.95</sub>** (which is the MOF with lowest copper content), hence, retains a good interaction with CO<sub>2</sub> even at higher gas pressures, while **Cu<sub>0.5</sub>Ni<sub>0.5</sub>** (the MOF with the highest copper content) dramatically decreases its interaction with the adsorbate when the CO<sub>2</sub> pressure increases.

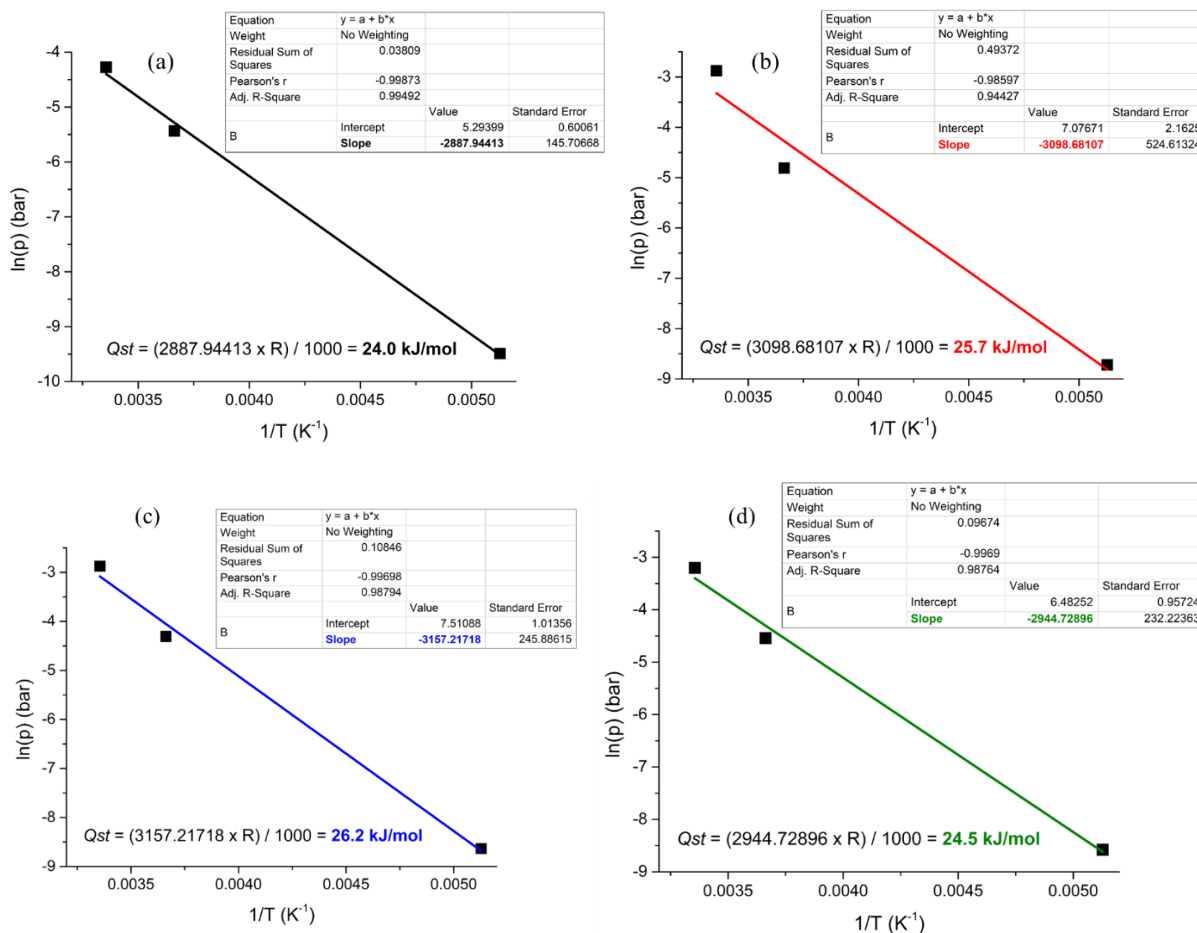


FIGURE 79 Linear fitting of the differential form of the Clausius-Clapeyron equation for (a)  $Cu_{0.05}Ni_{0.95}$ , b)  $Cu_{0.1}Ni_{0.9}$ , c)  $Cu_{0.2}Ni_{0.8}$  and d)  $Cu_{0.5}Ni_{0.5}$  at  $T = 195, 273$  and  $298 \text{ K}$ .

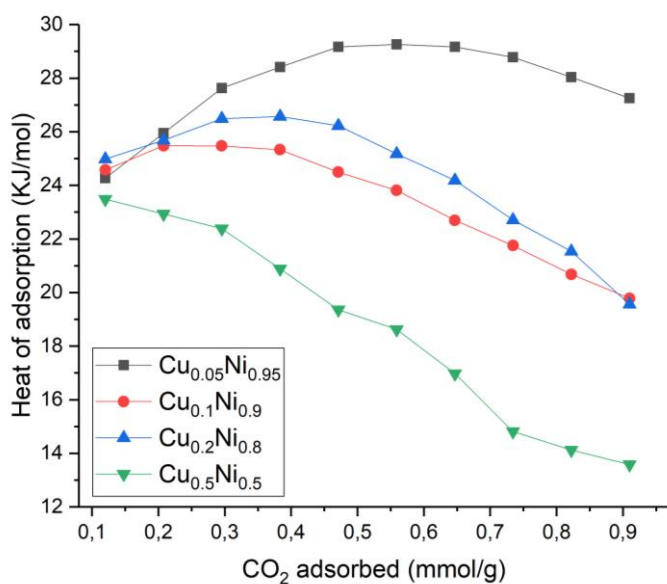


FIGURE 80 Representation of heat of adsorption of all the four Cu/Ni mixed MOFs as a function of the quantity of  $CO_2$  adsorbed.

### 5.3.6 Electrocatalytic performances of Cu/Ni mixed MOFs

The four mixed MOFs have been tested as heterogeneous catalysts in the electrocatalytic conversion of CO<sub>2</sub>. The tests were conducted applying three separate potentials (1.3 V, 1.5 V, and 1.7 V vs. Ag/AgCl). Excluding the inevitable formation of hydrogen gas as a by-product, a mixture of CO and CH<sub>4</sub> is formed from all the samples. In detail, Cu<sub>0.05</sub>Ni<sub>0.95</sub>, Cu<sub>0.1</sub>Ni<sub>0.9</sub>, and Cu<sub>0.2</sub>Ni<sub>0.8</sub> exhibited a better conversion at 1.5 V vs. Ag/AgCl, yielding CO as the major reduction product. Cu<sub>0.05</sub>Ni<sub>0.95</sub> turned out to be the best of all, producing over 200 ppm of CO+CH<sub>4</sub> mixture, as shown in Figure 81. Cu<sub>0.5</sub>Ni<sub>0.5</sub>, unlike the other MOFs, generates more CO than CH<sub>4</sub> at 1.3 and 1.7 V vs. Ag/AgCl. Such result agrees with the literature where Ni-MOFs are reported to produce more CO and Cu-MOFs more hydrocarbons such as methane.<sup>221,222</sup> Also in our case, it can therefore be deduced that the decrease in the copper content leads to the formation of CO rather than methane. The best Faradaic efficiency is achieved by Cu<sub>0.05</sub>Ni<sub>0.95</sub> with an overall value of ~50%, as observable in Figure 82.

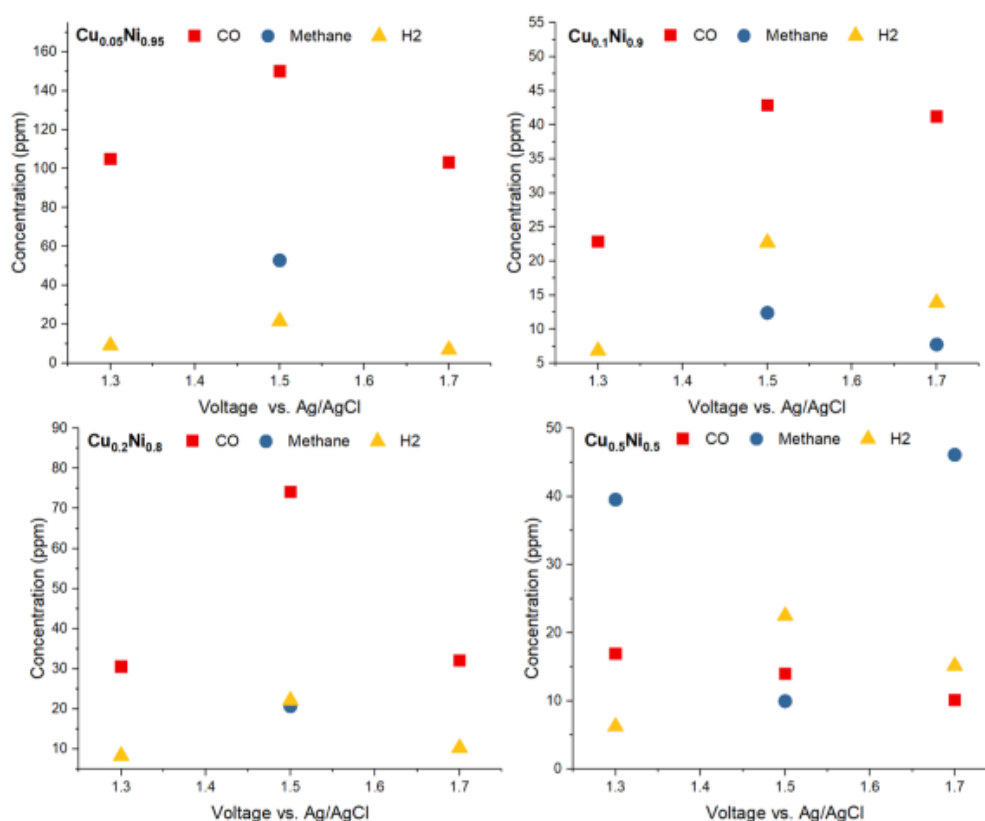


FIGURE 81 Products concentration in ppm after electroreduction of CO<sub>2</sub> at different voltages (1.3, 1.5 and 1.7 V vs. Ag/AgCl) with the four Cu/Ni mixed MOFs.

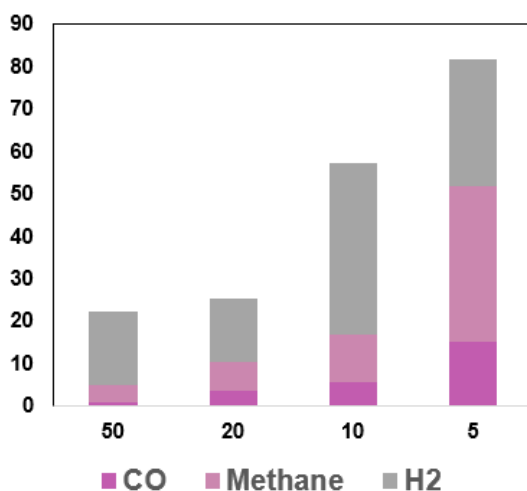


FIGURE 82 Faradaic efficiency calculated for electroreduction tests for (in order from right): 5)  $\text{Cu}_{0.05}\text{Ni}_{0.95}$ , 10)  $\text{Cu}_{0.1}\text{Ni}_{0.9}$ , 20)  $\text{Cu}_{0.2}\text{Ni}_{0.8}$  and 50)  $\text{Cu}_{0.5}\text{Ni}_{0.5}$ .

To the best of our knowledge, this work is the first example of  $\text{CO}_2$  electroreduction with mixed metal (Cu/Ni) MOFs. The four have been also characterized after electrocatalytic tests by TEM, PXRD and XPS analyses.

PXRD analyses (Figure 83) revealed that MOFs crystallinity is not already retained after dropping on carbon paper and there's a variation in the peaks observed before and after the electrocatalytic tests.

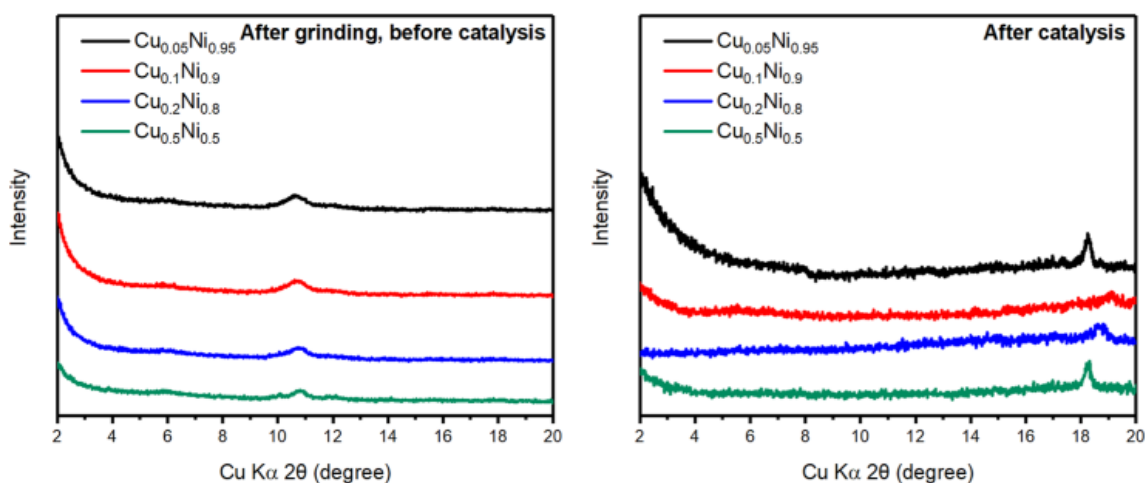


FIGURE 83 PXRD profiles of the four Cu/Ni mixed MOFs before and after electrocatalytic tests.

TEM images, instead, reveal the presence of nanoparticles of 2-4 nm for  $\text{Cu}_{0.05}\text{Ni}_{0.95}$  and  $\text{Cu}_{0.5}\text{Ni}_{0.5}$ , as highlighted in Figure 84. Ni 2p and Cu 2p XPS spectra prove the existence of Cu(II) and Ni(II) species for all Cu/Ni mixed MOFs. XPS spectra of  $\text{Cu}_{0.5}\text{Ni}_{0.5}$  are reported as representative in Figure 85. Peaks attributable to Cu(II)  $2p_{3/2}$  electronic states are detected at

binding energy (BE) of 934 eV and 944 eV (satellite peak) while the Cu(II) 2p<sub>1/2</sub> electronic states are observed at 955 eV and 965 eV. In the case of Ni(II), peaks related to Ni(II) 2p<sub>3/2</sub> electronic states are seen at 855 eV and 862 eV (satellite peak) while the Cu(II) 2p<sub>1/2</sub> electronic states are observed at 872 eV and 880 eV. New peaks are revealed after the catalysis, suggesting a decomposition of the MOF and the formation of the two species Ni(0) and Cu(0) and confirming the presence of nanoparticles .

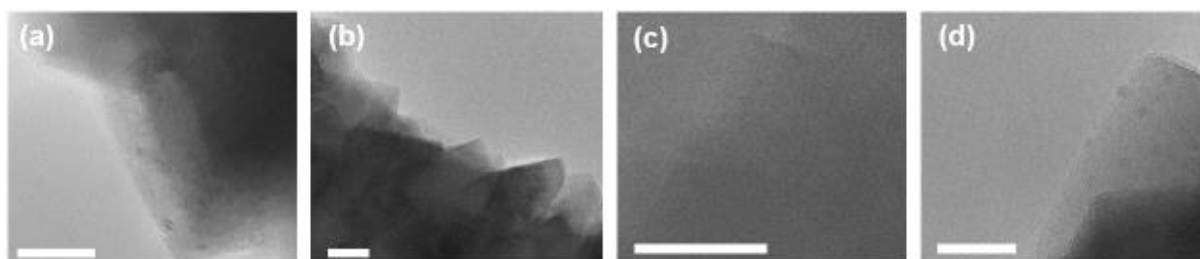


FIGURE 84 TEM images of (a)  $Cu_{0.05}Ni_{0.95}$ , (b)  $Cu_{0.1}Ni_{0.9}$ , (c)  $Cu_{0.2}Ni_{0.8}$  and (d)  $Cu_{0.5}Ni_{0.5}$ . Bars length correspond to 20 nm.

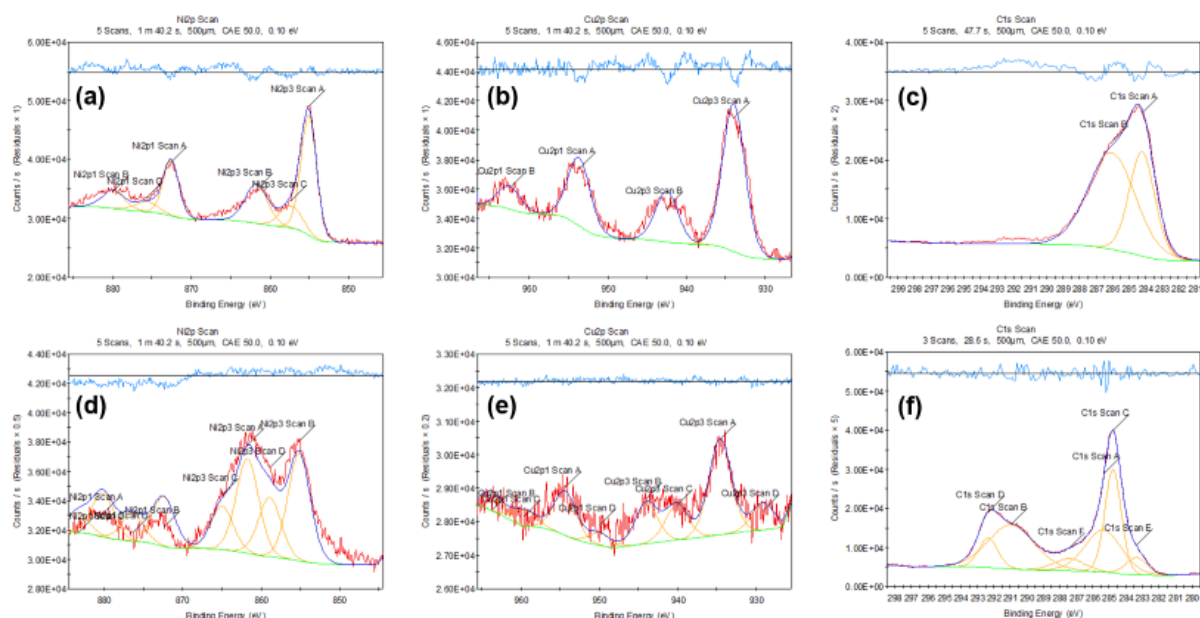


FIGURE 85 XPS spectra of  $Cu_{0.5}Ni_{0.5}$ : Ni 2p (a-b), Cu 2p (c-d) and C 1s (d-e).



## 5.4 Conclusions

Four Cu/Ni mixed MOFs (**Cu<sub>0.05</sub>Ni<sub>0.95</sub>**, **Cu<sub>0.1</sub>Ni<sub>0.9</sub>**, **Cu<sub>0.2</sub>Ni<sub>0.8</sub>** and **Cu<sub>0.5</sub>Ni<sub>0.5</sub>**) have been synthesized, characterized through a wide range of techniques (PXRD, TGA, IR, porosimetry, SEM, EDX, ICP, XPS), and tested as catalysts in the electroreduction of CO<sub>2</sub> into CH<sub>4</sub> and CO (CV and CA). ICP and EDX have confirmed the formation of the mixed MOFs in the expected Cu(II) / Ni(II) molar ratio. The four MOFs turned out to be macroporous with low BET surface area values (140-240 m<sup>2</sup>/g, N<sub>2</sub> at 77K). Nevertheless, the presence of two amino tags in the organic linker 3,5-diamino-4,4'-bipyrazolate, helped the CO<sub>2</sub> adsorption (4-20 wt. %), also proved by the evaluation of the heat of adsorption 24.0-26.2 KJ/mol). It is here reiterated that, as far as we know, this is the first example of electroreduction of carbon dioxide with mixed metal MOFs. CV and CA demonstrated a higher production of CO with a higher nickel content (**Cu<sub>0.05</sub>Ni<sub>0.95</sub>**), whereas CH<sub>4</sub> is the most abundant product with the MOF with the highest copper content (**Cu<sub>0.5</sub>Ni<sub>0.5</sub>**). In any case, **Cu<sub>0.05</sub>Ni<sub>0.95</sub>** exhibited generally the best performance with an overall production of 200 ppm of CH<sub>4</sub> + CO mixture. Catalytic tests, however, produce a partial decomposition of the MOFs structure, generating Cu(0) and Ni(0) nanoparticles (2-4 nm) observed in TEM images and detected by XPS spectra. Future perspectives are aimed at obtaining more stable systems with higher surface area, in order to improve CO<sub>2</sub> adsorption and its conversion.

## Bibliography

1. Batten, S. R. *et al.* Terminology of metal–organic frameworks and coordination polymers (IUPAC Recommendations 2013)\*. *Pure Appl. Chem.* **85**, 1715–1724 (2013).
2. Shibata, Y. No Titl. *J. Coll. Sci.* **37**, 1–17 (1916).
3. Mosca, N. Novel Metal-Organic Frameworks (MOFs) based on robust N-donor (and O-donor) ligands for Gas Adsorptions, Theoretical Insight, Thermal Behaviour, Structural Analysis and Biological Investigations. (University of Camerino, 2017).
4. Batten, S. R. *et al.* Coordination polymers, metal-organic frameworks and the need for terminology guidelines. *CrystEngComm* **14**, 3001–3004 (2012).
5. Boldog, I., Rusanov, E. B., Chernega, A. N., Sieler, J. & Domasevitch, K. V. One- and two-dimensional coordination polymers of 3,3',5,5'-tetramethyl-4,4'-bipyrazolyl, a new perspective crystal engineering module. *Polyhedron* **20**, 887–897 (2001).
6. Venkataraman, D. *et al.* Coordination Networks Based on Multitopic Ligands and Silver(I) Salts: A Study of Network Connectivity and Topology as a Function of Counterion. *Chem. Mater.* **8**, 2030–2040 (1996).
7. Qin, Z., Li, Y. & Gu, N. Progress in Applications of Prussian Blue Nanoparticles in Biomedicine. *Adv. Healthc. Mater.* **7**, 1–13 (2018).
8. Kuzevanova, I. S. *et al.* Spin crossover in iron(II) Hofmann clathrates analogues with 1,2,3-triazole. *Dalt. Trans.* **50**, 9250–9258 (2021).
9. Hofmann, K. A. & Küspert, F. No Titl. *Z. Anorg Chem.* **15**, 204–207 (1897).
10. Rungtaweeworanit, B., Diercks, C. S., Kalmutzki, M. J. & Yaghi, O. M. Spiers Memorial Lecture: Progress and prospects of reticular chemistry. *Faraday Discuss.* **201**, 9–45 (2017).
11. Kinoshita, M., Yanagida, S., Gessei, T. & Monkawa, A. Precursor concentration effects on crystallite size and enzyme immobilization efficiency of Enzyme@ZIF-8 composite. *J. Cryst. Growth* **600**, 126877 (2022).
12. Yaghi, O. M. *et al.* Reticular synthesis and the design of new materials. *Nature* **423**, 705–714 (2003).
13. Nabipour, H., Mozafari, M. & Hu, Y. *Nomenclature of MOFs. Metal-Organic Frameworks for Biomedical Applications* (Elsevier Inc., 2020). doi:10.1016/B978-0-12-816984-1.00002-0.
14. Bucior, B. J. *et al.* Identification Schemes for Metal-Organic Frameworks To Enable Rapid Search and Cheminformatics Analysis. *Cryst. Growth Des.* **19**, 6682–6697 (2019).
15. Yaghi, O. M., Kalmutzki, M. J. & Diercks, C. S. *Introduction to Reticular Chemistry: Metal-Organic Frameworks and Covalent Organic Frameworks.* (2019).
16. Yaghi, O. M. & Li, H. Hydrothermal Synthesis of a Metal-Organic Framework Containing Large Rectangular Channels. *J. Am. Chem. Soc.* **117**, 10401–10402 (1995).
17. Yaghi, O. M., Li, G. & Li Hailian. Selective binding and removal of guests in a microporous metal-organic framework. *Nature* **378**, 703–706 (1995).
18. Li, H., Eddaoudi, M., Groy, T. L. & Yaghi, O. M. Establishing microporosity in open metal-organic frameworks: Gas sorption isotherms for Zn(BDC) (BDC = 1,4-benzenedicarboxylate) [28]. *J. Am. Chem. Soc.* **120**, 8571–8572 (1998).

19. Hoskins, B. F. & Robson, R. Infinite Polymeric Frameworks Consisting of Three Dimensionally Linked Rod-like Segments. *J. Am. Chem. Soc.* **111**, 5962–5964 (1989).
20. Robson, R. A net-based approach to coordination polymers. *J. Chem. Soc. Dalton Trans.* 3735–3744 (2000) doi:10.1039/b003591m.
21. Li, H., Eddaoudi, M., O’Keeffe, M. & Yaghi, O. M. Design and synthesis of an exceptionally stable and highly porous metal-organic framework. **402**, 276–279 (1999).
22. Rosi, N. L. *et al.* Hydrogen Storage in Microporous Metal-Organic Frameworks. **300**, 1127–1129 (2003).
23. Yaghi, O. M. Reticular Chemistry in All Dimensions. *ACS Cent. Sci.* **5**, 1295–1300 (2019).
24. Liu, J. *et al.* Applications of metal-organic frameworks in heterogeneous supramolecular catalysis. *Chem. Soc. Rev.* **43**, 6011–6061 (2014).
25. Schneemann, A. *et al.* Flexible metal-organic frameworks. *Chem. Soc. Rev.* **43**, 6062–6096 (2014).
26. Ma, M. *et al.* Iron-based metal-organic frameworks MIL-88B and NH<sub>2</sub>-MIL-88B: High quality microwave synthesis and solvent-induced lattice ‘breathing’. *Cryst. Growth Des.* **13**, 2286–2291 (2013).
27. Loiseau, T. *et al.* A Rationale for the Large Breathing of the Porous Aluminum Terephthalate (MIL-53) Upon Hydration. *Chem. - A Eur. J.* **10**, 1373–1382 (2004).
28. Zhao, J. *et al.* One-dimensional coordination polymers based on metal–nitrogen linkages. *Coord. Chem. Rev.* **471**, 214735 (2022).
29. Leong, W. L. & Vittal, J. J. One-dimensional coordination polymers: Complexity and diversity in structures, properties, and applications. *Chem. Rev.* **111**, 688–764 (2011).
30. Wojciechowska, A. *et al.* Structural, spectroscopic, magnetic behavior and DFT investigations of L-tyrosinato nickel(II) coordination polymer. *New J. Chem.* **39**, 6813–6822 (2015).
31. Robin, A. Y. & Fromm, K. M. Coordination polymer networks with O- and N-donors: What they are, why and how they are made. *Coord. Chem. Rev.* **250**, 2127–2157 (2006).
32. Das, S., Madhavaiah, C., Verma, S. & Bharadwaj, P. K. A reusable zigzag copper(II) coordination polymer with bio-essential constituents as a facile DNA scission agent. *Inorganica Chim. Acta* **358**, 3236–3240 (2005).
33. Zhao, J. *et al.* Five naphthalene-Amide-bridged Ni(II) complexes: Electrochemistry, bifunctional fluorescence responses, removal of contaminants and optimization by CVD. *CrystEngComm* **22**, 1330–1339 (2020).
34. Dutta, B. *et al.* Synthesis of a Zn(II)-based 1D zigzag coordination polymer for the fabrication of optoelectronic devices with remarkably high photosensitivity. *Inorg. Chem. Front.* **6**, 1245–1252 (2019).
35. Zhang, X. *et al.* Syntheses, structural diversity and photocatalytic properties of three coordination polymers assembled by different N-heterocyclic ligands. *New J. Chem.* **43**, 320–329 (2019).
36. Han, Z. B., Zhang, G. X., Ji, J. W. & Zhang, P. Synthesis and crystal structure of a 1D coordination polymer [Cd(pydc)(phen)]<sub>n</sub> (H<sub>2</sub>pydc = pyridine-2,3-dicarboxylic acid, phen = 1,10-phenanthroline). *J. Chem. Crystallogr.* **39**, 169–172 (2009).
37. Kole, G. K., Peedikakkal, A. M. P., Toh, B. M. F. & Vittal, J. J. Solid-state structural transformations and photoreactivity of 1D-ladder coordination polymers of PbII. *Chem. - A Eur. J.* **19**, 3962–3968 (2013).
38. Sun, R. *et al.* Co-ligand tuned pyrimidine-2-carboxylate Mn(II) complexes from a 2D 63 layer to an

- interpenetrated srs-net. *Dalt. Trans.* **46**, 8593–8597 (2017).
39. Kajiro, H., Kondo, A., Kaneko, K. & Kanoh, H. Flexible two-dimensional square-grid coordination polymers: Structures and functions. *Int. J. Mol. Sci.* **11**, 3803–3845 (2010).
  40. Yin, Y. Y. *et al.* A 2D honeycomb coordination polymer of [Cd(TMA)]<sub>n</sub> (H<sub>2</sub>TMA = 3-thiophenemalonic acid) for humidity sensing applications. *Inorg. Chem. Commun.* **125**, 108440 (2021).
  41. Xiong, R. G. *et al.* Opto-electronic multifunctional chiral diamondoid-network coordination polymer: Bis{4-[2-(4-pyridyl)ethenyl]benzoato}zinc with high thermal stability. *Chem. Commun.* 2061–2062 (2000) doi:10.1039/b004980h.
  42. Chen, B., Fronczek, F. R., Courtney, B. H. & Zapata, F.  $\alpha$ -Po Nets of Copper(II)-trans-1,4-Cyclohexanedicarboxylate Frameworks Based on a Paddle-Wheel Building Block and Its Enlarged Dimer. *Cryst. Growth Des.* **2**, 4–7 (2006).
  43. Xiao, D. *et al.* A 3D interpenetrated rutile coordination framework formed by dinuclear cadmium clusters and 4,4'-sulfonyldibenzoate. *Solid State Sci.* **13**, 1573–1578 (2011).
  44. Abrahams, B. F., Elliott, R. W., Hudson, T. A. & Robson, R. PtS-Related {[CuI(F4TCNQII-)]-} $\infty$  Networks. *Cryst. Growth Des.* **13**, 3018–3027 (2013).
  45. Kalmutzki, M. J., Hanikel, N. & Yaghi, O. M. Secondary building units as the tuning point in the development of the reticular chemistry of MOFs. *Sci. Adv.* **4**, (2018).
  46. Eddaoudi, M. *et al.* Systematic design of pore size and functionality in isorecticular MOFs and their application in methane storage. *Science (80-. )*. **295**, 469–472 (2002).
  47. Forgan, R. S. Modulated self-assembly of metal-organic frameworks. *Chem. Sci.* **11**, 4546–4562 (2020).
  48. Sun, Y. & Zhou, H. C. Recent progress in the synthesis of metal-organic frameworks. *Sci. Technol. Adv. Mater.* **16**, 54202 (2015).
  49. Safaei, M. *et al.* A review on metal-organic frameworks: Synthesis and applications. *TrAC - Trends Anal. Chem.* **118**, 401–425 (2019).
  50. Stock, N. & Biswas, S. Synthesis of Metal-Organic Frameworks ( MOFs ): Routes to Various MOF Topologies, Morphologies, and Composites. *Chem. Rev.* **112**, 933–969 (2012).
  51. Sharanyakanth, P. S. & Radhakrishnan, M. Synthesis of metal-organic frameworks (MOFs) and its application in food packaging: A critical review. *Trends Food Sci. Technol.* **104**, 102–116 (2020).
  52. Duan, C. *et al.* Recent advancements in metal-organic frameworks for green applications. *Green Energy and Environment* (2021) doi:10.1016/j.gee.2020.04.006.
  53. Remya, V. R. & Kurian, M. Synthesis and catalytic applications of metal-organic frameworks: a review on recent literature. *Int. Nano Lett.* **9**, 17–29 (2019).
  54. Marthala, V. R. R. *et al.* Solvothermal synthesis and characterization of large-crystal all-silica, aluminum-, and boron-containing ferrierite zeolites. *Chem. Mater.* **23**, 2521–2528 (2011).
  55. Roth, W. J., Nachtigall, P., Morris, R. E. & Jir, C. Two-Dimensional Zeolites: Current Status and Perspectives. *Chem. Rev.* **114**, 4807–4837 (2014).
  56. Comins, D. L. & Joseph, S. P. N,N-Dimethylformamide. in *Encyclopedia of Reagents for Organic Synthesis* (2001).
  57. Banerjee, D., Kim, S. J., Borkowski, L. A., Xu, W. & Parise, J. B. Solvothermal synthesis and structural

- characterization of ultralight metal coordination networks. *Cryst. Growth Des.* **10**, 709–715 (2010).
58. Chen, C. *et al.* Microwave-Assisted Rapid Synthesis of Well-Shaped MOF-74 (Ni) for CO<sub>2</sub> Efficient Capture. *Inorg. Chem.* **58**, 2717–2728 (2019).
  59. Lee, Y. R., Kim, J. & Ahn, W. S. Synthesis of metal-organic frameworks: A mini review. *Korean J. Chem. Eng.* **30**, 1667–1680 (2013).
  60. Mueller U, Puetter H, Hesse M and Wessel H 2005 Patent WO 2005/049892.
  61. Zong, S. *et al.* Impact of linker functionalization on the adsorption of nitrogen-containing compounds in HKUST-1. *Dalt. Trans.* **49**, 12610–12621 (2020).
  62. Liu, Y. *et al.* Electrochemical Synthesis of Large Area Two-Dimensional Metal–Organic Framework Films on Copper Anodes. *Angew. Chemie - Int. Ed.* **60**, 2887–2891 (2021).
  63. Głowniak, S., Szcześniak, B., Choma, J. & Jaroniec, M. Mechanochemistry: Toward green synthesis of metal–organic frameworks. *Mater. Today* **46**, 109–124 (2021).
  64. Zahn, G. *et al.* A water-born Zr-based porous coordination polymer: Modulated synthesis of Zr-fumarate MOF. *Microporous Mesoporous Mater.* **203**, 186–194 (2015).
  65. Szcześniak, B., Borysiuk, S., Choma, J. & Jaroniec, M. Mechanochemical synthesis of highly porous materials. *Mater. Horizons* **7**, 1457–1473 (2020).
  66. Li, J. X., Qin, Z. Bin, Li, Y. H. & Cui, G. H. Sonochemical synthesis and properties of two new nanostructured silver(I) coordination polymers. *Ultrason. Sonochem.* **48**, 127–135 (2018).
  67. Farha, O. K. & Hupp, J. T. Rational Design, Synthesis, Purification, and Activation of Metal–Organic Framework Materials. *Acc. Chem. Res.* **43**, 1166–1175 (2010).
  68. Woodliffe, J. L., Ferrari, R. S., Ahmed, I. & Laybourn, A. Evaluating the purification and activation of metal-organic frameworks from a technical and circular economy perspective. *Coord. Chem. Rev.* **428**, 213578 (2021).
  69. Ma, J., Kalenak, A. P., Wong-Foy, A. G. & Matzger, A. J. Rapid Guest Exchange and Ultra-Low Surface Tension Solvents Optimize Metal–Organic Framework Activation. *Angew. Chemie* **129**, 14810–14813 (2017).
  70. Al Amery, N., Abid, H. R., Al-Saadi, S., Wang, S. & Liu, S. Facile directions for synthesis, modification and activation of MOFs. *Mater. Today Chem.* **17**, 100343 (2020).
  71. Mousavi, D. V. *et al.* Adsorption performance of UiO-66 towards organic dyes: Effect of activation conditions. *J. Mol. Liq.* **321**, 114487 (2021).
  72. Mondloch, J. E., Karagiari, O., Farha, O. K. & Hupp, J. T. Activation of metal-organic framework materials. *CrystEngComm* **15**, 9258–9264 (2013).
  73. Howarth, A. J. *et al.* Best practices for the synthesis, activation, and characterization of metal–organic frameworks. *Chem. Mater.* **29**, 26–39 (2017).
  74. Zhang, X. *et al.* A historical overview of the activation and porosity of metal-organic frameworks. *Chem. Soc. Rev.* **49**, 7406–7427 (2020).
  75. Mondloch, J. E. *et al.* Vapor-phase metalation by atomic layer deposition in a metal-organic framework. *J. Am. Chem. Soc.* **135**, 10294–10297 (2013).
  76. Lee, E. J., Bae, J., Choi, K. M. & Jeong, N. C. Exploiting Microwave Chemistry for Activation of Metal-

- Organic Frameworks. *ACS Appl. Mater. Interfaces* **11**, 34989–34996 (2019).
77. Thommes, M. *et al.* Physisorption of gases, with special reference to the evaluation of surface area and pore size distribution (IUPAC Technical Report). *Pure Appl. Chem.* **87**, 1051–1069 (2015).
  78. Eley, D. D., Moran, D. M. & Rochester, C. H. Infra-red study of interaction between hydrogen and supported platinum catalysts. *Trans. Faraday Soc.* **64**, 2168–2180 (1968).
  79. Sing, K. The use of nitrogen adsorption for the characterisation of porous materials. *Colloids Surfaces A Physicochem. Eng. Asp.* **187–188**, 3–9 (2001).
  80. Walton, K. S. & Snurr, R. Q. Applicability of the BET method for determining surface areas of microporous metal-organic frameworks. *J. Am. Chem. Soc.* **129**, 8552–8556 (2007).
  81. Bardestani, R., Patience, G. S. & Kaliaguine, S. Experimental methods in chemical engineering: specific surface area and pore size distribution measurements—BET, BJH, and DFT. *Can. J. Chem. Eng.* **97**, 2781–2791 (2019).
  82. Ambroz, F., Macdonald, T. J., Martis, V. & Parkin, I. P. Evaluation of the BET theory for the characterization of meso and microporous MOFs. *Small Methods* **2**, 1–17 (2018).
  83. Rouquerol, J., Llewellyn, P. & Rouquerol, F. Is the bet equation applicable to microporous adsorbents? *Stud. Surf. Sci. Catal.* **160**, 49,56 (2007).
  84. Islamoglu, T. *et al.* Are you using the right probe molecules for assessing the textural properties of metal-organic frameworks? *J. Mater. Chem. A* **10**, 157–173 (2022).
  85. Mohanan, K., Martin, A. R., Toupet, L., Smietana, M. & Vasseur, J.-J. Three-Component Reaction Using the Bestmann-Ohira Reagent: A Regioselective Synthesis of Phosphonyl Pyrazole Rings. *Angew. Chemie* **122**, 3264–3267 (2010).
  86. Campitelli, P. *et al.* Ionic liquids vs conventional solvents: A comparative study in the selective catalytic oxidations promoted by oxovanadium(IV) complexes. *Appl. Catal. A Gen.* **599**, 117622 (2020).
  87. Keter, F. K. & Darkwa, J. Perspective: The potential of pyrazole-based compounds in medicine. *BioMetals* **25**, 9–21 (2012).
  88. Bekhit, A. A., Ashour, H. M. A. & Guemei, A. A. Novel pyrazole derivatives as potential promising anti-inflammatory antimicrobial agents. *Arch. Pharm. (Weinheim)*. **338**, 167–174 (2005).
  89. De, A. *et al.* Lanthanide clusters of phenanthroline containing a pyridine-pyrazole based ligand: magnetism and cell imaging. *Dalt. Trans.* **50**, 3593–3609 (2021).
  90. Yu, S. Y. & Lu, H. L. From Metal-Metal Bonding to Supra-Metal-Metal Bonding Directed Self-Assembly: Supramolecular Architectures of Group 10 and 11 Metals with Ligands from Mono- to Poly-Pyrazoles. *Isr. J. Chem.* **59**, 166–183 (2019).
  91. Zhang, J. P., Zhang, Y. B., Lin, J. Bin & Chen, X. M. Metal azolate frameworks: From crystal engineering to functional materials. *Chem. Rev.* **112**, 1001–1033 (2012).
  92. Yuan, S. *et al.* Stable Metal–Organic Frameworks: Design, Synthesis, and Applications. *Adv. Mater.* **30**, 1–35 (2018).
  93. Masciocchi, N. *et al.* Metal imidazolato complexes: Synthesis, characterization, and x-ray powder diffraction studies of group 10 coordination polymers. *Inorg. Chem.* **38**, 3657–3664 (1999).
  94. Fujisawa, K., Nemoto, T., Morishima, Y. & Leznoff, D. B. Synthesis and structural characterization of a

- silver(I) pyrazolato coordination polymer. *Molecules* **26**, 1–12 (2021).
95. Marchetti, F., Pettinari, C. & Pettinari, R. Acylpyrazolone ligands: Synthesis, structures, metal coordination chemistry and applications. *Coord. Chem. Rev.* **249**, 2909–2945 (2005).
  96. Marchetti, F., Pettinari, C., Di Nicola, C., Tombesi, A. & Pettinari, R. Coordination chemistry of pyrazolone-based ligands and applications of their metal complexes. *Coord. Chem. Rev.* **401**, 213069 (2019).
  97. Cingolani, A. *et al.* Sorption - Desorption Behavior of Bispyrazolato - Copper ( II ) 1D Coordination Polymers. *J. Am. Chem. Soc.* 6144–6145 (2005).
  98. Ehler, M. K., Rettig, J., Storr, A., Thompson, R. C. & Trotter, J. Metal pyrazolate polymers. Part 2. Synthesis, structure, and magnetic properties of  $[\text{Cu}(4\text{-Xpz})_2]_x$ , polymers (where X = Cl, Br, Me, H; pz = pyrazolate). *Can. J. Chem.* **69**, 432–439 (1990).
  99. Di Nicola, C. *et al.* Investigation on the interconversion from DMF-solvated to unsolvated copper(II) pyrazolate coordination polymers. *CrystEngComm* **22**, 3294–3308 (2020).
  100. Burch, N. C., Jasuja, H. & Walton, K. S. Water stability and adsorption in metal-organic frameworks. *Chem. Rev.* **114**, 10575–10612 (2014).
  101. Wade, C. R., Corrales-Sanchez, T., Narayan, T. C. & Dincă, M. Postsynthetic tuning of hydrophilicity in pyrazolate MOFs to modulate water adsorption properties. *Energy Environ. Sci.* **6**, 2172–2177 (2013).
  102. Pettinari, C., Tăbăcaru, A. & Galli, S. Coordination polymers and metal-organic frameworks based on poly(pyrazole)-containing ligands. *Coord. Chem. Rev.* **307**, 1–31 (2016).
  103. Pettinari, C. *et al.* Novel coordination frameworks incorporating the 4,4'-bipyrazolyl ditopic ligand. *Inorg. Chem.* **51**, 5235–5245 (2012).
  104. Spirkl, S. *et al.* Single-Crystal to Single-Crystal Transformation of a Nonporous Fe(II) Metal-Organic Framework into a Porous Metal-Organic Framework via a Solid-State Reaction. *Inorg. Chem.* **56**, 12337–12347 (2017).
  105. Spirkl, S. *et al.* Fe/Ga-CFA-6 - Metal organic frameworks featuring trivalent metal centers and the 4,4'-bipyrazolyl ligand. *CrystEngComm* **17**, 313–322 (2015).
  106. He, T. *et al.* Functionalized Base-Stable Metal–Organic Frameworks for Selective CO<sub>2</sub> Adsorption and Proton Conduction. *ChemPhysChem* **18**, 3245–3252 (2017).
  107. Mosca, N. *et al.* CH<sub>3</sub>-Tagged Bis(pyrazolato)-Based Coordination Polymers and Metal-Organic Frameworks: An Experimental and Theoretical Insight. *Cryst. Growth Des.* **17**, 3854–3867 (2017).
  108. Tăbăcaru, A. *et al.* Enlarging an Isorecticular Family: 3,3',5,5'-Tetramethyl-4,4'- bipyrazolato-Based Porous Coordination Polymers. *Cryst. Growth Des.* **13**, 3087–3097 (2013).
  109. Baima, J., Macchieraldo, R., Pettinari, C. & Casassa, S. Ab initio investigation of the affinity of novel bipyrazolate-based MOFs towards H<sub>2</sub> and CO<sub>2</sub>. *CrystEngComm* **17**, 448–455 (2015).
  110. Timokhin, I. *et al.* Novel coordination polymers with (Pyrazolato)-based tectons: Catalytic activity in the peroxidative oxidation of alcohols and cyclohexane. *Cryst. Growth Des.* **15**, 2303–2317 (2015).
  111. Mosca, N. *et al.* Nitro-functionalized Bis(pyrazolate) Metal–Organic Frameworks as Carbon Dioxide Capture Materials under Ambient Conditions. *Chem. - A Eur. J.* **24**, 13170–13180 (2018).
  112. Vismara, R. *et al.* Amino-decorated bis(pyrazolate) metal-organic frameworks for carbon dioxide

- capture and green conversion into cyclic carbonates. *Inorg. Chem. Front.* **6**, 533–545 (2019).
113. Colombo, V. *et al.* Tuning the adsorption properties of isoreticular pyrazolate-based metal-organic frameworks through ligand modification. *J. Am. Chem. Soc.* **134**, 12830–12843 (2012).
  114. He, T. *et al.* Trace removal of benzene vapour using double-walled metal-dipyrazolate frameworks. *Nat. Mater.* **21**, 689–695 (2022).
  115. Mason, J. A. *et al.* Methane storage in flexible metal-organic frameworks with intrinsic thermal management. *Nature* **527**, 357–361 (2015).
  116. Choi, H. J., Dinca, M. & Long, J. R. Broadly Hysteretic H<sub>2</sub> Adsorption in the Microporous Metal-Organic Framework Co(1,4-benzenedipyrazolate). *J. Am. Chem. Soc.* 1–23 (2008).
  117. Taylor, M. K. *et al.* Tuning the Adsorption-Induced Phase Change in the Flexible Metal-Organic Framework Co(bdp). *J. Am. Chem. Soc.* **138**, 15019–15026 (2016).
  118. Gupta, M. & Vittal, J. J. Control of interpenetration and structural transformations in the interpenetrated MOFs. *Coord. Chem. Rev.* **435**, 213789 (2021).
  119. Farha, O. K. *et al.* Metal-organic framework materials with ultrahigh surface areas: Is the sky the limit? *J. Am. Chem. Soc.* **134**, 15016–15021 (2012).
  120. Shen, M. *et al.* Antibacterial applications of metal-organic frameworks and their composites. *Compr. Rev. Food Sci. Food Saf.* **19**, 1397–1419 (2020).
  121. Pettinari, C. *et al.* Antimicrobial MOFs. *Coord. Chem. Rev.* **446**, 214121 (2021).
  122. Zhao, X. *et al.* The application of MOFs-based materials for antibacterials adsorption. *Coord. Chem. Rev.* **440**, 213970 (2021).
  123. Pettinari, C. & Tombesi, A. Metal-organic frameworks for chemical conversion of carbon dioxide. *MRS Energy Sustain.* **7**, 1–14 (2020).
  124. Pettinari, C. & Tombesi, A. Metal-organic frameworks for carbon dioxide capture. *MRS Energy Sustain.* **7**, 1–43 (2020).
  125. Czaja, A. U., Trukhan, N. & Müller, U. Industrial applications of metal-organic frameworks. *Chem. Soc. Rev.* **38**, 1284–1293 (2009).
  126. Ryu, U. J. *et al.* Recent advances in process engineering and upcoming applications of metal-organic frameworks. *Coord. Chem. Rev.* **426**, 213544 (2021).
  127. Yang, J. & Yang, Y. W. Metal-Organic Frameworks for Biomedical Applications. *Small* **16**, (2020).
  128. Mallakpour, S., Nikkhoo, E. & Hussain, C. M. Application of MOF materials as drug delivery systems for cancer therapy and dermal treatment. *Coord. Chem. Rev.* **451**, 214262 (2022).
  129. Chen, W. & Wu, C. Synthesis, functionalization, and applications of metal-organic frameworks in biomedicine. *Dalt. Trans.* **47**, 2114–2133 (2018).
  130. Keskin, S. & Kizilel, S. Biomedical Applications of Metal Organic Frameworks. *Ind. Eng. Chem. Res.* **50**, 1799–1812 (2011).
  131. Sun, Y. *et al.* Metal-Organic Framework Nanocarriers for Drug Delivery in Biomedical Applications. *Nano-Micro Lett.* **12**, 1–29 (2020).
  132. Qiu, Q., Chen, H., Wang, Y. & Ying, Y. Recent advances in the rational synthesis and sensing applications of metal-organic framework biocomposites. *Coord. Chem. Rev.* **387**, 60–78 (2019).



133. McKinlay, A. C. *et al.* BioMOFs: Metal-organic frameworks for biological and medical applications. *Angew. Chemie - Int. Ed.* **49**, 6260–6266 (2010).
134. Liu, L., Zhou, Y., Liu, S. & Xu, M. The Applications of Metal–Organic Frameworks in Electrochemical Sensors. *ChemElectroChem* **5**, 6–19 (2018).
135. Boorboor Ajdari, F. *et al.* A review on the field patents and recent developments over the application of metal organic frameworks (MOFs) in supercapacitors. *Coord. Chem. Rev.* **422**, 213441 (2020).
136. Zhang, L., Liu, H., Shi, W. & Cheng, P. Synthesis strategies and potential applications of metal-organic frameworks for electrode materials for rechargeable lithium ion batteries. *Coord. Chem. Rev.* **388**, 293–309 (2019).
137. Wang, H., Zhu, Q. L., Zou, R. & Xu, Q. Metal-Organic Frameworks for Energy Applications. *Chem* **2**, 52–80 (2017).
138. Cheng, W., Tang, X., Zhang, Y., Wu, D. & Yang, W. Applications of metal-organic framework (MOF)-based sensors for food safety: Enhancing mechanisms and recent advances. *Trends Food Sci. Technol.* **112**, 268–282 (2021).
139. Wu, K. J. *et al.* Application of metal–organic framework for the adsorption and detection of food contamination. *TrAC - Trends Anal. Chem.* **143**, 116384 (2021).
140. Li, H. *et al.* Porous metal-organic frameworks for gas storage and separation: Status and challenges. *EnergyChem* **1**, 100006 (2019).
141. Li, H. *et al.* Recent advances in gas storage and separation using metal–organic frameworks. *Mater. Today* **21**, 108–121 (2018).
142. Zhang, Y. *et al.* Application of MOFs and COFs for photocatalysis in CO<sub>2</sub> reduction, H<sub>2</sub> generation, and environmental treatment. *EnergyChem* **4**, 100078 (2022).
143. Silva, A. R. M. *et al.* The Chemistry and Applications of Metal–Organic Frameworks (MOFs) as Industrial Enzyme Immobilization Systems. *Molecules* **27**, (2022).
144. Kuppler, R. J. *et al.* Potential applications of metal-organic frameworks. *Coord. Chem. Rev.* **253**, 3042–3066 (2009).
145. Yu, Y., Ren, Y., Shen, W., Deng, H. & Gao, Z. Applications of metal-organic frameworks as stationary phases in chromatography. *TrAC - Trends Anal. Chem.* **50**, 33–41 (2013).
146. Jun, B. M. *et al.* Applications of metal-organic framework based membranes in water purification: A review. *Sep. Purif. Technol.* **247**, 116947 (2020).
147. Zhou, H. C. J. & Kitagawa, S. Metal-Organic Frameworks (MOFs). *Chem. Soc. Rev.* **43**, 5415–5418 (2014).
148. Ricco, R. *et al.* Emerging applications of metal-organic frameworks. *CrystEngComm* **18**, 6532–6542 (2016).
149. Zhao, Y. Emerging applications of metal-organic frameworks and covalent organic frameworks. *Chem. Mater.* **28**, 8079–8081 (2016).
150. Li, S. & Huo, F. Metal-organic framework composites: From fundamentals to applications. *Nanoscale* **7**, 7482–7501 (2015).
151. Pettinari, C., Marchetti, F., Mosca, N., Tosi, G. & Drozdov, A. Application of metal – organic

- frameworks. *Polym. Int.* **66**, 731–744 (2017).
152. Jo, J. H., Kim, H. C., Huh, S., Kim, Y. & Lee, D. N. Antibacterial activities of Cu-MOFs containing glutarates and bipyridyl ligands. *Dalt. Trans.* **48**, 8084–8093 (2019).
  153. Zhang, W. *et al.* Recent Advances of Silver-Based Coordination Polymers on Antibacterial Applications. *Molecules* **27**, 7166 (2022).
  154. Li, R., Chen, T. & Pan, X. Metal-Organic-Framework-Based Materials for Antimicrobial Applications. *ACS Nano* **15**, 3808–3848 (2021).
  155. Kaur, N. *et al.* Metal-organic framework based antibiotic release and antimicrobial response: An overview. *CrystEngComm* **22**, 7513–7527 (2020).
  156. Cao, P. *et al.* Killing Oral Bacteria Using Metal-Organic Frameworks. *Ind. Eng. Chem. Res.* **59**, 1559–1567 (2020).
  157. André, V. *et al.* Mg- and Mn-MOFs Boost the Antibiotic Activity of Nalidixic Acid. *ACS Appl. Bio Mater.* **2**, 2347–2354 (2019).
  158. Sun, Z. *et al.* Research progress in metal-organic frameworks (MOFs) in CO<sub>2</sub> capture from post-combustion coal-fired flue gas: Characteristics, preparation, modification and applications. *J. Mater. Chem. A* **10**, 5174–5211 (2022).
  159. Dietzel, P. D. C. *et al.* Adsorption properties and structure of CO<sub>2</sub> adsorbed on open coordination sites of metal-organic framework Ni<sub>2</sub>(dhtp) from gas adsorption, IR spectroscopy and X-ray diffraction. *Chem. Commun.* **2**, 5125–5127 (2008).
  160. Martínez, F., Sanz, R., Orcajo, G., Briones, D. & Yáñez, V. Amino-impregnated MOF materials for CO<sub>2</sub> capture at post-combustion conditions. *Chem. Eng. Sci.* **142**, 55–61 (2016).
  161. Beyzavi, M. H. *et al.* A hafnium-based metal-organic framework as an efficient and multifunctional catalyst for facile CO<sub>2</sub> fixation and regioselective and enantioselective epoxide activation. *J. Am. Chem. Soc.* **136**, 15861–15864 (2014).
  162. Gao, W., Wu, H., Leng, K., Sun, Y. & Ma, S. Inserting CO<sub>2</sub> into Aryl C–H Bonds of Metal–Organic Frameworks: CO<sub>2</sub> Utilization for Direct Heterogeneous C–H Activation. *Angew. Chemie* **128**, 5562–5566 (2016).
  163. Wang, R. *et al.* Metal-Organic-Framework-Mediated Nitrogen-Doped Carbon for CO<sub>2</sub> Electrochemical Reduction. *ACS Appl. Mater. Interfaces* **10**, 14751–14758 (2018).
  164. Abdelkader-Fernández, V. K., Fernandes, D. M. & Freire, C. Carbon-based electrocatalysts for CO<sub>2</sub> electroreduction produced via MOF, biomass, and other precursors carbonization: A review. *J. CO<sub>2</sub> Util.* **42**, (2020).
  165. Huang, X. & Zhang, Y. B. Reticular materials for electrochemical reduction of CO<sub>2</sub>. *Coord. Chem. Rev.* **427**, 213564 (2021).
  166. Lin, S., Usov, P. M. & Morris, A. J. The role of redox hopping in metal-organic framework electrocatalysis. *Chem. Commun.* **54**, 6965–6974 (2018).
  167. Liu, J. *et al.* 2D Conductive Metal–Organic Frameworks: An Emerging Platform for Electrochemical Energy Storage. *Angew. Chemie* **133**, 5672–5684 (2021).
  168. Dong, B. X. *et al.* Electrochemical Reduction of CO<sub>2</sub> to CO by a Heterogeneous Catalyst of Fe-

- Porphyrin-Based Metal-Organic Framework. *ACS Appl. Energy Mater.* **1**, 4662–4669 (2018).
169. Rauf, A. *et al.* Copper(ii)-based coordination polymer nanofibers as a highly effective antibacterial material with a synergistic mechanism. *Dalt. Trans.* **48**, 17810–17817 (2019).
  170. Surendra Kumar, R., Arif, I. A., Ahamed, A. & Idhayadhulla, A. Anti-inflammatory and antimicrobial activities of novel pyrazole analogues. *Saudi J. Biol. Sci.* **23**, 614–620 (2016).
  171. Noriega, S., Cardoso-Ortiz, J., López-Luna, A., Cuevas-Flores, M. D. R. & Flores De La Torre, J. A. The Diverse Biological Activity of Recently Synthesized Nitro Compounds. *Pharmaceuticals* **15**, (2022).
  172. Coelho, A. A. Indexing of powder diffraction patterns by iterative use of singular value decomposition. *J. Appl. Crystallogr.* **36**, 86–95 (2003).
  173. Topas, V3.0; Bruker AXS: Karlsruhe, Germany, 2005.
  174. Coelho, A. A. Whole-profile structure solution from powder diffraction data using simulated annealing research papers. *J. Appl. Crystallogr.* 899–908 (2000).
  175. Young, R. . IUCr Monograph N. 5. *Oxford University Press: New York* (1981).
  176. Cheary, B. Y. R. W. & Coelho, A. A Fundamental Parameters Approach to X-ray Line-Profile Fitting. *J. Appl. Crystallogr.* 109–121 (1992) doi:10.1107/S0021889891010804.
  177. Regiec, A., Mastalarz, H. & Wojciechowski, P. Theoretical anharmonic Raman and infrared spectra with vibrational assignments and NBO analysis for 1-methyl-4-nitropyrazole. *J. Mol. Struct.* **1061**, 166–174 (2014).
  178. Salah, I., Parkin, I. P. & Allan, E. Copper as an antimicrobial agent: Recent advances. *RSC Adv.* **11**, 18179–18186 (2021).
  179. Jiménez-Jiménez, C., Moreno, V. M. & Vallet-Regí, M. Bacteria-Assisted Transport of Nanomaterials to Improve Drug Delivery in Cancer Therapy. *Nanomaterials* **12**, 1–24 (2022).
  180. Solioz, M., Abicht, H. K., Mermoud, M. & Mancini, S. Response of Gram-positive bacteria to copper stress. *J. Biol. Inorg. Chem.* **15**, 3–14 (2010).
  181. Quintana, J., Novoa-Aponte, L. & Argüello, J. M. Copper homeostasis networks in the bacterium *Pseudomonas aeruginosa*. *J. Biol. Chem.* **292**, 15691–15704 (2017).
  182. Yoneyama, H. & Nakae, T. Protein C (OprC) of the outer membrane of *Pseudomonas aeruginosa* is a copper-regulated channel protein. *Microbiology* **142**, 2137–2144 (1996).
  183. Bittner, L. M., Kraus, A., Schäkermann, S. & Narberhaus, F. The copper efflux regulator CueR is subject to ATP-dependent proteolysis in *Escherichia coli*. *Front. Mol. Biosci.* **4**, 1–13 (2017).
  184. Zhang, X. *et al.* Design and applications of water-stable metal-organic frameworks: status and challenges. *Coord. Chem. Rev.* **423**, 213507 (2020).
  185. Farha, O. K. *et al.* Designing higher surface area metal-organic frameworks: Are triple bonds better than phenyls? *J. Am. Chem. Soc.* **134**, 9860–9863 (2012).
  186. Cmarik, G. E., Kim, M., Cohen, S. M. & Walton, K. S. Tuning the adsorption properties of uio-66 via ligand functionalization. *Langmuir* **28**, 15606–15613 (2012).
  187. Marchetti, F. *et al.* Role of hydrazone substituents in determining the nuclearity and antibacterial activity of Zn(ii) complexes with pyrazolone-based hydrazones. *Dalt. Trans.* **51**, 14165–14181 (2022).
  188. Cao, L. & Caldeira, K. Atmospheric CO<sub>2</sub> stabilization and ocean acidification. *Geophys. Res. Lett.* **35**, 1–5

- (2008).
189. Domasevitch, K. V., Gospodinov, I., Krautscheid, H., Klapötke, T. M. & Stierstorfer, J. Facile and selective polynitrations at the 4-pyrazolyl dual backbone: Straightforward access to a series of high-density energetic materials. *New J. Chem.* **43**, 1305–1312 (2019).
  190. Vismara, R. *et al.* Efficient hexane isomers separation in isorecticular bipyrazolate metal-organic frameworks: The role of pore functionalization. *Nano Res.* **14**, 532–540 (2021).
  191. Mosca, N. *et al.* Nitro-Functionalized Bis ( pyrazolate ) Metal – Organic Frameworks as Carbon Dioxide Capture Materials under Ambient Conditions. *Chem. - A Eur. J.* **24**, 13059–13377 (2018).
  192. Schell, J., Casas, N., Pini, R. & Mazzotti, M. Pure and binary adsorption of CO<sub>2</sub>, H<sub>2</sub>, and N<sub>2</sub> on activated carbon. *Adsorption* **18**, 49–65 (2012).
  193. Boldog, I., Rusanov, E. B., Chernega, A. N., Sieler, J. & Domasevitch, K. V. Acentric extended solids by self assembly of 4,4'-bipyrazolyls. *Angew. Chemie - Int. Ed.* **40**, 3435–3438 (2001).
  194. Vismara, R. *et al.* Tuning Carbon Dioxide Adsorption Affinity of Zinc(II) MOFs by Mixing Bis(pyrazolate) Ligands with N-Containing Tags. *ACS Appl. Mater. Interfaces* **11**, 26956–26969 (2019).
  195. Blatov, V. A., Shevchenko, A. P. & Proserpio, D. M. Applied topological analysis of crystal structures with the program package Topospro. *Cryst. Growth Des.* **14**, 3576–3586 (2014).
  196. Ning, G. H., Matsumura, K., Inokuma, Y. & Fujita, M. A saccharide-based crystalline sponge for hydrophilic guests. *Chem. Commun.* **52**, 7013–7015 (2016).
  197. Zhang, H. X., Wang, F., Tan, Y. X., Kang, Y. & Zhang, J. Homochiral porous metal-organic frameworks containing only achiral building blocks for enantioselective separation. *J. Mater. Chem.* **22**, 16288–16292 (2012).
  198. Zhou, Z., He, C., Xiu, J., Yang, L. & Duan, C. Metal-Organic Polymers Containing Discrete Single-Walled Nanotube as a Heterogeneous Catalyst for the Cycloaddition of Carbon Dioxide to Epoxides. *J. Am. Chem. Soc.* **137**, 15066–15069 (2015).
  199. Khutia, A. & Janiak, C. Programming MIL-101Cr for selective and enhanced CO<sub>2</sub> adsorption at low pressure by postsynthetic amine functionalization. *Dalt. Trans.* **43**, 1338–1347 (2014).
  200. Watabe, T. & Yogo, K. Isotherms and isosteric heats of adsorption for CO<sub>2</sub> in amine-functionalized mesoporous silicas. *Sep. Purif. Technol.* **120**, 20–23 (2013).
  201. Mousavi, B. *et al.* CO<sub>2</sub> Cycloaddition to Epoxides by using M-DABCO Metal–Organic Frameworks and the Influence of the Synthetic Method on Catalytic Reactivity. *ChemistryOpen* **6**, 674–680 (2017).
  202. Mian, M. R. *et al.* Catalytic degradation of an organophosphorus agent at Zn-OH sites in a metal-organic framework. *Chem. Mater.* **32**, 6998–7004 (2020).
  203. Mercuri, G. *et al.* Carbon Dioxide Capture and Utilization with Isomeric Forms of Bis(amino)-Tagged Zinc Bipyrazolate Metal–Organic Frameworks. *Chem. - A Eur. J.* **27**, 4746–4754 (2021).
  204. Wang, C. *et al.* A promising single-atom Co-N-C catalyst for efficient CO<sub>2</sub> electroreduction and high-current solar conversion of CO<sub>2</sub> to CO. *Appl. Catal. B Environ.* **304**, 120958 (2022).
  205. Chen, X. *et al.* Promoting water dissociation for efficient solar driven CO<sub>2</sub> electroreduction via improving hydroxyl adsorption. *Nat. Commun.* **14**, 751 (2023).
  206. Qian, Y., Liu, Y., Tang, H. & Lin, B. L. Highly efficient electroreduction of CO<sub>2</sub> to formate by

- nanorod@2D nanosheets SnO. *J. CO2 Util.* **42**, 101287 (2020).
207. Zhang, K. *et al.* An iron-porphyrin grafted metal–organic framework as a heterogeneous catalyst for the photochemical reduction of CO<sub>2</sub>. *J. Photochem. Photobiol.* **10**, 100111 (2022).
  208. Kung, C. W. *et al.* Copper Nanoparticles Installed in Metal–Organic Framework Thin Films are Electrocatalytically Competent for CO<sub>2</sub> Reduction. *ACS Energy Lett.* **2**, 2394–2401 (2017).
  209. Hod, I. *et al.* Fe-Porphyrin-Based Metal–Organic Framework Films as High-Surface Concentration, Heterogeneous Catalysts for Electrochemical Reduction of CO<sub>2</sub>. *ACS Catal.* **5**, 6302–6309 (2015).
  210. Chen, R. *et al.* Toward High-Performance CO<sub>2</sub>-to-C<sub>2</sub> Electroreduction via Linker Tuning on MOF-Derived Catalysts. *Small* **18**, (2022).
  211. Huo, H., Wang, J., Fan, Q., Hu, Y. & Yang, J. Cu-MOFs Derived Porous Cu Nanoribbons with Strengthened Electric Field for Selective CO<sub>2</sub> Electroreduction to C<sub>2</sub>+ Fuels. *Adv. Energy Mater.* **11**, 1–7 (2021).
  212. Yang, D. & Wang, X. 2D  $\pi$ -conjugated metal–organic frameworks for CO<sub>2</sub> electroreduction. *SmartMat* **3**, 54–67 (2022).
  213. Zhao, Y. *et al.* Nanoengineering Metal–Organic Framework-Based Materials for Use in Electrochemical CO<sub>2</sub> Reduction Reactions. *Small* **17**, (2021).
  214. Zhou, Y. *et al.* Bimetallic metal–organic frameworks and MOF-derived composites: Recent progress on electro- and photoelectrocatalytic applications. *Coord. Chem. Rev.* **451**, 214264 (2022).
  215. Wu, J. X., Yuan, W. W., Xu, M. & Gu, Z. Y. Ultrathin 2D nickel zeolitic imidazolate framework nanosheets for electrocatalytic reduction of CO<sub>2</sub>. *Chem. Commun.* **55**, 11634–11637 (2019).
  216. Chang, F. *et al.* *Copper-Based Catalysts for Electrochemical Carbon Dioxide Reduction to Multicarbon Products. Electrochemical Energy Reviews* vol. 5 (Springer Nature Singapore, 2022).
  217. Bail, A. Le, Duroy, H. & Fourquet, J. L. Ab-initio structure determination of LiSbWO<sub>6</sub> by X-Ray powder diffraction. *Mat. Res. Bull.* **23**, 447–452 (1988).
  218. H. M. Rietveld. A Profile Refinement Method for Nuclear and Magnetic Structures. *J. Appl. Crystallogr.* **2**, 65–70 (1969).
  219. Biemmi, E., Christian, S., Stock, N. & Bein, T. High-throughput screening of synthesis parameters in the formation of the metal-organic frameworks MOF-5 and HKUST-1. *Microporous Mesoporous Mater.* **117**, 111–117 (2009).
  220. Julien, P. A., Mottillo, C. & Friščić, T. Metal-organic frameworks meet scalable and sustainable synthesis. *Green Chem.* **19**, 2729–2747 (2017).
  221. Ye, J., Yan, J., Peng, Y., Li, F. & Sun, J. Metal-organic framework-based single-atom catalysts for efficient electrocatalytic CO<sub>2</sub> reduction reactions. *Catal. Today* **410**, 68–84 (2023).
  222. Narváez-Celada, D. & Varela, A. S. CO<sub>2</sub> electrochemical reduction on metal-organic framework catalysts: current status and future directions. *J. Mater. Chem. A* **10**, 5899–5917 (2022).

## List of publications

*“Antibacterial Activity of Copper Pyrazolate Coordination Polymers”*

Corrado Di Nicola, Stefania Scuri, Fabio Marchetti, Alessia Tombesi, Sonila Xhafa, Patrizio Campitelli, Simona Galli, Iolanda Grappasonni, Claudio Pettinari (in preparation)

*“CO<sub>2</sub> capture and conversion to C1 chemicals with mixed-metal copper/nickel bis(amino)-bipyrazolate Metal-Organic Frameworks”*

Patrizio Campitelli, Alessia Tombesi, Corrado Di Nicola, Claudio Pettinari, Anna Mauri, Simona Galli, Tongan Yan, Dahuan Liu, Jiaxin Duan, Subhadip Goswami, Giulia Tuci, Giuliano Giambastiani, Joseph T. Hupp, Andrea Rossin (submitted)

*“Coordination polymers of d- and f-elements with (1,4-phenylene)dithiazole dicarboxylic acid”*

Kostiantyn Domasevich, Patrizio Campitelli, Marco Moroni, Simona Bassoli, Giorgio Mercuri, Matteo Pugliesi, Giuliano Giambastiani, Corrado Di Nicola, Andrea Rossin, Simona Galli  
Inorganica Chimica Acta, (2022), 537, 120923

*“Carbon Dioxide Capture and Utilization with Isomeric Forms of Bis(amino)-Tagged Zinc Bipyrazolate Metal-Organic Frameworks”*

Giorgio Mercuri, Marco Moroni, Kostiantyn V. Domasevitch, Corrado Di Nicola, Patrizio Campitelli, Claudio Pettinari, Giuliano Giambastiani, Simona Galli, Andrea Rossin  
Chemistry – A European Journal, (2021), 27, 4746 –4754

*“On the Capability of Oxidovanadium(IV) Derivatives to Act as All-Around Catalytic Promoters since the Prebiotic World”*

Patrizio Campitelli, Marcello Crucianelli  
Molecules, (2020), 25, 13, 3073

*“Ionic liquids vs conventional solvents: A comparative study in the selective catalytic oxidations promoted by oxovanadium(IV) complexes”*

Patrizio Campitelli, Massimiliano Aschi, Corrado Di Nicola, Fabio Marchetti, Riccardo Pettinari, Marcello Crucianelli  
Applied Catalysis A General (2020), 599, 1176222

## Contributions to conferences

Interregional Meeting of the Italian Chemical Society – Section Toscana, Umbria, Marche and Abruzzo (TUMA 2022), Perugia, September 1-2, 2022

Oral communication, entitled: *“Zinc and copper metal-organic frameworks based on a series of bipyrazolate linkers as potential antibacterial and antifungal agents”*

Authors: Patrizio Campitelli, Sonila Xhafa, Alessia Tombesi, Fabio Marchetti, Claudio Pettinari, Corrado Di Nicola, Riccardo Pettinari, Laura Olivieri, Stefania Scuri.

XXVII National Meeting of the Italian Chemical Society, Virtual Congress, September 14-23, 2021

Oral communication, entitled: *“Amino-decorated Zinc Bipyrazolate MOFs, an Example of Carbon Dioxide Capture and Reuse (CCR)”*

Authors: Patrizio Campitelli, Giorgio Mercuri, Kostiantyn V. Domasevitch, Corrado Di Nicola, Claudio Pettinari, Simona Galli, Andrea Rossin.

Poster Communication, entitled: *“Selenophene-based mixed-linker metal-organic frameworks: synthesis, characterization and luminescent properties”*

Authors: Giorgio Mercuri, Patrizio Campitelli, Corrado Di Nicola, Giuliano Giambastiani, Andrea Rossin, Andrea Fermi, Giacomo Bergamini, Marco Moroni, Simona Galli.

ISOC:13th International School of Organometallic Chemistry, Virtual Congress, September 1-3, 2021

Oral Communication, entitled: *“Cu(II) Pyrazolate-based Coordination Polymers: Synthesis, Characterization and Antibacterial Properties”*

Authors: Patrizio Campitelli, Corrado Di Nicola, Alessia Tombesi, Claudio Pettinari, Fabio Marchetti, Riccardo Pettinari, Simona Galli, Stefania Scuri.

SCI-sezione Abruzzo, I giovani e la Chimica in Abruzzo, Virtual Congress, July 5-6, 2021

Oral Communication, entitled: *“Investigation of Antibacterial activity of Cu(II)pyrazolate Coordination Polymers”*

Authors: Patrizio Campitelli, Corrado Di Nicola, Alessia Tombesi, Claudio Pettinari, Fabio Marchetti, Riccardo Pettinari, Simona Galli, Stefania Scuri.

Second International School on Porous Materials (MOFsSchool2021), Virtual Congress, June 21-25, 2021

**Poster Communication A**, entitled: *“Amino-decorated zinc bipyridolate MOFs for catalytic conversion of carbon dioxide: an experimental and computational study”*

**Authors:** Patrizio Campitelli, Giorgio Mercuri, Corrado Bacchiocchi, Kostiantyn V. Domasevitch, Corrado Di Nicola, Claudio Pettinari, Simona Galli, Andrea Rossin

**Poster Communication B** entitled: *“Zirconium Metal-Organic Frameworks containing a biselenophene linker: from synthesis to luminescent applications”*

**Authors:** Giorgio Mercuri, Patrizio Campitelli, Corrado Di Nicola, Andrea Fermi, Giacomo Bergamini, Marco Moroni, Simona Galli, Giuliano Giambastiani, Andrea Rossin.



## *Acknowledgements*

At the end of this PhD thesis work, I would like first to thank my supervisor Prof. Corrado Di Nicola immensely for guiding me through these three years of research and for his valuable advice, transmitting to me passion and expertise.

I would also to express my gratitude to Prof. Fabio Marchetti, Prof. Riccardo Pettinari and Prof. Claudio Pettinari who have made significant contributions to my academic education.

A special thought is dedicated to Dr. Stefania Scuri. It was great and fun to work together and thanks for patiently and rigorously introducing me to the world of microbiology.

I would also like to especially thank Prof. Omar Farha who hosted me for my six-month visiting period in his laboratories at Northwestern University in Evanston, IL, USA. It was truly an honor to work with his extraordinary research group.

At this point, I can't help but thank my work colleagues who have been sincere fellow travelers, in the good times but also in the bad times.

In particular, thank you Leonardo for putting up with me every day and for the long calls at a seven-hour time difference. Thank you Giorgio for your irony and for being able to always put me in a good mood and Federico for your awful jokes and for being sensitive and understanding at every opportunity. Thank you Andrea for being a pain in the neck but for always being there. Thank you Noemi: you're such a funny and crazy friend! Thanks Sonila for your directness, honesty and for being supportive. Thank you Alessia for teaching me so many things and for always being motivating as a colleague, a group leader and, most of all, as a friend.

Furthermore, I would like to express my gratitude to my family who never stops making his affection for me felt and who always tries to encourage me in achieving my goals.

Last but not least, a special thanks goes to Alice. I know, I am not an easy person to deal with, but you make me feel loved as I am and you are so deeply important to me.